Analytical Ultracentrifugation of Inorganic Colloids

Sedimentation Velocity of Interacting and Non-Interacting Particles

K.L. Planken

Analytical Ultracentrifugation of Inorganic Colloids

Sedimentation Velocity of Interacting and Non-Interacting Particles

Universiteit Utrecht

ISBN 978-90-393-4798-0

Keywords: Analytical Ultracentrifugation/Sedimentation Velocity/UltraScan/Particle Size and Shape Distributions/Polydispersity/Dipolar Attractions/Double-Layer Repulsions/Colloidal Spheres and Rods.

Analytical Ultracentrifugation of Inorganic Colloids

Sedimentation Velocity of Interacting and Non-Interacting Particles

Analytische Ultracentrifugatie van Anorganische Colloïden

Sedimentatiesnelheid van Wisselwerkende en Niet-Wisselwerkende Deeltjes

(met een samenvatting in het Nederlands)

Proefschrift

ter verkrijging van de graad van doctor aan de
Universiteit Utrecht op gezag van de rector magnificus,
prof. dr. J.C. Stoof, ingevolge het besluit van het
college voor promoties in het openbaar te verdedigen
op maandag 19 mei 2008 des middags te 14.30 uur

door

Karel Lodewijk Planken

geboren op 1 november 1975 te 's-Gravenhage

Promotor: Prof. dr. A.P. Philipse

"When the only tool you have is a hammer,
every problem begins to resemble a nail."

Abraham H. Maslow

"AUC is a lovely technique, but not necessarily
the best way to study everything!"

Allen P. Minton

BC Nederland B.V. contributed to the printing costs of this thesis

Cover: Fringe pattern (a negative of Figure 2.6) acquired with a Rayleigh interference optical system (Beckman Coulter^{TM} Optima^{TM} XL-I analytical ultracentrifuge) in the early stage of a sedimentation velocity analytical ultracentrifugation run. The refractive index gradients, corresponding to the sedimentation boundary (solvent-dispersion interface), results in the displacement (bending) of achromatic fringes. The sample is a dispersion of colloidal rigid rods (boehmite needles coated with silica, see chapter 8).
Design and layout: K.L. Planken with LaTeX

Contents

Part 1

Background

1

Thesis Introduction

Analytical ultracentrifugation (AUC) has been widely applied in biochemistry [1], biophysics and pharmacy [2]. In these fields proteins, DNA and RNA and their interactions are studied via sedimentation velocity and sedimentation-diffusion equilibrium ultracentrifugation [3,4]. AUC experiments provide a wealth of information on solution and dispersion compositions. Quantities that are obtained from such experiments are sedimentation and diffusion coefficients. From these quantities parameters as molecular weights, particle shapes, hydrodynamic radii and the shapes of particle size distributions for homogeneous and heterogeneous solutes or colloids (mono-, pauci- and polydisperse particles) can be computed. Furthermore, sedimentation velocity experiments allow determining whether the system shows self-association (equilibrium constants) or aggregation. In physical and colloid chemistry AUC has been less extensively employed compared to the field of biophysics, even though it was initially developed by Theodor Svedberg [5–7] (Fleräng 1884 – Örebro 1971, Sweden) and co-workers in the nineteen twenties (Figure 1.1) to study gold particle size distributions [8]. For his work on the ultracentrifuge, Svedberg was awarded the Nobel Prize for chemistry in 1926.

Remarkably, we found a symposium-report [9] on ultracentrifugation that was held in Utrecht (The Netherlands), during the Second World War, on March 15 in 1941. Various oil-turbine and pneumatically driven ultracentrifuges are discussed in the latter report. Developed in 1947, the Spinco (Specialized Instruments Corporation) Model E analytical ultracentrifuge was equipped with an optical system so that spinning macromolecules or particles could be detected via photography. For the data acquisition and analysis, only analog signals were processed. An image of the Spinco Model E analytical ultracentrifuge of the Van 't Hoff Laboratory is shown in Figure 1.2. The centrifuge was purchased in 1954, probably financially supported by the Marshall-plan, at the time (1946-1981) in which the laboratory was directed by Prof. J.T.G. Overbeek (1911-2007).

P.F. Mijnlieff [10] was the first PhD student (1958) at the Van 't Hoff Laboratory conducting research with special emphasis on analytical ultracentrifugation, studying colloidal electrolytes with some applications to proteins and sodium lauryl sulfate. Mijnlieff was followed by R.C. Groot [11], who studied via ultracentrifugation the stability of oil in water emulsions (1965). Other PhD student research projects conducted at the Van 't Hoff Laboratory, employing analytical ultracentrifugation, are: (1) the comparison of the concentration dependent static light scattering and sedimentation velocity measurements (1982) to check the validity of different theories, including hard-sphere and hydrodynamic interactions [12], (2) the influence of attractive interactions as a function of temperature on the concentration dependent sedimentation velocity for sterically stabilized silica particles [13] (1986), (3) the sedimentation and liquid permeation of inorganic colloids [14] (1995), (4) the concentration dependent sedimentation velocity of magnetic silica colloids [15] (1998) and (5) of DNA restriction fragments [16–18]

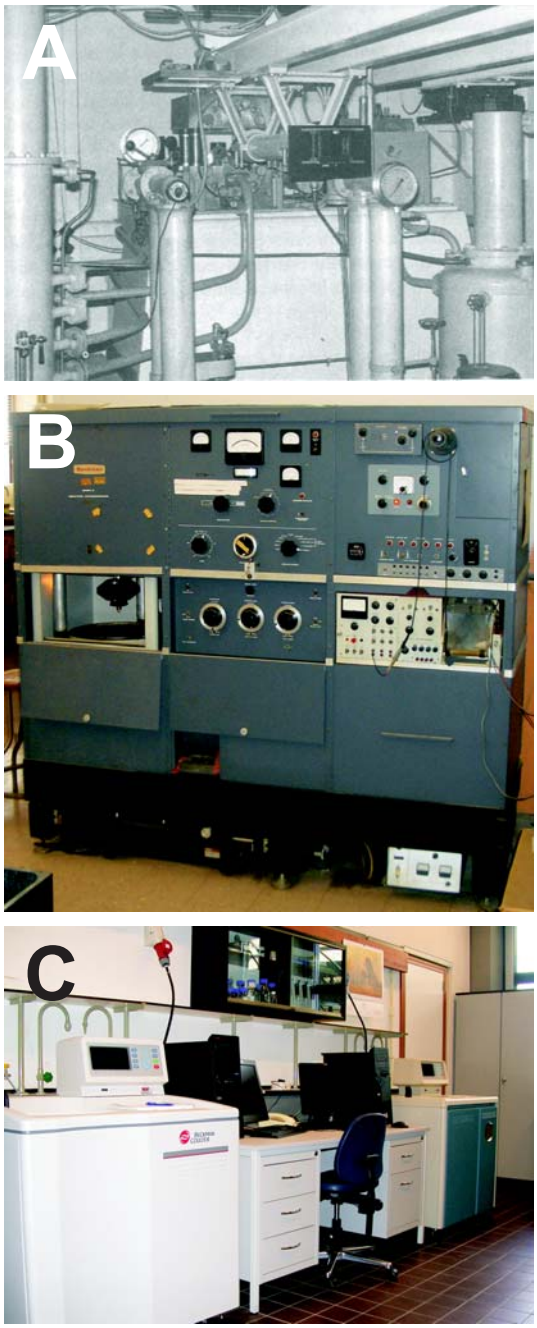

Figure 1.1: Images of various analytical ultracentrifuges. An early (oil turbine) analytical ultracentrifuge (reproduced from ref. [3] with kind permission of the Royal Society of Chemistry) as employed by T. Svedberg (image A). Image B shows the Specialized Instruments Corporation (Spinco/Beckman) Model E analytical ultracentrifuge. To date, the Beckman Coulter^{TM} Optima^{TM} XL-A (on the right of image C) and XL-I (on the left of image C) analytical ultracentrifuges are employed for sedimentation experiments. The AUC facility of our Van 't Hoff Laboratory in 2008 is shown in image C.

(2003, using a Beckman Coulter™ Optima™ XL-A), and (6) a study on the reversible association of silver iodide clusters and molybdenum oxides (2004) via sedimentation-diffusion equilibrium experiments to determine buoyant masses [19].

In the last decades substantial progress has been made regarding the instrumentation (see for example ref. [20] and Figure 1.1), mathematical analysis [21, 22], data-analysis software [23] and the implementation of relational data bases [23], laboratory information management systems (LIMS) and high throughput super computing using clusters that are connected via networks and the internet. A crucial step forward was the analog-to-digital conversion in the data acquisition process. These developments also further enhance the potential of AUC for the study of colloids and inorganic macromolecules, as is also illustrated by the work presented in this thesis.

The scope of this thesis is the investigation of inorganic colloids with special emphasis on their sedimentation velocity behavior and particle-interactions. After a brief introduction in chapter 2 of the basic theory and the instrumentation employed in AUC, the first case study in chapter 3 is on highly monodisperse polyoxometalates. In chapter 3 we show the direct evidence for the existence of $\{Mo_{132}\}$ Keplerate-type species in aqueous solution. A remarkable structural transformation in solution is found from sedimentation velocity absorbance optical data.

The sedimentation velocity analysis for monodisperse particles or solutes is relatively straightforward. However, the characterization of polydisperse particles with AUC, as discussed in chapter 4 for silica colloids, is much more challenging. Shapes of particle size distributions and the assessment of size polydispersity obtained from sedimentation velocity absorbance and interference optical data are compared. Results on particle radii from transmission electron microscopy images TEM and in particular hydrodynamic radii from dynamic light scattering experiments are matched with the results from analytical ultracentrifugation. One advantage of ultracentrifugation using the interference optics is that it also yields the specific particle volume via the differential refractive index for, in this case, homogeneous silica spheres.

Next, we return in chapter 5 to comparable monodisperse polyoxometalates as employed in chapter 3, to investigate the effect of an interaction energy that is on the order of several times the thermal energy at room temperature. This interaction results in the self-assembly of polyoxometalate monomers into supramolecular complexes, analogous to the formation of surfactant micelles or virus capsids. The self-association is unusually slow and occurs on a time scale of years, probably due to a high activation-energy. Since the association is relatively slow, the monomers and vesicles can be considered as non-interacting on the observation time scale of a sedimentation velocity experiment.

Spontaneous structure formation is also observed for magnetic colloids that are studied in chapters 6 and 7. In chapter 6 we discuss a simple dimerization model for the concentration dependent sedimentation of colloids with moderate attractions. For

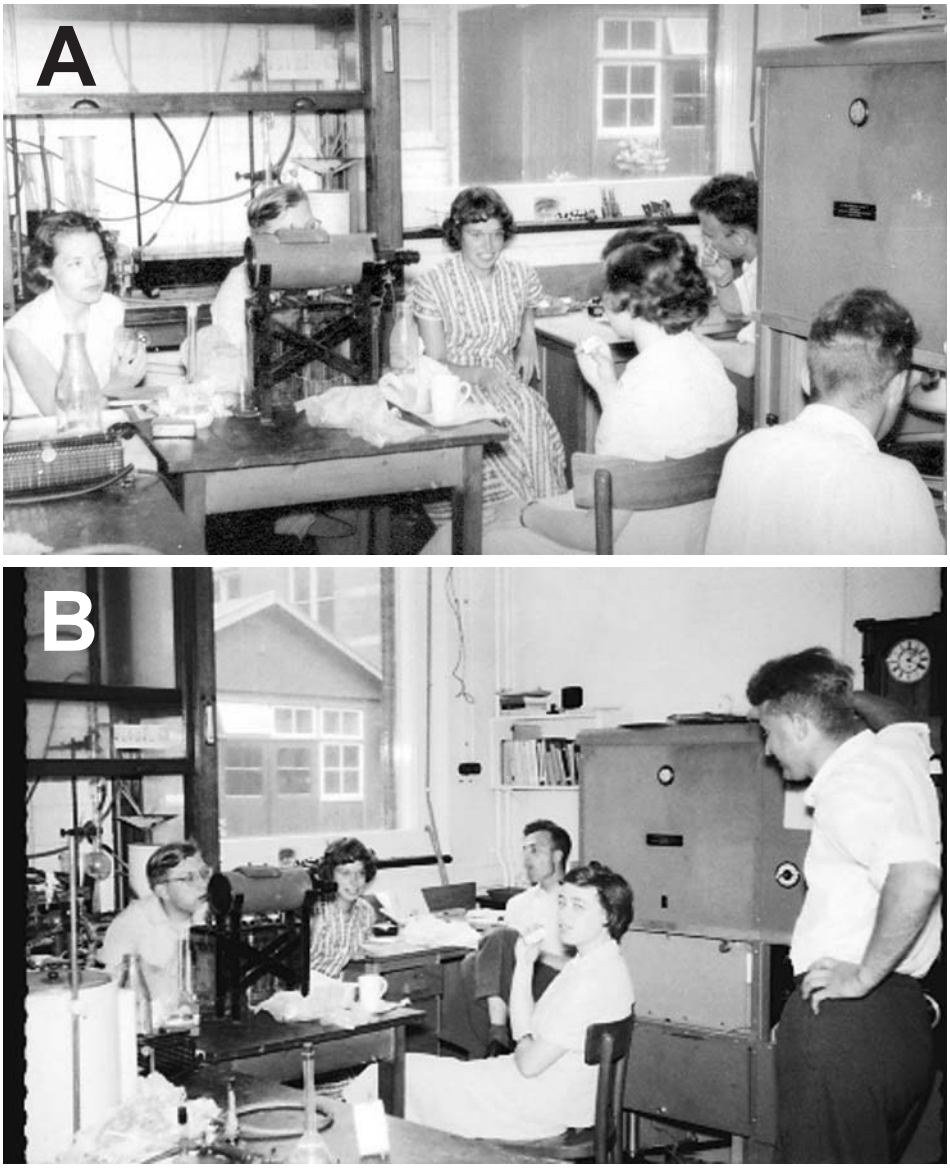

Figure 1.2: The Spinco Model E analytical ultracentrifuge at the Van 't Hoff Laboratory in 1957, on photographs taken by Jaap Lucassen. The centrifuge lab was also the lunch room. A lab-collaborator is placing a sample into the rotor (on the right of image A) while other people are having lunch or rolling a cigarette (Piet Mijnlieff). In image A, the people from left to right are Lydie Reintjes, Loek Jansen, unknown, Diete Rozemond-van Borselen, Piet Mijnlieff and unknown.

such attractive colloids that do not experience a significant activation-energy upon self-association, the modeling of the concentration dependent sedimentation in terms of dimerization thermodynamics is described in chapter 6. In chapter 7, the various theoretical predictions are compared to experimental results on the concentration dependent sedimentation velocity of magnetite colloids with tunable dipolar attractions. In contrast to the association of the polyoxometalates as studied in chapter 5, relatively small

magnetite colloids associate and dissociate rapidly, such that reversible association is observed on the time scale of sedimentation velocity runs. The common feature of the polyoxometalate and magnetite system is the presence of an inter-particle attraction. The main difference is the time scale of monomer association that results in a markedly different sedimentation behavior. The stoichiometry for these two associations are also very different: the relatively polydisperse magnetite monomers discretely associate into dimers, whereas the highly monodisperse polyoxometalate monomers form very polydisperse vesicles.

Finally, the salt- and concentration dependent sedimentation velocity of rigid colloidal rods is discussed in chapter 8. These rods are in many aspects quite different from the colloids studied in previous chapters: The colloidal rods have an elongated shape and due to their charge, the dominating interaction is repulsive, resulting in a *decrease* of the sedimentation rate with concentration in marked contrast to the *increase* observed for the magnetic colloids in chapter 7.

Acknowledgement

Jaap Lucassen and Hans Lyklema are acknowledged for providing historical information via personal communication and photographs. Henk N.W. Lekkerkerker drew our attention to ref. [9]. Marina Uit de Bulten-Weerensteyn and Emile Bakelaar are thanked for providing addresses of former lab workers and PhD thesis titles.

2

Analytical Ultracentrifugation Reviewed

Abstract

The basic analytical ultracentrifugation theory and the two fundamental types of experiments, namely sedimentation velocity and sedimentation-diffusion equilibrium, are discussed. Along with this discussion some instrumental issues are highlighted. The optical systems of the Beckman Coulter^{TM} Optima^{TM} XL-A and XL-I analytical ultracentrifuges, employed for the research reported in this thesis, are reviewed in more detail, including a discussion of potential pitfalls in conducting analytical ultracentrifugation experiments.

2.1. Introduction

In an analytical ultracentrifugation experiment, macromolecules or colloidal particles that are dissolved or dispersed in a liquid, are subjected to a centrifugal force proportional to the buoyant mass of the sedimenting species and the centrifugal field. The centrifugal field can be varied within a range of approximately $73 - 261,580 \times$ g for a radial position of 6.5 cm and with $g = 9.81\,m\,s^{-2}$. Such a centrifugal field range is sufficient to study even small molecules and ions. The centrifugal force causes the sedimentation of particles towards the cell-bottom or flotation of particles to the air-solution interface. Hereafter, only the sedimentation of particles is considered. Initially the particles are homogeneously distributed in the much weaker earth's gravitational field, but as soon as the rotor accelerates to attain the required angular velocity, the particles start to sediment. Eventually a time-invariant concentration distribution of colloids is developed, namely a sedimentation-diffusion (SD) equilibrium distribution. In a SD-equilibrium the weight of the colloids is balanced by a gradient in osmotic pressure. Dynamic sedimentation processes as well as the SD-equilibrium distribution can be monitored in an analytical ultracentrifuge with high resolution using optical techniques. In this chapter the two basic types of analytical ultracentrifugation experiments, namely sedimentation velocity and sedimentation-diffusion equilibrium experiments, as well as the instrument and the basic underlying theory of the latter two type experiments are briefly discussed. For more extensive overviews and more detailed information on analytical ultracentrifugal techniques and methods, the reader is referred to refs. [3] and [4].

Before entering this review it is appropriate to note the following. There are, of course, in addition to AUC many other analytical techniques that can be employed to investigate macromolecular solutions or colloidal dispersions. Examples are high-pressure liquid-, gas- and size exclusion-chromatography, surface plasmon resonance, mass spectrometry, calorimetry and capillary electrophoresis. As this thesis illustrates, AUC has some distinct advantages such as the resolving power with high resolution of particle sizes for even highly polydisperse samples. Further, AUC allows the characterization of shape, size and mass of statistically relevant numbers of macromolecules and colloids *in situ*. Moreover, AUC is a non-destructive analytical technique. There is, however, a certain price to pay [20]: AUC requires time and dedication to learn all ins and outs of the technique and to keep up with the developments regarding the instrumentation and in particular data analysis software [23]. For AUC, data acquisition and data analysis need careful attention, as will become clear in a closer look at various AUC studies that are addressed in this chapter.

2.2. The Basic Experiments

In analytical ultracentrifugation experiments, the distribution of the sedimenting or floating species in a liquid medium is determined via an optical signal that is proportional to the solute weight concentration. The signal is recorded at one single or many radial positions; i.e. distances from the center of rotation, as illustrated in Figure 2.1. In the case of sedimentation velocity experiments the signal also depends on time. Generally, cell-centerpieces (Figures 2.1 and 2.4) with two wedge-shaped sectors or compartments are employed for sedimentation velocity experiments and the like. One of these sectors is filled with a reference solvent or buffer, and the other with a sample solution containing solutes or colloids. For sedimentation-diffusion equilibrium experiments six-channel centerpieces are used, to increase the number of samples contained in a single AUC cell. Additionally, equilibrium is attained much earlier for shorter columns. The sectors in such six-channel centerpieces are rectangular. Cells containing the reference and sample solution are employed to record the signal that provides information on the sample composition. A sedimentation velocity run is performed at a relatively high angular velocity of the spinning rotor, such that the material is accumulated at the bottom of the cell within a few hours. During the experiment, which takes typically 2.5 hours, many radial scans are rapidly acquired one after another. One of these many sedimentation velocity scans is illustrated in panel A of Figure 2.1. Since the system attains a thermodynamic equilibrium state in a sedimentation-diffusion equilibrium experiment, typically after a few days or weeks, only one single radial scan for each rotor speed, wavelength and sample concentration is recorded (Figure 2.1, panel B).

2.3. Instrumentation

There are several optical systems available, such as absorbance optics or UV-Vis spectrophotometry, also with a multiwavelength detector [24], interference optics [25] and a fluorescence detection system [26–29], that have been successfully applied in analytical ultracentrifugation. For all these optical systems, the eventual digital data are send to a PC controller (Figure 2.2, 8 in image D) and stored on the computer's hard drive for analysis. The Beckman Coulter™ Optima™ XL-A and XL-I AUC, equipped with, respectively, the absorbance and the interference optical system, will be hereafter briefly discussed (Figure 2.4). Note that the absorbance optical system is also implemented in the Beckman Coulter™ Optima™ XL-I AUC, something which occasionally gives rise to confusion. In ref. [30], the interference and absorbance optical system with which the Beckman Coulter™ Optima™ XL-I AUC is equipped are mixed up: the experimental section mentions that the interference optics is employed though actually attenuance recordings are reported.

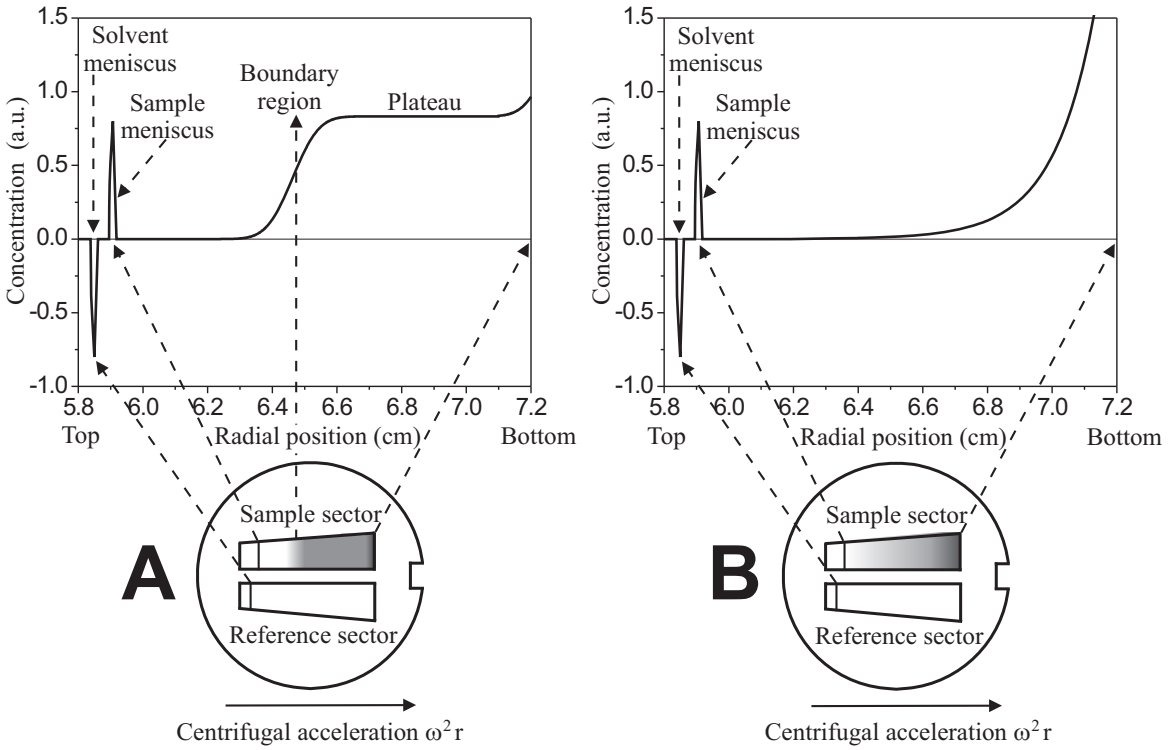

Figure 2.1: Schematic of a sedimentation velocity scan (panel A) and a sedimentation-diffusion equilibrium scan (panel B). Both scans were simulated with the Finite Element simulation module implemented in *UltraScan* [23]. The mid-run sedimentation velocity boundary is one out of many scans that are recorded during a sedimentation velocity experiment, whereas the sedimentation-diffusion equilibrium distribution yields one scan only for this particular concentration, wavelength and rotor speed.

Generally, the absorbance optics is used if (1) selectivity is required, (2) the concentrations of solutes absorbing light with a wavelength in between 200-600 nm is relatively low and (3) if the sample cannot be dialyzed. Contrary, the interference optics should be employed if (1) the reference solvent or buffer absorbs light of a wavelength below 675 nm (light source interference optics), (2) the solutes or particles do not absorb significantly and (3) a relatively high precision is required. The choice of the appropriate optical system for a given experiment is discussed in detail in ref. [25]. The advantages and drawbacks of these latter two optics and how the experimental sedimentation velocity results for colloidal dispersions are affected, are reported in chapter 4 for homogeneous silica particles and in chapter 8 for heterogeneous core-shell rods.

Though both optical systems are fundamentally different, the common feature is the synchronization of events as positioning the cell computed from the angular rotor velocity and the timing of the right moment at which the optical signal is detected during data acquisition.

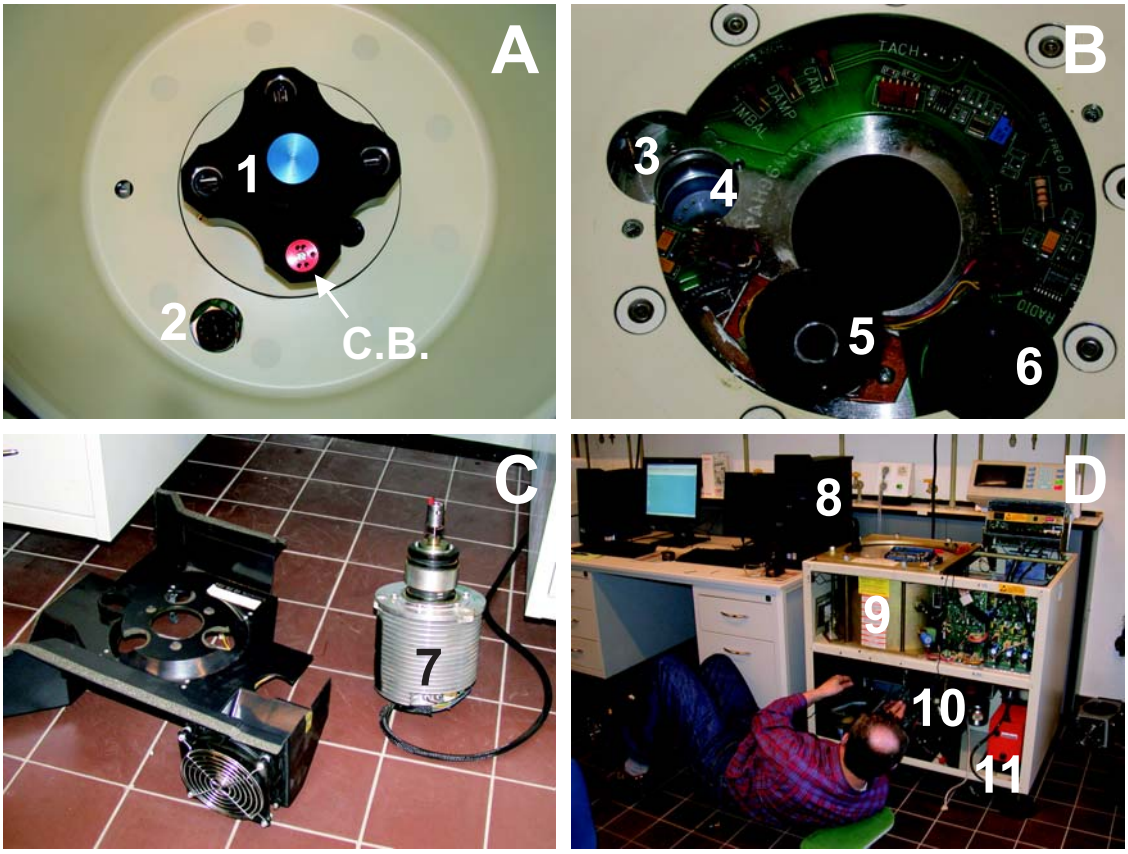

Figure 2.2: Some instrument parts of a Beckman Coulter™ Optima™ XL-A and XL-I AUC. Image A is a top view, showing the rotor chamber with an An-60 Ti rotor (1) loaded with 3 sample cells and a counterbalance (C.B.). The counterbalance has 4 reference holes for calibrating radial distances. A monochromator (Figure 2.3, 2 in image B) can be installed into the mounting receptacle (2). Removing consecutively the rotor, the safety plate, the PMT and the drive induction motor, the latter is shown in image C (7), gives image B. (3) is the pin of the radial step motor that drives the slit assembly, (4) is the PMT socket, (5) is the radiometer and (6) is the condenser lens (also see panel B of Figure 2.4) of the interference optical system. Furthermore, image D shows the PC controller (8), the rotor chamber (9) and the diffusion (10) and oil (11) pumps. In image D, Ronald de Vries (service engineer of Beckman Coulter International S.A.) is sorting electrical wires.

Every event during analytical ultracentrifugation is synchronized with the revolution and position of the rotor (Figure 2.2, 1 in image A). The rotor contains one or more samples for which the concentration distributions are to be measured as a function of the radial position and time. The synchronization is achieved by the detection of a small magnet implemented in the rotor. The location of rotor holes, containing AUC cell assemblies with reference and sample sectors (Figures 2.1 and 2.4), relative to the position of the magnet is achieved via a single delay-time calibration procedure. This delay-time calibration is performed when the rotor is accelerated to the intended angular velocity. Each rotor-hole position is then calculated from the magnet's position via

delay-times. The radial calibration is obtained from the counterbalance that has two holes for which the absolute radial position is known, see image A in Figure 2.2. We note here that the description in the Beckman Coulter™ ProteomeLab™ XL-A/XL-I instruction manual [31] of the radial calibration using the interference optical system is erroneous: the indicated positions of the inner and outer radii for the radial calibration are not accurate. We suggest to overlay a radial transmission scan obtained with the absorbance optics after radial calibration and an interference scan, both recorded through the counterbalance (image A in Figure 2.2), to check that the radial positioning is properly calibrated for the interference optics.

The radial calibration is only done at 3,000 rpm, to avoid a radial calibration off-set due to rotor stretching, which is significant above approximately 15,000 rpm. The rotor stretch may lead to radial calibration off-sets that exceed 200 μm at rotor speeds above 50,000 rpm.

The rotor temperature can be varied in the range from 0 to 30 °C with an accuracy of 0.5 °C and a precision of 0.3 °C. The temperature of the rotor chamber and in particular of the rotor should be equilibrated before rotor acceleration or while rotating at 3,000 rpm before the actual run is started. Also if experiments are performed at 4 °C it is good practice to pre-cool the rotor in a refrigerator. The vacuum in the rotor chamber is usually achieved within 20 minutes, at which the pressure is less than $2.6 \cdot 10^{-5}$ atm. The Beckman Coulter™ Optima™ AUC indicates the rotor chamber pressure in microns, which is equivalent to μm Hg. Such low pressures are achieved with an oil and diffusion pump (Figure 2.2, 10 and 11 in image D) that are connected to the rotor chamber. The diffusion pump is activated as soon as the rotor starts to spin. Acceleration of the rotor to angular velocities that exceed 6,000 rpm is not allowed if the rotor chamber pressure is above 50 μm Hg. Since the pressure in the rotor chamber is extremely low during a sedimentation run, the temperature should be monitored via a radiometer that is positioned underneath the rotor (5 in image B, Figure 2.2). The radiometer is based on the black body radiation principle. Initially, above 100 μm Hg, the temperature is determined with a thermocouple and adjusted according to the temperature change monitored by a thermistor. Below 100 μm Hg the temperature sensing switches to the radiometer.

2.3.1. Absorbance Optics

The absorbance optics comprises several components. The light source is a Xenon-flash lamp (Figure 2.3, 1 in image A), which is an electric discharge lamp that flashes with a maximum rate of 100 Hz. The emitted light from the Xenon lamp is directed through a pinhole into a monochromator (Figure 2.3, 2 in image B) where it is projected on a toroidal diffraction grating unit. The intended wavelength, for which the transmitted intensity through the reference and the sample sector is to be measured, is selected

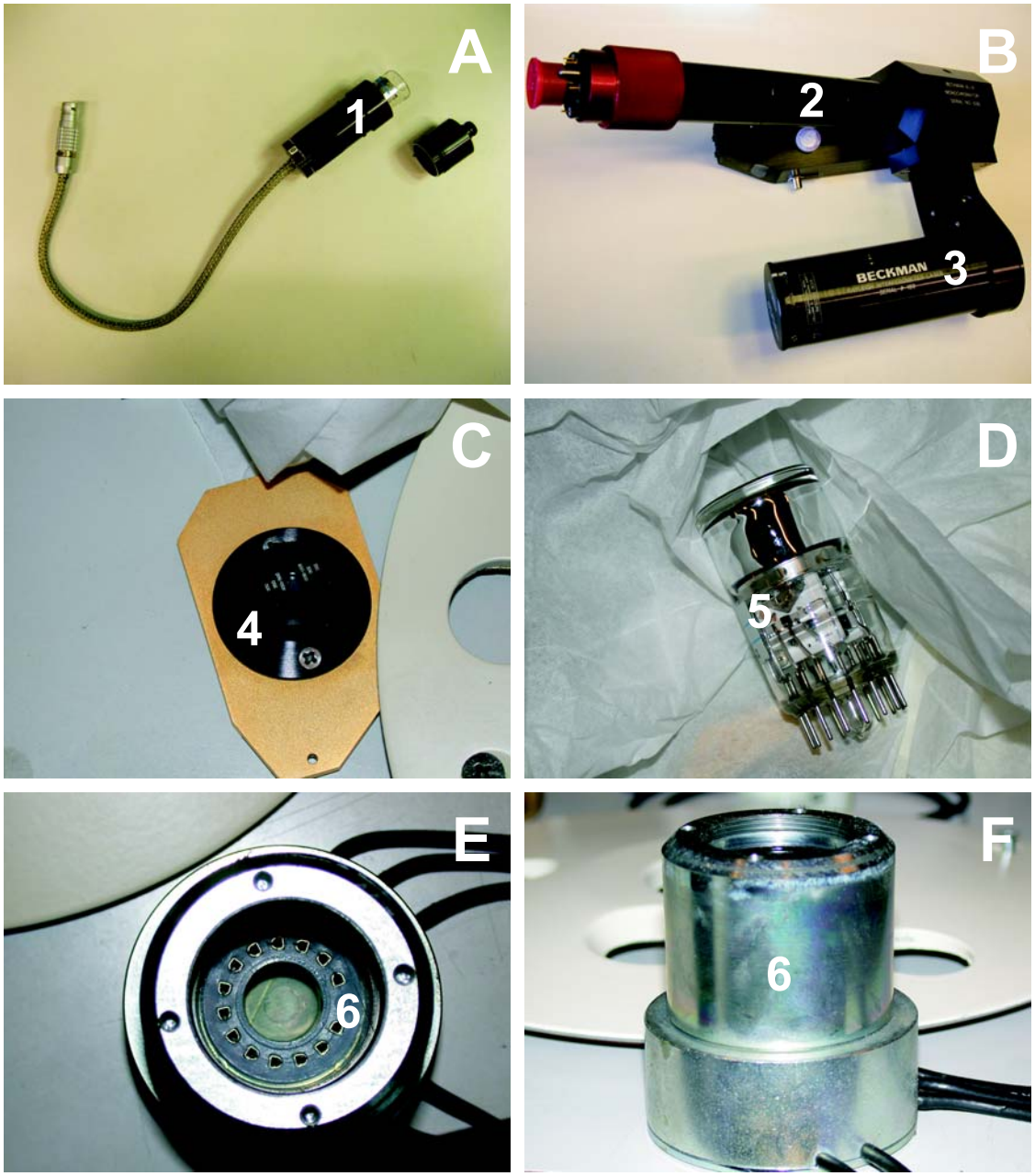

Figure 2.3: Essential parts of the absorbance optical system of a Beckman Coulter™ Optima™ XL-A AUC. The Xenon-flash lamp (1), serving as a light source is shown with its cap unscrewed in image A. A light beam of the Xenon-flash lamp passes through the monochromator (2), onto which also the laser diode for the interference optical system is mounted. The monochromator directs the light of a certain wavelength through the reference and sample sector, after which it falls onto the slit assembly that allows selecting a radial position. The intensity of light at that radial position is amplified via a photo-multiplier tube (PMT), shown in image D (5), which is mounted into a socket (6) that transmits the signal for processing.

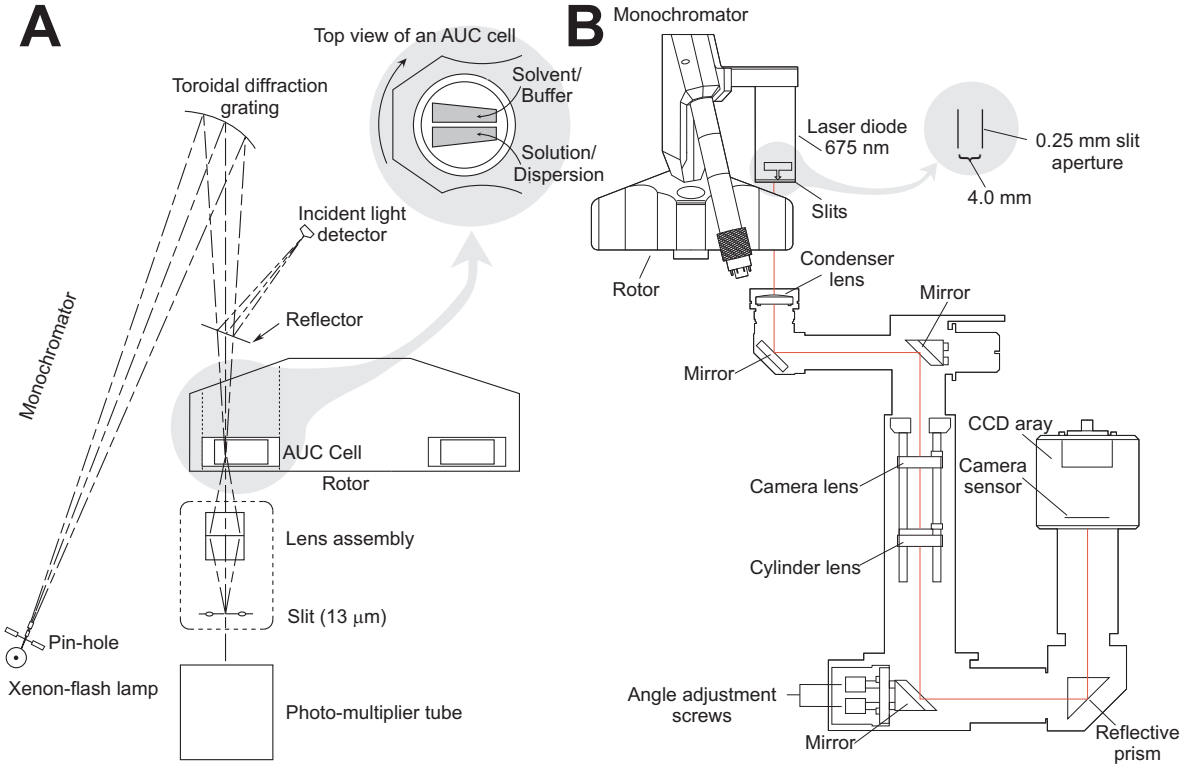

Figure 2.4: Absorbance (panel A, Beckman Coulter^{TM} Optima^{TM} XL-A and XL-I AUC) and interference (panel B, Beckman Coulter^{TM} Optima^{TM} XL-I AUC) optical systems (reproduced from ref. [31] with kind permission of Beckman Coulter^{TM}). Note that the laser diode is mounted onto the monochromator that is part of the absorbance optics (Figure 2.3, image B). The inset shows a top view of an AUC double-sector cell that can be put into the rotor. The sectors contain, respectively, the reference solvent or buffer, and the sample solution with solvent and solutes or colloids.

from the Xenon lamp emission spectrum by adjusting the angle of the diffracting grating unit. After the wavelength selection, which can be set with an accuracy of 4 nm, the intensity of the incident light beam is determined by directing the beam via a reflector onto an incident light detector (see panel A in Figure 2.4). The Xenon lamp flashes with a frequency that depends on the rotor speed to illuminate the complete reference sector after which the whole sample sector is illuminated. Above 6,000 rpm the flash rate of 100 Hz limits the scan rate for a given step-size of the slit-assembly (Figure 2.3, 4 in image C). The radial position at which the transmission of light is measured is selected by adjusting the position of the slit-assembly. This slit-assembly is composed of an hour glass made up of two lenses with underneath a small piece of aluminum foil that has a slit of approximately 13 μm perpendicular to the rotor radius. After passing the slit the intensity of transmitted light is detected by a photo-multiplier tube. To complete a radial scan at a fixed wavelength (λ) the slit-assembly is re-positioned continuously or by discrete increments (continuous or step mode) from the inner to the outer radial

position (Figure 2.1) by a radial positioning system. The step size can be varied from 10 μm to 0.5 cm. The transmissions recorded for, respectively, the reference ($I_{r,\lambda}$) and sample ($I_{s,\lambda}$) sectors are converted into an attenuance, $A_\lambda(r)$, via:

$$\log\left(\frac{I_{r,\lambda}}{I_{s,\lambda}}\right) = A_\lambda(r) = \epsilon_\lambda cl \tag{2.1}$$

with ϵ_λ the extinction coefficient, c the solute weight concentration and l the path length. The latter can be either 3 or 12 mm with which the concentration range can be increased maintaining a sufficiently high signal-to-noise ratio.

The signal-to-noise ratio is very important in acquiring high-quality absorbance optical data. The higher the signal-to-noise ratio, the smaller the root-mean-square deviations when the data are analyzed in for example whole-boundary fitting routines. Therefore the lenses and windows in the optical path as well as the light bulb should be clean. Due to the oil pump these lenses, windows and especially the lamp get contaminated by oil-vapor deposition which then burns onto the light bulb. The effect of a so-called bull's-eye on the light bulb is shown in Figure 2.5 graph A. Oil deposition onto the light bulb strongly diminishes the intensity in the UV region due to absorption. Cleaning the lamp regularly is required to maintain a high light intensity (Figure, graph B) and the associated high signal-to-noise ratio.

In principle, the analytical ultracentrifuge absorbance optical data can be acquired as intensity or absorbance data (eq 2.1). Furthermore, a wavelength spectrum at a fixed radial position or a radial scan at a fixed wavelength can be performed. Before accelerating the rotor to the speed at which the experiment is to be performed, several diagnostic scans should be performed at 3,000 rpm. Below 3,000 rpm, variations in the angular velocity become significant. The diagnostic scans serve to assure that the instrument is working properly and to determine the appropriate parameter values to optimize the sedimentation experiment using the absorbance optical system. The first scan is an intensity wavelength spectrum at 6.5 cm through an empty rotor hole to determine the intensity and the positions of emission peaks (Figure 2.5 graph B). This scan is performed along with a radial calibration using the counterbalance. The second scan is a radial intensity scan with $\lambda = 400$ nm through the counterbalance, to assure that the radial calibration is correct and to check that the slit is clean and not obstructed with dust. In case of dust contamination, the lines at 5.85 and 7.15 cm corresponding to the inner and outer reference radial positions will then not be vertical. The third scan is a wavelength attenuance spectrum at 6.5 cm through the sample cell to determine the wavelength range for which the absorbance is in between 0.5 and 0.9 OD (optical density). Exceeding an OD of 0.9, the signal-to-noise ratio decreases significantly, since only 10% of the total intensity is transmitted if the attenuance is 1.0 OD. When the attenuance values exceed 0.9 OD up to approximately 1.5 OD, the

signal-to-noise ratio is significantly affected as can be seen in refs. [32] and [33],. Moreover, above OD = 1.0 the dependence of the absorbance on the solute concentration may become non-linear. The wavelength corresponding to the highest intensity of an emission peak of the Xenon-flash lamp (Figure 2.3, 1 in image A) that falls in the wavelength range for which the sample's OD is between 0.5 and 0.9 is then selected to record the absorbance from 5.8 to 7.3 cm (fourth scan). With the latter scan the minimum and maximum radial positions are determined to minimize the radial range that should be scanned in order to increase the scan rate. The latter is especially important for sedimentation velocity runs. Additionally, displaying only the last acquired radial scan in a sedimentation velocity run on the PC controller increases the scan rate.

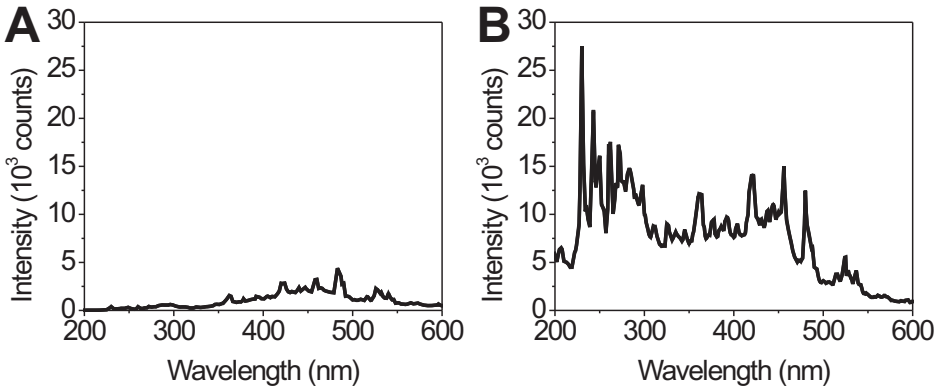

Figure 2.5: Emission spectra for a Xenon-flash lamp (electric discharge) with oil deposited onto the light bulb (graph A) and after cleaning the lamp with a cotton tip swab, toothpaste, water and ethanol (graph B).

2.3.2. Interference Optics

The interference optical system is composed of a laser-diode (675 nm, 30 mW, 3 in image B of Figure 2.3), lenses, mirrors, a reflective prism and a camera with a CCD array, as shown in Figure 2.4. The laser beam passes a single and a double slit and, consequently, the beam is split. The length of these slits is longer than the centerpiece sectors and the solution columns are therefore fully covered. An achromatic fringe pattern resulting from the constructive and destructive interference of the electromagnetic waves is formed after the beam is split. The fringe pattern is directed through the sample and reference sector (Figures 2.1 and 2.4) and projected via mirrors, lenses and a reflective prism onto a CCD array, i.e. a charge-coupled device. The refractive index in the sample sector changes along the radial direction of the rotor due to the sedimentation or flotation of solutes. If the solute or colloid refractive index is different from the solvent or buffer refractive index, then sedimentation fronts, i.e. reference-solvent and sample-solution interfaces, correspond to refractive index gradients that result in

shifts of the achromatic fringes formed along the optical axis, see Figure 2.6. Thus the fringes are shifted at the sedimentation fronts. Since the fringe shifts are caused by refractive index differences, the reference sector should contain an appropriate solvent or buffer with a refractive index that matches the supernatant solvent or solution in the sample sector. If the sample solution contains buffer agents or salts, the reference solution should be the liquid against which the sample was dialyzed.

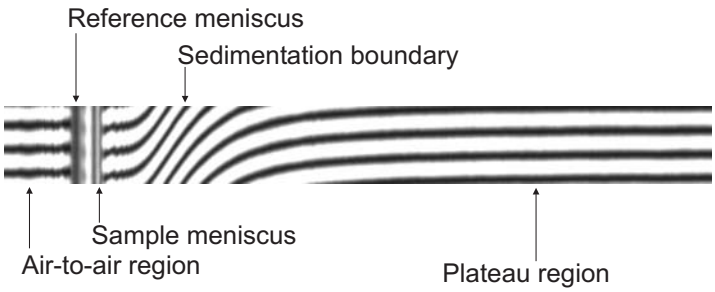

Figure 2.6: Interference pattern composed of fringes. One fringe corresponds to one black and one white region. Note that the fringes shift at the solvent-solution interface, due to refractive index gradients. The sample is a dispersion of colloidal rigid rods (boehmite needles coated with silica, see chapter 8).

The fringes produced by the interference optics (see Figure 2.6) are eventually converted via 'Fast Fourier-Transformation' (FFT) into a single sedimentation velocity profile, which is the total fringe displacement versus radial position, resembling the scan shown in panel A of Figure 2.1. The total fringe displacement, Y_{tot}, is proportional to the refractive index increment, Δn_i, caused by the presence of solutes or particles i, the path length l and the wavelength, λ, of the incident laser beam:

$$Y_{\mathrm{tot}} = \sum (\Delta n_i) \frac{l}{\lambda} \tag{2.2}$$

The total fringe displacement is directly proportional to the concentration of solutes, as can be inferred from:

$$\sum \Delta n_i = \sum \left(c_{\mathrm{i}} \frac{\partial n}{\partial c_{\mathrm{i}}} \right) \tag{2.3}$$

The signal thus depends on the refractive index difference between on the one hand solutes or particles and on the other hand solvent or buffer. Consequently all species with a refractive index that is different from the solvent will be detected with the interference optics provided, of course, the concentration is sufficiently high. This also implies that salts and other buffer components will give rise to the displacement of fringes. Therefore, the sample solution should be dialyzed to obtain the appropriate reference solution. Matching the menisci of the reference and sample solution also prevents the sedimentation of small solutes as salts or buffer components from obscuring the analysis

of interference optical data acquired from sedimentation velocity experiments. Choosing an inappropriate reference solution is also a frequently encountered pitfall in AUC. The use of either a mismatched reference solution or low molecular weight contamination can be seen in ref. [34]. On the other hand, for aqueous systems the purity can be assessed by filling the reference sector with water, as further discussed in chapter 8.

The specific refractive index or the concentration of sedimenting species should be large enough to achieve a satisfactory signal-to-noise ratio. Generally, the initial loading concentration employed for interference sedimentation experiments is much higher than for samples for the absorbance optics.

Because the laser-diode is mounted onto the monochromator (Figure 2.3, image B) that is, in turn, mounted onto the heat-sink of the XL-I, the sedimentation interference optical data suffer from radial-invariant (RI) noise in the form of baseline off-sets. The data also show varying integral fringe shifts that are introduced by the FFT. The RI noise is superimposed on the time-invariant (TI) noise as the jitter observed in interference optical data. The baseline off-sets are caused by small temperature variations during the run, which cause the heat-sink to expand and shrink, thereby increasing and decreasing the optical path length. The changes in the optical path length result in a baseline that varies in time. Editing sedimentation velocity interference optical data therefore requires some additional steps compared to editing absorbance optical data [35]. The baseline off-sets are corrected by aligning the scans in the air-to-air region (Figure 2.6). Furthermore, the factors to correct the relative integral fringe shift of each scan can be determined from a fit of some polynomial function to the integral fringe displacement, because the decrease of the integrated fringe displacements should follow some smooth function that decays in time.

In comparison with the absorbance optical data, the scan rate of the interference optical system is approximately 5 to 10 times faster and therefore allows to perform sedimentation velocity runs at much higher rotor speeds than the angular velocities applied when using the absorbance optics.

2.4. Sedimentation Velocity

Sedimentation is a transport process that provides information on particle sizes, as discussed also in chapters 3 and 4, and shapes and masses of particles as shown in chapter 5 as well as their distributions, dealt with in chapters 3-8. The range of molecular weights and shapes covered by a single sedimentation velocity run is very large compared to a single sedimentation-diffusion equilibrium distribution. However, the molecular weight-range depends, obviously, on the density difference of solutes and solution. Sedimentation velocity experiments allow to identify self-association and even binding stoichiometry as exemplified in chapters 6 and 7, aggregation behavior (chapter 8) and to determine sample composition (chapters 3-8). Furthermore, time-dependent

processes (chapter 5) and concentration-dependent non-ideality (chapters 6-8) can be monitored. Since different solution components are fractionated, sedimentation velocity experiments can be done on samples without the requirement of purification or isolation, see chapters 5 and 8. For such experiments, the initially steep concentration gradient at the solvent-solution interface for particles that are depleted from the meniscus region declines during the time course of the experiment due to translational diffusion and separation of particles that sediment at different rates. The superimposed sedimentation and diffusion are discussed in the next section.

2.4.1. Theory

Below, some theoretical aspects of analytical ultracentrifugation will be discussed; more extensive treatments can be found in ref. [1]. The flux $J_s(r)$, which is the mass dM_s transported via sedimentation through a cylindrical surface $\phi r l$ in a time dt, can be defined as:

$$J_s = \frac{dM_s}{dt} = c\phi r l s \omega^2 r \tag{2.4}$$

At the radial position r the concentration of solutes, c, with a sedimentation coefficient s, is monitored through a path length l. In eq 2.4, ϕ is the angle in radians of the wedge-shaped sector (Figures 2.1 and 2.4) and $\omega^2 r$ is the centrifugal acceleration, with the rotor's angular velocity ω in radians per second. Provided that the sedimentation velocity does not depend on concentration, the velocity of particles increases throughout the sedimentation velocity run, whereas the velocity per unit field is constant. This constant is the sedimentation coefficient s. The definition of the sedimentation coefficient follows from eq 2.4:

$$s = \frac{dr/dt}{\omega^2 r} \tag{2.5}$$

and is generally expressed in units of Svedberg ($\mathrm{S} = 1 \cdot 10^{-13}\,\mathrm{s}$).

The settling rate at radial position r, however, can assumed to be constant. In a centrifugal field, three forces act on a particle that is dispersed in a liquid. These forces are (1) the centrifugal force ($F_{\mathrm{cf}} = V_{\mathrm{p}}\rho_{\mathrm{p}}\omega^2 r$), (2) the buoyancy force ($F_{\mathrm{b}} = -V_{\mathrm{p}}\rho_{\mathrm{s}}\omega^2 r$) and (3) the translational friction force ($F_{\mathrm{f}} = -fs\omega^2 r$). An expression for the sedimentation coefficient is obtained from the balance of these three forces:

$$s = \frac{V_{\mathrm{p}}\left(\rho_{\mathrm{p}} - \rho_{\mathrm{s}}\right)}{f} = \frac{m_{\mathrm{p}}\left(1 - \overline{\nu}_{\mathrm{p}}\rho_{\mathrm{s}}\right)}{f} \tag{2.6}$$

Here, V_{p} and m_{p} are, respectively, the particle volume and mass, $\overline{\nu}_{\mathrm{p}}$ is the partial specific volume of the particles, ρ_{p} is the particle density and f is the friction factor. Since eq 2.6 is derived for finite concentrations, ρ_{s} is the solution density. The solution density enters eq 2.6 via the hydrostatic pressure when it is derived using classical thermodynamics (for details see ref. [36]). A balance of the centrifugal, buoyancy and

friction forces is almost instantaneously reached as can be seen as follows. Particles that are initially at rest relative to the solvent accelerate as soon as the rotor is spinning. Initially the centrifugal force is not balanced by the friction force. A stationary sedimentation velocity is attained as soon as the centrifugal force equals the friction force. The attainment of a stationary sedimentation velocity is described by [37]:

$$u\left(t\right) = \frac{V_{\mathrm{p}}\left(\rho_{\mathrm{p}} - \rho_{\mathrm{s}}\right)}{f}\omega^2 r\left[1 - \exp\left(-\frac{f}{m_{\mathrm{p}}}t\right)\right] \tag{2.7}$$

Substitution of physically relevant parameters for a silica colloid with a diameter of 12 nm in water in eq 2.7, yields $t \approx 63\,\mathrm{ps}$ for the time after which the particles have achieved 99% of their constant settling rate $u\left(t=\infty\right) \approx 1.2\,\mu\mathrm{m\,s}^{-1}$ ($s \approx 560\,\mathrm{S}$) for a given $\omega^2 r$ value. Note that for a sphere with radius a_{b} in a solvent with visocity η_s, the friction factor is $f^{\circ} = 6\pi\eta_{\mathrm{s}}a_{\mathrm{h}}$ [38], with the corresponding, so-called Stokes sedimentation coefficient:

$$s = \frac{2}{9}\,a_{\mathrm{b}}^2\,\frac{\left(\rho_{\mathrm{p}} - \rho_{\mathrm{s}}\right)}{\eta_{\mathrm{s}}} \tag{2.8}$$

where we have assumed that the bare particle radius equals the hydrodynamic particle radius ($a_{\mathrm{b}} = a_{\mathrm{h}}$).

The flux or the amount of material transported through the area ϕrl due to translational diffusion during sedimentation is:

$$J_D = \frac{dM_D}{dt} = -D\phi rl\frac{\partial c}{\partial r} \tag{2.9}$$

where we have used Fick's first law [39]. D is the diffusion coefficient and $\partial c/\partial r$ the concentration gradient at r that causes collective diffusion towards the meniscus. Collective diffusion and single particle diffusion are related through the diffusion coefficient. The average squared displacement, $< r_{\mathrm{D}}^2 >$, of a particle in a time t is according to ref. [40]:

$$< r_{\mathrm{D}}^2 >= 2Dt \tag{2.10}$$

Combining eqs 2.4 and 2.9 yields the net transport per unit time across the cylindrical surface ϕrl:

$$J_{\mathrm{tot}}\left(r\right) = \frac{dM_{\mathrm{tot}}}{dt} = \phi rl\left(cs\omega^2 r - D\frac{\partial c}{\partial r}\right) \tag{2.11}$$

The net accumulation of material Γ in a time t in a volume element, $\phi rldr$, is the difference of the net transport through the surface at r and $r + dr$ and reads:

$$\Gamma = -\frac{\partial}{\partial r}\left[r\left(cs\omega^2 r - D\frac{\partial c}{\partial r}\right)\right]\phi ldr \tag{2.12}$$

Now the change in the concentration with time in the volume element is the net transport of material Γ (eq 2.12) divided by that volume element $\phi rldr$:

$$\frac{\partial c}{\partial t} = \frac{1}{r}\frac{\partial}{\partial r}\left[\left(D\frac{\partial c}{\partial r} - cs\omega^2 r\right)r\right] \tag{2.13}$$

This equation has been first derived by Lamm [41]. If the transport by sedimentation and diffusion is independent of concentration, then eq 2.13 reads:

$$\frac{\partial c}{\partial t} = D\left[\frac{\partial^2 c}{\partial r^2} + \frac{1}{r}\frac{\partial c}{\partial r}\right] - s\omega^2\left[r\frac{\partial c}{\partial r} + 2c\right] \tag{2.14}$$

Eq 2.13 is fundamental to all types of ultracentrifugation in the case of low Reynolds number (ratio of inertial forces to viscous forces). It should be stressed, however, that sedimentation velocity and diffusion in many cases are dependent on concentration, as will be discussed shortly.

Assuming that the ultracentrifuge cell is infinitely long, the sedimentation velocity boundaries, which broaden during the settlement of particles due to diffusion, can be described after meniscus depletion by eq 2.14 [42]. Due to the wedge-shape of the cell-sector (Figures 2.1 and 2.4), the horizontal plateau concentration (Figure 2.1, panel A), for which $\partial c/\partial r = 0$, decreases. This radial dilution can also be described via eq 2.14. To date, many analysis methods that solve the differential Lamm-equation (eq 2.14) numerically are available [3, 4].

We note here that a proper positioning of the cell into the rotor is very important. In ref. [33], radial concentration instead of radial dilution (as it should be) is observed, indicating that the instrument is not properly functioning or, more likely, that the cell is not positioned correctly in the rotor. Generally, an analytical ultracentrifugation cell employed for sedimentation velocity experiments is equipped with a centerpiece that has two wedge-shaped sectors (Figures 2.1 and 2.4) containing, respectively, reference and sample solution. The cell should be positioned such that the widths (spacing perpendicular to the radial direction of the centrifuge) of the sectors increase with the radial position from the center of rotation. If the cell is rotated 180°, these cell-sector widths decrease with the radial position and, consequently, the plateau concentration (Figure 2.1, panel A) increases in time due to the sedimentation of solutes or particles.

Eq 2.13 clearly shows that transport due to sedimentation and translational diffusion are superimposed (also see chapter 4, Figure 2). Sedimentation and diffusion are interdependent since the friction factor f appears in eq 2.6 and in the expression for the diffusion coefficient [40]:

$$D = \frac{k_\mathrm{B}\mathrm{T}}{f^\circ} \tag{2.15}$$

For a single sphere with a hydrodynamic radius a_{h} at low Reynolds number this expression reduces to the Stokes-Einstein relation [38, 40], namely:

$$D = \frac{k_{\mathrm{B}}\mathrm{T}}{6\pi\eta_{\mathrm{s}}a_{\mathrm{h}}} \tag{2.16}$$

The sedimentation boundaries for polydisperse particles may be smooth if the difference in size and or shape is relatively small or almost continuously distributed. In the latter case, the particles are not well-resolved and without further analysis it is impossible to discriminate boundary broadening due to diffusion from broadening due to different sedimentation rates. The deconvolution of sedimentation and diffusion can be achieved, for example, by the enhanced van Holde-Weischet [43, 44] analysis, as shown in chapters 3 and 5 and discussed in chapter 4.

However, important shape information can be obtained from fitting sedimentation velocity data with a sum of (numerical) Lamm-equation solutions (eq 2.13) constituting the model that describes the experimental data. Moreover, if the sedimentation and diffusion coefficients are obtained from experimental sedimentation velocity data, a molecular weight can be computed via eq 2.20, provided the partial specific volume is known. In chapter 5 the determination of molecular weights from multi-speed sedimentation velocity experiments is discussed. The multi-speed sedimentation were analyzed using the enhanced van Holde-Weischet analysis, 2-dimensional spectrum analysis and Genetic Algorithm optimization [45] with and without Monte Carlo iterations [46]. Since the latter analyses are computationally intensive we employed supercomputers [47], *UltraScan* [23] (a comprehensive data analysis software package for AUC experiments), *UltraScan* public Laboratory Information Management System, controlled with the local software program *UltraScan* via a relational database and Web portals.

If there is a significant concentration effect on the sedimentation rate, due to hydrodynamic and colloid-colloid interactions, then the sedimentation coefficient can be approximated by the empirical s versus c relation [22]:

$$s = \frac{s^{\circ}}{1 + kc} \tag{2.17}$$

The validity of this equation is limited to fairly low concentrations. For sufficiently dilute dispersions, eq 2.17 can be replaced by the first term of its Taylor expansion:

$$s = s^{\circ}\left(1 - k_c c\right) \tag{2.18}$$

can be applied for dilute dispersions. In eqs 2.17 and 2.18, k and k_c are proportionality constants. Clearly this approach requires the input of the limiting sedimentation coefficient, s°, that is generally obtained by extrapolation of eq 2.18 to $c = 0$ (see chapters 7 and 8). For repulsive interactions k_c is positive and the first order correction to the sedimentation coefficient at infinite dilution results in a decreased sedimentation rate for relatively concentrated solutions or dispersions (see chapter 8). On the other hand,

for sufficiently strong attractions k_c changes sign, enhancing the sedimentation velocity with concentration. The enhancement of sedimentation rate is discussed in detail in chapters 6 (theory) and 7 (experiments) employing magnetite particles that exhibit dipolar attractions.

2.4.2. Experiments

A sedimentation velocity run is typically performed on a single sample when employing the absorbance optics, to prevent the monochromator's incorrect wavelength resetting and to enhance the scan rate. An example of such incorrect wavelength resets are the sedimentation boundaries reported in ref. [18]. The sedimentation velocity absorbance optical scans inflate and collapse from time to time during the course of the sedimentation velocity run due to variations of the wavelength at which the scans are recorded. Employing a single wavelength is especially important if the attenuance is measured on either side of a steep attenuance peak. The plateau absorbance of the sedimentation velocity scans in ref. [18] varies due to variations of the wavelength. During a sedimentation velocity run the selected wavelength for attenuance readings may change if concentration distributions for multiple cells are monitored at different wavelengths. The variation in wavelength from one radial scan to the other, is due to the monochromator's incorrect wavelength resetting.

In case of sedimentation velocity runs with the interference optics, which employs a single wavelength, the scan rate is very fast and, consequently, multiple samples may be loaded into the rotor. For absorbance measurements it is good practice to minimize the radial range that needs to be scanned to increase the scan rate. Setting the step size for the slit-assembly to $\approx 30\,\mu$m and employing the continuous mode also increases the scan rate. Furthermore, the intensity of the transmitted light should not be averaged over multiple measurements at a single radial position and the radial transmission scans must be recorded without an inter-scan delay-time to acquire as many scans as possible.

To achieve a high s-resolution the rotor speed should be sufficiently large, such that approximately 40 to 50 scans can be included in the sedimentation velocity absorbance optical data analysis. In other words, the sedimentation velocity experiment should be well designed. The appropriate angular velocity for the sedimentation velocity run can be initially determined from a simulation and may be optimized experimentally to achieve a sufficient s-resolution. This pitfall, i.e. applying too low rotor speeds, is exemplified in ref. [48] where the sedimentation velocity runs were conducted at too low rotor speeds.

If a molecular weight needs to be determined, low- and high-speed experiments should be performed on an identical sample. The optical data are then globally fitted (see chapter 5). The low-speed data contains the shape information, since the diffusion signal

is relatively large. On the other hand, particle diffusion is suppressed in high-speed sedimentation velocity runs, allowing the determination of accurate and precise sedimentation coefficients. The effect of rotor speed on sedimentation velocity runs is illustrated in chapter 5.

2.5. Sedimentation-Diffusion Equilibrium

A time-independent distribution is eventually reached during a sedimentation-diffusion equilibrium experiment. Because there is no net transport of particles or macromolecules, direct information on particle shapes is lost. Such experiments, however, allow the determination of thermodynamic parameters as equilibrium constants (reversibly self-associating systems) [3, 4, 21, 22], osmotic and swelling pressures [8, 49–51], and molecular weights. Furthermore, recently developed theories [52,53] may be applied to determine a particle charge from the inflated sedimentation-diffusion equilibrium distribution [54–56] for charged colloids provided, of course, the effective molecular weight is known. Generally, sedimentation-diffusion equilibrium experiments are suited for samples that are at least 95% pure with respect to the solutes or particles and can only be used if the molecular weights contained in the sample are not too disparate, i.e. 10%-70% (w/w) of each other. The sedimentation-diffusion equilibrium distribution for single, ideal and non-interacting particles is derived in the following section.

2.5.1. Theory

During a sedimentation-diffusion equilibrium experiment a constant concentration distribution is reached where the sedimentation and diffusion fluxes are balanced. Therefore the concentration at any radial position does not change in time; i.e. $\partial c/\partial t = 0$ for all r. Rearranging and integrating the expression in which eqs 2.4 and 2.9 for monodisperse particles are combined, yields a single-exponential sedimentation-diffusion equilibrium distribution:

$$c\left(r\right) = c\left(r_{\mathrm{m}}\right) \exp\left[\frac{s\omega^2}{2D}\left(r^2 - r_{\mathrm{m}}^2\right)\right] \tag{2.19}$$

whith r_{m} the sample meniscus position (Figure 2.1). In eq 2.19 we recognize Svedberg's equation:

$$\frac{s}{D} = \frac{m_{\mathrm{p}}\left(1 - \overline{\nu}_{\mathrm{p}}\rho_{\mathrm{s}}\right)}{k_{\mathrm{B}}\mathrm{T}} \tag{2.20}$$

Equivalently, eq 2.19 can be directly obtained from eq 2.11, realizing that the net flux is zero for a system which is at equilibrium, i.e. $J_{\mathrm{tot}}\left(r\right) = dM_{\mathrm{tot}}/dt = 0$. For a monomer-dimer self-association, eq 2.19 is transformed into a bi-exponential function, as derived and discussed in chapter 6. Note, however, that for such a bi-exponential distribution, the concentrations of monomers and dimers are interdependent since the association obeys the equilibrium constant (see chapter 6). On the other hand, for ideal

non-interacting particles, such as the polydisperse silica colloids at high ionic strength in chapter 4, the concentration distribution is a superposition of the individual single-exponential sedimentation-diffusion equilibrium distributions. This superposition hampers the determination of molecular weights since the contributions of the individual particles to the multi-exponential distribution cannot be discriminated.

2.5.2. Experiments

Sedimentation-diffusion equilibrium experiments are generally performed at multiple rotor speeds on samples containing different concentrations, to obtain sufficient signal from the large and small components, as well as to cover a large concentration range from which an interpolated equilibrium constant can be determined. We note here that in refs. [57] and [58], the authors report sedimentation-diffusion equilibrium experiments from which only a small portion of the information that could have been acquired was obtained, since they applied only a single rotor speed. The loading concentrations, however, are smaller than for sedimentation velocity experiments. The scans acquired (absorbance optics: step size 10 μm, 20 averages, step mode) with an 8 hour delay are subtracted to determine if equilibrium has been reached. The scans collected at different rotor speeds for the various concentrations should be globally fitted (non-linear least squares fitting routines) with an appropriate model. Choosing an inappropriate model to fit experimental data is a pitfall in AUC data analysis. Similarly, the misconception of using only the absolute average root-mean-square deviation to quantify the fit-quality of models to experimental sedimentation-diffusion equilibrium distributions is frequently encountered. The absolute average root-mean-square deviation and variance are important, but strongly depend on the signal-to-noise ratio. The actual fit-quality should be assessed from the distribution of the residuals, i.e. concentration distribution according to the fitted model subtracted from the experimental concentration distribution, versus radial position. Systematic deviations, i.e. sinusoidal shape of the overall residual distribution, are easily observed from a plot of residuals versus radial position and indicate that the model employed is inappropriate (see refs. [57] and [48]). A random distribution of residuals generally indicates a good fit or that the model may have too many fit-parameters. The latter is encountered in ill-posed problems, i.e. multi-exponential functions can be fitted with a number of different functions. Frequently such fit-quality assessments are not awarded with sufficient attention. In refs. [32] and [33], for example, the authors do not report any root-mean-square deviation, variance or residuals plots.

Having provided some background for instrumental and theoretical aspects of analytical ultracentrifugation (much more information can be found in the quoted references,

also in the introduction), we now turn in the next chapter to the AUC analysis of inorganic model colloids, namely two different $\{Mo_{132}\}$ molybdenum clusters that belong to the group of polyoxometalates.

Acknowledgement

Borries Demeler and Thomas Laue are thanked for helpful discussions and for sharing their many AUC insights. Ronald de Vries is acknowledged for explaining various technical aspects and some electronics of the AUC.

Part 2

Non-Interacting Colloids

3

Direct Evidence for the Existence of $\{Mo_{132}\}$ Keplerate-Type Species in Aqueous Solution

Abstract

We demonstrate the existence of discrete single molecular $\{Mo_{132}\}$ Keplerate-type clusters in aqueous solution. Starting from a discrete spherical $\{Mo_{132}\}$ cluster the formation of an 'open' basket type $\{Mo_{116}\}$ defect structure is shown for the first time in solution using analytical ultracentrifugation sedimentation velocity experiments.

3.1. Introduction

Giant polyoxomolybdates, especially the spherical $\{Mo_{132}\}$ Keplerate-type [59] anionic clusters have gained significant interest as cation carriers [60–62], nanosponges [63, 64] and for various other material science applications in solid-state chemistry [65]. Recently, it has been shown, also in solid-state, that it is possible to 'open' such a $\{Mo_{132}\}$ type cluster to form a basket-like $\{Mo_{116}\}$ type defect cluster [66]. Although a significant volume of literature is available on these clusters in solid-state, their chemistry in solution has only been studied qualitatively [67]. Hence questions arise as: (1) Is it possible to demonstrate experimentally the existence of discrete single molecular $\{Mo_{132}\}$ clusters in aqueous solution? (2) Can the opening of such a molecular $\{Mo_{132}\}$ cluster to generate an 'open' basket-like $\{Mo_{116}\}$ cluster be demonstrated *in situ* in aqueous solution? Here we present experimental results to answer these questions for the first time.

3.2. $\{Mo_{132}\}$ Clusters in Solution

To answer the questions addressed in 3.1, analytical ultracentrifugation sedimentation velocity (AUC SV) experiments were conducted on two model $\{Mo_{132}\}$ clusters **1** and **2**, Table 3.1.

Table 3.1: Chemical Formulae of Molybdenum Clusters **1**, **2** and **3**.

$(NH_4)_{72}\{Mo^{VI}_{72}Mo^{V}_{60}O_{372}(H_2O)_{72}(SO_4)_{30}\} \cdot$ ca. $280\,H_2O$	**1** [68]
$(NH_4)_{42}\{Mo^{VI}_{72}Mo^{V}_{60}O_{372}(H_2O)_{72}(CH_3COO)_{30}\} \cdot$ ca. $300\,H_2O \cdot 10\,CH_3COONH_4$	**2** [69]
$(NH_4)_{46}\{Mo^{VI}_{66}Mo^{V}_{50}O_{331}(H_2O)_{56}(CH_3COO)_{30}\} \cdot$ ca. $300\,H_2O$	**3** [66]

Cluster **1** is less stable than **2**, since **1** is more prone to oxidation. Upon controlled oxidation, however, cluster **2** is known to form a basket-like defect structure $\{Mo_{116}\}$ with one missing $\{Mo_{16}\}$ unit as compared to $\{Mo_{132}\}$. Therefore, we employed **1** and **2** as model systems for our experiments. More explicitly, with the expectation that **1** will allow the assessment of the existence of discrete single molecular $\{Mo_{132}\}$ clusters, whereas **2** may show the coexistence of discrete $\{Mo_{132}\}$ clusters and 'open' basket-like $\{Mo_{116}\}$ structures, as **3** in Table 3.1, in solution. To date, cluster **3** is isolated and observed as crystals only.

All these clusters are colored and hence can be monitored quantitatively using an AUC (Beckman Coulter™ Optima™ XL-I AUC) equipped with absorbance optics. Each cluster type has a distinct attenuance spectrum and since the optical density at the wavelengths used here is linear with concentration, the absolute amounts can be

determined from the attenuance. AUC has been used extensively for, among others, the analysis of protein-protein and protein-DNA/RNA interactions [3,4], polymers [70], oxomolybdates [32] and even polyoxometalate based dendrimers in solution [71]. The earliest AUC experiments on polyoxometalates [72] we are aware of date back to 1950, where the sedimentation and diffusion behavior of silico-12-tungstic acid in aqueous solution was investigated, to critically and accurately test the AUC technique. In this test, the obtained molecular weight agrees well with results from crystallographic data for silico-tungstic acid [72].

For the AUC SV experiments ca. 2.5 mM aqueous solutions were obtained by dissolving freshly prepared dried crystals of **1** and **2** in water. A 2.2 mM solution of **1** and a 2.7 mM solution of **2** were prepared by dissolving 61 mg of **1** and 75 mg of **2** in 1 mL Millipore-Q water. The EAS of these dispersions were recorded using a Varian Cary 1E UV-Vis spectrophotometer and after achieving the desired dilution, the solutions were transferred to the AUC cells with aluminum double-sector centerpieces together with water as a reference. SV boundaries were recorded with a step size of 10 μm in continuous mode at 46,000 rpm and 20 $\pm$ 0.1 °C, employing a Beckman Coulter^{TM} Optima^{TM} XL-I AUC with an An-60 Ti rotor, until all material was pelleted. For each sample 100 scans were recorded of which 50 SV scans were analyzed. To achieve a maximum signal to noise ratio the absorbance maxima of **1** and **2**, with an attenuance between 0.6-0.9 OD, were matched with local emission maxima of the Xenon flash lamp. The absorbance bands in the electronic absorption spectra of clusters **1** and **2** are in the region of 460-480 nm. The red-brown color of these clusters stems from a transition within the $\{Mo_2^{V}O_4\}^{2+}$ groups containing localized metal-metal bonds [68, 69]. Clusters **1** and **2** share the same architecture with the icosahedral disposition of the 12 pentagonal $\{Mo^{VI}Mo_5^{VI}O_{21}(H_2O)_6\}$ units linked by 30 $\{Mo_2^{V}O_4(L)\}$ linkers where $L = SO_4^{2-}$ and CH_3COO^- for **1** and **2** respectively. For our experiments the absorbance at $\lambda = 459$ nm and 484 nm for **1** and **2** was monitored. An enhanced van Holde-Weischet analysis [44], implemented in *UltraScan* [23, 73], on the SV data was performed to obtain integral and differential sedimentation coefficient distributions (see ref. [43] for the classic vHW analysis).

The envelope of the differential sedimentation coefficient distribution for **1** shows the dominant abundance (ca. 96%) of a monodisperse species with a sedimentation coefficient of 8.7 S, Figure 3.1. We now ascertain the nature of this species using:

$$s = \frac{M_W\left(1 - \overline{\nu}_p \rho_s^\circ\right)}{6\pi\eta_s a_h N_{AV}} \tag{3.1}$$

Substitution of the crystallographic molar weight [68] $M_W = 28,237.2\,\mathrm{g\,mol^{-1}}$ (accounting for the loss of 50 water molecules) of **1**, solvent density [74] $\rho_s = 0.99821\,\mathrm{g\,mL^{-1}}$ at 20 °C [74], partial specific volume $\overline{\nu}_p = 0.470\,\mathrm{mL\,g^{-1}}$ [68], solvent viscosity [74]

$\eta_s = 1.002\,\mathrm{mPa\,s}$, cluster hydrodynamic radius $a_h = 1.5\,\mathrm{nm}$ and Avogadro's constant N_{AV} in eq 3.1 yields a sedimentation coefficient s of 8.8 S for cluster **1**. This s value corresponds to the rate at which the clusters would sediment in an aqueous solution at infinite dilution, provided they exist as discrete molecular entities without any interparticle interaction, i.e. no electrostatic, hydrodynamic and excluded volume effects, and that the single molecular composition as in the crystals is retained.

The calculated and the experimental values agree well. The agreement confirms that in aqueous solution, discrete single molecular clusters of **1** exist. Moreover, these clusters are highly monodisperse since the integral and differential sedimentation coefficient distribution shown in Figure 3.1 are extremely narrow.Having shown the monodisperse

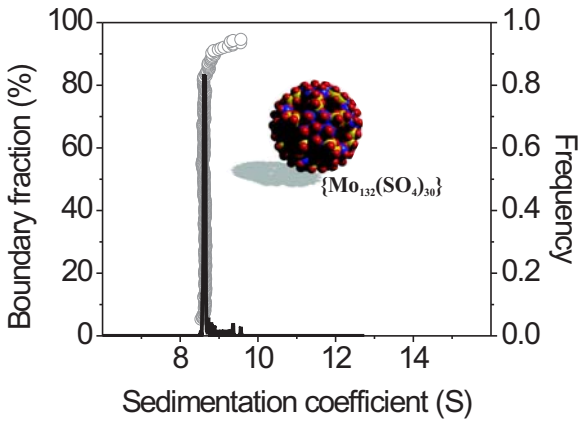

Figure 3.1: Integral G(s), left y-axis (○), and differential (envelope of histogram, ——), right y-axis, sedimentation coefficient distributions for **1**, obtained from an enhanced van Holde-Weischet analysis [44], implemented in *UltraScan* [23,73]. A space-filling representation (generated with DIAMOND 2.1 from Dr. K. Brandenburg, Crystal Impact GbR, 2001 and POV-Ray 3.5 freeware from C. J. Cason, same holds for Figure 3.2) of **1** [68] is shown.

existence of discrete single molecular $\{Mo_{132}\}$ clusters in aqueous solution, we now address our second question. Can we show the coexistence of the discrete $\{Mo_{132}\}$ cluster **2** with its oxidized 'open' basket-like $\{Mo_{116}\}$, i.e. cluster **3**?

Assuming that both clusters **2** and **3** are spherical, the sedimentation coefficients for **2** and **3** are, according to eq 3.1, 8.4 ($M_W = 26,456.2\,\mathrm{g\,mol^{-1}}$, $\overline{\nu}_p = 0.457\,\mathrm{mL\,g^{-1}}$, $a_h = 1.5\,\mathrm{nm}$) [68,69] and 7.5 S ($M_W = 23,494.3\,\mathrm{g\,mol^{-1}}$, $\overline{\nu}_p = 0.457\,\mathrm{mL\,g^{-1}}$, $a_h = 1.5\,\mathrm{nm}$) [66,68] respectively. The friction coefficient f, which is for a sphere $f = 6\pi\eta_s a_h$ [38], is not significantly increased upon removal of a cap from cluster **2**, since it is likely that in aqueous solution the clusters are hydrated resulting in a nearly overall spherical geometry. The sedimentation profiles of **2** revealed an interesting pattern. In contrast to **1**, the envelope of the differential sedimentation coefficient distribution is a broad

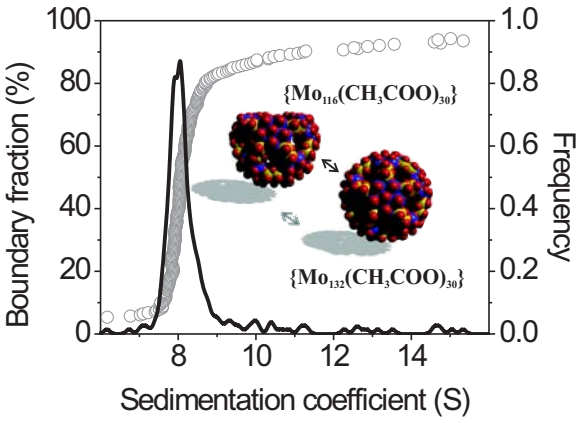

Figure 3.2: Integral G(s), left y-axis (○), and differential (envelope of histogram, ——), right y-axis, sedimentation coefficient distributions for **2** [69], obtained from an enhanced van Holde-Weischet analysis [44] that is implemented in *UltraScan* [23, 73]. A space-filling representation of **2** [69] and a defect cluster **3** [66], which may coexist in solution is shown, see text for further details.

Gaussian peak and reveals ca. 85% abundance of a species with a sedimentation coefficient of 8.1 S, but without any peak at 8.4 S or 7.5 S, as calculated above, Figure 3.2. The broad distribution implies an abundance of a heterogeneous species in solution. This observed broad distribution, with a peak centered at 8.1 S, should be interpreted as an overall picture for two coexisting species in the solution. The two cluster types **2** and **3**, are not resolved during the sedimentation velocity run and sediment, apparently, as one fairly polydisperse species because the sedimentation coefficients are similar and both species have large diffusion coefficients. The fact that two species with similar particle densities that have sedimentation coefficients of 7.5 and 8.4 S are not resolved can already be demonstrated by a Finite Element SV simulation [75, 76] (implemented in *UltraScan* [23, 73]) for single non-interacting species. In line of our explanation and interpreting the broad peak in Figure 3.2 as a weight-average s-value, the solution is comprised of ca. 67% of **2**, which sediment individually at 8.4 S, and ca. 33% of the defect 'open' basket type structure **3**, which sediment individually at 7.5 S. {Mo$_{132}$} and {Mo$_{116}$} structures apparently coexist in solution almost in a ratio of 2:1, which is demonstrated for the first time *in situ* in solution. In fact what we observe from our envelope of the differential sedimentation coefficient distribution for **2** is: the opening of a complete {Mo$_{132}$} cluster **2** to form, by the loss of a {Mo$_{16}$} cap, an 'open' basket-like {Mo$_{116}$} **3** in course of oxidation. This observation is interesting in the sense that it offers the option to 'open' a structure under mild condition, i.e. aerial oxidation or in this case oxidation by dissolved oxygen. If the opening of **2** is reversible, then the closing of the 'open' basket structure **3** by introducing reducing agents should be possible. In principle the study of such a dynamic opening and closing of a structure in solution

can be performed employing ion transport.

Additionally, we also observe the presence of larger aggregates (ca. 12%) constituted of type **2** clusters, with a weight-average sedimentation coefficient of 11.7 S. These species might allude to aggregates or small superstructures which have been reported recently [77–79], a detailed discussion on which is beyond the scope of the present contribution.

It is worth to compare and contrast the behavior of the clusters **1** and **2** in aqueous solution: (1) Both the clusters are essentially monodisperse. (2) The distribution of **1** is narrower than that of **2** due to the oxidation of **2**. (3) In case of **1** the clusters exist only as discrete $\{Mo_{132}\}$ whereas in case of **2** the complete $\{Mo_{132}\}$ cluster slowly gets oxidized under experimental conditions to form a more 'open' basket-like $\{Mo_{116}\}$ structure. Structures **2** and **3** coexist in a ratio of approximately 2:1. (4) In contrast to **1**, the aqueous solution of **2** contains almost 12% larger aggregates. This suggests that cluster **2** spontaneously forms super-structures. However the issue of super-structure formation requires further experimentation.

3.3. Conclusions

We have shown in this contribution that in aqueous solution of $\{Mo_{132}\}$ type cluster discrete single molecular clusters exist. In case of the cluster compound with acetate, in addition to discrete molecular clusters, we suggest that oxidation results in the opening of clusters to form an 'open' basket-like $\{Mo_{116}\}$, which then coexists with the closed $\{Mo_{132}\}$ type cluster. Such coexistence is shown for the first time in aqueous solution experimentally. Results of this study further imply that it is possible to open these clusters by controlled oxidation. If the opening is reversible, the clusters can be filled with cations. This entire phenomenon could be monitored in a fashion similar to that described here. We believe that the study presented here can be further extended to understand the 'uptake' and 'release' of various cations involving these clusters. Furthermore, we demonstrated the potential of AUC in studying intricate phenomenon involving large inorganic clusters *in-situ* as described here.

Acknowledgement

This work was financially supported by The Netherlands Organization for Scientific Research (NWO/Stichting Chemische Wetenschappen). Willem K. Kegel and Soumyajit Roy are thanked for their contribution.

4

Model Independent Size Distribution Determination of Colloidal Silica via Analytical Ultracentrifugation

Abstract

We report a method to determine the particle size distribution of small colloidal silica spheres via analytical ultracentrifugation and show that the average particle size, variance, standard deviation and relative polydispersity can be obtained from a single sedimentation velocity (SV) analytical ultracentrifugation (AUC) experiment. The particle size distribution (*psd*) from the enhanced van Holde-Weischet analysis, which also accounts for the dynamic light scattering results quite well, equals the *psd* from a continuous distribution of sedimentation coefficients analysis. The SV AUC interference optical data also yield the specific particle volume such that distributions of sedimentation coefficients for colloidal spheres can be converted directly to particle size distributions. Our results show that SV AUC experiments may yield a quantitative particle size distribution without a priori knowledge of the particle size and the shape of the size distribution.

4.1. Introduction

In physical and colloid chemistry model colloidal systems are studied to improve the understanding of physical-chemical principles. Generally, synthetic macromolecules and in particular colloids are always to a certain degree heterogeneous with respect to size and shape. Since the size of particles directly affects the physical behavior of colloids and the colloidal system as a whole, it is of relevance to know the particle dimensions and shapes.

For the size and shape determination, as well as the overall particle size distribution (*psd*) several techniques are available as transmission electron microscopy (TEM, or variations on this technique as scanning electron microscopy and cryo-TEM) and atomic force microscopy (AFM). These microscopic techniques, except cryo-TEM, do not image *in situ*. Drying of TEM-samples may lead to particle shrinkage and distortion of particle structures, including aggregation due to capillary forces. Moreover, the electron beam may seriously damage the colloids via the melting and sintering of nanoparticles, as is the case for the small silica particles that are subject of the present study. Even if TEM-images are fairly representative for the colloids in solution, many counts are needed for reliable statistics. For example, in case of a polydispersity around 30 *per cent*, typically at least 1000 counts are needed for a representative size distribution (see the case studies for various colloids in ref. [37]).

Other techniques that sample colloids *in situ* are static light scattering (SLS) and dynamic light scattering (DLS). For sufficiently narrow size distributions, SLS data in the Guinier region can be analyzed with a momentum-expansion, to obtain an effective radius that is independent of the detailed shape of the distribution function [37]. For a broad size distribution, however, it is hardly possible to extract in any a priori fashion reliable distribution parameters from static light scattering profiles. DLS may be conducted on polydisperse colloids for which the particle shape is known, to obtain an apparent average particle size and standard deviation. The shape of the particle size distribution from DLS, however, may be highly questionable because of the ill-conditioned inversion problem encountered in DLS [80]. Since the scattered light intensity scales with the particle volume squared, small particles in the presence of relatively large particles are difficult to detect with DLS. The scaling of the scattered light intensity also implies that DLS experiments are strongly affected if dust contaminated samples are employed.

Despite the possibilities of analytical ultracentrifugation (AUC), the method has hardly been applied to analyze the *psd* of inorganic colloids and nanoparticles. This is partly due to the fact that AUC is primarily applied in biochemistry and cell-biology, and much less in the field of inorganic colloids and nanoparticles (see, however,

refs. [8, 81–83]). In addition, the potentiality of AUC (including the improved data-analysis explained later) to quantify a *psd* of nanoparticles may have been overlooked or underestimated due to the absence of a convincing case study. The aim of this contribution is to provide such a study and to demonstrate that sedimentation velocity (SV) AUC may quantitatively yield a *psd*, without a priori information about the range and shape of this distribution.

For this case study we choose an aqueous dispersion of amorphous silica nanoparticles for several reasons. Such silica sols are readily available, being produced and applied commercially on a large scale (e.g. Eka Chemicals AB Colloidal Silica Group, Bohus, Sweden). Moreover, the small silica colloids have precisely the features that makes their *psd* difficult to obtain via other techniques than AUC: their shape is uncertain, they easily melt in an electron beam (Figure 4.1), and according to the product data sheet little more than a single (approximate) particle size is available.

Our approach in more detail is as follows. From the enhanced van Holde-Weischet (vHW) analysis [43, 44] method (*UltraScan* [23]) the sedimentation coefficient distribution, corrected for diffusion, is obtained, which allows the computation of a *psd*. To verify the validity of the sedimentation coefficient distribution into an equivalent sphere radius distribution, we use the 2-dimensional spectrum analysis (2DSA [47] implemented in *UltraScan* [23]) that allows to determine the sedimentation and frictional ratio distributions simultaneously. We also show how the specific particle volume, required for the sedimentation coefficient distribution into a radius distribution, can be obtained from the same interference optical data without conducting any additional experiments. This AUC SV procedure without any prior knowledge of the range of sedimentation coefficients or, equivalently, particle sizes and particle shapes, allows the determination of the average size and the overall *psd* in a model independent manner. The results obtained from the enhanced vHW analysis are compared with the results of a continuous sedimentation coefficients distribution analysis method [84, 85] and with results from experimental dynamic light scattering (DLS) data which were fitted using, among others, the *psd* as obtained from the SV AUC experiment.

4.2. Theory

4.2.1. Sedimentation Velocity

A macromolecule or colloid in a centrifugal field is subjected to a centrifugal force, a friction force and a buoyant force. A balance of these forces is almost instantaneously achieved, from which an expression for the sedimentation coefficient at infinite dilution (s°), i.e. the ratio of the sedimentation velocity and acceleration, is easily obtained:

$$s^\circ = \frac{V_\mathrm{p}\left(\rho_\mathrm{p} - \rho_\mathrm{s}^\circ\right)}{f^\circ} = \frac{m_\mathrm{p}\left(1 - \overline{\nu}_\mathrm{p}\rho_\mathrm{s}^\circ\right)}{f^\circ} \tag{4.1}$$

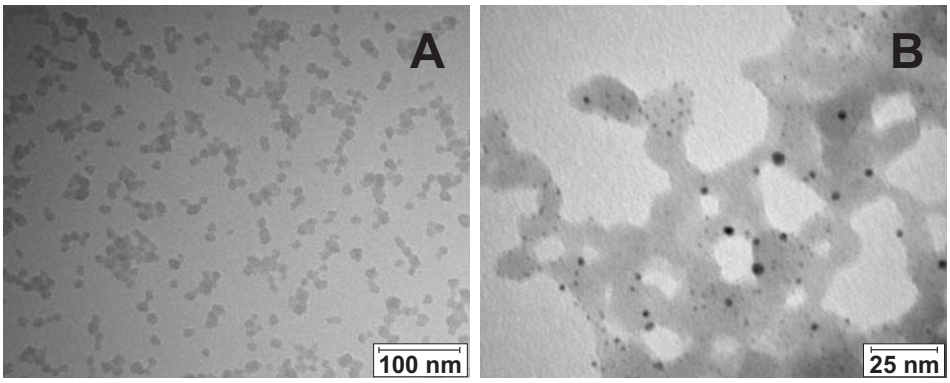

Figure 4.1: TEM micrographs of bare Bindzil® 30/360 particles, image A, and with gold nanoparticles attached (for details see ref. [86]), image B. Clearly, the small amorphous silica nanoparticles melt in the electron-beam and fuse into big liquid-like silica blobs. Since no individual particles are observed, the size and shape of such small silica particles cannot be precisely determined from TEM micrographs.

Here, f° is the frictional coefficient of a sphere with radius a_h according to Stokes' equation [38]:

$$f^\circ_\mathrm{sphere} = 6\,\pi\,\eta^\circ_\mathrm{s}\,a_\mathrm{h} \tag{4.2}$$

Furthermore, V_p is the particle volume, ρ_p and ρ°_s are, respectively, the particle and solvent densities and η°_s the solvent viscosity. The radius of the particle can be obtained from eq 4.1 assuming that the particle mass m_p and its partial specific volume $\overline{\nu}_\mathrm{p}$, or, equivalently, the particle volume and its density are known. If the bare particle radius a_b equals the hydrodynamic radius a_h, then eq 4.1 reduces to:

$$s^\circ = \frac{2}{9}\,a_\mathrm{b}^2\,\frac{\left(\rho_\mathrm{p} - \rho^\circ_\mathrm{s}\right)}{\eta^\circ_\mathrm{s}} \tag{4.3}$$

For monodisperse non-interacting spheres the size determination, from eq 4.3 would be straight forward if diffusion, which broadens the sedimentation boundary, would be absent provided, of course, that the particle density is known.

Generally, sedimentation and diffusion are superimposed in an analytical ultracentrifugation (AUC) sedimentation velocity experiment [1], as illustrated in Figure 4.2 by the simulated sedimentation velocity boundaries for a solution containing 9 different solutes using the adaptive space-time finite element method [76] simulation module in *UltraScan* [23]. Since particle size and shape heterogeneity also lead to sedimentation velocity boundary broadening, a model independent analysis, i.e. without any prior knowledge of the range of sedimentation coefficients and particle shapes, is required to obtain diffusion deconvoluted sedimentation coefficients to eventually determine a particle size distribution (*psd*). Such an analysis is the enhanced van Holde-Weischet analysis [44] (vHW, *UltraScan* [23]).

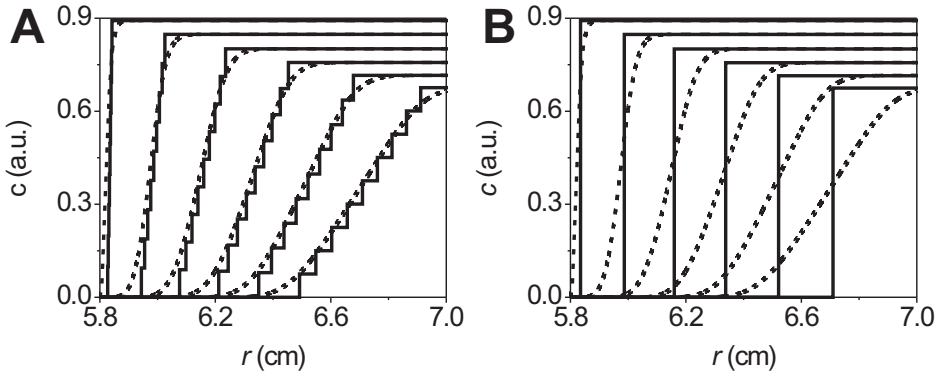

Figure 4.2: Simulated sedimentation velocity scans (ASTFEM simulation module [76] implemented in *UltraScan* [23]), with (----) and without (——) diffusion, accounting for rotor acceleration. In this case the solution contains equal amounts of 9 different solutes (graph A). The simultaneous sedimentation and diffusion of solutes give rise to sigmoidal boundaries. Without prior knowledge of the composition of the sample, the boundaries may also correspond to the sedimentation and diffusion of a single component (graph B). Therefore, without further analysis to determine diffusion deconvoluted sedimentation coefficients it is impossible to differentiate boundary broadening due to heterogeneity from diffusional boundary spreading.

The vHW analysis is based on the principle that transport due to sedimentation is proportional to time, whereas the displacement by diffusion is proportional to the square-root of time. Briefly, for a vHW analysis the m sedimentation velocity boundaries are each discretized in n equally sized fractions between the lower (baseline) and upper stable plateaus (horizontal regions). For each boundary division j, at radial position r_j of scan i recorded at time t_i, a corresponding apparent sedimentation coefficient ($s^*_{i,j}$) is calculated via:

$$s^*_{i,j} = \frac{1}{\omega^2 (t_i - t_0)} \ln \left[\frac{r_j (t_i)}{r_a (t_0)} \right] \tag{4.4}$$

where $1 \leqslant i \leqslant m$, $1 \leqslant j \leqslant n$. In eq 4.4, ω is the angular velocity, r_{a} is the position of the sample meniscus and t_0 is the start time of the SV AUC run (corrected for rotor acceleration). The apparent sedimentation coefficients are then plotted versus the inverse square-root of the corresponding scan time-stamp i. Diffusion corrected sedimentation coefficients are obtained by extrapolating each linear fit of apparent sedimentation coefficients for the boundary fractions j to infinite time. The linear extrapolation to $t = \infty$ in the vHW analysis method is achieved via a formula based on a Faxén-type approximate solution of the Lamm equation (e.g. infinite solution column length), which introduces restrictions to the scans for analysis. The modified and so-called enhanced vHW analysis circumvents the majority of the drawbacks associated with the classic vHW method [43]. For example, the enhanced vHW analysis allows inclusion of scans

that have not cleared the meniscus and that lack stable lower and upper horizontal regions, in contrast to the classical vHW. For a detailed derivation and discussion of the enhanced vHW analysis see ref. [44].

In contrast to a continuous distribution of sedimentation coefficients analysis [84,85], $c(s)$, where the sedimentation velocity boundaries for the species under consideration are fitted with a single frictional ratio, i.e. all particles have the same shape, the vHW analysis can be used for any kind of colloids, regardless of their shape. The deconvolution of diffusion and sedimentation via the enhanced vHW analysis is of special importance for spherical particles, because the assessment of size polydispersity with this analysis is then straightforward. For other particle shapes or for particles that exhibit shape heterogeneity an equivalent sphere radius may be introduced to assess an apparent size polydispersity.

The *psd* can be obtained by converting the sedimentation coefficient distribution, corrected for diffusion, via eq 4.1 or, for spherical particles, via eq 4.3. This conversion requires the input of particle density, solvent viscosity and density. The particle density, however, can be determined via several (other) techniques, e.g. density gradient centrifugation or refractive index measurements. Here we use a specific particle volume (equivalent to the inverse particle density) that is obtained from a single analytical ultracentrifugation sedimentation velocity run using the interference optics (Beckman Coulter^{TM} Optima^{TM} XL-I AUC, see the Appendix for details on this method).

It should be noted that increasing the angular velocity of the AUC rotor containing a sample with a sufficiently long solution column, suppresses sedimentation boundary broadening due to diffusion and therefore enhances the sedimentation coefficient resolution. For a vHW analysis it is therefore recommended to apply the fastest angular velocity possible. The maximum angular velocity, however, is restricted by the speed with which the scans are recorded, the degree of polydispersity and the minimum amount of scans that need to be included in the analysis. Also, excluding early scans, where the fractionation of different sized particles is minimum and the diffusion due to the initially steep concentration gradient is maximal, improves the sedimentation coefficient resolution.

The diffusion on the other hand, can provide important shape information. For such an experiment the angular velocity should be relatively low to obtain as much information on particle shapes as possible. Regarding the assessment of particle shape, an analysis method is available (implemented in *UltraScan* [23]) that allows to simultaneously determine the sedimentation coefficients and frictional ratio's via a sedimentation velocity whole boundary fitting routine. This 2-dimensional spectrum analysis (2DSA [47]) was initially intended for the parameter initialization to confine the search space for the genetic algorithm optimization [45] for sedimentation velocity data fitting. The 2DSA decomposes the experimental sedimentation velocity data into a sum of finite

element solutions to the Lamm equation, describing the non-interacting settling particles present in solution. Because the computational effort to decompose sedimentation and diffusion can quickly become very large (typically several gigabytes of RAM are required), the implementation of parallel computing using supercomputers (clusters) facilitates this analysis method. The solution obtained, thus provides information on the distribution of sedimentation coefficients and shapes (frictional ratios). Clearly, this analysis works best if fast and slow speed sedimentation velocity experiments are combined in a global fitting routine. In principle, if accurate sedimentation and diffusion coefficients are obtained, this method allows the determination of molecular weights via the so-called Svedberg-relation.

We emphasize here that the analysis methods addressed previously, to determine the *psd*, hold for non-interacting macromolecules or colloids. Inter-particle attractions and repulsions may have pronounced effects on the sedimentation behavior, resulting in a non-representative *psd*.

4.2.2. Dynamic Light Scattering

The ensemble averaged scattering intensity measured for dilute dispersions in static light scattering experiments is the sum of the intensity scattered by individual colloids in the so-called scattering volume. The intensity scattered by a single particle is proportional to the squared scattering amplitude $B(\kappa, a)$ that depends on the particle radius a and on the scattering wave vector magnitude κ. The latter quantity follows from a transformation of the scattering angle θ:

$$\kappa = \frac{4\pi n_{\mathrm{d}}}{\lambda_{\circ}} \sin\frac{\theta}{2} \tag{4.5}$$

Here, n_{d} is the dispersion refractive index and $\lambda_{\circ}$ is the wavelength of the incident light *in vacuo*. The scattering amplitude B scales with the particle volume and, consequently, for spherical particles B^2 scales with a^6.

In dynamic light scattering (DLS) [87] experiments, the fluctuations of the intensity I due to the Brownian motion of particles, is characterized by the intensity autocorrelation function (IACF) defined as:

$$g_I = \langle I(\kappa, t_0)\, I(\kappa, t + t_0)\rangle \tag{4.6}$$

In the case of monodisperse spheres, the normalized IACF appears to be [88]:

$$\hat{g}_I = 1 + \exp\left[-2D_{\circ}\kappa^2 t\right] \tag{4.7}$$

with $D_{\circ}$ the Stokes-Einstein [38, 40] translational diffusion coefficient that is inversely proportional to the particle radius a. In other words, the decay of the IACF reflects the diffusion of particles in the solution. For a polydisperse system, the contribution of all particles to the normalized IACF ($\hat{g}_I^{\sigma}(\kappa, t)$) may be averaged by a weighted integral

in terms of the particle radius as [88]:

$$\widehat{g}_I^{\sigma}(\kappa,t) = 1 + C \left| \frac{\int_0^{\infty} da\, f_{psd}(a)\; B^2 \exp\left(-D_{\circ}\kappa^2 t\right)}{\int_0^{\infty} da\, f_{psd}(a)\; B^2} \right|^2 \tag{4.8}$$

where the constant in the denominator normalizes the correlation function and the *dynamic* contrast factor C, required to account for experimental limitations, allows the intercept of the normalized correlation function for $t \to 0$ to be smaller than 2.

Computing particle shapes from light scattering experiments is difficult because this problem is ill-posed. Since the measured quantity in SLS is the intensity, the phase information is lost, something which hampers an inverse Fourier-transformation. Different particle shapes may correspond to a single scattering intensity pattern that varies with the scattering angle θ. Nevertheless, using e.g. high resolution small angle scattering employing bio-macromolecules, which generally lack shape heterogeneity, over-sampling techniques can be used to obtain a low resolution particle shape [89]. Another applicant is coherent X-ray diffraction to reveal the structure of nanocrystals [90].

Regarding the ill-conditioning of the inversion problem [80], the shape of the particle size distribution should be known a priori for the analysis of the DLS correlation function. Generally, for polydisperse spherical colloids with an unimodal size distribution, the weight factor $f_{psd}(a)$ is assumed to be a log-normal radius distribution, whose logarithm is normally distributed. Even if the shape is known, several combinations of mean particle radius a_{AV} and polydispersity σ_{p} can be described with the same correlation function. Therefore, we generate a theoretical IACF using the discrete *psd* computed from the differential (envelope) vHW sedimentation coefficient distribution (including 99% of each interference sedimentation boundary) obtained from the SV AUC interference optical data (Figure 4.3). Consequently, the integral in eq 4.8 is exchanged for a summation over the k distinct particle radii a_i (see eqs 4.14 and 4.15) that comprise the discrete particle size distribution (histogram) $h_{psd}(a_i)$:

$$\widehat{g}_I^{\sigma}(\kappa,t) = 1 + C \left| \frac{\sum_{i=1}^{k} h_{psd}(a_i)\; B^2 \exp\left(-D_{\circ}\kappa^2 t\right)}{\sum_{i=1}^{k} h_{psd}(a_i)\; B^2} \right|^2 \tag{4.9}$$

For comparison, we also use a continuous *psd* that is obtained by fitting:

$$f_{psd}(a) = A \exp\left[-\exp(-z) - z + 1\right] \tag{4.10}$$

to the discrete *psd*. In eq 4.10, z is equal to:

$$z = \frac{(a - a_c)}{w} \tag{4.11}$$

Table 4.1: Bindzil® 30/360 Dispersion Characteristics [a]

SiO_2:	30.5% w/w
Particle diameter:	9 nm
Titrable alkali as Na_2O:	0.60% w/w
pH:	10.0
Dispersion density: [b]	1.218 g cm^{-3}
Dispersion viscosity: [b]	4 mPa s
Average specific surface area:	360 m^2 g^{-1}

[a] Quantities according to the product data sheet (Eka Chemicals AB Colloidal Silica Group, Bohus, Sweden).
[b] Determined at 20 °C.

a is the radius, a_c, w and A are, respectively, the center radius, the width and the amplitude of the *psd*. This *psd* (eq 4.10) is normalized such that:

$$\int_0^\infty da\, f_{psd}(a) = 1 \tag{4.12}$$

Another approach is the frequently used second cumulant analysis method [91] valid for spherical particles with a sufficiently narrow size distribution (often assumed to be log-normal) that is expanded to first order in standard deviation. The drawback of this approach is that it restricts the polydispersity to a relative small number (i.e. $\leqslant 10\%$). The second cumulant, which is directly related to the polydispersity, is very sensitive to the truncation of the correlation function [92]. Moreover, the second cumulant analysis is valid only for the limit of $\kappa \to 0$.

4.3. Materials and Methods

The colloidal dispersion employed here, is commercially available as Bindzil® 30/360 (Eka Chemicals AB Colloidal Silica Group, Bohus, Sweden). According to the product data sheet it consists of discrete spherical silica particles, which are charge stabilized due to a small amount of sodium hydroxide, in an aqueous solution. These sub-microscopic particles consist of pure amorphous silicon dioxide (SiO_2). According to the manufacturer, the particle size is uniform with 9 nm diameter. Typical dispersion properties are shown in Table 4.1. Since colloidal silica partly dissolves in aqueous solution due to the hydrolysis of SiO_2 mediated by a base as OH^-, the small Bindzil® 30/360 are subjected to Ostwald-ripening [93] and the particles may therefore change in time; i.e. larger particles grow at the expense of small particles because the systems tends to reduce its surface area and, consequently, the average particle size increases [37].

4.3.1. Sedimentation Velocity Analytical Ultracentrifugation

The stock dispersion as obtained from the manufacturer was diluted approximately 24 times (42 μL stock dispersion + 958 μL MilliQ water) to achieve an optical density ($OD_{229\,nm}$) that is in between 0.5 and 0.9 at 229 nm. The latter wavelength is the shortest wavelength with an optimal signal-to-noise ratio when using the absorbance optics of the Beckman Coulter^{TM} Optima^{TM} XL-I AUC. The stock dispersion was diluted to avoid concentration effects e.g. hydrodynamic and/or electrostatic interactions. According to Table 4.1, the SV AUC sample contains approximately 15.6 mg mL^{-1} SiO_2 spheres (pH $\approx$ 9.0).

An estimate for the angular velocity from a Finite Element [75] (FE) simulation (*UltraScan* [23]) was further optimized experimentally for a SV run employing the absorbance optics to resolve the whole range of s-values to obtain 45 scans that cover the solution column length. SV AUC experiments were conducted employing 12 mm standard double sector epon charcoal-filled centerpieces equipped with quartz (absorbance optics) or sapphire (interference optics) windows.

The sedimentation rate was determined with the absorbance and interference optics in two separate experiments on an identical sample ($\omega = 18,800$ rpm, T = 20 $\pm$ 0.1 °C) to allow a comparison of data analysis results (see section 4.4).

SV data were analyzed with the enhanced vHW analysis [44] and the 2DSA [47] both implemented in *UltraScan* [23] and with the $c(s)$ analysis (sedfit [84,85]) methods. The latter was performed with and without maximum entropy regularization [84] (confidence levels of 0.70 and 0.95).

The relative polydispersity (σ_p) in terms of the standard deviation (σ_{std}) obtained from a sedimentation coefficient distribution reads:

$$\sigma_p = \frac{\sigma_{std}}{a_{AV}} 100\% \tag{4.13}$$

The standard deviation follows from the square-root of the variance $V(a)$:

$$V(a) = \frac{1}{N} \sum_{i=1}^{k} n_i (a_i - a_{AV})^2 \tag{4.14}$$

with N the sum of frequencies (n_i) of the k distinct sedimentation coefficients and a_{AV} the average (arithmetic mean) radius that follows from:

$$a_{AV} = \frac{\sum_{i=1}^{k} n_i a_i}{\sum_{i=1}^{k} n_i} \tag{4.15}$$

n_i is directly proportional to the concentration c_i of solute(s) or colloid(s) i. For a vHW analysis n_i is proportional to the amount of linear extrapolations for which the

intercept at $1/\sqrt{t} = 0$ or $t = \infty$ is in between two consecutive sedimentation coefficients s_i and s_{i+1}.

4.3.2. Dynamic Light Scattering

The dispersion available for DLS measurements was a silica sol that had been dialyzed extensively in a previous study [86] against ethanol. This dialysis was needed for a surface functionalization, which cannot be done in water [86]. Since this dialysis transfer to ethanol does not affect the colloidal stability of the silica particles [86], we can compare the results from DLS and SV AUC measurements on aqueous silica sols.

Correlation functions at 6 equally spaced scattering angles, ranging from $\theta = 35°$ to $140°$, were determined for a diluted Bindzil® 30/360 sample employing a Krypton-ion laser (Spectra Physics, type 2025-11) as the incident light beam for which the *in vacuo* wavelength is $\lambda_\circ = 647.1\,\text{nm}$. The correlation functions were recorded with a multiple tau digital correlator (ALV, type 6010/160). In the detector (ALV/SO-SPID) the beam passes a splitter and is directed into two single-photon photo-multiplier tubes (PMT's), from which a pseudo-correlation function was produced to suppress the dark current generated by after-pulsing and thermal noise. Since the scattering power of the Bindzil® 30/360 particles is relatively low due to the small particle dimensions, the correlation function at each scattering angle was measured during 2 hours, to increase the signal-to-noise ratio and, consequently, to obtain smooth correlation functions.

For the theoretical correlation functions, the hydrodynamic radii required to compute translational diffusion coefficients in eqs 4.8 and 4.9 via the Stokes-Einstein [38,40] relation, are assumed to equal the bare particle radii.

4.4. Results and Discussion

As already addressed, the size and shape of Bindzil® 30/360 particles cannot be precisely determined from TEM micrographs (Figure 4.1), since the small silica particles easily melt in the electron beam. The average particle size and shape, as well as their distributions, however, can be assessed straightforward by a single SV AUC experiment. In the following section 4.4.1 the results from SV AUC experiments are discussed and compared, in section 4.4.2, with the DLS correlation functions.

4.4.1. Sedimentation Velocity Experiments

The sedimentation coefficients distribution, corrected for diffusion, obtained from an enhanced vHW analysis, shows that the Bindzil® 30/360 particles exhibit size and/or shape polydispersity (graph A and C in Figure 4.3). The sedimentation coefficients of these particles range from approximately 20 to 250 S.

The range and overall shape of the vHW differential and the 2DSA sedimentation coefficient distributions shown in Figures 4.3 (graph A) and 4.4 are almost identical. Furthermore, figure 4.4 clearly shows that the particle size is very heterogeneous,

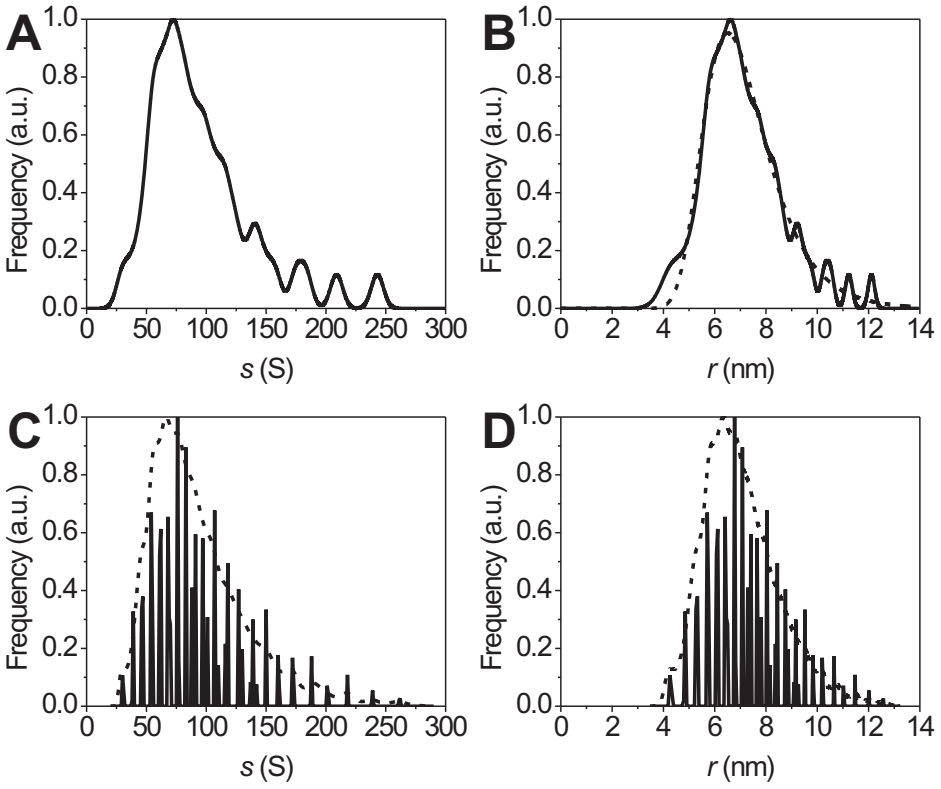

Figure 4.3: Apparent (i.e. not corrected for solvent density and viscosity) differential (envelope) sedimentation coefficient distribution (——, graph A) as obtained from the enhanced vHW analysis [44] (*UltraScan* [23]) including 99% of each SV boundary. The corresponding *psd* (——) is shown in graph B. The sedimentation coefficient distribution (graph C) and the *psd* (graph D) obtained from a $c\,(s)$ analysis (sedfit [84, 85]) with (- - - -) and without (——) maximum entropy regularization [84] are equal to the enhanced vHW distributions. The continuous *psd* (- - - -, graph B), obtained by fitting eq 4.10 to the discrete differential *psd*, was used to fit the DLS correlation functions. All distributions were derived from SV AUC interference optical data.

whereas the particle shape appears to be uniform; i.e. the frictional ratio for all silica nanoparticles is $f/f^\circ = 1$, indicating that all particles are spherical.

Having determined the uniform spherical shape of the Bindzil® 30/360 particles, the conversion of the sedimentation coefficient distribution into a radius distribution is straightforward. This conversion can be done as follows.

First, the specific particle volume (or partial specific volume) should be available and may be obtained independently or from the same experimental SV AUC interference optical data (single run) that was acquired to determine the sedimentation coefficient and particle shape distribution. Here, we use a specific particle volume of $\overline{\nu}_\mathrm{p} = 1/\rho_\mathrm{p} = 0.57\,\mathrm{mL\ g^{-1}}$, which is determined as described in the Appendix.

Second, the solvent viscosity and density are required. According to Table 4.1, the aqueous SV AUC sample solution contains approximately 77 mM NaOH. Therefore, the

Table 4.2: vHW Particle Size Distributions [a]

	Absorbance [b]	Interference [c]
a_{AV} (nm) [d]	7.7	7.4
$V(a)$ (nm^2) [e]	1.6	1.2
σ_{std} (nm) [f]	1.3	1.1
σ_{p} (%) [g]	16.3	14.8

[a] vHW analysis results including 90% of each boundary (Figure 4.3).
[b] Results for SV AUC absorbance data.
[c] Results for SV AUC interference data.
[d] Average particle radius (eq 4.15).
[e] Variance (eq 4.14).
[f] Absolute standard deviation.
[g] Size polydispersity (eq 4.13).

density and viscosity of the solution in which the silica particles sediment are, respectively, $\rho_{\mathrm{s}} = 1.0019\,\mathrm{g\,mL^{-1}}$ and $\eta_{\mathrm{s}} = 1.0125\,\mathrm{mP\ s}$ (computed with the buffer correction module implemented in *UltraScan* [23]).

Third, substituting all required parameters previously addressed in eq 4.3, yields the radius distributions (Figure 4.3, graph B and D). The average (arithmetic mean) radius, the variance, the standard deviation and the relative polydispersity can be computed from the *psd* via eqs 4.13, 4.14 and 4.15. Clearly, the Bindzil® 30/360 particles exhibit

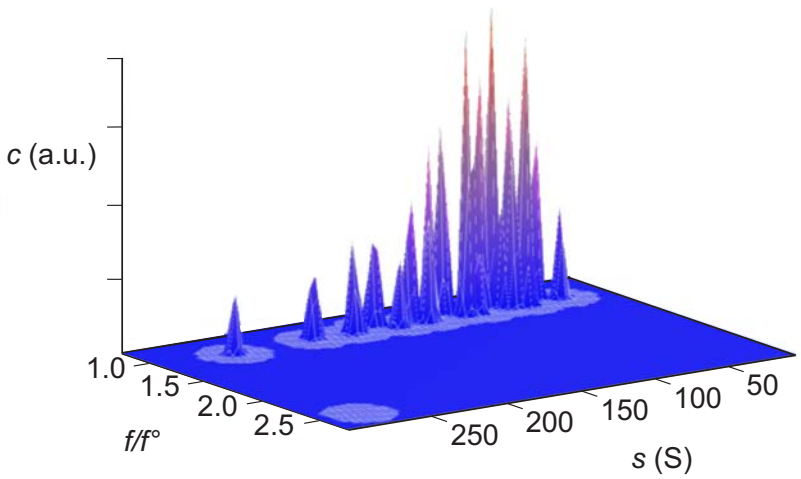

Figure 4.4: 3-dimensional plot of particle concentration (c in arbitrary units) vs. the frictional ratio (f/f°) and sedimentation coefficient (s) as obtained from a 2-dimensional spectrum analysis (*UltraScan* [23]) on the SV AUC interference optical data. All particles are spherical, i.e. the frictional ratio for all silica nanoparticles within this large sedimentation coefficient range is equal or close to $f/f^\circ = 1.0$, assuring that the conversion of the vHW differential sedimentation coefficient distribution into a radius distribution via eq 4.3 is appropriate.

Table 4.3: vHW, 2DSA and $c(s)$ Analysis Results [a]

	vHW [b]	2DSA [c]	$c(s)$ [d]	$c(s)$ [e]
a_{AV} (nm) [f]	7.4	7.5	7.3	7.3
$V(a)$ (nm^2) [g]	2.7	2.6	2.4	2.4
σ_{std} (nm) [h]	1.6	1.6	1.5	1.5
σ_{p} (%) [i]	22.0	21.4	21.0	21.2

[a] All values are obtained from the SV AUC interference optical data.
[b] van Holde-Weischet analysis results including 99% of each boundary.
[c] 2-dimensional spectrum analysis (Figure 4.4).
[d] Continuous distribution of sedimentation coefficients analysis [84, 85].
[e] $c(s)$ analysis [84, 85] with maximum entropy regularization [84].
[f] Average particle radius (eq 4.15).
[g] Variance (eq 4.14).
[h] Absolute standard deviation.
[i] Size polydispersity (eq 4.13).

a large size polydispersity (Tables 4.2 and 4.3). The SV AUC results from the interference and absorbance optics data including 90% of each sedimentation boundary on the size determination are similar (Table 4.2). Identical results would assure that using a single extinction coefficient for 'all' species contained in the dispersion is appropriate, in contrast to the case of polydisperse colloidal dispersions that cover a very broad size range. For the latter system, the fraction of large particles may be overestimated since the scattered intensity scales with the particle volume squared. The small deviation of the average size and relative polydispersity (Table 4.2) is likely due to this fact.

However, the almost quantitative agreement of the *psd* from the SV AUC absorbance optical data with the interference optical data is remarkably good, considering that absorbance data generally have a much lower signal-to-noise ratio compared to interference data, in particular for particles that have a relative large refractive index difference and a relatively small extinction coefficient. For colloids that have a much larger refractive index than the dispersion medium, a steep concentration gradient and, consequently, a steep gradient in refractive index, develops during the early stage of the sedimentation velocity experiment. Such gradients result in reflection of light. These peaks are equivalent to the meniscus phenomenon associated with the absorbance optical system. This effect decreases during the time course of the sedimentation velocity run because of diffusion and radial dilution. Together with the time invariant noise, the reflection of light contributes to the deviations previously addressed. Therefore a *psd* of silica colloids from interference optical data will, in general, be more accurate than from absorbance optical data.

The effect of excluding 5% of each sedimentation boundary at the top and the bottom in a vHW analysis is evident from Tables 4.2 and 4.3. The smallest and largest colloids are not covered by the *psd* if upper and lower portions of sedimentation velocity

boundaries are clipped off. Generally, a small portion of each sedimentation boundary is excluded in a vHW analysis to maintain the correlation of divisions. This exclusion may result in an apparent decreased polydispersity. Here, the data quality is sufficient to include 99% of each sedimentation velocity boundary (this is usually not the case for SV AUC absorbance optical data).

It can be seen from Figure 4.3 that the enhanced vHW (including 99% of each SV boundary) and the $c(s)$ (whole boundary fitting routine) sedimentation coefficient distributions and *psd's*, derived from the same SV AUC interference optical data, are almost equal. Consequently, the average radius, the variance and the relative polydispersity obtained from these sedimentation coefficient distributions are not significantly different. Furthermore, the $c(s)$ analysis (sedfit [84,85]) was performed with and without maximum entropy regularization [84]. In contrast to what is reported for the size distribution of a multiprotein sample [94], we show here that the model independent sedimentation coefficient distribution obtained via a vHW analysis yields the same results as the $c(s)$ method. This equality is likely due to the large spread in s-values and in particular to the fact that the 'true' *psd* of Bindzil is nearly continuous. In this case, for a sufficiently large amount of divisions, the resolution of the vHW analysis is just as good as the resolving ability of whole boundary fitting methods. The only effect of regularization on the sedimentation coefficient distribution and the corresponding *psd* is smoothing. The s and a distributions do not change, even if the confidence interval is varied from 0.70 to 0.95. Since regularization has no effect and taking into account that the $c(s)$ constrains the frictional ratio to a single value, the enhanced vHW analysis is the preferred method to assess the polydispersity of colloids. Moreover, the vHW analysis is, in principle, model independent and the determination of a *psd* with this analysis is therefore straightforward.

The results shown in Table 4.3 conform well to particle dimensions obtained from TEM (image A in Figure 4.1). But are the results obtained from SV AUC consistent with the experimental DLS correlation functions?

4.4.2. SV AUC and DLS Compared

The consistency of SV AUC and TEM particle dimensions can be verified by an overlay of the theoretical polydisperse intensity auto-correlation functions computed via eqs 4.8 and 4.9 for, respectively, the continuous and discrete *psd* and the experimental IACF (Figure 4.5). The theoretical correlation functions closely follow the experimental IACF. The root-mean-square (rms) deviations of the theoretical and experimental correlation functions reveal that the predicted correlation function using the discrete and the continuous *psd* are not significantly different.

Conform our expectation, the second cumulant analysis method yields for the Bindzil® 30/360 particles an apparent polydispersity of 30% or larger, which is much larger than

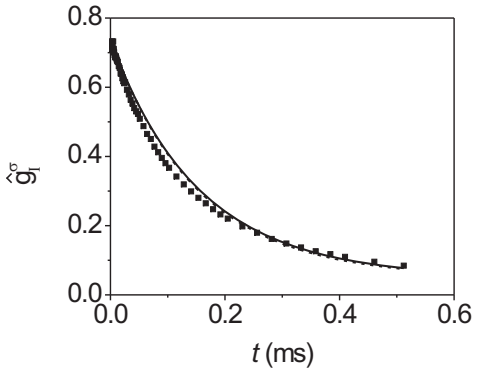

Figure 4.5: Theoretical polydisperse intensity auto-correlation functions calculated via eqs 4.8 and 4.9 for, respectively, the continuous (——) and discrete (- - - -) *psd*. The experimental IACF (▪, $\theta = 56°$ or $\kappa = 1.24 \cdot 10^7\,\mathrm{m}^{-1}$) follows the theoretical IACF's closely. The discrete *psd* obtained from the enhanced vHW analysis (including 99% of each sedimentation boundary) results in the same IACF as the continuous *psd*, which is a fit of eq 4.10 to the discrete *psd*.

all other results obtained here, implying that this apparent polydispersity is physically not relevant. Another approach is to determine the theoretical correlation function for spherical particles with a log-normal size distribution. As mentioned earlier, several combinations of a mean radius and polydispersity result in the same correlation function. Defining the mean radius as obtained from the enhanced vHW analysis (Table 4.3) and using the polydispersity as a fit parameter, the rms of the residuals of the theoretical and experimental correlation can be minimized. In the limit of $\kappa \to 0$, the resulting polydispersity is 23% and agrees well with the polydispersities determined from the SV AUC optical interference data (Table 4.3). However, rms deviations of the IACF generated using the vHW *psd's* and the experimental correlation function are significantly smaller (30 %) compared to the IACF for a log-normal *psd*.

4.5. Conclusions

We have shown that sedimentation velocity analytical ultracentrifugation (SV AUC) is very suited for the *in situ* determination of average sizes and shapes of small colloids in solution. A single SV AUC experiment already contains sufficient information to determine the particle size- and shape distributions, as well as the specific particle volume. From the *psd* all relevant quantities as the average radius, variance, standard deviation and relative polydispersity can be computed.

Whole boundary fitting methods and in particular the continuous distribution of sedimentation coefficients, $c(s)$, do not offer any advantage compared to the model independent enhanced van Holde-Weischet analysis. Additionally, it should be noted that the procedure reported here including sample preparation, to eventually obtain

the *psd* and all relevant statistical parameters can in principle be conducted within a single day. Our method to determine the average size and polydispersity from SV AUC experiments may also be applied to other particle shapes to obtain an apparent polydispersity, for which the concept of equivalent sphere radii may be introduced.

For colloidal silica dispersions an AUC equipped with interference optics yields data with a higher signal-to-noise ratio compared to absorbance optics, and in addition provides information on the specific particle volume. Therefore, using the interference optics for dispersed particles that have a relatively large refractive index compared to the solvent and that absorb only weakly in the UV-Vis region, yield more reliable results.

Furthermore, the experimental DLS data are significantly better described by the theoretical intensity auto-correlation function generated with the SV AUC *psd* compared to the correlation function for polydisperse spheres with a log-normal size distribution. Additionally, we found that the second cumulant analysis fails and is indeed not valid for the relatively large polydispersity of the silica particles employed here.

Acknowledgement

This work was done in collaboration with Bonny W.M. Kuipers. We thank E. Maria Claesson for providing TEM images and DLS data, and Stefano Sacanna for helpful discussions. Ben H. Erné and Kees C.G. de Kruif are thanked for helpful discussions and suggestions that improved this contribution. Eka Chemicals AB Colloidal Silica Group (Bohus, Sweden) is thanked for providing the Bindzil® 30/360 dispersion.

Appendix: Specific Particle Volume from SV Interference Data

The specific particle volume can be obtained from a single analytical ultracentrifugation sedimentation velocity run using the interference optics (Beckman Coulter™ Optima™ XL-I AUC), provided that all species have the same refractive index, which can be obtained from literature (e.g. ref. [74]), and that the initial sample loading concentration is known. The key parameter is the total fringe displacement, Y_{tot}, via [25]:

$$Y_{\text{tot}} = \sum \left(c_i \frac{\partial n}{\partial c_i} \right) \frac{l}{\lambda} \tag{A-4.1}$$

with c_i the concentration of component i, l the cell path length (12 mm) and λ the optical wavelength (675 nm). Y_{tot} for the total initial loading concentration, can be determined from a sedimentation velocity run by extrapolating the fitted plateau concentrations (fringe displacement) of each sedimentation velocity scan included in the analysis with a polynomial to the time at which the rotor started to accelerate $t = 0$. If the dispersion contains one species only, $\partial n/\partial c_i$ in eq A-4.1 can be taken out of the summation and the specific refractive index can be calculated by substitution of Y_{tot},

$\sum c_i = c_{\mathrm{tot}}$, l and λ into eq A-4.1. The specific particle volume then follows from the differential refractive index $\partial n/\partial c_{\mathrm{tot}}$ (i.e. specific index of refraction) by substitution of the particle (n_{p}) and solvent (n_{s}, corrected for added salt concentration) refractive indices in:

$$\frac{\partial n}{\partial c_{\mathrm{tot}}} = \frac{n_{\mathrm{p}} - n_{\mathrm{s}}}{\rho_{\mathrm{p}}} \tag{A-4.2}$$

The total fringe displacement from the exponential fit (enhanced vHW analysis, *UltraScan*) for the initial loading concentration of $c_{\mathrm{tot}} = 15.6\,\mathrm{mg\ mL^{-1}}$ (using the weight concentration from Table 4.1 and accounting for the dilution) is $Y_{\mathrm{tot}} = 18.8$. Substitution of Y_{tot}, c_{tot}, the laser's wavelength $\lambda = 675\,\mathrm{nm}$ and the centerpiece path length $l = 12\,\mathrm{mm}$ in eq A-4.1 yields a differential refractive index of $\partial n/\partial c_{\mathrm{tot}} = 6.78 \cdot 10^{-5}\,\mathrm{mL\ mg^{-1}}$. Next, the specific particle volume, $\overline{\nu}_{\mathrm{p}} = 1/\rho_{\mathrm{p}} = 0.57\,\mathrm{mL\ g^{-1}}$, for the Bindzil® 30/360 particles employed here follows from eq A-4.2 upon substitution of $n_{\mathrm{s}} = 1.33$ and $n_{\mathrm{SiO_2}} = 1.45$ (amorphous SiO_2) from ref. [74].

Part 3

Attractive Colloids

5

Sedimentation Velocity of Self-Associating $\{Mo_{72}Fe_{30}\}$ Monomers

Abstract

We report a sedimentation velocity study of spherical polyoxometalates that exhibit supramolecular structure formation. The self-assembly can be monitored by UV-Vis spectrophotometry. Particle shape and absolute molar weight of the $\{Mo_{72}Fe_{30}\}$ monomers and trends in the sedimentation coefficient distributions for 'giant' vesicles are determined from sedimentation velocity experiments. For the monomers, the procedure of the sedimentation velocity data analysis comprises a sequence of analyses involving the van Holde-Weischet analysis, 2-dimensional spectrum analysis and Genetic Algorithm optimization to obtain sedimentation coefficients, diffusion coefficients and molecular weights from globally fitted multi-speed sedimentation velocity experimental data. The analysis of experimental data via this method is, to our knowledge, reported for the first time. Combined with dynamic light scattering data, the sedimentation velocity experiments reveal that after 3 years at room temperature, the vesicles are constituted of two $\{Mo_{72}Fe_{30}\}$ layers. Furthermore, we found proof that in aqueous solution the $\{Mo_{72}Fe_{30}\}$ monomers release small solutes that are possibly ligands. The critical aggregation concentration for $\{Mo_{72}Fe_{30}\}$ is at least 2 to 4 times smaller than reported elsewhere.

5.1. Introduction

Self-assembly or association is a process that is observed for many different systems, ranging from solutions containing surfactants that spontaneously form micelles or lipid bilayers to virus capsids. It recently became clear [95] that also single molecular inorganic clusters known as polyoxometalates (POMs) spontaneously assemble into supramolecular structures in a fashion that is globally comparable to the self-association behavior of surfactants and virus capsids. POMs have been shown to spontaneously and reversibly associate into large hollow spheres [96,97], something which strongly reminds of surfactant micelles and virus capsids. The common feature of these diverse systems is a critical micelle or critical aggregation concentration. Interestingly, some of the POMs (monomers that constitute the superstructures) are spherically symmetric, as is the case for the POMs studied here (see Figure 5.1), yet they form spherical vesicle-like supramolecular associates. The superstructure formation from the well-defined {$Mo_{72}Fe_{30}$} monomers (weak acid [78]) caused by attractions [98], however, is unusually slow [99] and, depending on the temperature, may even take several years before the supramolecular vesicles adopt their thermodynamic equilibrium size and layer number. To date, studies on such systems are focused on the characterization of the structures present in these solutions via static and dynamic light scattering [96, 98–100]. Despite the wealth of information that can be obtained employing the latter techniques, important features of POMs solutions and their self-association behavior may be overlooked. Here, we demonstrate that several earlier studies [96, 100, 101] on parameter values at thermodynamic equilibrium have actually been conducted on meta-stable associates of {$Mo_{72}Fe_{30}$}. Moreover, in addition to the reported flow-field fractionation study [102], a simple and ordinary technique as UV-Vis attenuance readings already allows to monitor the self-assembly of {$Mo_{72}Fe_{30}$}. We note here that analytical ultracentrifugation has proven to be a very suitable technique for the analysis of POMs [72, 81]. It has, to our knowledge, never been used for the characterization of {$Mo_{72}Fe_{30}$} solutions.

Our aim here is to study, via multi-speed sedimentation velocity (SV) analytical ultracentrifugation (AUC) experiments, the temperature and time dependent self-assembly of POMs. This study involves the determination of the absolute molar weight and shape of the {$Mo_{72}Fe_{30}$} monomers and trends in the sedimentation coefficient distributions of supramolecular vesicles. The latter distributions are combined with hydrodynamic radii obtained from dynamic light scattering experiments. Sedimentation velocity experiments also allow to detect free {$Mo_{72}Fe_{30}$} monomers or other small components, such as ligands that can be released from the monomers. The nanometer sized {$Mo_{72}Fe_{30}$} cluster exchanges ligands with the bulk solution [103], but the release of relative large or dense ligands compared to water has not been reported to date. In principle, the critical aggregation concentration for {$Mo_{72}Fe_{30}$} can be determined via SV AUC.

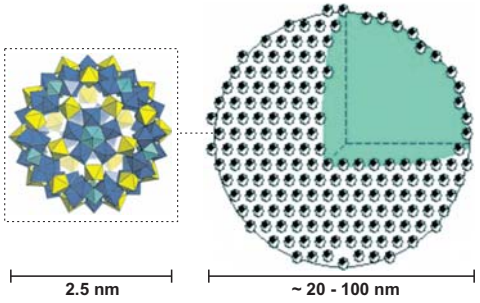

Figure 5.1: Schematic representation of a $\{Mo_{72}Fe_{30}\}$ monomer (left, molecular formula **1** and **2**) and a supramolecular assembly (vesicle) of $\{Mo_{72}Fe_{30}\}$ monomers (right) (DIAMOND 2.1 from Dr. K. Brandenburg, Crystal Impact GbR, 2001 and POV-Ray 3.5 freeware from C. J. Cason).

5.2. Materials and Methods

5.2.1. Preparation of $\{Mo_{72}Fe_{30}\}$

The procedure reported in ref. [104] was followed for the synthesis of $\{Mo_{72}Fe_{30}\}$ monomers (Figure 5.1):

$$\{Mo^{VI}_{72}Fe^{III}_{30}O_{252}L_{102}\} \cdot \text{ca. } 180\,H_2O \quad \mathbf{1} \text{ [104]}$$

with:

$$L = H_2O/CH_3COO^-/Mo_2O^{n-}_{8/9} \qquad \mathbf{2} \text{ [104]}$$

5.5 g $FeCl_3 \cdot 6\,H_2O$, 5.5 g $CH_3COONa \cdot 3H_2O$ and 7.1 g $\{Mo_{132}\}$ were dissolved in 375 mL water and stirred for one day. During that time the color changed from dark red to light brown. 10 g NaCl and 10 mL 1 M hydrochloric acid were added to the solution that was subsequently heated to approximately 90 °C and filtrated while still hot through a glass filter (Schott Geräte Jena^{er} Glas G5). After five days, the precipitated yellow crystals from the filtrated solution were recovered using a glass filter (Schott Geräte Jena^{er} Glas G5) and washed with ice-water after which the crystals were dried in air.

5.2.2. Sedimentation Velocity Analytical Ultracentrifugation

Sedimentation velocity (SV) analytical ultracentrifugation (AUC) experiments were done employing a solution of 7.28 mg of the crystals obtained from synthesis dissolved in 100 mL Milli-Q demiwater. This solution was filtered through a disposable filter (Schleicher & Shuell, pore size 0.2 μm) to remove dust particles and flocs or aggregates. As confirmed by attenuance readings (Varian Cary 1E UV-Visible Spectrophotometer) no $\{Mo_{72}Fe_{30}\}$ material was lost. Since the specific refractive index of $\{Mo_{72}Fe_{30}\}$ is $\partial n/\partial c = 1.42 \pm 0.01\,\text{mg mL}^{-1}$ [96, 97], the expected fringe displacements for the concentration of the $\{Mo_{72}Fe_{30}\}$ monomer solution are too small and are almost equal

to the radial invariant noise observed with the interference optical system. We therefore employ the absorbance optical system. To obtain SV AUC absorbance optical data with a maximum signal-to-noise ratio, the optical wavelengths, matching with local emission maxima of the Xenon flash lamp, were chosen such that the attenuance of SV AUC samples were in between 0.6−0.9 OD (12 mm path length). Only for the characterization of the $\{Mo_{72}Fe_{30}\}$ monomers, the stock solution was diluted. We emphasize here that the sedimentation coefficients corrected for solvent density and viscosity variations, denoted as s, reported in this contribution are sedimentation coefficients in water at 20 °C ($s_{20,w}$).

5.2.3. Sedimentation Velocity of $\{Mo_{72}Fe_{30}\}$ Monomers

Within a week after dissolving and filtration of the synthesis material, the $\{Mo_{72}Fe_{30}\}$ monomers were characterized by monitoring the sedimentation velocity for a 23.1 μg mL^{-1} $\{Mo_{72}Fe_{30}\}$ solution (stored at 20 °C), in two separate runs at, respectively, 40,000 and 60,000 rpm. The two SV absorbance optical data sets were analyzed using the enhanced van Holde-Weischet analysis (vHW) [44] (for the classical vHW analysis see ref. [43]), 2-dimensional spectrum analysis (2DSA) [47] and Genetic Algorithm (GA) optimization [45] (all implemented in *UltraScan* [23]). Since the models required to accurately describe the transport phenomena involved in SV AUC experiments are nonlinear in the parameters (sedimentation coefficients, diffusion coefficients and concentrations of solutes or particles) a complex error surface (tilted egg-carton) has to be explored to determine the global mininum. Nonlinear least squares optimization fitting routines [75] for adjusting the parameter values may easily get stuck in local minima. The Genetic Algorithm is in essence a stochastic optimization that is employed for its immunity to local minima convergence traps which increases the likelihood of locating the 'true' global minimum corresponding to the real solution. However, this GA optimization must be performed within a constraint range of sedimentation coefficients and frictional ratios to confine the search space. Without such a confinement the GA optimization exceeds, in view of practical purposes, a reasonable computational effort despite the implementation of parallel computation [47] using super-computers (clusters).

The Genetic Algorithm optimization works as follows [45]. An initial random population of individuals is simulated, and each individual's fitness is evaluated and the population is allowed to evolve. Parameter vectors are treated as genes which can exchange or modify parameters (bases, i.e. sedimentation and diffusion coefficients) by crossover with other parameter vectors or by mutation, insertion or deletion operators. Multiple populations (demes) can evolve independently, or experience a controlled migration rate, which allows for exchange of parameter information among multiple demes. Evolution of the best fit parameter combination within a population is controlled by a multi-generational selection process, which favors survival of individuals with a better

fit. The survival pressure, migration rate, crossover frequency, mutation, insertion and deletion probability can be independently controlled by random number operators, and each probability rate needs to be optimized for best efficiency.

For the characterization of the $\{Mo_{72}Fe_{30}\}$ monomers the following (model independent) analysis procedure was performed to avoid any user introduced bias that may lead to a solution (sets of sedimentation coefficients s, f/f° and concentrations c) that corresponds to a local minimum. At first, the range of sedimentation coefficients that should be explored is determined from an enhanced vHW analysis. This range of sedimentation coefficients constrains the subsequently conducted 2DSA. For the first 2DSA an estimate for the frictional ratio range is required to narrow the search space. The shape of solutes or particles that are not extremely elongated can be modeled with a frictional ratio that is in between $1 \leqslant f/f^\circ \leqslant 4$ [105]. In this 2DSA, Lamm-equation solutions (sets of sedimentation coefficients s, diffusion coefficients D and concentrations) and the time-invariant (TI) noise that appears in all scans are determined simultaneously. Generally, for monodisperse and paucidisperse systems the distribution of s versus f/f° obtained from the first 2DSA is degenerate; i.e. it contains non-existing solutes. After TI noise subtraction, the majority of non-existing solutes are filtered out with a second 2DSA that is performed with 50 Monte Carlo (MC50) iterations [46]. A Monte Carlo approach is based on randomly selecting parameters from the search space, simulating a model function based on these parameters, and evaluating the fitness function. The Monte Carlo iterations serve to amplify the signal, which is directly proportional to the number of MC iterations, relative to the noise that amplifies with the square-root of the number of MC iterations. With this 2DSA-MC50 distribution, the search space for the GA analysis is constraint, from which a distribution is obtained that, similar to the first 2DSA, also contains non-existing solutes. A second GA is performed, initialized with the former GA distribution, with 50 MC iterations to obtain only real solutes. Finally, the two GA-MC50 distributions for the low- and high-speed experiment are combined to initialize a global GA, which is further refined by performing a second global GA-MC50.

5.2.4. Sedimentation Velocity of $\{Mo_{72}Fe_{30}\}$ Vesicles

Three portions of the filtrated $72.8 \pm 0.2\,\mu g\,mL^{-1}$ stock solution were separately stored at, respectively, 20 °C, 55 °C and 80 °C during approximately 100 days to allow superstructure formation. During this storage, wavelength spectra (Varian Cary 1E UV-Visible Spectrophotometer) were regularly recorded to monitor changes in the attenuance associated with the self-assembly of $\{Mo_{72}Fe_{30}\}$ monomers into 'giant' spherical (mono-layered) vesicles. The $\{Mo_{72}Fe_{30}\}$ supramolecular structures contained in each sample (pH $\approx$ 5) were characterized with two-speed SV AUC experiments. The first low speed was applied to monitor the sedimentation velocity of supramolecular

structures, after which the rotor was accelerated to sediment the {$Mo_{72}Fe_{30}$} monomers that may be present if their critical aggregation concentration (CAC) is well above the detection limit of the absorbance optics. Also, at this high speed, other small solutes that may be released by the {$Mo_{72}Fe_{30}$} monomers upon superstructure formation will be detected either from a moving solvent-solution interface or as a baseline. Additionally, for comparison a 3 year old {$Mo_{72}Fe_{30}$} solution, which was stored at 20 °C, with a comparable concentration was also employed for the SV AUC and DLS experiments. The sedimentation coefficient distribution for the superstructures contained in the latter solution was determined when the sample was 1 and 3 years old.

5.2.5. Dynamic Light Scattering

Dynamic light scattering experiments were done on the same samples, stored at 20 °C, 55 °C and 80 °C during approximately 100 days (72.8 ± 0.2 $\mu g\,mL^{-1}$), 1 and 3 years respectively, as employed for the SV AUC experiments on {$Mo_{72}Fe_{30}$} superstructures.

Correlation functions at three scattering angles, namely 35.0°, 77.5° and 120.0°, were determined for the three {$Mo_{72}Fe_{30}$} samples employing an Argon-ion laser (Spectra Physics, type 2025-11) as the incident light beam with an *in vacuo* wavelength of $\lambda_\circ = 514.5\,nm$. The correlation functions were recorded with a multiple tau digital correlator (ALV, type 6010/160). In the detector (ALV/SO-SPID) the beam passes a splitter and is directed into two single-photon photomultiplier tubes (PMT), from which a pseudo-correlation function was produced to suppress the dark current generated by after-pulsing and thermal noise. The correlation functions were analyzed with the standard second cumulant analysis method that is valid only for a system for which the relative particle size polydispersity is $\lesssim 10\%$.

5.3. Results and Discussion

In the following section 5.3.1 the results obtained for the freshly prepared monomer solution are discussed. The trends observed for the SV AUC of the {$Mo_{72}Fe_{30}$} supramolecular structures are reported in section 5.3.2, in which also the results for the supramolecular vesicles contained in the solutions that were stored for 100 days at 20 °C, 55 °C and 80 °C and the 1 and 3 years old solution (20 °C) are compared.

5.3.1. {$Mo_{72}Fe_{30}$} Monomers

The attenuance of the {$Mo_{72}Fe_{30}$} monomer stock solution is linear with concentration (Figure 5.2). The extinction coefficient increases with decreasing wavelength. At 229 and 333 nm the extinction coefficients obtained from a linear unconstrained fit are, respectively, $\epsilon_{333\,nm} = 13.50 \pm 1.28\,mL\,OD\,mg^{-1}\,cm^{-1}$ (correlation coefficient $R = 0.99992$) and $\epsilon_{229\,nm} = 30.78 \pm 1.35\,mL\,OD\,mg^{-1}\,cm^{-1}$ ($R = 0.99639$). The extinction of the SV AUC sample for the low- and high-speed SV {$Mo_{72}Fe_{30}$} monomer

Table 5.1: $\{Mo_{72}Fe_{30}\}$ Molar Weights

L [a]	M_W [b] $g\,mol^{-1}$
H_2O	17,695
CH_3COO^-	21,880
$Mo_2O_{8/9}^{n-}$	50,117

[a] Ligand L as in **2**.
[b] See molecular formula **1**.

experiment, measured through a 1 cm path length was determined to be 0.69 and conforms well to the initial loading concentration of $0.85\,OD_{229\,nm}$ determined with the AUC (Beckman Coulter™ Optima™ XL-I Analytical Ultracentrifuge, 12 mm path length). Considering the uncertainty of the extinction coefficient, the solution indeed contains $23.1\,\mu g\,mL^{-1}$ $\{Mo_{72}Fe_{30}\}$ synthesis material.

The absolute molar weight (M_W) of a $\{Mo_{72}Fe_{30}\}$ monomer ranges, according to the molecular formulae **1** and **2**, from approximately 17 to 50 kg mol^{-1} if we assume that $L = H_2O$ for the former M_W and $L = Mo_2O_9$ for the latter M_W (Table 5.1). However, the $\{Mo_{72}Fe_{30}\}$ monomer unit in aqueous solution is very likely hydrated,

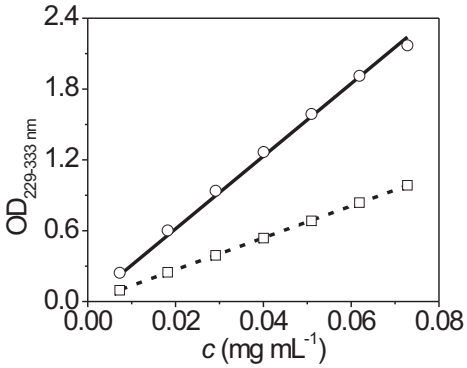

Figure 5.2: Fit of the attenuance at 229 (exp. data ○, linear fit ——) and 333 nm (exp. data ▫, linear fit ----) for a monomer dilution series prepared from the same solution that was used for the SV AUC experiments. From these data the extinction coefficients at 229 nm ($\epsilon_{229\,nm}$) and 333 nm ($\epsilon_{333\,nm}$) were determined.

which increases the particle radius and decreases the partial specific volume. For the SV AUC absorbance optical data analysis we assume that the partial specific volume of a $\{Mo_{72}Fe_{30}\}$ monomer in solution is $\overline{\nu}_p = 0.38794\,mL\,g^{-1}$, which was computed from the effective molecular weight of 12,700 Da and a radius of 1.25 nm (Figure 5.1), both reported in ref. [96, 97].

For the solute(s) contained in the $23.1\,\mu g\,mL^{-1}$ $\{Mo_{72}Fe_{30}\}$ solution, the effect of the

rotor's angular velocity on the vHW differential (envelope) sedimentation coefficient distribution for the SV AUC data from which the TI noise was subtracted, is pronounced (Figure 5.3). At high angular velocities the s-resolution is maximal, whereas the (apparent) sedimentation coefficient distribution obtained from the low-speed experiment seems much broader, indicating that at low rotor speeds the solute's sedimentation coefficient is not well resolved from diffusion with a vHW analysis. As can be seen from

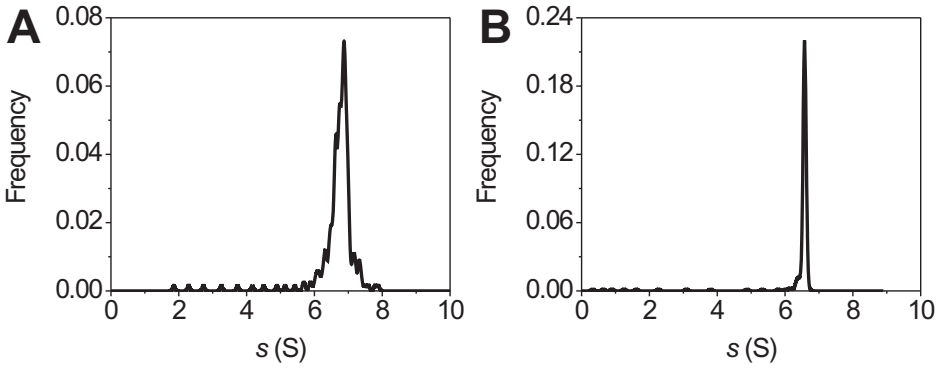

Figure 5.3: Enhanced van Holde-Weischet differential distributions (envelope) from the low- (40 krpm, graph A) and high- (60 krpm, graph B) speed SV AUC experiments (SV AUC absorbance optical data, TI noise subtracted) on the $23.1\,\mu g\,mL^{-1}$ {$Mo_{72}Fe_{30}$} monomer solution. Note that a relatively low rotor speed increases the sedimentation coefficient distribution width. The presence of small solutes in the range of 0 to 5 S for the low speed data and 0 to 2 S for the high speed data is hardly visible.

the vHW differential sedimentation coefficient distributions, the {$Mo_{72}Fe_{30}$} monomer solution contains, in addition to the {$Mo_{72}Fe_{30}$} monomers, small solutes with sedimentation coefficients ranging from 0.1 S up to the monomer's sedimentation coefficient. Following the analysis procedure as described in section 5.2.3, the final results from the global GA-MC50 optimization for the low- and high-speed SV AUC absorbance optical data sets on sedimentation coefficients, diffusion coefficients, frictional ratios and molar weights for the solutes present in the {$Mo_{72}Fe_{30}$} monomer solution were obtained (Table 5.2). An estimate for the sedimentation coefficient for a spherical {$Mo_{72}Fe_{30}$} monomer with a hydrodynamic radius of $a_h = 1.5\,nm$, a molar weight of $M_W = 18\,kg\,mol^{-1}$ (from ref. [101]), a partial specific volume of $\overline{\nu}_p = 0.38794\,mL\,g^{-1}$ in a solvent with viscosity η_s and density ρ_s, follows from:

$$s = \frac{M_W\left(1 - \overline{\nu}_p \rho_s\right)}{6\pi\eta_s a_h N_{AV}} \tag{5.1}$$

with N_{AV} Avogadro's constant. Substitution of relevant parameters in eq 5.1 yields a sedimentation coefficient of $s \approx 6.46\,S$. Considering the uncertainty in the estimated

molar weight M_W, $\overline{\nu}_p$ and a_h, the value obtained from the enhanced vHW analysis (Figure 5.3 graph B, 6.56 S for 95.60%) agrees very well with the predicted sedimentation coefficient.

According to the global GA-MC50 results the $\{Mo_{72}Fe_{30}\}$ monomer sediments at 6.64 S and has a spherical to oblate ellipsoidal shape; i.e. $f/f^\circ = 1.10$ (Figure 5.4 and Table 5.2). The exchange of water molecules with the bulk [103] and the deprotonation in pH neutral aqueous solution lead to a frictional coefficient that is larger compared to the equivalent sphere frictional coefficient. The monomer molar weight is approximately 19.6 kg mol^{-1} (Table 5.2), suggesting that the number of $Mo_2O_{8/9}$ ligands (see molecular formulae **1** and **2**) that may be incorporated in the $\{Mo_{72}Fe_{30}\}$ monomer is much smaller than 102 and is possibly negligible. From this molar weight it may also be inferred that most of the CH_3COO^- is released by the $\{Mo_{72}Fe_{30}\}$ monomers in aqueous solution. The presence of small solutes is evident from the global GA-MC50 results. These small solutes also appeared in the 2DSA(-MC50) and non-global GA(-MC50) f/f° versus s distributions as a mixture of solutes with equal sedimentation coefficients; i.e. covering a relatively large range of frictional ratios compared to the narrow sedimentation coefficient range. The shape of the second small solute ($s = 0.28$ S) is less well defined and more elongated ($f/f^\circ = 1.41$), which indicates that this component is actually a mixture of possibly ligands (molecular formula **2**) with different diffusion coefficients but with comparable sedimentation coefficients. Such a mixture of solutes is still very difficult to resolve, even with a GA optimization routine.

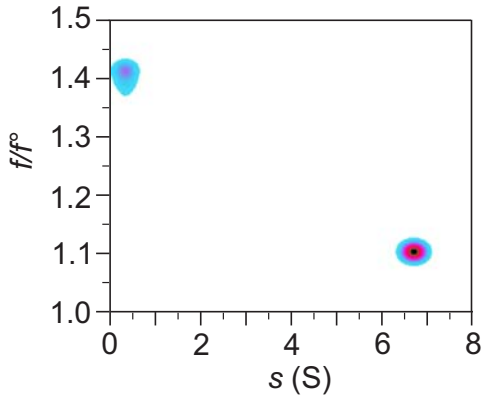

Figure 5.4: Pseudo 3-D plot of frictional ratios f/f° vs. sedimentation coefficients s and solute concentrations (third dimension), imaging the analysis results from the global Genetic Algorithm optimization (50 Monte Carlo iterations). This 2-component (non-interacting) model best describes the low- and high-speed SV AUC absorbance optical data (23.1 μg mL^{-1} $\{Mo_{72}Fe_{30}\}$ solution).

Table 5.2: Global GA-MC50 Analysis Results for the $\{Mo_{72}Fe_{30}\}$ Monomer Solution [a]

Solute	s [b]	D [c]	f/f° [d]	M_W [e]	a_h [e]
	S	$10^{-6}\,cm^2s^{-1}$		$kg\,mol^{-1}$	nm
'Small'	0.28 (0.26; 0.29)	4.6104 (4.4977; 4.7137)	1.41 (1.38; 1.42)	0.233 (0.225; 0.248)	0.5
Monomer	6.64	1.3492	1.10	19.577	1.6

[a] Residual mean square deviation for the global GA-MC50 fit of the low- and high-speed SV AUC absorbance optical data is, respectively, $5.75 \cdot 10^{-3}$ and $6.82 \cdot 10^{-3}$. The residuals, which are not reported here, are randomly distributed. 95% confidence limits are shown between parentheses. Regarding the $\{Mo_{72}Fe_{30}\}$ monomer parameters, only the uncertainty of the concentration is significant (neglecting the uncertainty of $\overline{\nu}_p$).

[b] Sedimentation coefficient.

[c] Diffusion coefficient.

[d] Frictional ratio.

[e] Molar weights from $s/D = M(1 - \overline{\nu}_p\rho_s)/RT$ with $\overline{\nu}_p = 0.38794\,mL\,g^{-1}$.

[e] Equivalent sphere hydrodynamic radius from $f^\circ = 6\pi\eta a_h$ [38].

5.3.2. Supramolecular $\{Mo_{72}Fe_{30}\}$ Assemblies

As already addressed in section 5.1, the formation of equilibrium $\{Mo_{72}Fe_{30}\}$ supramolecular structures is unusually slow. A solution of $\{Mo_{72}Fe_{30}\}$ for which the concentration is above the critical aggregation concentration (CAC) attains equilibrium after a time that is of the order of years. Obviously, as will be discussed later, this time strongly depends on the temperature at which the solution is kept. The temperature dependence in turn is indicative for an activation energy (energy barrier) that is associated with the overall exothermic self-assembly of $\{Mo_{72}Fe_{30}\}$ monomers into 'giant' vesicles. The effect of the history and aging time of aqueous $\{Mo_{72}Fe_{30}\}$ solutions regarding the size and polydispersity of supramolecular structures is pronounced. Here, we varied the storage time and the temperature. Other parameters that may influence the size and polydispersity of (equilibrium) $\{Mo_{72}Fe_{30}\}$ supramolecular structures are e.g. pH and ionic-strength. We found that lowering the pH to approximately 3 destabilizes the $\{Mo_{72}Fe_{30}\}$ monomers and causes rapid non-directional aggregation. Also, adding a small amount of a 1:1 (10-100 mM NaCl) electrolyte results in the random aggregation of $\{Mo_{72}Fe_{30}\}$ monomers well before supramolecular structure formation. Therefore no salt was added to any of the solutions employed here.

Upon superstructure formation the wavelength spectrum of the $\{Mo_{72}Fe_{30}\}$ solutions, containing initially only monomers, changes drastically (Figure 5.5). The attenuance at approximately 333 nm, characteristic for the $\{Mo_{72}Fe_{30}\}$ monomers, decreases in time. Since the intensity of light that is scattered by particles varies as $I \sim \lambda^{-4}$, the attenuance decreases with increasing wavelength for samples that contain sufficiently large structures. Therefore, the $\{Mo_{72}Fe_{30}\}$ supramolecular structure formation can be monitored via UV-Vis wavelength spectra.

As can be seen from Figure 5.5, the solution stored for 85 days at 20 °C still contains

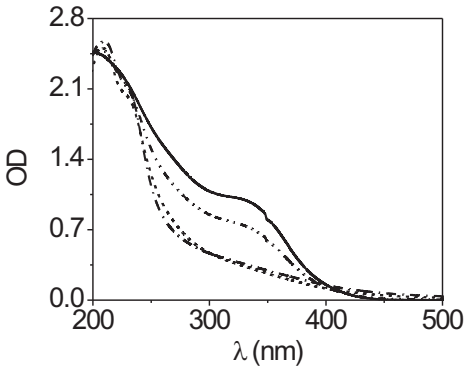

Figure 5.5: UV-Vis wavelength spectra for the three solutions ($72.8 \pm 0.2\,\mu g\,mL^{-1}$) on $t = 0$ days (——) and on $t = 85$ days that were stored at, respectively, 20 °C (– · ·), 55 °C (- - - -) and 80 ° C (– · –).

a substantial amount of $\{Mo_{72}Fe_{30}\}$ monomers. Contrary, the wavelength spectrum for the $\{Mo_{72}Fe_{30}\}$ solutions stored for 100 days at, respectively, 55 °C and 80 °C are identical and do not contain a monomer concentration that is detected by attenuance readings. Based on the wavelength spectra in Figure 5.5, the solution stored at 20 °C has not attained equilibrium after 85 days.

The superstructure formation, confirmed by the change of the wavelength spectra, can also be monitored by DLS. The hydrodynamic radii, computed from cumulant fits to the dynamic light scattering intensity auto correlation functions recorded at 35.0°, 77.5° and 120.0°, for all $\{Mo_{72}Fe_{30}\}$ solutions that are stored at different temperatures, reflect the supramolecular structure dimensions. From DLS experiments (Figure 5.6 and Table 5.3) it is evident that the solution stored at 80 °C contains supramolecular structures with dimensions that are much larger than the solutions stored at 20 °C and 55 °C. The latter two solutions exhibit structure dimensions that are comparable. Remarkably, the supramolecular structures contained in the solution stored for 100 days at 55 °C seem to be smaller than the structures that are formed during 100 days at 20 °C. If the superstructures formed are initially larger and eventually shrink, then the difference in dimensions observed for the 20 °C and 55 °C solutions can be possibly explained by the temperature dependent kinetics associated with the self-assembly of $\{Mo_{72}Fe_{30}\}$ monomers. The same line of reasoning can be applied to explain the small decrease in the average hydrodynamic radius after 1 year observed for the solution that was stored at 20 °C during 3 years (Table 5.3); i.e. the average a_h after 3 years is decreased by a few nanometers from $a_h \approx 40$ nm to $a_h \approx 35$ nm.

Similar trends for the dimensions of supramolecular structures present in the $\{Mo_{72}Fe_{30}\}$ solutions that were stored for 100 days at, respectively, 20 °C, 55 °C and 80 °C follow from the enhanced vHW sedimentation coefficient distributions computed from the SV AUC absorbance optical data.

Table 5.3: *s*-Distributions and Hydrodynamic Radii [a]

Sample [b]		s_{AV} [c]	σ_s [d]	a_h [e]
T	t	S	%	nm
20 °C	100 days	635.9	25	-
20 °C	1 year	671.0	54	40
20 °C	3 years	1247.5	34	35
55 °C	100 days	467.9	34	20
80 °C	100 days	3923.4	36	202

[a] The *s*-Distributions and Hydrodynamic Radii for the {$Mo_{72}Fe_{30}$} supramolecular structures were obtained from, respectively, the vHW analyses of SV AUC data and cumulant fits of DLS data.

[b] Storage temperature T and time t.

[c] Weight-average sedimentation coefficients.

[d] Relative standard deviations of the vHW sedimentation coefficient distributions.

[e] Hydrodynamic radius from DLS correlation functions recorded at 35.0°.

The weight-average sedimentation coefficient, s_{AV}, for the supramolecular structures that are formed in 100 days at 20 °C is approximately 636 S (Figure 5.7, graph A), whereas s_{AV} for the same solution stored at 55 °C is approximately 468 S (Figure 5.7, graph C), indicating that the size of supramolecular structures contained in the 55 °C solution is indeed smaller. The growth of vesicles due to self-assembly at 80 °C during 100 days (Figure 5.7, graph D) is greatly enhanced, leading to much larger superstructures that sediment on average approximately 6 times faster ($s_{AV} \approx 4000$ S) compared to the latter 20 °C and 55 °C solutions. Whether the supramolecular complexes are still spherical vesicles is uncertain and goes beyond the scope of this contribution.

The relative standard deviation of the vHW sedimentation coefficient distributions (σ_s, Table 5.3) initially increases with time and, at 20 °C, decreases if the solution is stored for longer than 1 year. This can be interpreted as another indication that the {$Mo_{72}Fe_{30}$} vesicles initially grow beyond a certain size, after which the vesicles shrink. This finding is in accordance with observations reported elsewhere [99]. At 80 °C the process of the initial growth to a maximum (extreme) size and subsequent shrinkage may possibly be much more pronounced. A continuous distribution of sedimentation coefficients analysis [84, 85] reveals that the supramolecular structures in the 100 days old 20 °C, 55 °C and the 1-3 years old 20 °C solutions are indeed spherical ($f/f°$=1). The spherical shape is in accordance with the assumptions/observations reported elsewhere [78, 96–101]. Since all the supramolecular structures contained in the solutions that were stored for 100 days to 3 years at 20 °C are spherical (vesicle-like structures), the sedimentation coefficient distributions, the weight-average sedimentation coefficient together with the average hydrodynamic radii from DLS experiments determined for

these solutions can be compared. For this comparison an expression for the sedimentation coefficient is required. The sedimentation coefficient for hollow spheres, with a mass proportional to the radius squared, reads:

$$s = \frac{2}{3}\frac{a_{\mathrm{h}} n_{\mathrm{l}} \delta_{\mathrm{l}} (\rho_{\mathrm{l}} - \rho_{\mathrm{s}})}{\eta_{\mathrm{s}}} \tag{5.2}$$

with n_{l} the number of layers, δ_{l} the $\{Mo_{72}Fe_{30}\}$ monomer layer thickness, $(\rho_{\mathrm{l}} - \rho_{\mathrm{s}})$ the difference of the layer and solvent density, and η_{s} the solvent viscosity.

To date, the hollow $\{Mo_{72}Fe_{30}\}$ supramolecular spheres (vesicles) are assumed to be shells of a single $\{Mo_{72}Fe_{30}\}$ layer. The inter-monomer surface-to-surface spacing in this layer is according to ref. [96,97] on the order of 1 nm. Contrary, the weight-average sedimentation coefficient together with the average hydrodynamic radius clearly prove that the monomer surface-to-surface spacing in single-layer vesicles is much smaller. If this spacing would indeed be 1 nm, then a layer density of 1496 g mL^{-1} follows from the density of a bare (not hydrated) $\{Mo_{72}Fe_{30}\}$ monomer, 2.878 g mL^{-1} computed from the global GA-MC50 results (Table 5.2), solvent density and the respective volume fractions. Substitution in eq 5.2 of this density and $a_{\mathrm{h}} \approx 40$ nm for a single-layer vesicle as formed after 1 year at 20 °C, yields a sedimentation coefficient of 331 S. Obviously, the surface-to-surface monomer spacing is much smaller such that the single-layer vesicles with $a_{\mathrm{h}} \approx 40$ nm (DLS) in the solution stored for 1 year at 20 °C sediment at $s_{\mathrm{AV}} \approx 671$ S (Table 5.3). According to the DLS data, acquired at the time that this solution was,

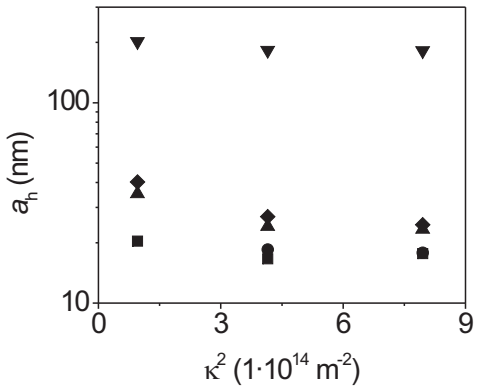

Figure 5.6: Hydrodynamic radii for the $\{Mo_{72}Fe_{30}\}$ vesicles vs. the scattering wave vector magnitude κ squared (chapter 4 section 4.2.2), obtained from cumulant fits to DLS correlation functions recorded at 35.0°, 77.5° and 120.0° for the solutions that were stored for 100 days at, respectively, 20 °C (•), 55 °C (▪) and 80 °C (▾). Note that the hydrodynamic radius has slightly changed during 3 years of storage at 20 °C (▴) compared to the DLS results obtained when that solution was 1 year old (♦).

respectively, 1 and 3 years old, the average hydrodynamic vesicle radius only slightly changed after 1 year storage (3 year old sample, $a_{\mathrm{h}} \approx 35$ nm). After 3 years, however, the weight-average sedimentation coefficient is increased by approximately a factor 2

($s_{AV} \approx 1247$ S). Consequently, the mass of the vesicles must have increased, something which can only be accomplished by increasing the number of {$Mo_{72}Fe_{30}$} monomer layers (n_l in eq 5.2), because the inter-monomer distance of 1 nm or less within the vesicle layer prevents the incorporation of additional 'free' monomers from solution. Therefore, the only plausible explanation for the increased sedimentation velocity after 2 more years of storage while maintaining a temperature of 20 °C, is the deposition of another {$Mo_{72}Fe_{30}$} monomer layer onto the already existing single-layered vesicles.

Our observations can be confirmed almost quantitatively via eq 5.2 as follows. Assuming that the {$Mo_{72}Fe_{30}$} monomers are hexagonally close-packed, then the volume fraction occupied by the monomers is approximately 60%. Using the density of water ($\rho_s = 0.99821\,g\,mL^{-1}$), the density of the layer (thickness = monomer diameter, δ_l in eq 5.2) constituting the supramolecular vesicle is $2.135\,g\,mL^{-1}$. Substituting $a_h = 40$ nm and $\eta_s = 1.002$ mPa s together with the layer density in eq 5.2, yields a sedimentation coefficient of 756 S for $n_l = 1$ (single monomer layer) and 1513 S for $n_l = 2$ (double monomer layer). These s-values are in good agreement with the results obtained from the enhanced vHW analysis. Realizing that we assumed a maximal packing fraction of monomers within the layer and that the hydration of the monomer layer has been neglected here, both resulting in a monomer layer density that is overestimated, the agreement of predicted and experimental s-values is excellent.

5.3.3. Residual Solutes and the CAC of {$Mo_{72}Fe_{30}$} Monomers

After sedimentation of the {$Mo_{72}Fe_{30}$} supramolecular structures a second SV AUC at the maximal rotor speed was performed to determine the presence and concentration of free {$Mo_{72}Fe_{30}$} monomers and small solutes that were also detected in the freshly prepared monomer solution.

The enhanced vHW differential sedimentation coefficient distributions for the {$Mo_{72}Fe_{30}$} solutions stored at, respectively, 20 °C, 55 °C and 80 °C for 100 days and 3 years clearly show the abundance of small solutes with sedimentation coefficients that are in between 0 and 2 S. These small solutes, however, seem to be somewhat larger than the small species observed in the freshly prepared monomer solution (section 5.3.1).

As already addressed in section 5.3.2 the {$Mo_{72}Fe_{30}$} solution stored at 20 °C for 100 days has indeed not attained equilibrium. After 100 days a substantial amount of monomers is still present (Figure 5.8, graph A), confirming that the interpretation of the wavelength spectrum shape is correct. Furthermore the ratio of monomer and small solute concentration has significantly decreased compared to the composition of the freshly prepared monomer solution (Figure 5.3). This indicates that the {$Mo_{72}Fe_{30}$} monomers release small solutes that may be associated with the self-assembly, something which has not been reported to date. Further evidence for this release of possibly ligands, comes from the vHW differential sedimentation coefficient distributions for the

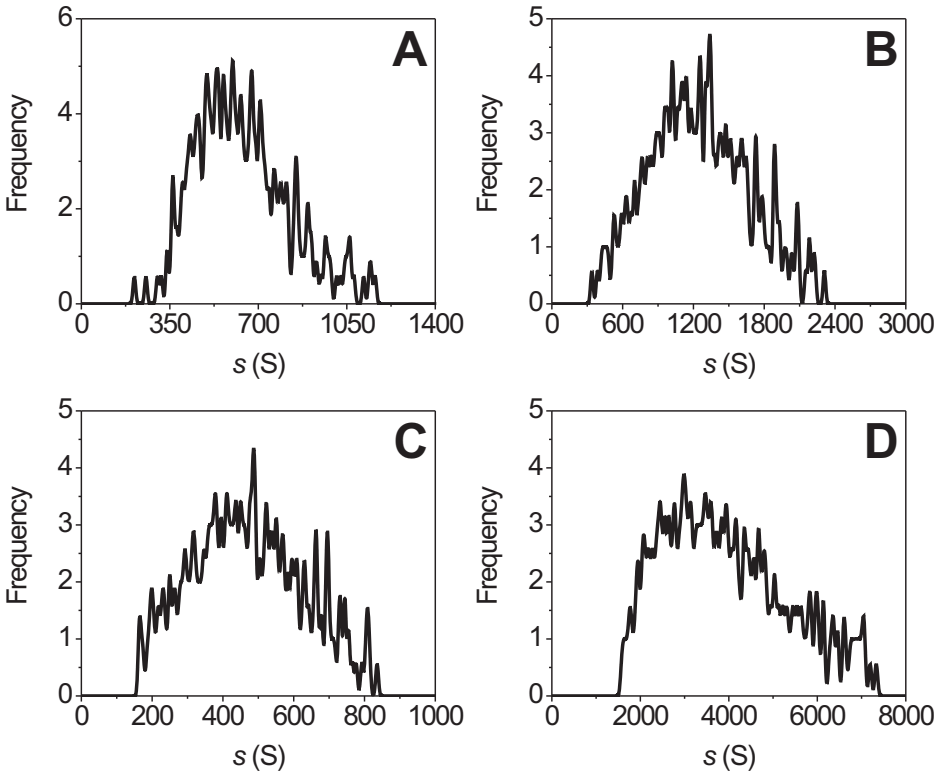

Figure 5.7: Enhanced van Holde-Weischet differential distributions (envelope) for supramolecular structures (monolayer vesicles) contained in the 72.8 $\pm$ 0.2 μg mL^{-1} $\{Mo_{72}Fe_{30}\}$ solutions that were stored for approximately 100 days at, respectively, 20 °C (graph A), 55 °C (graph C) and 80 °C (graph D). Graph B shows the distribution for the sample that was stored over three years at 20 °C. The distributions were obtained from the low-speed SV AUC experimental data from which the TI noise (determined in the first 2DSA) was subtracted.

solutions stored at 55 °C and 80 °C for 100 days (Figure 5.8, graph C and D) and the solutions stored at 20 °C for 3 years (Figure 5.8, graph B). For the latter three solutions large baseline values were observed (baseline of $\approx$ 0.6 OD vs. an initial concentration of $\approx$ 0.2 OD of small solutes with sedimentation coefficients between 0 and 2 S). These baselines also point to the presence of small solutes that are released by the monomers upon association. Release of for example CH_3COO^- from $\{Mo_{72}Fe_{30}\}$ (see molecular formulae **1** and **2**) can give rise to such baselines.

Remarkably, no free $\{Mo_{72}Fe_{30}\}$ monomers in solution are detected after complete sedimentation of the $\{Mo_{72}Fe_{30}\}$ supramolecular structures in the solutions stored at, respectively, 55 °C and 80 °C for 100 days and the solution stored at 20 °C for over 3 years. Possibly, the critical aggregation concentration (CAC) is very small and, consequently, the absorbance optics fails to detect the free monomers that are present. Moreover, if the CAC is indeed as reported in ref. [98, 101] (2.4 μg mL^{-1}) than the free $\{Mo_{72}Fe_{30}\}$ monomers should be detected. Since the extinction coefficient at

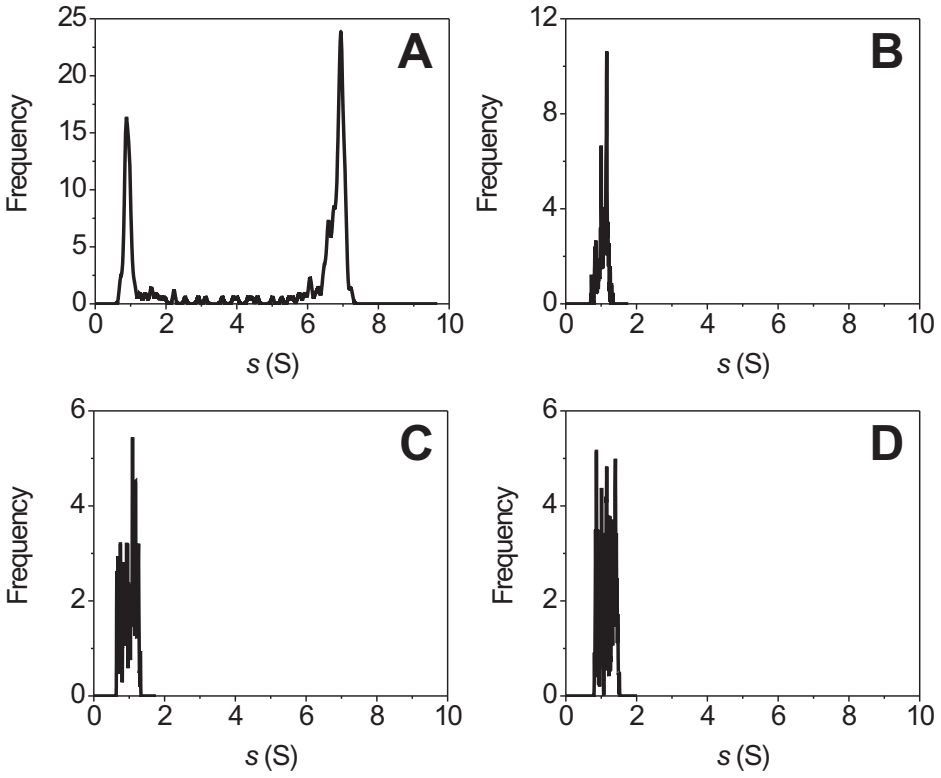

Figure 5.8: Differential (envelope) sedimentation coefficient distributions (enhanced van Holde-Weischet analysis, TI noise subtracted) for the high-speed SV AUC data, which were acquired at 60 krpm after sedimentation of the supramolecular structures. The small solutes that are abundant after vesicle formation in the $72.8 \pm 0.2\,\mu g\,mL^{-1}$ {$Mo_{72}Fe_{30}$} solutions that were stored for approximately 100 days at, respectively, 20 °C (graph A), 55 °C (graph C) and 80 °C (graph D). Graph B shows the distribution for the sample that was stored over three years at 20 °C. Clearly, after 100 days at 20 °C a significant amount of {$Mo_{72}Fe_{30}$} monomers is still present. Contrary, all {$Mo_{72}Fe_{30}$} monomers seem to have disappeared in the solutions that were stored for three years at 20 °C and 100 days at 50 °C and 80 °C.

229 nm for the freshly prepared monomer solution was determined here as $\epsilon_{229\,nm} = 30.78 \pm 1.35\,mL\,OD\,mg^{-1}\,cm^{-1}$ and taking into account that this solution contains a mixture of small solutes (see section 5.3.1) that contribute approximately 10% to the total signal, an attenuance of $0.1\,OD_{229\,nm}$ for a $2.4\,\mu g\,mL^{-1}$ free monomer concentration is expected.

A solvent-solution interface of 0.1 OD sedimenting at $s \approx 6.6$ S superimposed on a 0.8 OD boundary moving at $s \approx 0.3$ S or $s \approx 1.0$ S will be detected by a vHW analysis. The absorbance optics will fail to detect free monomers if the actual CAC is approximately a factor 4 smaller than $2.4\,\mu g\,mL^{-1}$. Since the chemical potential difference of free and assembled monomers scales with the logarithm of the CAC, the lower

CAC found here indicates that the $\{Mo_{72}Fe_{30}\}$ inter-monomer attractions should be somewhat stronger than reported in ref. [101].

5.4. Conclusions

In this contribution it is shown that an absolute molar mass of a $\{Mo_{72}Fe_{30}\}$ monomer in aqueous solution can be obtained from globally fitting experimental multi-speed sedimentation velocity data. We found that, well before supramolecular structure formation has occurred, small solutes are present in freshly prepared $\{Mo_{72}Fe_{30}\}$ solutions. Similar small solutes but in much larger amounts are observed in solutions containing superstructures of $\{Mo_{72}Fe_{30}\}$. The release of various small solutes from the $\{Mo_{72}Fe_{30}\}$ monomers may or may not be associated with superstructure formation. Some of these small solutes sediment in a centrifugal field, while the majority of small solutes is either too small to sediment or nearly density matched with water, which prevents sedimentation, causing the observed baselines.

The association of $\{Mo_{72}Fe_{30}\}$ monomers into supramolecular structures depends, among other variables, on sample storage time and temperature. At 80 °C very large structures are observed. Furthermore, the supramolecular vesicles seem to initially grow beyond a certain size after which the radii of the $\{Mo_{72}Fe_{30}\}$ vesicles shrink. For the $\{Mo_{72}Fe_{30}\}$ solutions studied here, the critical aggregation concentration is much lower than the value reported in earlier studies [98] on the $\{Mo_{72}Fe_{30}\}$ solutions.

Our sedimentation velocity experiments revealed that the structures formed at 20 °C are indeed spherical hollow structures. A remarkable result follows from sedimentation velocity data combined with dynamic light scattering data: the number of layers comprising the $\{Mo_{72}Fe_{30}\}$ supramolecular structures increases and, eventually, after 3 years the vesicles have a double $\{Mo_{72}Fe_{30}\}$ layer. This suggests that the single-layer vesicles are thermodynamically meta-stable. The weight-average sedimentation coefficient of single and double monomer-layer vesicles together with the hydrodynamic radii from dynamic light scattering data show that the $\{Mo_{72}Fe_{30}\}$ monomers are relatively close-packed.

Acknowledgement

This research was conducted in collaboration with Willem K. Kegel, Jan Groenewold, Marieke Bode, Sandra J. Veen, Alletta A. Verhoeff, Bonny W. M. Kuipers, Roel Vos and Pepijn Huizinga.

6

A Dimerization Model for the Concentration Dependent Sedimentation of Attractive Colloids

Abstract

An equation is derived for the linear concentration dependent sedimentation velocity of attractive colloids that reversibly associate into dimers. Within our approach, which includes an anisotropic interaction potential, the magnitude of this concentration dependence is primarily determined by the dimerization equilibrium constant. We also show how this dimerization affects the osmotic equation of state and conclude that, in principle, both the sedimentation velocity and the sedimentation-diffusion equilibrium may be employed to determine the binding energy from the equilibrium constant for associating colloids or macromolecules, at concentrations low enough for only dimerization to occur.

6.1. Introduction

The sedimentation velocity for colloidal particles in a sufficiently concentrated dispersion is sensitive to the nature and strength of any interaction between the colloids [106]. For example, long-range electrical double-layer repulsions may produce a pronounced retardation of the sedimentation rate, even at fairly low colloid concentrations [54,107]. In that case, the average sedimentation velocity $\langle s \rangle$ of the charged colloids may even be an exponential function of the colloid volume fraction $\phi_{\text{tot}}^{\alpha}$ [88,107], with $0 < \alpha < 1$. When sufficient salt is added to compress the electric double-layer and, consequently, screen the inter-particle repulsions, the concentration dependence weakens and eventually becomes linear in ϕ_{tot} [107]. For this linear dependence, the normalized (reduced) sedimentation coefficient is expressed as:

$$\frac{\langle s \rangle}{s^{\circ}} = 1 - K_s \phi_{\text{tot}} + O\left(\phi_{\text{tot}}^2\right) \tag{6.1}$$

with the Batchelor coefficient K_s, being the first order correction to the sedimentation coefficient s° for non-interacting particles.

For monodisperse hard spheres Batchelor [108] calculated $K_s = 6.55$ (see also section 6.5.4), manifesting a relatively small decrease of the settling rate due to the hard-sphere repulsion and the associated hydrodynamic interaction between two spheres. Additional repulsions due to screened surface charges [107] or steric stabilization will increase the value of K_s in eq 6.1. Attractions, on the other hand, will weaken the concentration dependence in comparison to the pure hard-sphere behavior. Qualitatively this is related to the enhanced probability for attractive colloids to 'shield' each other against the solvent backflow that always accompanies particle settling in a container. This accelerating effect of attractions on colloidal sedimentation has been studied, for example, by Jansen *et al.* [109] for the case of 'sticky' silica spheres in an organic solvent; the authors show that for their colloids, K_s in eq 6.1 is indeed significant below the hard-sphere value, though K_s remains positive.

Several models have been presented for the calculation of K_s in eq 6.1 for attractive colloids, which are addressed in more detail in section 6.5.3. Batchelor [108] derived an expression for adhesive spheres that was applied by Jansen *et al.* [109] to 'sticky' silica spheres modeling the interaction as a square well potential. Dhont [88] calculated K_s for a colloid-colloid attraction in the form of a weak isotropic magnetic attraction. For the latter model, using realistic input parameters, the coefficient K_s remains positive, i.e. the concentration dependence of $\langle s \rangle$ remains negative. However, we have investigated the sedimentation velocity of magnetic colloids in an analytical ultracentrifuge (chapter 7) and found, for sufficiently strong magnetic attractions, a linear and *positive* concentration dependence, with K_s values as large as -250. Such a large, positive concentration dependence is difficult to reconcile with Dhont's calculation [88], presumably

because this calculation assumes attractions to be a weak perturbation to a hard-sphere potential.

Our ultracentrifugation experiments (chapter 7) therefore prompted us to reconsider the sedimentation of attractive colloids from a thermodynamic perspective, assuming that the inter-particle attraction is sufficiently strong for colloid-colloid association to occur. We were guided by the observation that magnetic colloids of the type we studied in chapter 7 may form reversible clusters [110, 111] due to the anisotropic magnetic dipole attraction. Clearly, at sufficiently low colloid concentration the dominating clustering will be a reversible monomer-dimer association. This suggests that, at least for such magnetic dipolar colloids, sedimentation at sufficiently low particle densities is essentially the settling of an equilibrium bi-disperse mixture of monomers and dimers. If that is the case, the concentration dependence of the sedimentation velocity may be calculated from the relative amounts of monomers and dimers in solution, which is the main point of this contribution.

In section 6.2 we discuss the monomer-dimer equilibrium for attractive colloids and use equilibrium concentrations to evaluate the average sedimentation velocity in section 6.3, as well as the sedimentation-diffusion equilibrium in section 6.4. In the discussion in section 6.5, among other things, we compare our prediction for the concentration dependent sedimentation with the other models referred to above.

6.2. Dimerization Equilibrium

6.2.1. Time Scales

A reversible monomer-dimer self-association is represented by:

$$A + A \rightleftarrows A_2 \tag{6.2}$$

For a rapid monomer-dimer self-association, the dimer-lifetime will be short compared to the typical observation time of an analytical ultracentrifugation experiment. The dimer-lifetime is set by the time τ it takes for a monomer with radius a_{tot} in a medium with viscosity η_{s}, to escape over a potential barrier by Brownian motion. Here this potential barrier is the contact attraction $|U_{\text{eff}}|$. From Kramer's analysis [112, 113] of diffusion in a force field it can be shown that in order of magnitude:

$$\tau \sim \frac{a_{\text{tot}}^2}{D_{\text{eff}}} = \frac{3a_{\text{tot}}^3 \pi \eta_{\text{s}}}{k_{\text{B}}\text{T}} \exp\left(-U_{\text{eff}}\right) \tag{6.3}$$

where k_{B} is the Boltzmann constant, T is the absolute temperature and D_{eff} is an effective diffusion coefficient of the form:

$$D_{\text{eff}} \sim 2\,D \exp\left(U_{\text{eff}}\right) \tag{6.4}$$

in which D is the diffusion coefficient of a free particle. For two contacting magnetite (Fe_3O_4) spheres, each having a diameter of 11 nm, the contact attraction is about

$U_{\text{eff}} \approx -4.2\, k_{\text{B}}\,\text{T}$ (see also chapter 7) such that the dimer-lifetime τ in eq 6.3 is of the order of milliseconds. On the other hand, the collision frequency of monomers must be sufficiently large to accomplish reversible dimer formation. The diffusional collision frequency J_{c} can be approximated by [114]:

$$J_{\text{c}} \sim \frac{2k_{\text{B}}\text{T}}{\pi\eta_{\text{s}}a_{\text{tot}}^3}\,\phi_{\text{tot}} \tag{6.5}$$

and is of the order of kHz to MHz, which corresponds to a collision time less than a millisecond, for systems with $\phi_{\text{tot}} \approx 0.1\%$.

The observation time in an analytical ultracentrifugation experiment (chapter 7) is typically of the order of minutes for a single radial scan using the absorbance optics (Beckman Coulter™ Optima™ XL-A AUC), which is much longer than the formation and break-up times of magnetite nano-spheres associates. Thus for such spheres the analytical ultracentrifuge monitors an equilibrium mixture of monomers and dimers (see Figure 6.1), provided, of course, that the total colloid concentration is sufficiently low for trimers to be absent.

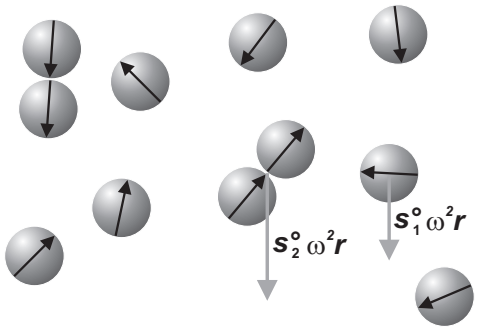

Figure 6.1: Schematic representation of a magnetite dispersion that exhibits monomer-dimer self-association due to the dipolar attraction (magnetic dipole moments are shown with black arrows). As indicated by the vectors that represent the sedimentation rates of the monomers and dimers, the larger mass of a dimer is not fully compensated by the increase of the viscous drag force.

6.2.2. Mass Action Law

Reversible monomer-dimer self-association at a fixed particle weight concentration, c_{tot}, and fixed temperature, T, eventually results in an equilibrium monomer-dimer distribution. Conservation of mass implies that the total particle weight concentration in terms of monomer and dimer concentrations, respectively c_1 and c_2, is:

$$c_{\text{tot}} = \sum_{i=1}^{n} c_i = c_1 + c_2 \tag{6.6}$$

According to the mass action law, practical equilibrium constants K_i^{c} can be expressed in terms of the monomer weight concentration c_1:

$$c_i = K_i^{\mathrm{c}} c_1^i, \text{ with } K_1^{\mathrm{c}} \equiv 1 \tag{6.7}$$

For a reversible monomer-dimer self-associating system eq 6.7 reduces to:

$$K_2^{\mathrm{c}} = \frac{c_2}{c_1^2} = \frac{c_{\mathrm{tot}} - c_1}{c_1^2} \tag{6.8}$$

where we have substituted eq 6.6. Solving eq 6.8 for the monomer weight concentration yields:

$$c_1 = \frac{-1 + \sqrt{1 + 4K_2^{\mathrm{c}} c_{\mathrm{tot}}}}{2K_2^{\mathrm{c}}} \tag{6.9}$$

For $4K_2^{\mathrm{c}} c_{\mathrm{tot}} << 1$, c_1 can be approximated by:

$$c_1 \approx c_{\mathrm{tot}} \left(1 - K_2^{\mathrm{c}} c_{\mathrm{tot}}\right) + O\left(c_{\mathrm{tot}}^3\right) \tag{6.10}$$

where we have Taylor expanded the root term to second order in c_{tot}. The superscript c for K_i^{c} expresses that the equilibrium constant as defined in eq 6.7 is in units of an inverse weight concentration; i.e. unit of K_i^{c} is:

$$\left(\mathrm{m}^3\,\mathrm{kg}^{-1}\right)^{i-1} \text{ for } i > 1$$

In contrast, each quantity in the dimensionless thermodynamic equilibrium constant for dissolved particles is expressed as the ratio of molar concentrations of each species to its concentration in its standard state. Generally, for solutes this standard state is chosen to be 1 M [115], but for colloids such a standard state has no physical relevance since their dimensions are much larger than atoms and small molecules. Equivalently, the thermodynamic equilibrium constant can be expressed as the ratio of monomer and dimer weight fractions, x_1 and x_2 respectively. In the next section 6.2.3, we derive the dimerization equilibrium from statistical thermodynamics to eventually obtain an expression that relates the thermodynamic equilibrium constant in terms of the monomer and dimer weight fractions, K_2^x, to the pair-interaction potential, U_{eff}, for attractive colloids at close contact.

6.2.3. Thermodynamic Equilibrium

We consider identical hard spheres with an embedded dipole moment as depicted in Figure 6.1. The system is considered to be sufficiently dilute such that the partition sum can be written as a product of a gas of $N - 2N_2$ monomers and N_2 dimers:

$$Z = \sum {N_2}^{N/2} \frac{Z_1^{N-2N_2}}{(N-2N_2)!} \frac{Z_2^{N_2}}{N_2!} \tag{6.11}$$

Here Z_1 is the monomer partition sum:

$$Z_1 = \int_V d\mathbf{r} \int d\mathbf{n}\, 1 \tag{6.12}$$

in which V is the volume of the system, $\mathbf{r}$ a vector indicating the coordinate of the monomer and $\mathbf{n}$ is the vector indicating the orientation of a dipole moment. The kinetic degrees of freedom are left out since these are the same for each particle regardless of being part of a dimer or a monomer. The kinetic degrees of freedom will therefore not show up in the equilibrium conditions. The one-particle partition sum is easily evaluated to obtain:

$$Z_1 = V\, 4\pi \tag{6.13}$$

Here, V stems from the positional integral and 4π stems from the angular integration of the particle orientation. The partition sum of a dimer can be written as:

$$Z_2 = \int_V d\mathbf{r} \int d(\mathbf{r}-\mathbf{r}') \int d\mathbf{n} \int d\mathbf{n}' \exp\left(\psi_1\right) \tag{6.14}$$

with $\psi_1 = -\beta\Phi(\mathbf{r}-\mathbf{r}'|\mathbf{n},\mathbf{n}')$ and $\beta = 1/k_{\mathrm{B}}\,\mathrm{T}$. The inter-particle potential $\Phi(\mathbf{r}-\mathbf{r}'|\mathbf{n},\mathbf{n}')$ is a function of the inter-particle distance $\mathbf{r}-\mathbf{r}'$ and the orientation vectors of the dipole moment of both particles $\mathbf{n}$ and $\mathbf{n}'$. The position of the central particle $\mathbf{r}$ translates freely. Z_2 can be simplified as follows:

$$Z_2 = V \int d\mathbf{r} \int d\mathbf{n} \int d\mathbf{n}' \exp\left(\psi_2\right) \tag{6.15}$$

Now the position of the 'central' particle has been integrated out to obtain a factor V and $\psi_2 = -\beta\Phi(\mathbf{r}|\mathbf{n},\mathbf{n}')$. The distance between the particles is now indicated by $\mathbf{r}$.

To obtain the equilibrium equation for dimerization, the number of dimers N_2 for which the term in the partition sum is maximal needs to be determined. This is equivalent to minimizing the logarithm of the terms within the sum of eq 6.11 and the result reads:

$$\frac{n_2}{n_1^2} = \int d\mathbf{r} \int \frac{d\mathbf{n}}{4\pi} \int \frac{d\mathbf{n}'}{4\pi} \exp\left(\psi_2\right) \tag{6.16}$$

Here n_1 and n_2 are, respectively, the number densities of monomers and dimers ($n_i = N_i/V$) and $\mathbf{r}$ is the separation vector between the particles. This expression is valid for potentials for which one can expect dimerization to occur. In other words, the potential should have a sufficiently deep well that results in an effective attraction between the particles at close approach.

The equilibrium constant in terms of the weight fractions of monomers, x_1, and dimers, x_2, is expressed as:

$$K_2^x \equiv \frac{x_2}{x_1^2} \tag{6.17}$$

Considering that the monomer and dimer weight fractions read:

$$x_i = \frac{i\rho_{\mathrm{p}} v n_i}{\rho_{\mathrm{s}}}, \text{ with } i = 1, 2 \tag{6.18}$$

where we have assumed that the total weight equals the solvent weight, the expression for the number densities ratio (eq 6.16) can be used to find an expression for K_2^x. Here v is the volume of a single particle (monomer) and ρ_{s} and ρ_{p} are the density of the solvent and particle respectively.

To get an asymptotic expression for K_2^x in terms of the potential that pertains to systems with magnetic interactions the integral in 6.16 has to be evaluated. The approximate result reads:

$$\frac{n_2}{n_1^2} \approx 4\pi a_{\mathrm{tot}}^2 \delta \frac{\Delta\omega_K}{4\pi} \frac{\Delta\omega_K}{4\pi} \exp(-U_{\mathrm{eff}}) \tag{6.19}$$

Here $-U_{\mathrm{eff}}$ is the absolute depth of the potential well, δ is the range of the potential and $\Delta\omega_K$ is the solid angle in square radians for which the attraction occurs. Using the above, the following approximation for the logarithm of the equilibrium constant can be found:

$$\ln K_2^x \simeq -U_{\mathrm{eff}} + \ln\left(\frac{a_{\mathrm{tot}}^2 \rho_{\mathrm{s}} \delta \Delta\omega_K^2}{2\pi v \rho_{\mathrm{p}}}\right) \tag{6.20}$$

which can be further simplified to:

$$\ln K_2^x \simeq -U_{\mathrm{eff}} + \ln\left(\frac{3\rho_{\mathrm{s}} \delta \Delta\omega_K^2}{8\pi^2 a_{\mathrm{tot}} \rho_{\mathrm{p}}}\right) \tag{6.21}$$

The two mass action constants in eqs 6.8 and 6.17 are related as:

$$K_2^{\mathrm{c}} \rho_{\mathrm{s}} = K_2^x \tag{6.22}$$

6.3. Sedimentation Velocity

The dimerization equilibrium from the previous section can be used to evaluate the concentration dependence of the sedimentation coefficient. When measured with an AUC (chapter 7), this coefficient is generally a weight-average as can be seen as follows.

To monitor the sedimentation velocity (chapter 7) using the Beckman Coulter™ Optima™ XL-A/I AUC equipped with absorbance optics, the light intensities I_{r} and I_{s} transmitted through the reference (r) and sample (s) sector of the AUC-cell are recorded. These intensities are converted into an attenuance via:

$$A_\lambda\left(r_j\right) = \log\left(\frac{I_{\mathrm{r},\lambda}}{I_{\mathrm{s},\lambda}}\right) \tag{6.23}$$

The total attenuance $A_{\mathrm{tot},\lambda}$ is, for relatively dilute solutions or dispersions where $A_{\mathrm{tot},\lambda}$ increases still linearly with concentration according to the law of Lambert-Beer, directly

proportional to the path length l and the sum of the products of extinction coefficients $\epsilon_{i,\lambda}$ and weight concentrations c_i of the n-different species:

$$A_{\mathrm{tot},\lambda}(r_j) = l \sum_{i=1}^{n} \epsilon_{i,\lambda} c_i \tag{6.24}$$

Since the signal recorded to measure sedimentation is proportional to the weight concentration, the average sedimentation coefficient from experiment is generally a weight-average. The same line of reasoning as above applies to an AUC equipped with interference optics. This weight-average sedimentation coefficient, $\langle s \rangle$, can be expressed in terms of the constituent particle weight concentrations c_i and sedimentation coefficients at infinite dilution s_i° of monomer and n-mers [1, 116]:

$$\langle s \rangle = \frac{\sum_{i=1}^{n} c_i s_i^\circ}{\sum_{i=1}^{n} c_i} \tag{6.25}$$

For a monomer-dimer mixture eq 6.25 reduces to:

$$\frac{\langle s \rangle}{s_1^\circ} = \chi + (1-\chi)\frac{c_1}{c_{\mathrm{tot}}} \tag{6.26}$$

where χ is the ratio of sedimentation coefficients at infinite dilution of the monomer and dimer:

$$\chi = \frac{s_2^\circ}{s_1^\circ} \tag{6.27}$$

The sedimentation coefficient at infinite dilution s_i° in a solvent s at 20 °C with density ρ_{s}° and viscosity η_{s}° is:

$$s_{20,\mathrm{s}}^\circ = \frac{m_{\mathrm{p}}\left(1-\overline{\nu}_{\mathrm{p}}\rho_{\mathrm{s}}^\circ\right)}{6\pi\eta_{\mathrm{s}}^\circ a_h} \approx \frac{2}{9}\, a_{\mathrm{b}}^2 \frac{\left(\rho_{\mathrm{p}} - \rho_{\mathrm{s}}^\circ\right)}{\eta_{\mathrm{s}}^\circ} \tag{6.28}$$

with m_{p} the molecular weight, a_{h} and a_{b} the hydrodynamic and bare particle radii respectively, $\overline{\nu}_{\mathrm{p}}$ the partial specific volume, and $f^\circ = 6\pi\eta_{\mathrm{s}}^\circ a_h$ the Stokes [38] friction factor. If the bare particle radius a_{b} equals the hydrodynamic radius a_{h}, then the middle expression in eq 6.28 reduces to the right-hand side expression. $s_{20,\mathrm{s}}^\circ$ and $s_{20,\mathrm{s}}$ are further denoted as s° and s respectively.

Finally, substitution of eq 6.10 in eq 6.26 yields the first-order linear concentration dependence of $\langle s \rangle$:

$$\frac{\langle s \rangle}{s_1^\circ} \approx 1 - (1-\chi)K_2^{\mathrm{c}} c_{\mathrm{tot}} + O\left(c_{\mathrm{tot}}^2\right) \tag{6.29}$$

with the equilibrium constant K_2^{c} given by eqs 6.21 and 6.22. We will further comment upon eq 6.29 in section 6.5.2.

6.4. Sedimentation-Diffusion Equilibrium

6.4.1. Osmotic Pressure

For a mixture of monomers and dimers with masses m_1 and $m_2 = 2m_1$ respectively, van 't Hoff's law for the osmotic pressure, Π, reads:

$$\frac{\Pi}{k_{\mathrm{B}}\mathrm{T}} = \frac{c_1}{m_1} + \frac{c_2}{m_2} = \frac{c_{\mathrm{tot}} + c_1}{2m_1} \tag{6.30}$$

including the mass conservation from eq 6.6. Substitution of the monomer concentration c_1 from eq 6.9 yields:

$$2m_1\frac{\Pi}{k_{\mathrm{B}}\mathrm{T}} = c_{\mathrm{tot}} + \frac{\sqrt{1 + 4K_2^{\mathrm{c}}c_{\mathrm{tot}}} - 1}{2K_2^{\mathrm{c}}} \tag{6.31}$$

One easily verifies that in the limit $c_{\mathrm{tot}} \to 0$ this equation of state approaches:

$$\frac{\Pi}{k_{\mathrm{B}}\mathrm{T}} \sim \frac{c_{\mathrm{tot}}}{m_1}, \text{ for } c_{\mathrm{tot}} << \frac{1}{K_2^{\mathrm{c}}} \tag{6.32}$$

which is the osmotic pressure for a pure monomer fluid. On the other hand when the equilibrium constant is very large such that predominantly dimers are present, the osmotic pressure in eq 6.31 drops to:

$$\frac{\Pi}{k_{\mathrm{B}}\mathrm{T}} \sim \frac{c_{\mathrm{tot}}}{2m_1}, \text{ for } K_2^{\mathrm{c}} >> \frac{1}{c_{\mathrm{tot}}} \tag{6.33}$$

Thus, as expected, the osmotic pressure for a self-associating system rises less steeply with c_{tot} than for a fluid containing monomeric species only.

6.4.2. Sedimentation-Diffusion Equilibrium Distributions

From the equation of state addressed above, it is straight forward to derive the concentration distribution that results from the sedimentation-diffusion (SD) equilibrium when the osmotic pressure gradient balances the weight of the colloids. The equilibrium force balance in a centrifugal field is:

$$\frac{\partial\Pi}{\partial r} = -c_{\mathrm{tot}}\left(1 - \overline{\nu}_{\mathrm{p}}\rho_{\mathrm{s}}^{\circ}\right)\omega^2 r \tag{6.34}$$

where $\omega^2 r$ is the centrifugal acceleration with ω the angular velocity in radians per second and r the radial distance from the center of rotation.

For monomers only, substitution of the osmotic pressure of eq 6.32 in eq 6.34 yields:

$$c_{\mathrm{tot}} = c_{\mathrm{tot}}^{\circ}\exp\left(\sigma\Xi\right), \text{ with } \Xi = r^2 - r_{\circ}^2 \tag{6.35}$$

In this single-exponential concentration distribution, the quantity σ is the effective reduced molecular weight [117] and is, for monomers, defined as:

$$\sigma = \frac{m_1\left(1 - \overline{\nu}_{\mathrm{p}}\rho_{\mathrm{s}}^{\circ}\right)\omega^2}{2k_{\mathrm{B}}\mathrm{T}} \tag{6.36}$$

Further, c°_{tot} is the total colloid weight concentration at the reference of integration position $r_{\circ}$ from the center of rotation. For a monomer-dimer mixture the SD-equilibrium distribution is no longer a single-exponential function. Substitution of eq 6.31 in eq 6.34 yields a differential equation for c_{tot} with the solution:

$$c_{\mathrm{tot}}\, h\left(c_{\mathrm{tot}}\right) = c^{\circ}_{\mathrm{tot}}\, h\left(c^{\circ}_{\mathrm{tot}}\right) \exp\left(2\sigma\Xi\right) \tag{6.37}$$

using the standard integral 135 from ref. [74]. Here the function h is defined as:

$$h\left(x\right) = \frac{\sqrt{1+4K_2^{\mathrm{c}}\, x}-1}{\sqrt{1+4K_2^{\mathrm{c}}\, x}+1} \tag{6.38}$$

Eq 6.37 can be re-written as a bi-exponential function in terms of the reference monomer weight concentration, c°_1, by substitution of eqs 6.6–6.9:

$$c_{\mathrm{tot}} = c^{\circ}_1 \exp\left(\sigma\Xi\right) + \left(c^{\circ}_1\right)^2 K_2^{\mathrm{c}} \exp\left(2\sigma\Xi\right) \tag{6.39}$$

With the SD-profile in the form as in eq 6.39 it is easily verified that in the limit $K_2^{\mathrm{c}} \rightarrow 0$ we obtain the monomer SD-equilibrium distribution, whereas for $K_2^{\mathrm{c}} c_{\mathrm{tot}} >> 1$ and, consequently, $h\left(x\right) \approx 1$ we retain the exponential profile for a pure dimer fluid (Figure 6.2). Thus the bi-exponential density profile, eqs 6.37 and 6.39, is 'sandwiched' between the SD-equilibrium distributions for monomers and dimers only (Figure 6.2). It should be noted that the latter two distributions are the equivalent of van 't Hoff's law for the osmotic pressure of monomers (eq 6.32) and dimers (eq 6.33) respectively.

6.5. Discussion

Our main interest here is the concentration dependent sedimentation velocity in eq 6.29 in view of our sedimentation velocity experiments (chapter 7) on attractive magnetic colloids. Nevertheless, it is pertinent to also briefly discuss the SD-equilibrium distribution derived in the previous section.

6.5.1. Sedimentation-Diffusion Equilibrium

An SD-equilibrium is equivalent to the osmotic equation of state, which can in principle be obtained from an experimental SD-profile, as has been demonstrated for the case of hard spheres [118] and charged colloids [55]. Somewhat peculiar at first sight is the non-linearity in the equation of state eq 6.31 – and the corresponding non single-exponentiality of the profile eq 6.37 – even though both monomers and dimers obey van 't Hoff's law (see eq 6.30). The reason for this non-linearity is the mass action law in eq 6.8: the ratio of monomers to dimers changes with the total weight concentration c_{tot} (i.e. c_1, c_2 and c_{tot} are interdependent) and, consequently, the osmotic pressure is not simply linear in c_{tot}. The non-ideality 'hidden' in the equation of state is, of course,

the attraction responsible for the dimerization of the colloids. Expanding the pressure in eq 6.31 to second order in concentration yields:

$$m_1 \frac{\Pi}{k_B T} = c_{tot} - \frac{1}{2} K_2^c c_{tot}^2 \tag{6.40}$$

Thus the first correction to ideal behavior, i.e. linear increase of pressure with c_{tot}, reminds of a second virial term with a second virial coefficient equal to $-\frac{1}{2}K_2^c$. The term 'virial', however, should be used with some caution here because the osmotic pressure in eq 6.31 is derived from a phenomenological mass action law without reference to a virial expansion.

With respect to an experimental verification of the SD-profile in eq 6.37 it should be noted that the limiting case of monomers will always be reached sufficiently high in the profile on approach of the depleted solvent supernatant phase, which is near the meniscus region for AUC experiments. However, a full exponential profile for the pure dimer fluid will only be observable for 'monovalent' colloids that cannot form n-mers with n > 2. For the majority of attractive colloids, those n-mers will also contribute in the concentrated region of a SD-equilibrium distribution. Nevertheless, one could in principle determine a monomer-dimer equilibrium constant K_2^c by integrating the SD-profile to determine the quadratic term in eq 6.40.

According to eq 6.29, K_2^c can also be obtained from the sedimentation velocity of attractive colloids at sufficiently low concentration. In what follows, we compare this prediction to other models for the concentration dependent sedimentation velocity of attractive colloids.

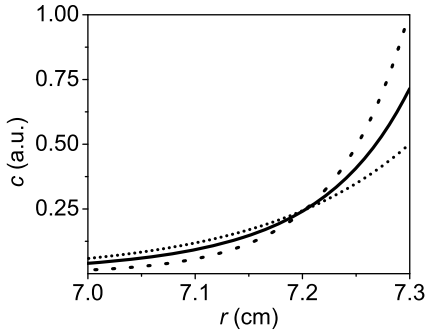

Figure 6.2: Computer generated sedimentation-diffusion equilibrium distributions (concentration c_{tot} vs. radial position r) for monomers with $c_1^\circ = 2.43$ a.u. (·····, eq 6.35 with $\sigma = 1.0$), dimers with $c_2^\circ = 2.37$ a.u. (- - -, eq 6.35 with $\sigma = 0.5$) and for species that exhibit reversible monomer-dimer self-association (——, eqs 6.37 and 6.39) with $c_1^\circ = 1.41$ a.u. and $K_2^c = 0.5$ a.u.$^{-1}$. The angular velocity resulting in an effective reduced molecular weight of $\sigma = 0.5$ and $\sigma = 1.0$ for monomers and dimers respectively, initial loading concentrations ($c_{tot} = 0.7$ a.u.), meniscus and bottom positions (5.9 and 7.3 cm respectively) are equal for all three distributions.

6.5.2. Sedimentation Velocity

Eq 6.29 for the weight-average sedimentation velocity of an equilibrium monomer-dimer mixture as shown in Figure 6.1, predicts an increase relative to the sedimentation velocity s_1° of the monomeric species at infinite dilution: the larger mass of a dimer is not fully compensated by the increase of the viscous drag force coefficient f_2°. This is quantified by the parameter χ in eq 6.29 that always exceeds unity (see eq 6.63). Note that at infinite dilution $\langle s \rangle$ in eq 6.29 reduces to s_1° as it should.

An alternative expression for $\langle s \rangle$ in eq 6.29 is in terms of the fraction γ of the total amount of monomers that is present in dimers:

$$\gamma = 1 - \frac{c_1}{c_{\mathrm{tot}}} \tag{6.41}$$

Substituting c_1 from eq 6.9, again taking the low-concentration limit (eq 6.10) to obtain:

$$\gamma \approx K_2^{\mathrm{c}} c_{\mathrm{tot}} + O\left(c_{\mathrm{tot}}^2\right) \tag{6.42}$$

one readily finds:

$$\frac{\langle s \rangle}{s_1^\circ} \approx 1 - (1-\chi)\gamma + O\left(c_{\mathrm{tot}}^2\right) \tag{6.43}$$

Note that within our treatment there is no concentration dependence resulting from hydrodynamic interactions and excluded volume effects that may also contribute to the coefficient K_s. The coefficient in eq 6.1, with which the volume fraction is multiplied, accounts for the concentration dependence of s and reads:

$$K_s = \frac{(1-\chi)\, K_2^{\mathrm{c}}}{\overline{\nu}_{\mathrm{p}}} \tag{6.44}$$

with K_2^{c}:

$$K_2^{\mathrm{c}} \approx \frac{1}{\rho_{\mathrm{s}}} \exp\left[-U_{\mathrm{eff}} + \ln\left(\frac{3\rho_{\mathrm{s}}\delta\Delta\omega_K^2}{8\pi^2 a_{\mathrm{tot}}\rho_{\mathrm{p}}}\right)\right] \tag{6.45}$$

according to eqs 6.21 and 6.22.

The effect of self-association may be quite pronounced, as will become clear when comparing eq 6.44 to other predictions for the concentration dependence coefficient for attractive colloids, i.e. the sedimentation rate with colloid volume fraction.

6.5.3. Comparison to Other Models

Various calculations for the sedimentation of attractive spheres have been published, based on the calculation of K_s via the pair-distribution function [88, 108, 109] (pdf). First we briefly recapitulate the results for hard spheres, followed by the incorporation of colloid-colloid attraction in order to make a comparison with our eq 6.29.

6.5.4. Calculation of Batchelor's Coefficient

The Batchelor coefficient K_s in eq 6.1 for the sedimentation coefficient s can be evaluated from [88, 108, 119]:

$$\frac{\langle s \rangle}{s^\circ} = 1 - \phi_{\text{tot}} + V' + V'' + W + O\left(\phi_{\text{tot}}^2\right) \tag{6.46}$$

The terms V' and V'', accounting for back flow effects and near-field hydrodynamic interaction, are given by:

$$V' = \frac{3\phi_{\text{tot}}}{a_{\text{tot}}^2} \int\limits_{r_{1,2}>a_{\text{tot}}}^{\infty} \left[g\left(r_{1,2}\right) - 1\right] r_{1,2}\, dr_{1,2} \tag{6.47}$$

and

$$V'' = \frac{1}{2}\phi_{\text{tot}} \tag{6.48}$$

Here, $g(r_{1,2})$ in eq 6.47 is the pair-distribution function and $r_{1,2}$ is the center-to-center distance between two spheres, each having a total diameter of d_{tot}. The term W in eq 6.46 comprises the effect of far-field hydrodynamic interactions. See e.g. refs. [88, 108, 119] for an explicit expression for W and the hydrodynamic mobility functions appearing in it.

The pair-correlation function $g_{\text{HS}}\left(r_{1,2}\right)$ for a hard-sphere repulsion is:

$$\left.\begin{aligned} g_{\text{HS}}\left(r_{1,2}\right) &= 0, \quad r_{1,2} < d_{\text{tot}} \\ &= 1, \quad r_{1,2} \geqslant d_{\text{tot}} \end{aligned}\right\} \tag{6.49}$$

From eq 6.47 one readily finds $V' = -(9/2)\phi_{\text{tot}}$ and for hard spheres it turns out [88] that $W_{\text{HS}} = -1.441\phi_{\text{tot}}$. So from eq 6.46 we obtain:

$$\frac{\langle s \rangle}{s^\circ} = 1 - K_s\phi_{\text{tot}} + O\left(\phi_{\text{tot}}^2\right);\ K_s = 6.441 \tag{6.50}$$

A more accurate calculation for W, including higher order terms in $d_{\text{tot}}/r_{1,2}$, yields $K_s = 6.55$ instead of $K_s = 6.441$ [88,108]. The incorporation of colloid-colloid attraction in addition to hard-sphere repulsion is straight forward, once the appropriate pdf is known. We will first consider magnetic attraction and then 'sticky' spheres.

6.5.5. Dipolar Magnetic Spheres

For the case of spheres with an embedded magnetic moment, eqs 6.46–6.48 still apply provided that [88]: (1) the spheres are torque free, having internally freely rotating dipoles (Néel relaxation) and (2) the pair-correlation function in eq 6.47 is replaced by its orientational average. Chan *et al.* [120] derived an analytic expression for the

orientational average pair-correlation function of dipolar spheres. The first terms of the expansion in $z = d_{\text{tot}}/r_{1,2}$ for *weak* magnetic interactions are [120]:

$$\frac{g\left(r_{1,2}\right)}{g_{\text{HS}}\left(r_{1,2}\right)} = \left[1 + \frac{\lambda^2}{3}\left(z\right)^6 + \frac{\lambda^4}{25}\left(z\right)^{12} + \cdots\right] \tag{6.51}$$

The dipolar coupling constant λ equals half the absolute maximum magnetic contact attraction and is, for monodisperse magnetic spheres with equal magnetic dipole moments, defined as:

$$\lambda = \frac{\mu_{\text{mag}}^2 \mu_\circ}{32\pi k_{\text{B}} \text{T} a_{\text{tot}}^3} \tag{6.52}$$

Here, μ_{mag} is the magnitude of the magnetic dipole moment and $\mu_\circ = 4\pi{\cdot}10^{-7}\ \text{J A}^{-2}\,\text{m}^{-1}$ is the magnetic permeability of vacuum. μ_{mag} for a magnetite sphere with a magnetic radius a_{mag} follows from:

$$\mu_{\text{mag}} = \frac{4}{3}\,\pi\, a_{\text{mag}}^3\, m_s \tag{6.53}$$

substituting a bulk magnetization for magnetite of $m_s = 4.84{\cdot}10^5\ \text{A m}^{-1}$ at 298 K [121]. Note that dipolar structure formation is expected when the dipolar potential energy exceeds thermal fluctuations ($\lambda > 2$) [110], if other interactions than hard-sphere and magnetic dipole interactions are absent.

On inspection of W in eq 6.46, explicitly given in e.g. ref. [88], it appears that the dipolar part of eq 6.51 hardly contributes and that, consequently, $W \approx W_{\text{HS}} = -1.441\phi_{\text{tot}}$ is a reasonable approximation. The dipolar attraction is mainly manifested in the backflow effect quantified by V' and V''. After evaluation of V' in eq 6.47 for $g\left(r_{1,2}\right)$ in eq 6.51 we find on substitution of all terms in eq 6.46 for the conentration dependence coefficient for weakly magnetic spheres:

$$K_s = -6.44 + \lambda^2 + \frac{6}{125}\lambda^4 \tag{6.54}$$

Dhont calculated [88] $g\left(r_{1,2}\right)$ up to the λ^2-term in eq 6.51 and found for the reduced sedimentation coefficient of weakly interacting superparamagnetic spheres:

$$\frac{\langle s\rangle}{s^\circ} = 1 - \left(6.55 - 0.97\,\lambda^2\right)\phi_{\text{tot}} + O\left(\phi_{\text{tot}}^2\right) \tag{6.55}$$

The numerical coefficients 6.55 and 0.97 are due to a more accurate evaluation of W. Only for $\lambda \gtrsim 2$, the λ^4-term in eq 6.54 starts to contribute significantly, confirming numerical calculations [88] showing that eq 6.55 is indeed accurate up to $\lambda \approx 2$.

6.5.6. Square-Well Attraction

The result from the previous section (eq 6.55) on magnetic spheres is valid for weak interactions only. One way to avoid this restriction is to start from a dimerization equilibrium as treated in section 6.2. Within the framework of Batchelor's theory

(eqs 6.46-6.48) requiring as input an isotropic pdf, an alternative is to model the (magnetic or any other) colloid-colloid attraction with a square-well potential for which K_s can be calculated analytically.

Batchelor [108] considered a short-range attraction such that a sphere 'adsorbs' onto another sphere at a center-to-center distance $r_{1,2} = d_{\text{tot}}$. This adsorption, as Batchelor points out [108], leads to (nearly) touching pairs of spheres, in excess of the number of pairs one would find for pure hard spheres, which will increase the average sedimentation rate. This picture, of course, resembles very much the dimerization from section 6.2. If all adsorbed particles are placed at $r_{1,2} = d_{\text{tot}}$, the pdf is given by [108, 109]:

$$g\left(r_{1,2}\right) = g_{\text{HS}}\left(r_{1,2}\right) + \alpha\,\frac{a_{\text{tot}}}{12}\,\delta\left(r_{1,2} - 2a_{\text{tot}}\right) \tag{6.56}$$

Here the parameter α depends on the interaction potential $U\left(r_{1,2}\right)$ via:

$$\alpha = \frac{3}{a_{\text{tot}}^3}\int_{d_{\text{tot}}}^{\infty}\left\{e^{\left[-U_{\text{eff}}\left(r_{1,2}\right)\right]} - 1\right\} r_{1,2}^2\,dr_{1,2} \tag{6.57}$$

Its physical meaning is that $\alpha\,\phi_{\text{tot}}$ (see also eq 6.60) is the excess number of pairs of spheres referred to above. Further, properties of the Dirac delta-function in eq 6.56 are:

$$\left.\begin{array}{rcll}\delta\left(r_{1,2} - 2a_{\text{tot}}\right) &=& \infty, & r_{1,2} = d_{\text{tot}} \\ &=& 0, & r_{1,2} \neq d_{\text{tot}}\end{array}\right\} \tag{6.58}$$

and:

$$\int \delta\left(r_{1,2} - 2a_{\text{tot}}\right) f\left(r_{1,2}\right) dr_{1,2} = f\left(d_{\text{tot}}\right) \tag{6.59}$$

For the pdf in eq 6.56, the sedimentation rate in eq 6.46 turns out to be:

$$\frac{\langle s\rangle}{s^\circ} = 1 - \left(6.55 - 0.44\,\alpha\right)\phi_{\text{tot}} + O\left(\phi_{\text{tot}}^2\right) \tag{6.60}$$

This result, first reported by Batchelor [108], has been used by various authors (e.g. Jansen *et al.* [109] and Rouw *et al.* [122]) to interpret sedimentation experiments of 'sticky' colloids. For a square-well potential with depth ϵ and width Δ:

$$\left.\begin{array}{rcll}U\left(r_{1,2}\right) &=& \infty & r_{1,2} \leqslant d_{\text{tot}} \\ &=& \epsilon, & d_{\text{tot}} < r_{1,2} < d_{\text{tot}} + \Delta \\ &=& 0, & r_{1,2} \geqslant d_{\text{tot}} + \Delta\end{array}\right\} \tag{6.61}$$

the integral in eq 6.57 is easily evaluated, and α in eq 6.60 becomes:

$$\alpha_{\text{swp}} = 8\left(e^{-\epsilon} - 1\right)\left[\left(1 + \frac{\Delta}{d_{\text{tot}}}\right)^3 - 1\right] \tag{6.62}$$

Clearly, the attraction, i.e. the well depth $\epsilon < 0$, has a pronounced effect on the concentration dependent sedimentation rate, as will be further illustrated in the comparison of the various predictions in the next section.

6.5.7. Comparison for Magnetite Spheres

To compare our eq 6.29 to results obtained via the pair-distribution function we employ the reference magnetic spheres already introduced in section 6.2.1. Their diameter is $d_{\mathrm{tot}} = 11\,\mathrm{nm}$, corresponding to a contact attraction of $-4.2\,k_{\mathrm{B}}\,\mathrm{T}$, i.e. $\lambda = 2.1\,k_{\mathrm{B}}\mathrm{T}$. This is the only input needed for Dhont's eq 6.55, with the result $K_s = 2.24$, leading to the negative concentration dependence shown in Figure 6.3.

For eq 6.60, the magnetic attraction is mapped onto the square-well potential from eq 6.61. One option to achieve this mapping is to demand that the second virial coefficient is the same for both interactions. This mapping is done in the Appendix, for simplicity for the orientationally averaged pdf from eq 6.51; we are primarily interested in the trend in K_s. This trend is that for a physically reasonable choice of square-well parameters (see the Appendix) $K_s \approx -4.50$, i.e. a significantly positive concentration dependence (see Figure 6.3).

For the evaluation of the Batchelor coefficient for the dimerization model in eq 6.44, we need to specify χ from eq 6.27 and the dimerization equilibrium constant K_2^x from eq 6.21. For identical spheres that associate to form dimers, χ becomes:

$$\chi = \frac{2\,f_1^\circ}{f_2^\circ} = \sqrt[3]{4}\left(\frac{f_2^\circ}{f_{2,\mathrm{sphere}}^\circ}\right)^{-1} \tag{6.63}$$

The frictional ratio [123] of the dimer and the equivalent dimer sphere friction factors is $f_2^\circ/f_{2,\mathrm{sphere}}^\circ = 1.06$, which leads to $\chi \approx 1.50$. An estimate for the equilibrium constant is obtained by substitution of $\rho_{\mathrm{p}} = 5 \cdot 10^3\,\mathrm{kg\ m^{-3}}$, $\rho_{\mathrm{s}} = 0.88 \cdot 10^3\,\mathrm{kg\ m^{-3}}$, $\delta = a_{\mathrm{tot}}$ and $\Delta\omega_K = 2\,\mathrm{rad}^2$ in eq 6.45. The resulting $K_s \approx -5.16$ (see Figure 6.3) is similar to the prediction from the square-well model.

Our equation (eq 6.29) predicts a positive concentration dependence of the sedimentation velocity just as the square-well potential model with physically reasonable values for the input parameters, in contrast to Dhont's model. Eqs 6.29 and 6.60 have in common that the concentration dependence coefficient scales exponentially with the contact attraction, whereas K_s in Dhont's equation originates from a perturbation to a hard-sphere potential and scales with the square of the interaction energy. The latter two differences very likely explain the deviation in the prediction from eq 6.29 or 6.55 and eq 6.60. In addition, it is physically plausible that our dimerization model produces a negative K_s. Settlement of a significant fraction of colloids in the form of reversible dimers will indeed greatly enhance K_s. The dimers sediment about $\chi \approx 1.50$ as fast as monomers (see Figure 6.1) and since the volume fractions are still very low (see Figure 6.3), K_s needs to be negative to produce this increase in sedimentation velocity. This makes it understandable why our dimer-approach leads to a much stronger concentration dependence than the calculation based on a weak perturbation on a hard-sphere potential as in eqs 6.54 and 6.55.

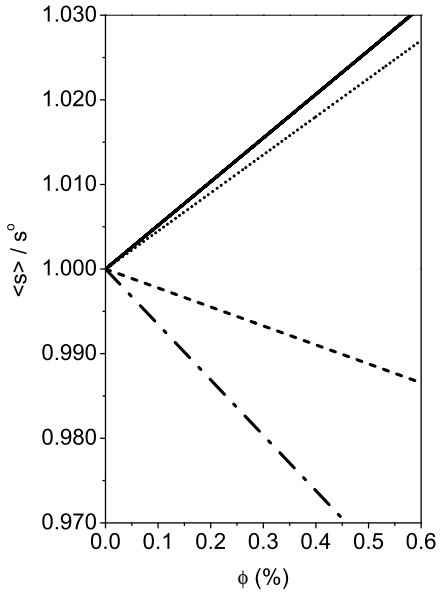

Figure 6.3: Predictions for the normalized sedimentation coefficient, $\langle s \rangle / s^\circ$, vs. volume fraction (eq 6.1) for magnetic spheres with a diameter of 11 nm. Eq 6.55 (- - -) predicts a decrease of the sedimentation rate with concentration in contrast to eqs 6.29 (——) and 6.60 (·····) that both predict a positive concentration dependence. See section 6.5.7 for the input parameter values. As a reference, the settling behavior of monodisperse hard spheres with $K_s = 6.55$ is included (–·–).

Furthermore, our dimerization approach includes an (magnetic) anisotropic interaction potential, which is much more relevant from a physical perspective than an isotropic potential for magnetic particles. Using eq 6.29 to fit experimental sedimentation velocity data an equilibrium constant can be obtained straightforward, from which the attraction energy may be calculated. Experiments, of course, will have to show which prediction for the concentration dependent sedimentation velocity of dipolar interacting spheres in Figure 6.3 is physically realistic. For such experiments on magnetic colloids the reader is referred to (chapter 7).

6.5.8. Experiments

It is interesting to note that a positive concentration dependence of the sedimentation velocity has already been observed in early sedimentation studies [7, 124], though there are insufficient data at sufficiently low concentration for an accurate determination of K_s. The increase of $\langle s \rangle$ with c_{tot} for interacting proteins has already been observed qualitatively by Svedberg and Pederson [7] and by Schwert [124]. For dilute horse hemoglobin solutions, Svedberg and Pederson determined that upon increasing the concentration the equilibrium distribution shifts towards larger dimer concentrations and as a result the sedimentation rate increases. Above a certain concentration

virtually all horse hemoglobin molecules are dimers, leading to a negative concentration dependence. Schwert investigated rapid association and dissociation in his studies on the molecular size and shape of chymotrypsinogen and α- and γ-chymotrypsin [124]. In addition to the positive concentration dependence of $\langle s \rangle$, he observed in those experiments on solutions containing appreciable amounts of monomers and dimers that the sedimentation boundary spreading (solvent-solution interface) is much more pronounced than that observed for either monomers or dimers alone, where the boundary spreading is mainly attributed to diffusion. An overview on early results for associating systems has been reported by Schachman [1].

6.6. Conclusions

Thermodynamic equilibrium between monomers and dimers in a dilute dispersion of attractive colloids (or macromolecules) allows an approximate calculation of the linear sedimentation concentration dependence from the dimerization equilibrium constant. This latter constant can in principle also be determined from the sedimentation-diffusion equilibrium distributions of a monomer-dimer self-associating system.

Our expression (eq 6.29) for the sedimentation velocity predicts a positive concentration dependence for reference magnetic spheres, for which Dhont's equation (6.55) leads to a negative (linear) density dependence. This difference probably originates in the assumption of a weak attractive perturbation to a hard-sphere potential underlying eq 6.55, whereas our model assumes a sufficiently strong contact attraction such that a significant fraction of colloids settles as reversible dimers. Modeling the reference magnetic spheres with a square-well potential may also lead to a positive concentration dependence of the sedimentation velocity. A drawback here, however, is the choice of the two square-well parameters (ϵ and Δ), whereas in our approach the input is the dimerization equilibrium constant, which can, in principle, be calculated from the properties of the (magnetic) attractive colloids.

Several early sedimentation studies on various biomolecules show – be it qualitative – evidence for a positive concentration dependence due to inter-molecular attractions. In the accompanying experimental sedimentation velocity study (chapter 7) of magnetic colloids we quantitatively compare experimental Batchelor coefficients to the various predictions discussed in this contribution.

Acknowledgement

Jan Groenewold contributed significantly to the work presented here. We thank Andrei V. Petukhov, Willem K. Kegel, Cornelis G. de Kruif, Henk N.W. Lekkerkerker and Ben H. Erné for helpful discussions.

Appendix: Mapping of B_2 for Isotropic Potentials

The second virial coefficient for an isotropic interaction potential $U\left(r_{1,2}\right)$ is:

$$B_2 = 2\pi \int_0^\infty \left\{1 - \exp\left[-U\left(r_{1,2}\right)\right]\right\} r_{1,2}^2 \, dr_{1,2}^2 \tag{A-6.1}$$

Substitution of the square-well potential from eq 6.61 yields:

$$\frac{B_2}{B_2^{\mathrm{HS}}} = 1 + \left(1 - e^{-\epsilon}\right)\left[\left(1 + \frac{\Delta}{d_{\mathrm{tot}}}\right)^3 - 1\right] \tag{A-6.2}$$

where $B_2^{\mathrm{HS}} = 2\pi d_{\mathrm{tot}}^3$ is the second virial coefficient for a hard sphere with diameter d_{tot}. For weakly interacting dipolar spheres the orientationally averaged pair-distribution function (pdf) $g\left(r_{1,2}\right)$ is given by eq 6.51. Bearing in mind that $g\left(r_{1,2}\right) = \exp\left[-U\left(r_{1,2}\right)\right]$, the second virial coefficient for the pdf from eq 6.51 turns out to be:

$$B_2 = B_2^{\mathrm{HS}} - \frac{2}{9}\pi\lambda^2 d_{\mathrm{tot}}^3 \tag{A-6.3}$$

where we have omitted the λ^4-term in eq 6.51.

Equating the virial coefficients defined by eqs A-6.2 and A-6.3 yields an expression for the depth ϵ of the square-well potential:

$$\epsilon = -\ln\left[1 + \frac{\lambda^3}{3\left(1 + \frac{\Delta}{d_{\mathrm{tot}}}\right)^3 - 3}\right] \tag{A-6.4}$$

A choice for the sphere diameter d_{tot} also fixes the dipolar coupling parameter λ in eq 6.52. The value chosen in section 6.5.7 for d_{tot} is 11 nm and the corresponding dipolar coupling parameter is $\lambda \approx 2.1\, k_{\mathrm{B}}\,\mathrm{T}$. Combinations of the square-well parameters that obey eq A-6.4 are shown in Table A-6.1. It is seen from Table A-6.1 that the magnitude of the Batchelor coefficient given by eq 6.60 (combined with eq 6.62) is independent of the choice of any combination of square-well parameters that obey eq A-6.4.

Table A-6.1: Square-Well Parameters

Width Δ nm	Depth ϵ $k_{\mathrm{B}}\,\mathrm{T}$	K_s [a]
0.17	-4.22	
0.20	-4.05	
0.30	-3.65	-4.50
0.40	-3.36	
0.50	-3.14	

[a] Batchelor coefficient according to eq 6.60 combined with eq 6.62.

7

Concentration Dependent Sedimentation Velocity of Magnetite Colloids with Tunable Dipolar Attractions

Abstract

We investigated systematically, via analytical ultracentrifugation, the concentration dependent sedimentation velocity of magnetic iron oxide (Fe_3O_4) colloids as a function of magnetic dipole moment, which was tuned by adjusting the particle volume. The sedimentation velocity behavior of the smallest particles, core diameter $\approx 4.8\,\mathrm{nm}$, resembles that of isotropic repulsive spheres. On increase of the dipole moment, however, a sharp transition occurs to a large, still linear positive concentration dependence, manifesting a strong effect of dipolar attractions. We compare our observations with calculations based on a pair-distribution function, as well as a phenomenological model that quantifies the concentration dependent sedimentation rate via the mass action law for reversible colloid-colloid association. Furthermore, we show that colloids with sufficiently large magnetic dipoles exhibit sedimentation velocity boundary broadening. Increasing the concentration of such colloids, shifts the sedimentation coefficient distribution towards larger sedimentation coefficients in contrast to repulsive colloids.

7.1. Introduction

Dipolar magnetic colloids have been studied with emphasis on dipolar structure formation and thermodynamics. The majority of these explorations concern theory and simulations [125, 126], though also experiments on dipolar structure formation have been reported [110, 111, 127, 128]. In contrast, less is known about transport phenomena as sedimentation and diffusion of particles that interact anisotropically, such as magnetic colloids. Rotational diffusion measurements on magnetic colloids where reported recently [129, 130], whereas various authors [127, 131–134] have also addressed the sedimentation of magnetic particles. The sedimentation of colloids from magnetotactic bacteria [127], core-shell colloids [131, 132], and synthetic magnetite [133] was investigated via analytical ultracentrifugation [131–133] and also via gravitational settling [127]. Drawbacks of the latter systems, which hamper a quantitative comparison to theory [88], are primarily the size and shape polydispersity associated with the conventional magnetite synthesis [121, 135], but also the weak magnetic dipole moments [131, 132].

Recently, well-defined, monodisperse, sterically stabilized magnetite spheres with adjustable size and, consequently, tunable dipolar magnetic interactions have become available, following a seed-mediated growth method using an organic iron precursor [110]. Our primary aim here is to employ these magnetic model colloids to investigate the concentration dependent sedimentation velocity for particles with increasing average size, i.e. with increasing magnetic attraction. Specifically we are interested to assess what happens to the sedimentation velocity when the colloids are large enough for the magnetic attractions to dominate the interaction potential.

In section 7.2 we report the preparation and properties of the magnetic colloids, followed by a description of sedimentation velocity (SV) analytical ultracentrifugation (AUC) experiments and data analysis methods, which are required to obtain accurate sedimentation coefficients. In section 7.3 we discuss the time-resolved concentration profiles and the eventual sedimentation coefficients as a function of colloid concentration. The latter results are compared to Dhont's calculations [88] for sedimenting dipolar colloids, the equation employed by Jansen *et al.* [108,109] for colloids interacting via a square well potential and a thermodynamic analysis (chapter 6) of sedimenting attractive colloids exhibiting a monomer-dimer equilibrium.

7.2. Materials and Methods

7.2.1. Magnetic Colloids

Magnetite particle dispersions labeled A to E, were synthesized following ref. [110], reporting a modification of the synthesis by Sun *et al.* [136]. Conventional magnetite dispersions are synthesized by a co-precipitation of ferrous and ferric ions in aqueous

alkaline solution [121,135]. In contrast, our well-defined spherical magnetite colloids are synthesized by a seed-mediated growth method employing iron (III) acetylacetonate in phenylether in presence of 1,2-hexadecanediol, oleic acid and oleylamine. If no further growth was required, the colloidal magnetite particles were dispersed in a *cis-trans*-decalin mixture and oleic acid that reversibly adsorbs onto the surface of magnetite particles (see ref. [137] and Figure A-7.1), which maintains the stability of the magnetite dispersions and inhibits particle aggregation (Figure 7.1).

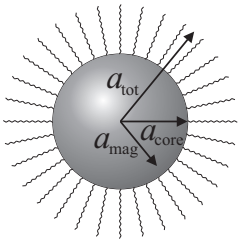

Figure 7.1: Schematic representation of a core-shell magnetite colloid, with a total radius a_{tot}. The iron oxide core, Fe_3O_4, is coated with reversibly adsorbed oleic acid, $C_{18}H_{34}O_2$. Generally, the magnetic radius, a_{mag}, is slightly smaller than the core radius, a_{core} [138].

Radii and relative polydispersities were determined from TEM images measuring 100 particles for dispersion A to E using analySIS® 3.2 Soft Imaging System GmbH. All TEM images were recorded using a Philips Tecnai 12 at Electron Microscopy Utrecht University (EMU). Magnetic dipole moments, μ_{mag}, were obtained from magnetization curves recorded at 25 °C with an alternating gradient magnetometer (AGM, Micromag 2900 Princeton Measurements Corporation) and fitted with a modified Langevin equation [121, 139]:

$$M(H) = M_s \left[\coth(\xi) - \frac{1}{\xi} \right] + bH + c \tag{7.1}$$

with:

$$\xi = \frac{\mu_{\mathrm{mag}} \mu_\circ H}{k_{\mathrm{B}} \mathrm{T}} \tag{7.2}$$

Here, H is the applied magnetic field, M_s is the saturation magnetization, b and c are constants to correct for, respectively, the diamagnetic contribution of cuvet and the offset of the magnetization curve. In eq 7.2, $\mu_\circ = 4\pi \cdot 10^{-7}\,\mathrm{J\,A^{-2}\,m^{-1}}$ is the magnetic permeability of vacuum, k_{B} is the Boltzmann constant and T is the absolute temperature. Thus in eq 7.1, M_s, μ, b and c are the fit-parameters. Furthermore, from the magnetic dipole moment, the magnetic radius, a_{mag}, can be obtained via:

$$a_{\mathrm{mag}} = \sqrt[3]{\frac{3}{4} \frac{\mu_{\mathrm{mag}}}{\pi m_s}} \tag{7.3}$$

using a bulk saturation magnetization per volume for magnetite of $m_s = 4.84 \cdot 10^5\,\mathrm{A\,m^{-1}}$ at 298 K [121]. As illustrated in Figure 7.1, a_{mag} is generally smaller [138] than the iron oxide core radius.

7.2.2. Sample Preparation

Particle dispersions were processed for analytical ultracentrifugation (AUC) experiments as follows. 0.5 mL of each synthesis product was 6 times precipitated by addition of ethanol, using a magnet to collect the particles, to remove oleylamine and excess oleic acid. After removal of the supernatant, the precipitate was re-dispersed in a solution of 15.6 mM oleic acid in *cis-trans*-decalin (this stock solution used in all experiments is hereafter denoted as OAD) to retain particle stability, minimize signal loss for attenuance measurements and to avoid depletion induced inter-particle attraction (see also section 7.4.1).

Complete removal of ethanol was achieved by drying the precipitate under a continuous N_2-gas flow. It is likely that the oleylamine contained in the synthesis product is completely removed by this washing procedure. Absence of oleylamine was confirmed by the low optical density (OD) of the supernatant after SV experiments.

Stock solutions were prepared having an attenuance of approximately 0.9 $\mathrm{OD}_{541\,\mathrm{nm}}$ through a 3 mm path length. Dilution series of 7 equidistant concentrations for dispersion A to E were obtained from the stock solutions with the lowest concentrations having an attenuance of approximately 0.9 $\mathrm{OD}_{229\,\mathrm{nm}}$ through a 12 mm path length.

Magnetite weight concentrations were obtained by evaporating the solvent of 200 μL of each stock solution using a precision balance (Mettler Toledo AX205 Delta Range). To compute the particle volume fractions from particle weight concentrations, we assume that the partial specific volume equals the specific volume, which is the inverse particle mass density. We determined the magnetite particle density ρ_{p} (Figure 7.1) via:

$$\rho_{\mathrm{p}} = \frac{a_{\mathrm{core}}^3 \rho_{\mathrm{mag}} + \left(a_{\mathrm{tot}}^3 - a_{\mathrm{core}}^3\right) \rho_{\mathrm{oa}}}{a_{\mathrm{tot}}^3} \tag{7.4}$$

substituting an iron oxide core radius, a_{core}, as obtained from TEM images and density $\rho_{\mathrm{mag}} = 5.17\,\mathrm{g\,cm^{-3}}$ [74]. The layer thickness and density of the reversibly adsorbed oleic acid are assumed to be, respectively, 2 nm and $\rho_{\mathrm{oa}} = 0.891\,\mathrm{g\,cm^{-3}}$ [140]. If solvent molecules interact strongly with the dispersed - and therefore dissolved - particles, the partial specific volume will not equal the specific volume and eq 7.4 should be used with caution.

Furthermore, viscosities and densities of an OAD solution dilution series, with oleic acid concentrations in the range of 5-50 mM, were determined using an Ubbelohde capillary viscometer and a Anton Paar DMA 5000 Density Meter respectively. All apparent sedimentation coefficients were corrected for solution viscosity, η_{s}, and density,

ρ_s, to obtain $s_{20,d}$-values (sedimentation coefficient for particles in *cis-trans*-decalin at 20.0 °C, hereafter denoted as s or s°) using:

$$\left\langle s_{20,d} \right\rangle = \left\langle s_{app} \right\rangle \left[\frac{\eta_s}{\eta_d^\circ} \frac{\left(1 - \overline{\nu}_p \rho_d^\circ\right)}{\left(1 - \overline{\nu}_p \rho_s\right)} \right] \tag{7.5}$$

The same OAD dilution series was used to determine oleic acid in *cis-trans*-decalin extinction coefficients at 228, 229 and 230 nm (Varian Cary 1E UV-Visible Spectrophotometer) to anticipate the monochromator's incorrect wavelength resetting of the Beckman Coulter™ Optima™ XL-A AUC. For results on density, viscosity and extinction coefficient determinations and the resulting correction factors see Appendix A.

7.2.3. Sedimentation Velocity

The range of the sample initial loading concentrations for the sedimentation velocity (SV) experiments with the AUC (Beckman Coulter™ Optima™ XL-A AUC absorbance optics) is determined by the extinction coefficient(s) of the particles or solutes, the path length of the double sector centerpieces and by the emission peaks of the Xenon flash lamp. Double sector epon charcoal-filled centerpieces of 3 and 12 mm were used to cover a large concentration range. For each concentration of each dilution series a wavelength spectrum was recorded in addition to the Xenon flash lamp emission spectrum (200 to 600 nm) through an empty hole in the An-50 Ti rotor. Using these spectra we maximized the signal to noise ratio by matching the wavelength of a local emission maximum with an attenuance that is in between 0.6 and 0.9 OD to obtain high quality data as shown in Figure 7.4. SV boundaries were recorded with a step size of 10 μm in the continuous mode during 2 hours to collect 70 scans. Because for each sample the wavelength had to be adjusted, each SV run was done loading only a single cell to avoid wavelength variations larger than $\pm\,1$ nm. Since our particles are dispersed in an organic solution, the experiments were conducted at 20.0 $\pm$ 0.1 °C to avoid the automatically applied temperature correction for aqueous solutions implemented in *UltraScan* [23]. Initial angular velocities for SV experiments were obtained from Finite Element [75] (FE) simulations as implemented in *UltraScan* [23] and adjusted, after some exploring SV experiments, to achieve high s-resolutions with at least 35 scans suited for analysis. A proper design of SV experiments is also required to facilitate the comparison of recorded sedimentation profiles of dispersion A to E particles.

We note here that an appropriate and model independent analysis for the recorded sedimentation velocity data should be used to obtain diffusion deconvoluted sedimentation coefficients, since the settling of particles is partly counteracted by diffusion which results in the broadening of the solvent-solution interface. Therefore, data collected during SV experiments containing at least 35 scans were analyzed using the second moment analysis (SM) [141] and the enhanced van Holde-Weischet analysis (vHW) [43, 44], both implemented in *UltraScan* [23]. Integral sedimentation coefficient

distributions G(s) and differential sedimentation coefficient distributions (envelope of histogram) obtained from the vHW analysis were compared with results of the SM analysis. The corrected weight-average sedimentation coefficients were computed from the apparent weight-average sedimentation coefficients via eq 7.5. Free oleic acid concentrations, required for this correction, were calculated from the ODs below and close to the sample meniscus using the experimentally determined extinction coefficients. The OAD ODs were determined from radial scans at a wavelength of 229 ± 1 nm, recorded in step mode, 14 hours after the SV experiment was completed (see Figure A-7.1). This method can be applied because the centrifugal lengths for the particles of dispersion A to E at angular velocities ω at which the sedimentation velocities were monitored are extremely small. For dispersion A to E particles the centrifugal lengths in our experiments are in between $L_\omega = 0.8$ to 1.3 mm, as follows from:

$$L_\omega = \sqrt{\frac{2k_\mathrm{B}\mathrm{T}}{m_\mathrm{p}\left(1-\overline{\nu}_\mathrm{p}\rho_\mathrm{s}\right)}} \tag{7.6}$$

Here, m_p is the particle mass, $\overline{\nu}_\mathrm{p}$ is the partial specific volume and ρ_s is the solution density. A similar quantity is the effective reduced molecular weight [117] $\sigma = 1/L_\omega$, which is in between 59 to 156 cm^{-2} for dispersion A to E. Assuming complete absence of magnetite particles near the menisci is legitimate, since σ-values larger than 2 cm^{-2} for dilute solutions, result in meniscus depletion according to Correia *et al.* [142].

Sedimentation coefficients at infinite dilution, s°, were obtained by extrapolating an unconstrained fit (slope and y-intercept are set to float) of corrected sedimentation coefficients versus concentration to zero concentration using:

$$\langle s\rangle = s^\circ - k_s c_\mathrm{tot} + O\left(c_\mathrm{tot}^2\right) \tag{7.7}$$

The concentration dependence coefficient, K_s in:

$$\frac{\langle s\rangle}{s^\circ} = 1 - K_s\phi_\mathrm{tot} + O\left(\phi_\mathrm{tot}^2\right) \tag{7.8}$$

were obtained from a linear constrained fit (y-intercept = 1, slope is fitted) of reduced sedimentation coefficients versus calculated volume fraction using the magnetite weight concentration and eq 7.4.

The radius a_h of a sphere with a frictional coefficient f° at infinite dilution according to Stokes' equation [38]:

$$f^\circ_\mathrm{sphere} = 6\,\pi\,\eta^\circ_\mathrm{s}\,a_\mathrm{h} \tag{7.9}$$

can be determined from s° via:

$$s^\circ = \frac{V_\mathrm{p}\left(\rho_\mathrm{p}-\rho^\circ_\mathrm{s}\right)}{f^\circ} = \frac{m_\mathrm{p}\left(1-\overline{\nu}_\mathrm{p}\rho^\circ_\mathrm{s}\right)}{f^\circ} \tag{7.10}$$

if the particle mass, m_p, and its partial specific volume, $\overline{\nu}_p$, is known. If the bare particle radius a_b equals the hydrodynamic radius a_h, then eq 7.10 reduces to:

$$s^\circ = \frac{2}{9}\, a_b^2\, \frac{\left(\rho_p - \rho_s^\circ\right)}{\eta_s^\circ} \tag{7.11}$$

Particle radii were obtained from eqs 7.10 and 7.11 using s° and all other required parameters as determined from experiments. For eq 7.10 we assume that $\overline{\nu}_p = 1/\rho_p$, which is appropriate for impenetrable particles that do not interact with solvent molecules.

7.3. Results and Discussion

7.3.1. Particle Characterization

In contrast to conventional magnetite particles synthesized by a co-precipitation of ferrous and ferric ions in aqueous alkaline solution [121,135], the size and shape polydispersity of our magnetite particles is fairly small (Figure 7.2 and Table 7.1). Remarkably, the size polydispersity increases with average particle size, which is probably due to secondary nucleation while growing the seeds during the early synthesis steps. Secondary nucleation is not expected during later synthesis steps because the temperature was increased gradually [110]. Presence of secondary nucleation particles was confirmed by the sedimentation velocity experiments in which the smaller particles were only resolved at low concentrations due to the Johnston-Ogston effect [143] that is discussed in the next section.

The results on magnetite particle properties (see Table 7.1) confirm that the particle size and magnetic dipole moment can be adjusted to tune the dipolar magnetic interactions.

The dipolar coupling constant, λ in eq 7.14, for dispersion E particles is at the onset of dipolar structure formation ($\lambda \gtrsim 2$) [110]. Typical *in situ* cryo-TEM images of vitrified magnetite dispersion D and E in zero external magnetic field (Figure 7.3) clearly show the effect of increasing dipolar attraction, reflected by the particle positions. In dispersion E, particles tend to form dipolar chains, whereas smaller magnetic interactions, as in the case for dispersion D, result in a relatively more homogeneous distribution of particles. However, it should be noted that the systems shown in Figure 7.3 are much more concentrated than the samples used for AUC SV experiments reported here.

Radii determined from TEM images, s° values and magnetic dipole moments (using eqs 7.10, 7.11 and 7.3, Table 7.1) agree well; i.e. hydrodynamic radii, a_h, computed from the sedimentation coefficients at infinite dilution are larger than the magnetic radii, a_{mag}, and the TEM radii, a_{TEM}, are in between. The discrepancy between the hydrodynamic radii obtained using eqs 7.10 and 7.11, is indicative for particle-solvent interaction. As a result, the assumption that the partial specific volume equals the

inverse particle density, introduces an uncertainty in the calculated volume fractions and, consequently, in K_s in eq 7.8 (see Table 7.2).

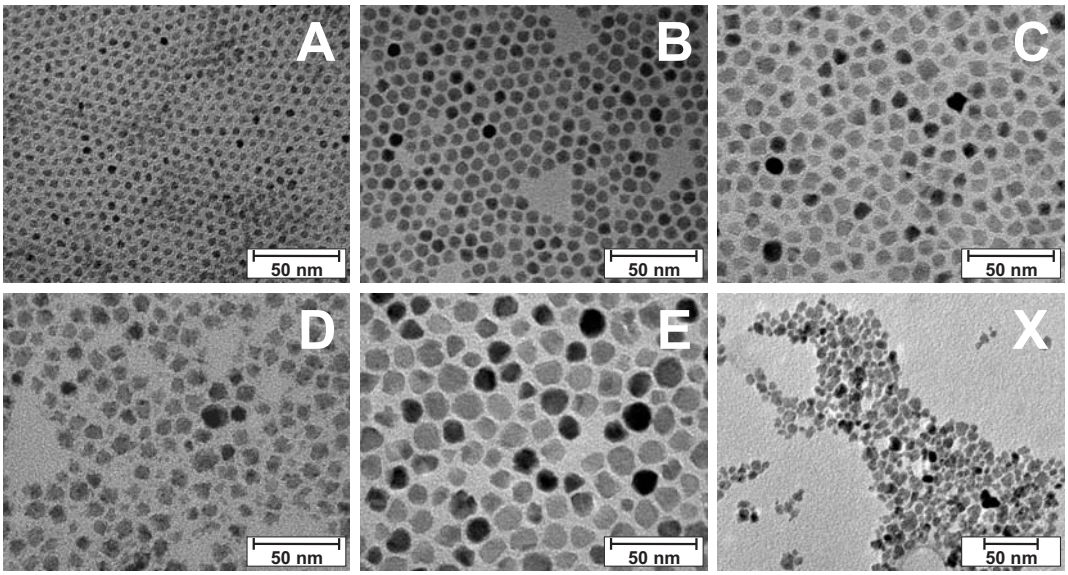

Figure 7.2: TEM images of magnetite particles in dispersion A, B, C, D and E. The shape and size polydispersity (Table 7.1) is relatively small in comparison to the magnetite particles in image X, prepared according to the conventional co-precipitation in aqueous iron chloride solution [135].

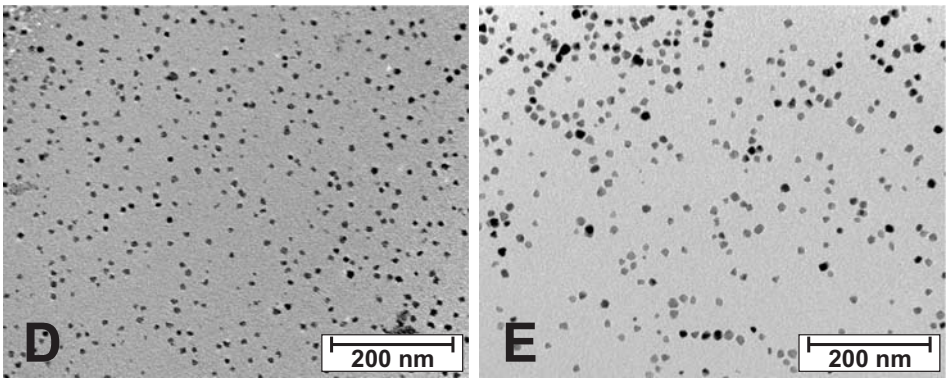

Figure 7.3: Typical *in situ* cryo-TEM images of vitrified films, which are quasi 2-D systems, of magnetite dispersions D and E in zero external magnetic field. Increasing the dipolar attraction, results in the association of magnetite colloids and leads to dipolar structure formation.

7.3.2. Concentration Distributions

Remarkable trends can already be observed by visually inspecting the concentration distributions that develop during sedimentation for the most concentrated and most diluted samples of dispersion A and E (see Figure 7.4). The sedimentation boundaries

Table 7.1: Particle Characteristics

Disp.	a_{core} [a] nm	a_{h} [b] nm	a_{b} [c] nm	σ [d] %	μ_{mag} [e] A nm^2	a_{mag} [f] nm	U_{mag} [g] k_{B} T
A	2.4	3.7	4.8	5.5	0.024 ± 0.002	2.3	-0.04 ± 0.01
B	3.8	4.6	6.5	7.0	0.114 ± 0.014	3.8	-0.41 ± 0.09
C	4.6	5.4	7.3	9.2	0.168 ± 0.017	4.4	-0.60 ± 0.13
D	4.8	6.0	7.2	10.1	0.183 ± 0.018	4.5	-0.65 ± 0.15
E	7.1	8.6	9.4	11.3	0.658 ± 0.067	6.9	-3.55 ± 0.86

[a] Iron oxide core radii determined from 100 particle diameters on TEM images taken at magnifications between 350,000 to 570,000 x.

[b] Hydrodynamic radii (eq 7.10) from s°.

[c] Radii from s° for particles with $a_{\mathrm{h}} = a_{\mathrm{b}}$ (eq 7.11).

[d] Number-average radii polydispersity determined from TEM images using the ratio of the standard deviation of the mean iron oxide core radius and the mean radius plus a 2 nm thick oleic acid layer.

[e] Determined by fitting the magnetization curves using a modified Langevin equation (eq 7.1). Uncertainties in magnetic moments were determined from the AGM Micromag 2900 Princeton Measurements Corporation system specifications.

[f] Calculated from the magnetic moment using eq 7.3.

[g] Magnetic pair-interaction energy [88] for a close contact head-to-tail configuration, calculated using the magnetic moments, TEM-radii and assuming an oleic acid layer thickness of 2 nm.

of the most concentrated dispersion A sample (graph A-1 in Figure 7.4) are relatively steep, which is indicative for a negative concentration dependency of s. Self-sharpening boundaries are also observed for repulsive, non-magnetic colloids [1]. Particles in the trailing part of the sedimentation boundary migrate more rapidly than those in the leading part. As a result, there is a continuing tendency for the boundary to sharpen itself which counteracts the boundary spreading by diffusion. An early crossover of the linear fits of the full boundaries, i.e. 100% of the concentration profiles, in the vHW-extrapolation plot also indicates negative concentration dependency. Furthermore, by comparing the graphs A-1 and A-2 in Figure 7.4, the Johnston-Ogston effect [143] is evident for dispersion A; i.e. at high concentrations, fast-settling particles are slowed down because they must move through a layer of slowly sedimenting particles as well as solvent. The slowly moving species increase the apparent viscosity of the solution, leading to a concentration-dependent decrease of the sedimentation coefficient. The Johnston-Ogston effect leads to distortion of the boundary, as the apparent concentrations of the slower moving species are enhanced, while those of the faster moving species, moving through a more concentrated solution, are correspondingly reduced. Typically, this effect is greatest for molecules that display large concentration dependence of s, and becomes vanishingly small as the concentration is lowered. Smaller and larger particles are therefore only resolved during sedimentation at sufficiently low concentrations (graph A in Figure 7.6). It is plausible that the Johnston-Ogston effect

contributes to the deviation from the hard-sphere behavior, i.e. $K_s = 12$ instead of 6.55, for dispersion A. Size heterogeneity counteracts the self-sharpening of the sedimentation boundary that is enhanced by the Johnston-Ogston effect. These two effects obscure the visual inspection of sedimentation boundaries.

In contrast to the settling behavior of dispersion A particles, boundary broadening is observed for dispersion E. The sedimentation velocity of particles that attract each other is enhanced in sufficiently concentrated regions where even particle association may occur. Particles at more diluted concentrations experience the full backflow and, therefore, sediment slower than at infinite dilution. The boundary broadening observed for dispersion E (graph E-1 in Figure 7.4) cannot be assigned straight forward to interparticle attraction by visual inspection since the relative polydispersity of dispersion E is approximately 11%.

Opposite trends in the concentration dependent sedimentation velocity of dispersion A and E particles are further discussed in the next section 7.3.3.

7.3.3. Sedimentation Velocity

The linear correlation of the corrected sedimentation coefficients versus concentration (Figure 7.5) obtained from the SM analysis for dispersions A-E, confirms that modeling the sedimentation velocity to first order in volume fraction (eq 7.8) is allowed. Since eq 7.8 can be applied only if $|K_s|\,\phi_{\mathrm{tot}} << 1$ and that for dispersion A to E $-2.9 \cdot 10^{-2} < K_s\phi_{\mathrm{tot}} < 8.6 \cdot 10^{-2}$, we have another confirmation that it is allowed to use eq 7.8 here.

7.3.4. Reversible Association

Trends in the sedimentation velocity, discussed in section 7.3.1, observed by visual inspection of the sedimentation boundaries (Figure 7.4) are confirmed; the coefficient K_s already changes sign going from dispersion A to B. The increase of dipolar attraction from dispersion A to E appears to have a pronounced effect on the sedimentation velocity that, it should be noted, still depends linearly on concentration.

The linear increase of the sedimentation velocity with concentration for dispersion B to E manifests attractions that, however, are not strong enough to form permanent aggregates. Magnetic particles with sufficiently large dipole moments in zero external magnetic field spontaneously form linear structures and may even form flux-closure rings [110,144,145]. Apparently, in the concentration range studied here the probability of formation of structures is restricted to dimers. Thus the sedimentation coefficients in Figure 7.5 relate to an equilibrium mixture of monomers and dimers, a point to which we will return in section 7.4. It should be noted that permanent or irreversible associates that give rise to step function-like sedimentation boundaries are completely absent.

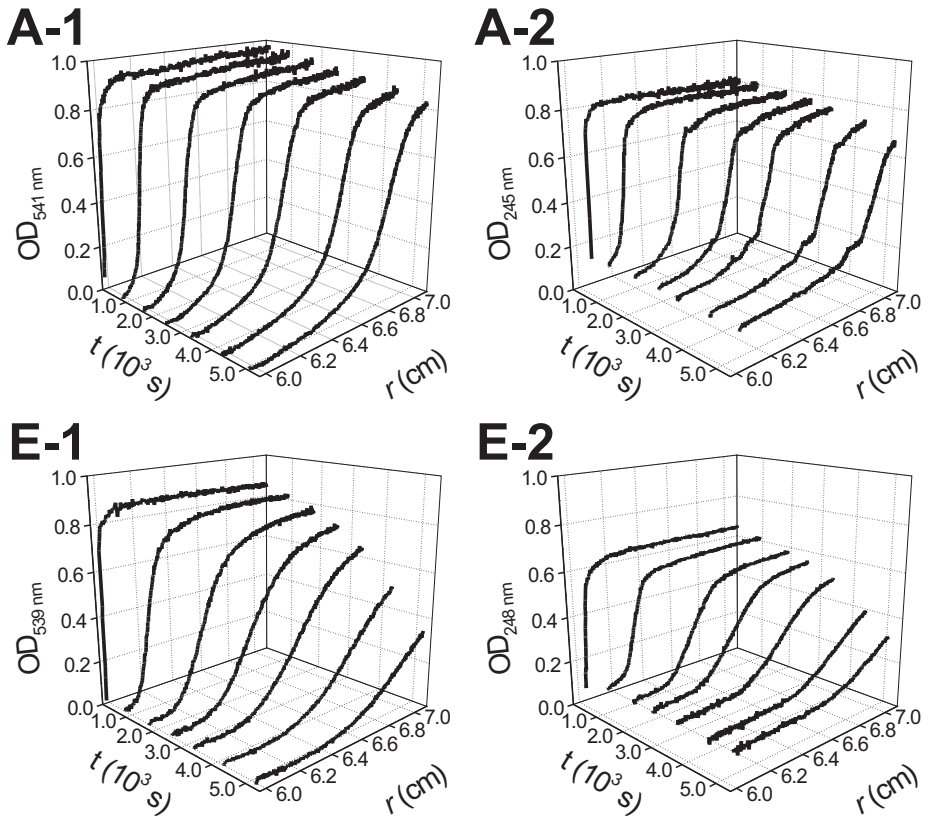

Figure 7.4: Selection of sedimentation velocity attenuance profiles: attenuance (z-axis) vs. distance from the center of rotation r (x-axis) and vs. time t (y-axis) corrected for rotor acceleration. Graphs A-1 and E-1 show the sedimentation for the most concentrated samples of, respectively, dispersion A ($c_{\mathrm{tot}} = 3.90\,\mathrm{mg\ mL^{-1}}$) and E ($c_{\mathrm{tot}} = 1.03\,\mathrm{mg\ mL^{-1}}$). Graphs A-2 and E-2 show the sedimentation for the most diluted samples of, respectively, dispersion A and E (both with $c_{\mathrm{tot}} = 0.02\,\mathrm{mg\ mL^{-1}}$). Here, the sedimentation velocity for dispersion A particles is $\mathrm{v} \approx 1.8\,\mu\mathrm{m\ s^{-1}}$ and for dispersion E particles $\mathrm{v} \approx 2.0\,\mu\mathrm{m\ s^{-1}}$, according to $\mathrm{v} = s^{\circ}\,\omega^2\,r$ with $r = 6.5\,\mathrm{cm}$.

7.3.5. vHW Analysis of s-Distributions

In addition to the second moment analysis (SM), trends in the concentration dependent sedimentation velocity were also determined using the enhanced van Holde-Weischet analysis (vHW). As pointed out earlier, the particles of dispersions A-E are heterogeneous in size, which is immediately assessed by a vHW analysis. Here, for the most concentrated dispersion A sample, which shows a negative concentration dependent sedimentation, both heterogeneity and concentration dependency of s are present and consequently the negative slope of the integral sedimentation coefficient distribution $\mathrm{G}(s)$ due to the concentration dependency is partially cancelled by the positive slope caused by the apparent heterogeneity (graph A in Figure 7.6). The heterogeneity is an apparent heterogeneity because upon dilution we observe two distinct almost discrete species, which are not resolved in the more concentrated regime due to the

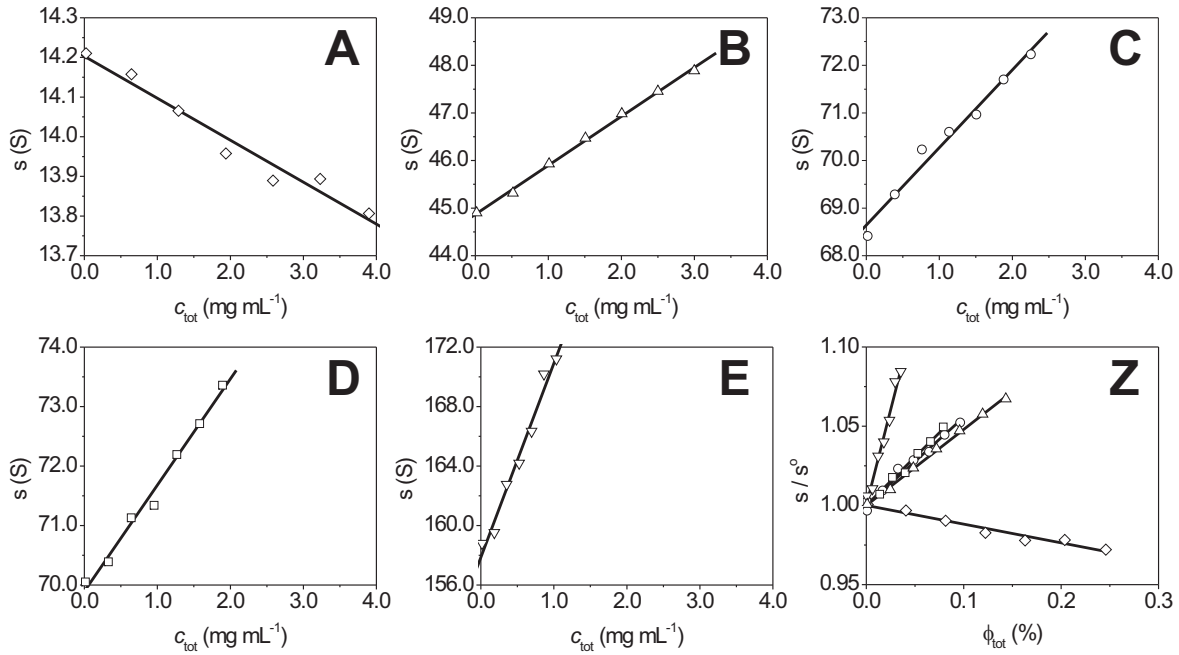

Figure 7.5: Sedimentation coefficients, s corrected for solution viscosity and density variations, vs. the total weight concentration c_{tot} for dispersion A (◇), B (△), C (○), D (□) and E (▽). Solid lines (——) in graph A to E are linear unconstrained fits whereas in graph Z the solid lines are linear constrained fits. Graph Z shows the reduced sedimentation coefficients vs. volume fraction. Volume fractions were calculated from particle weight concentrations and $\overline{\nu}_{\mathrm{p}} = 1/\rho_{\mathrm{p}}$ (eq 7.4) via $\phi_{\mathrm{tot}} = c_{\mathrm{tot}}\overline{\nu}_{\mathrm{p}}$. Fit results are shown in Table 7.2.

Johnston-Ogston effect, resulting in a continuous sedimentation coefficient distribution. The strong concentration dependency of dispersion A is also seen throughout a single sedimentation velocity run. The increase of the sedimentation velocity that is most notable in the upper boundary divisions as a result of radial dilution due to the wedge-shaped double sector centerpieces prevents in principle linear extrapolation to infinite time. As a consequence, a full boundary vHW analysis of dispersion A samples, results in an early intersection of linear extrapolations, indicative for the increase of the sedimentation velocity upon dilution.

In contrast, a full boundary vHW analysis for the most concentrated dispersion E sample results in a very broad sedimentation coefficient distribution and the linear extrapolations to infinite time do not converge at all. The enhanced width of this sedimentation coefficient distribution is not governed by the size and shape polydispersity of monomers only. Instead, this broad distribution can be explained by particle association due to particle attraction.

The shift of the integral G(s) and differential (envelope of histogram) sedimentation coefficient distribution (graph A in Figure 7.6) for dispersion A towards larger s-values

Table 7.2: Concentration Dependent Sedimentation Velocity

Disp.	Experiment				Theory			
	$\overline{\nu}_p$ [a]	s_1° [b]	k_c [c]	K_s [d]	s_2° [e]	K_s [f]	K_s [g]	K_s [h]
	mL g^{-1}	S	S mL g^{-1}		S			
A	0.631	14.2	105 ± 6	12 ± 2	–	6.55	6.55	–
B	0.476	44.9	-1,028 $\pm$ 61	-48 $\pm$ 3	67.2	6.51	6.55	-0.04
C	0.427	68.6	-1,631 $\pm$ 112	-56 $\pm$ 4	102.8	6.46	6.54	-0.04
D	0.417	69.9	-1,784 $\pm$ 120	-61 $\pm$ 4	104.7	6.45	6.53	-0.05
E	0.342	157.9	-13,051 $\pm$ 1752	-242 $\pm$ 33	236.4	3.50	2.90	-0.42

[a] Partial specific volume obtained via eq 7.4 assuming that $1/\rho_p = \overline{\nu}_p$.

[b] Monomer sedimentation coefficient at infinite dilution (eq 7.7). Slope and y-intercept are fitted.

[c] Concentration dependence coefficients obtained from a linear unconstrained fit (eq 7.7).

[d] Obtained from a linear constrained fit (eq 7.8), i.e. y-intercept = 1 and slope is floated.

[e] Dimer sedimentation coefficient (two touching spheres) at infinite dilution, calculated using a frictional ratio of 1.06 [123] (eq 7.24).

[f] Prediction from Dhont's theory [88], substituting $a_{tot} = a_{core} + 2\,\text{nm}$ and magnetic moments from experiments (Table 7.1) in eq 7.13.

[g] Prediction from the theory of Jansen *et al.* [109] (eq 7.18), substituting $\epsilon = U_{eff}$, Δ according to eq 7.20 with $\lambda = U_{eff}/2$ (Table 7.3), and $a_{tot} = a_{core} + 2\,\text{nm}$ (Table 7.1) in eq 7.19.

[h] Prediction from the theory for a monomer-dimer equilibrium mixture, i.e. eqs 7.21 and 7.22 (also see chapter 6).

upon dilution, clearly confirms the negative concentration dependent sedimentation velocity. The differential sedimentation coefficient distribution broadens with decreasing concentration which is indicative for the self-sharpening of sedimentation velocity boundaries. Corrected group weight-average s-values and sedimentation coefficient distributions from the enhanced vHW analysis for dispersions A and E (graph A and E in Figure 7.6) agree well with corrected SM weight-average sedimentation coefficients, ensuring a reliable data analysis. The two group weight-average s-values of the sedimentation coefficient distributions for dispersion A are 13.7 S and 14.2 S, and are in excellent agreement with the values found using the SM analysis, which are 13.8 S and 14.2 S.

Such confirmations are also found for the trends in the concentration dependent sedimentation velocity of dispersion E to a quantitative level. The two group weight-average s-values of the differential sedimentation coefficient distributions are 172.3 S and 158.9 S and are equal to those determined using the SM analysis, which are 171.2 S and 158.8 S. The shift of the integral and differential sedimentation coefficient distributions for dispersion E towards smaller s-values upon dilution indicates a positive concentration dependent sedimentation velocity (graph E in Figure 7.6). In contrast to the self-sharpening of sedimentation boundaries observed for dispersion A, the integral and differential sedimentation coefficient distribution widths increase with concentration resulting from the sedimentation boundary broadening with increasing concentration for dispersion E (see Figure 7.4).

The sedimentation boundary broadening and the vHW s-distributions indicate that a significant amount of dipolar structures comprised of two single particles are present in relatively concentrated magnetite dispersions where particle attractions are sufficiently large. The onset of dimer formation estimated from the results obtained here is $-0.4 < U_{\text{eff}}\,(k_{\text{B}}\,\text{T}) < 0$. The peak around 210 S in the differential sedimentation coefficient distribution (graph E in Figure 7.6) is indeed close to but smaller than the sedimentation coefficient of a dimer comprised of two perfect spherical dispersion E particles, which is 236.4 S (Table 7.2). During a sedimentation velocity run, monomers and dimers in dispersion B to E samples are not well resolved, confirming that the monomer association and dimer dissociation are very rapid compared to the typical observation time of the experiment. The shortest typical (absorbance) AUC experiment observation time is 1-2 min., required to record a sedimentation velocity profile, and the longest observation time, i.e. duration of the entire run, is typically 2.5 h.

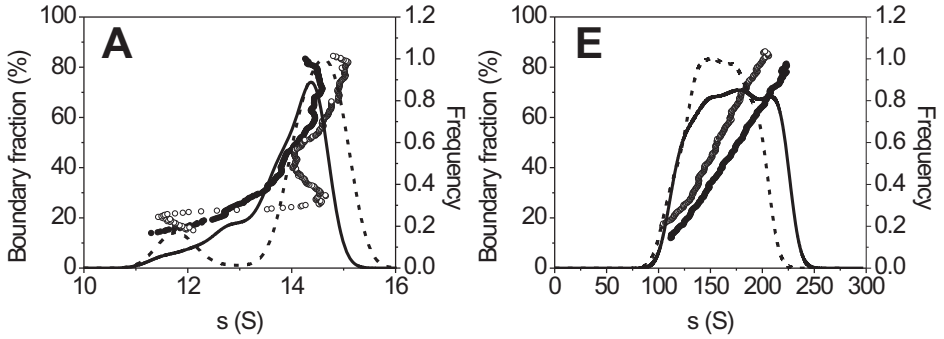

Figure 7.6: Integral G(s), left y-axis (• and ○), and differential (envelope of histogram, —— and ----), right y-axis, sedimentation coefficient distributions for the most concentrated (• and ——) and diluted (○ and ----) dispersion A (graph A) and E (graph E) samples. The sedimentation coefficient distributions reflect 70% of 35 sedimentation velocity scans with 250 divisions. Note the shift of the distribution to larger s-values and the increase of the distribution-width upon dilution in graph A, resulting from the self-sharpening of the sedimentation boundaries at larger concentrations. Furthermore, for dispersion A the Johnston-Ogston effect is evident from these sedimentation coefficient distributions; i.e. two distinct particle sizes are resolved only at sufficiently low concentrations. In contrast, the s-distributions for dispersion E shift to smaller s-values and the differential distribution-width decreases upon dilution, due to broadening of the sedimentation boundaries with increasing concentration

7.4. Comparison with Theory

To interpret and explain the effect of concentration and particle dipole moment on the sedimentation velocity of colloidal magnetite spheres, discussed in sections 7.3.2 and 7.3.3, the pair-interaction potential for two magnetite spheres in a head-to-tail configuration (Figure 7.7), including all relevant interactions, needs to be evaluated.

After the discussion of the pair-interaction potential, experimental results are compared to predictions from theory.

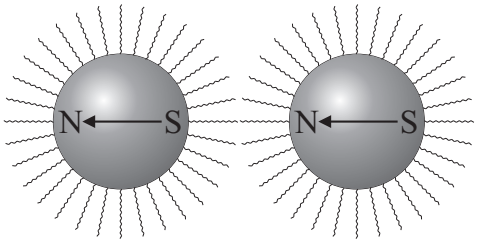

Figure 7.7: Schematic representation of two core-shell magnetite spheres in a close contact head-to-tail configuration.

7.4.1. Pair-Interaction Potentials

The magnetic interaction (see Appendix B) is dominant but, obviously, not the only attraction. The large refractive index difference of magnetite and the OAD solution results in significant London-van der Waals attractions. Therefore, this interaction needs to be evaluated and included in the overall pair-interaction potential.

In contrast to the Hamaker constant $A = 9.9\,k_\mathrm{B}\,\mathrm{T}$ reported by Scholten [146] and Ewijk [147], we calculate in Appendix C a Hamaker constant of $A = 39.3\,k_\mathrm{B}\,\mathrm{T}$ at 293.15 K for magnetite in decalin (eq 11.14 in ref. [148] with $\nu_e = 3 \cdot 10^{15}\,\mathrm{s}^{-1}$, $\epsilon_1 = 20.0$, $\epsilon_3 = 2.2$, $n_1 = 2.42$ and $n_3 = 1.474$ obtained from ref. [74, 140]). Note that the London-van der Waals interaction does not diverge for a close contact configuration since the magnetite colloids employed here are sterically stabilized by an oleic acid layer, which has approximately the same refractive index as decalin (see Appendix C).

As discussed in Appendix D, the strength of the depletion induced attraction is negligible and is not accounted for in the overall pair-interaction potential used here.

There may also be a (modest) repulsive contribution to the pair-interaction, because the Batchelor coefficient $K_s = 12$ for dispersion A is larger than the pure hard-sphere value $K_s = 6.55$. Already a small effective diameter increase of $\Delta a = 1\,\mathrm{nm}$ can account for this difference (Appendix E); possibly a short-range solvation force is operative here, as further discussed in Appendix E.

The pair-interaction potential $U_\mathrm{eff}\left(r_{1,2}\right)$ as a function of the inter-particle center-to-center distance therefore reads:

$$U_\mathrm{eff} = U_\mathrm{mag} + U_\mathrm{LvdW} + U_\mathrm{si} \tag{7.12}$$

Here, U_mag, U_LvdW and U_si are the magnetic [88], the London-van der Waals [149] and the solvation interaction [148, 150, 151] respectively. The former interaction is anisotropic, whereas the latter two interactions are isotropic. Substituting values for all required

Table 7.3: Pair-Interaction Potentials

Disp.	U_{mag} [a] $k_B\,\mathrm{T}$	U_{LvdW} [b] $k_B\,\mathrm{T}$	U_{eff} [c] $k_B\,\mathrm{T}$	Δ [d] Å
A	-0.04	-0.05	-0.02	0.0
B	-0.41	-0.20	-0.26	0.1
C	-0.60	-0.33	-0.44	0.3
D	-0.65	-0.37	-0.49	0.3
E	-3.55	-0.94	-2.92	3.5

[a] Magnetic dipole interaction for a close contact head-to-tail configuration (Figure 7.7, Appendix B).

[b] London-van der Waals interaction for two contacting magnetite spheres (Figure 7.7, Appendix C).

[c] Minimum of the pair-interaction potential (Figure 7.8, eq 7.12).

[d] Potential well width Δ obtained via eq 7.20 substituting $\epsilon = U_{\mathrm{eff}}$ and $\lambda = -U_{\mathrm{eff}}/2$.

parameters in eq 7.12 obtained from experiments and handbooks [74, 140] yields the pair-interaction potential (Figure 7.8) for particles A to E.

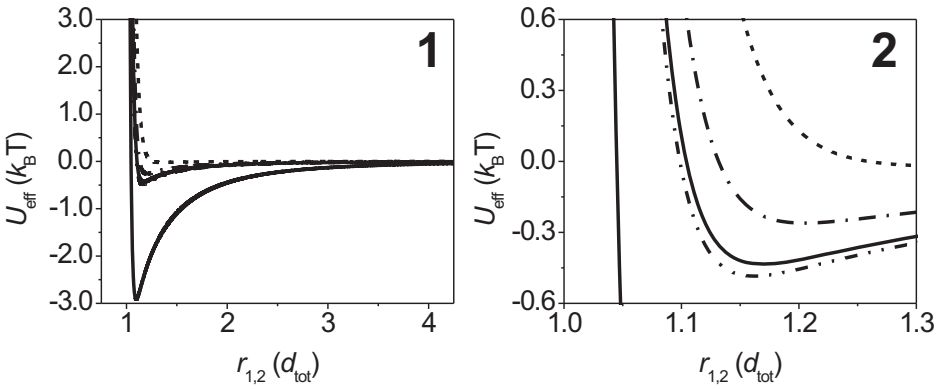

Figure 7.8: Total pair-interaction potential (eq 7.12) as a function of the inter-particle center-to-center distance $r_{1,2}$ in total particle diameters d_{tot} for dispersion A (----), B (- · -), C (——), D (- · ·) and E (——) particles with aligned dipole moments as shown in Figure 7.7. Graph 1 is the full interaction potential and graph 2 is a zoom-in on the potential well region. See Appendices B to E for details on the magnetic, London-van der Waals and the solvation interaction potentials that contribute to the total pair-interaction potential shown here.

7.4.2. Batchelor Coefficients

In what follows, the three calculations [88,109] and chapter 6 for Batchelor coefficients (K_s) for attractive spherical colloids are briefly discussed and compared to results from our SV experiments.

7.4.3. Magnetic Potential

According to Dhont [88] the concentration dependent sedimentation coefficient for weakly magnetic colloidal spheres, i.e. magnetic interactions up to $\lambda \approx 2$, reads:

$$\frac{\langle s \rangle}{s^\circ} = 1 - \left(6.55 - 0.97\,\lambda^2\right)\phi_{\mathrm{tot}} + O\left(\phi_{\mathrm{tot}}^2\right) \tag{7.13}$$

assuming that the spheres are torque-free (freely rotating dipoles, i.e. Néel relaxation). Eq 7.13 is based on a perturbative expansion of the hard-sphere pair-correlation function, to which a weak, orientationally averaged dipolar contribution is added, as explained in more detail in ref. [88] and chapter 6. In eq 7.13, the term multiplying ϕ_{tot} is K_s in eq 7.8 with the dipolar coupling parameter λ:

$$\lambda = \frac{\mu_{\mathrm{mag}}^2 \mu_\circ}{32\pi k_{\mathrm{B}} \mathrm{T} a_{\mathrm{tot}}^3} \tag{7.14}$$

In chapter 6 we calculate the next λ-dependent term with the result:

$$K_s = -6.44 + \lambda^2 + \frac{6}{125}\lambda^4 \tag{7.15}$$

Only for $\lambda \gtrsim 2$, the λ^4-term in eq 7.15 starts to contribute significantly, confirming numerical calculations [88] showing that eq 7.13 is indeed accurate up to $\lambda \approx 2$. Since $\lambda \approx 1.78$ for dispersion E is the highest value for λ in our experiments, one would expect that eq 7.13 holds for all particle sizes studied here. Nevertheless, even for $\lambda \lesssim 2$ the concentration dependence coefficient from eq 7.13 does not change sign and, consequently, according to eq 7.13 the sedimentation velocity for all dispersions A-E should decrease with concentration. Inclusion of λ^4-term from eq 7.15 does not change this prediction. If additional terms in the λ-expansion in eq 7.13 do not explain the discrepancy with our experiments in Figure 7.5, then we should look for another assumption underlying eq 7.13 that is not justified for our magnetite colloids. Very likely this is the assumption that the magnetic particles are torque-free, i.e. the assumption that the magnetic moments rotate fast and freely such that an orientationally averaged pdf can be substituted in the terms that appear in the formula for the Batchelor coefficient [88] and chapter 6. The Néel relaxation time $\tau_{\mathrm{Néel}}$ is given by:

$$\tau_{\mathrm{Néel}} \sim \frac{1}{2\pi f_{\mathrm{N}}^\circ} \exp\left(\frac{K_{\mathrm{ac}} V_{\mathrm{mag}}}{k_{\mathrm{B}}\,\mathrm{T}}\right) \tag{7.16}$$

where V_{mag} is the magnetic particle volume. Here we use a characteristic frequency [129] of $f_{\mathrm{N}}^\circ = 10^9\,\mathrm{Hz}$ and an anisotropy constant [152] of $K_{\mathrm{ac}} = 41\,\mathrm{kJ\,m^{-3}}$ for magnetite. At first sight this formula implies that the assumption of freely rotating dipoles always holds for sufficiently small particles. However, the Néel relaxation time should be compared to the lifetime $\tau_{\mathrm{D\text{-}L}}$ of a dimer (chapter 6):

$$\tau_{\mathrm{D\text{-}L}} \sim \frac{3a_{\mathrm{tot}}^3 \pi \eta_{\mathrm{s}}}{k_{\mathrm{B}}\,\mathrm{T}} \exp\left(-U_{\mathrm{eff}}\right) \tag{7.17}$$

For eqs 7.16 and 7.17 we assume that $a_{\text{tot}} = a_{\text{mag}}$. So what matters is the ratio $\tau_{\text{D-L}}/\tau_{\text{Néel}}$, signaling whether or not dipole orientations are fixed during the lifetime of a doublet. Figure 7.9 shows this ratio as a function of particle size. Note that in the limit of point particles $\tau_{\text{D-L}}/\tau_{\text{Néel}} \sim 0$ because the lifetime of a doublet vanishes. For increasing larger diameters, the doublet lifetime increases slower than the Néel relaxation time, thus the time-ratio also approaches zero for sufficiently large particles. The plot in Figure 7.9 is quite sensitive to the input parameters, but nevertheless illustrates the possibility that the assumption of torque-free particles may not hold for the magnetite dispersions. This implies that the interaction anisotropy has to be included in the calculation of the Batchelor coefficient from the start [88]. This calculation, to our knowledge, has not been addressed yet.

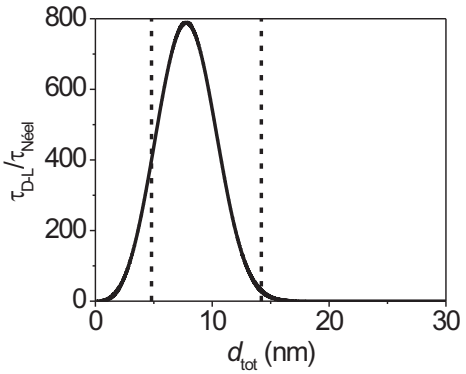

Figure 7.9: Ratio of the doublet lifetime and Néel relaxation time as a function of the particle diameter for magnetite particles (——) for which $a_{\text{tot}} = a_{\text{mag}}$. The minimum and maximum iron oxide core diameters studied here are indicated by the vertical dashed lines (- - -).

7.4.4. Square-Well Potential

Jansen *et al.* [109] investigated the sedimentation velocity of colloids interacting via an attractive square-well potential. Their equation for the reduced sedimentation coefficient in terms of the particle (sphere) volume fraction reads [108, 109]:

$$\frac{\langle s \rangle}{s^{\circ}} = 1 - \left(6.55 - 0.44\,\alpha_{\text{swp}}\right)\phi_{\text{tot}} + O\left(\phi_{\text{tot}}^2\right) \tag{7.18}$$

The parameter α_{swp} is defined by:

$$\alpha_{\text{swp}} = 8\left(e^{-\epsilon} - 1\right)\left[\left(1 + \frac{\Delta}{d_{\text{tot}}}\right)^3 - 1\right] \tag{7.19}$$

Here, ϵ and Δ are the potential well depth and width respectively (Table 7.3). If we take $\epsilon = U_{\text{eff}}$, then Δ can be obtained via:

$$\epsilon = -\ln\left[1 + \frac{\lambda^3}{3\left(1+\frac{\Delta}{d_{\text{tot}}}\right)^3 - 3}\right] \tag{7.20}$$

as further explained in the Appendix of chapter 6.

Clearly, the predictions from eq 7.18 for K_s are far above of what we have observed for dispersion B to E particles (Table 7.2); i.e. the predicted sedimentation rates with concentration all decrease and does not even change sign going from dispersion A to E. Nevertheless, this theory predicts a slightly more pronounced effect of inter-particle attractions exceeding $-0.5\,k_{\text{B}}\,\text{T}$ compared to eq 7.13.

7.4.5. Monomer-Dimer Association

One way to avoid a perturbation approach as for eq 7.13 and the assumption that the particles interact via an isotropic square-well potential is to model the effect of particle attractions via an association equilibrium (chapter 6). In the low-concentration range studied here this means the reversible monomer-dimer association only, with a sedimentation velocity obtained as an average for a bi-disperse mixture of monomers and noncovalent dimers.

Using equilibrium thermodynamics and considering an anisotropic magnetic interaction, an expression for reversibly monomer-dimer self-associating systems to predict $\langle s \rangle$ depending on concentration and particle attraction was derived in chapter 6. For such an equilibrium the normalized sedimentation coefficient reads:

$$\frac{\langle s \rangle}{s_1^\circ} \approx 1 - (1-\chi)K_2^{\text{c}} c_{\text{tot}} + O\left(c_{\text{tot}}^2\right) \tag{7.21}$$

Here K_2^c is the practical equilibrium constant for dimerization in units of $\text{m}^3\ \text{kg}^{-1}$:

$$K_2^{\text{c}} \approx \frac{1}{\rho_{\text{s}}} \exp\left[-U_{\text{eff}} + \ln\left(\frac{3\rho_{\text{s}}\delta\Delta\omega_K^2}{8\pi^2 a_{\text{tot}}\rho_{\text{p}}}\right)\right] \tag{7.22}$$

an expression discussed in more detail in chapter 6. In eq 7.22 $-U_{\text{eff}}$ is the absolute depth of the potential well, δ is the range of the potential and $\Delta\omega_K$ is the solid angle in square radians for which the attraction occurs. Note that:

$$K_2^x = \frac{x_2}{x_1^2} = \rho_{\text{s}} K_2^{\text{c}} \tag{7.23}$$

is the true thermodynamic equilibrium constant in terms of the monomer and dimer weight fractions, x_1 and x_2 respectively.

Furthermore, χ in eq 7.21 is the ratio of the monomer and dimer sedimentation

Table 7.4: Equilibrium Constants

Disp.	Experiment [a]		Theory [b]
	K_2^c mL mg^{-1}	K_2^x (10^2)	K_2^x
B	0.046	0.96	0.08
C	0.048	1.12	0.09
D	0.051	1.23	0.09
E	0.166	4.86	0.85

[a] Equilibrium constants from experiments via eqs 7.21 and 7.23.

[b] Computed from eqs 7.22 and 7.23.

coefficients at infinite dilution:

$$\chi = \frac{2\, f_1^\circ}{f_2^\circ} = \sqrt[3]{4} \left(\frac{f_2^\circ}{f_{2,\text{sphere}}^\circ} \right)^{-1} \approx 1.50 \tag{7.24}$$

$f_2^\circ / f_{2,\text{sphere}}^\circ$ for a dimer comprised of two touching spheres is according to Garcia de la Torre [123] 1.06. Using eq 7.21 we determined K_2^c from sedimentation velocity experiments (Table 7.4).

Because the entropy change, i.e. the logarithmic term in eq 7.22, is fairly constant, the logarithm of the equilibrium constant K_2^x increases linearly with $-U_{\text{eff}}$. Therefore the validity of equilibrium constants obtained from experiments can be tested (Figure 7.10). The relation of $\ln K_2^x$ and $-U_{\text{eff}}$ indeed appears to be linear with a proportionality constant of 0.6, which is close to the value of 1.0 from eq 7.22. In contrast, a fit of $\ln K_2^x$ vs. $-U_{\text{mag}}$ yields a slope of 0.5, indicating that the attractions calculated from the overall interaction potential (Figure 7.8) are more appropriate here. However, equilibrium constants determined from SV experiments deviate from the prediction from eq 7.22 (Table 7.4), which may indicate that the attractions are actually quite stronger than reported in Table 7.3. Addition of depletion induced attraction to $-U_{\text{eff}}$ does not explain this deviation. On the other hand the logarithmic term in eq 7.22 is uncertain and may be smaller and, consequently, the predicted equilibrium constants are much larger. In addition, it should be noted that the equilibrium constants determined from SV experiments are not very precise. Still, it is surprising that the y-intercept of the two linear fits shown in Figure 7.10 is positive, for reasons that are yet unclear.

Can we validate the experimentally determined equilibrium constants or the dimer and monomer concentrations ratio found here by a comparison to other experiments? An alternative quantity for the equilibrium constant is the fraction γ of monomers present in dimers vs. the total weight concentration, which shows the degree of association (Figure 7.11). In fact, this is just another representation of the data shown in Figure 7.5. The maximum amount of associated monomers (i.e. amount of monomers present in dimers) we observed is approximately 17% (w/w) and conforms well to the

probabilities for the presence of noncovalent dimers, increasing up to 30%, which are reported in ref. [111] for similar magnetite particles. Additionally, it can already be inferred from *in situ* cryo-TEM images that the degree of association for dispersion E particles is appreciable (Figure 7.3).

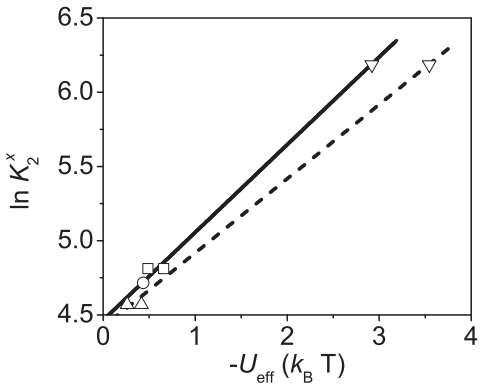

Figure 7.10: Equilibrium constants, K_2^x as in eq 7.23 (Table 7.4), vs. interaction energies for dispersion B (▵), C (○), D (▫) and E (▿) (Table 7.3). The dashed line (----) is a linear fit of $\ln K_2^x$ vs. the maximum magnetic interaction energy and the solid line (——) is a linear fit of $\ln K_2^x$ vs. the minimum of the sum of all interactions (eq 7.12).

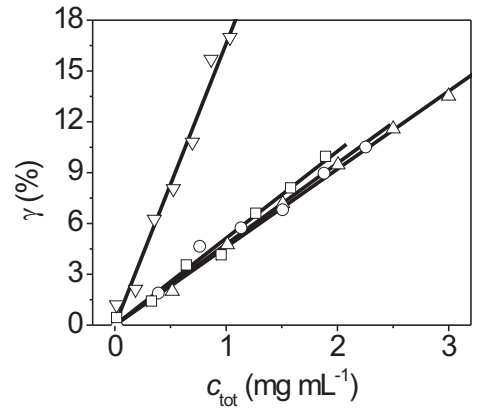

Figure 7.11: Fraction γ of the total number of monomers present in dimers vs. the total particle weight concentration c_{tot} for dispersion B (▵), C (○), D (▫) and E (▿). Solid lines (——) are linear constrained fits.

7.5. Conclusions

We have shown that well-defined synthetic magnetite particles, prepared following a seeded growth synthesis, are very suitable for a systematic study of the sedimentation

velocity as a function of concentration and magnetic dipole moment. Analytical ultracentrifugation appears to be suited for studying correlations in dipolar fluids and allows to asses subtle differences in magnetic inter-particle attractions.

Dipolar attractions have a pronounced effect on the concentration dependent sedimentation velocity. For small magnetic dipole moments, the sedimentation velocity still decreases with increasing concentration. The concentration dependence coefficient K_s rapidly changes sign with increasing magnetic dipole moment. This positive concentration dependence is also manifested in the sedimentation coefficient distributions that shift towards lower s-values upon dilution. In contrast to the self-sharpening of sedimentation boundaries for charged colloids, the opposed effect of boundary broadening due to dipole-dipole attraction and self-association is confirmed by the enhanced vHW analysis and is evident from our study.

Perturbative calculations (ref. [88] and chapter 6) for weakly magnetic spheres with an orientationally averaged pair-distribution function predict a much weaker concentration dependence for the sedimentation velocity than observed in our experiments. We argue that, for a theoretical description of sedimenting magnetic particles as in our study, the interaction anisotropy should be incorporated into the hydrodynamics from the start; a challenge which has not been addressed yet.

To model the effect of significant dipolar attractions in a non-perturbative manner, we have calculated the average sedimentation velocity depending on the total concentration for an equilibrium mixture of monomers and dimers. This model explains the positive concentration dependence of the sedimentation velocity with increasing particle dipole moment in terms of a dimerization equilibrium constant.

Acknowledgement

Mark Klokkenburg made an appreciable contribution to this work. Henk N.W. Lekkerkerker, Willem K. Kegel, Andrei V. Petukhov, Cornelis (Kees) G. de Kruif, Jan Groenewold, S. Martijn Oversteegen and Gert Jan Vroege are thanked for helpful discussions. Chantal Vonk is thanked for recording TEM images at the Electron Microscopy Utrecht University (EMU).

Appendix A: Solutions of Oleic Acid and Decalin

Apparent sedimentation coefficients must be corrected for solution viscosity and density variations since the free oleic acid concentration changes upon dilution of magnetite colloids that are sterically stabilized by reversibly adsorbed oleic acid. Three parameters must be known, namely: (1) the free oleic acid concentration, (2) the density- and (3) the viscosity variations with oleic acid concentration. In what follows, each determination is addressed.

Extinction coefficients for oleic acid in a mixture of *cis-trans*-decahydronaphtalene (decalin), $C_{18}H_{34}O_2$ and $C_{10}H_{18}$ respectively, were obtained from OD recordings for a dilution series with oleic acid concentrations in the range of 5-50 mM. These extinction coefficients are required to determine the free oleic acid concentration (see Figure A-7.1) after finishing a SV run. The oleic acid in decalin extinction coefficients determined with a Varian Cary 1E UV-Visible Spectrophotometer agree well with the values found using a Beckman Coulter^{TM} Optima^{TM} XL-A AUC (Table A-7.1 and A-7.2).

Table A-7.1: Spectrophotometer

λ [b]	ϵ_λ [c]	R^2 [d]
nm	OD_λ cm^{-1} mM^{-1}	
228	0.02296 ± 0.00007	0.9998
229	0.02146 ± 0.00006	0.9998
230	0.02005 ± 0.00006	0.9998

[a] Varian Cary 1E UV-Vis.
[b] Wavelengths.
[c] Oleic acid in decalin extinction coefficients from a linear constrained fit.
[d] Correlation coefficient.

Table A-7.2: AUC

λ [b]	ϵ_λ [c]	R^2 [d]
nm	OD_λ cm^{-1} mM^{-1}	
228	0.02220 ± 0.00018	0.9982
229	0.02122 ± 0.00024	0.9965
230	0.01932 ± 0.00027	0.9947

[a] Beckman Coulter^{TM} Optima^{TM} XL-A.
[b] Wavelengths.
[c] Oleic acid in decalin extinction coefficients from a linear constrained fit.
[d] Correlation coefficient.

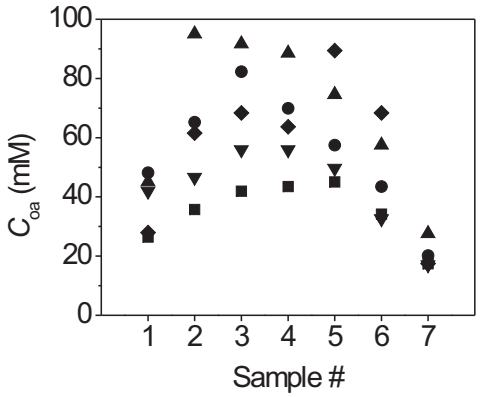

Figure A-7.1: Free oleic acid concentrations in dispersion A (♦), B (▲), C (●), D (■) and E (▼) samples, determined 14 hours after the SV experiments were finished. Magnetite concentrations decrease with increasing sample number. Note the increase and subsequent decrease of the free oleic acid concentration upon dilution, indicating that oleic acid reversibly adsorbs onto the surface of magnetite particles.

The variations of the viscosity and density with oleic acid concentration was determined, using an Ubbelohde capillary viscometer (capillary 0a) and Anton Paar DMA 5000 Density Meter respectively, to calculate the correction factor with which the apparent sedimentation coefficients should be multiplied (using eq 7.5) to correct for solution

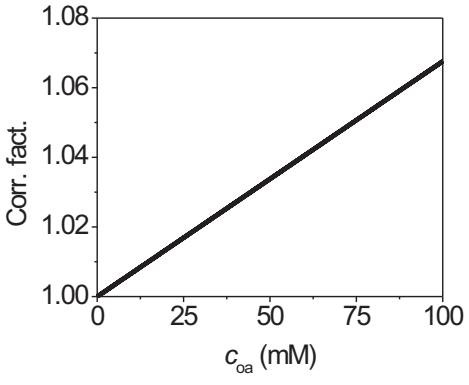

Figure A-7.2: Correction factors (eq 7.5) calculated from the viscosity and density variations with oleic acid concentration. Correction factors were used to correct the apparent sedimentation coefficients obtained from SM and vHW analyses to determine the $s_{20,d}$ values.

viscosity and density. The change in density with increasing oleic acid concentration is almost negligible (Table A-7.3) compared to the change in viscosity with increasing oleic acid concentration (Table A-7.4). Nevertheless, both the variations in density and viscosity were computed to a correction factor as a function of the free oleic acid concentration (Figure A-7.2).

Table A-7.3: Density Fit Results

a [a]	b [a]	R^2 [b]
g cm^{-3}	g cm^{-3} mM^{-1}	
0.879830	$1.29 \cdot 10^{-6}$	0.9857

[a] Fit parameters in $y = a + b\,c_{oa}$, in which c_{oa} is the oleic acid in decalin concentration.
[b] Correlation coefficient.

Table A-7.4: Viscosity Fit Results

a [a]	b [a]	R^2 [b]
mPa s	mPa s mM^{-1}	
2.52429	0.00169	0.9988

[a] Fit parameters in $y = a + b\,c_{oa}$, in which c_{oa} is the oleic acid in decalin concentration.
[b] Correlation coefficient.

Appendix B: Magnetic Dipole Interactions

The dipolar coupling parameter λ in eq 7.14 equals half the maximum magnetic dipole pair-interaction energy and follows from the evaluation of the magnetic dipole pair-interaction potential [88]:

$$U_{\text{mag}} = \frac{\mu_\circ}{4\pi}\left(\frac{\boldsymbol{\mu}_1 \cdot \boldsymbol{\mu}_2}{r^3} - \frac{3\,(\boldsymbol{\mu}_1 \cdot \boldsymbol{r})\,(\boldsymbol{\mu}_2 \cdot \boldsymbol{r})}{r^5}\right) \tag{B-7.1}$$

for two contacting magnetic spheres in a head-to-tail configuration. In eq B-7.1, $\boldsymbol{\mu}_1$ and $\boldsymbol{\mu}_2$ are the magnetic dipole moments of particle 1 and 2, and $\boldsymbol{r}$ is the center-to-center distance between particle 1 and 2. Note that if no other interactions than hard-sphere and magnetic dipole interactions are present, dipolar structure formation

is expected when the dipolar potential energy exceeds thermal fluctuations ($\lambda \gtrsim 2$). For two particles with aligned magnetic dipoles in a head-to-tail configuration (Figure 7.7), eq B-7.1 reduces to an expression of scalars only:

$$U_{\mathrm{mag}}\left(r_{1,2}\right) = -\frac{\mu_{\mathrm{mag}}^2 \mu_\circ}{2\pi k_{\mathrm{B}}\mathrm{T}} \frac{1}{\left(r_{1,2}\right)^3} \tag{B-7.2}$$

describing the magnetic potential (see Figure B-7.1) energy as a function of the inter-particle distance $r_{1,2} \geqslant d_{\mathrm{tot}}$, with $d_{\mathrm{tot}} = 2a_{\mathrm{tot}}$ as in Figure 7.1.

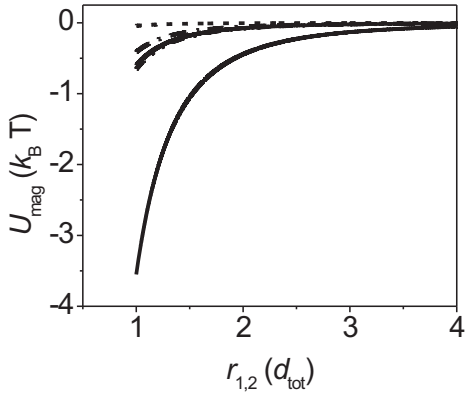

Figure B-7.1: The magnetic interaction energy U_{mag} in $k_{\mathrm{B}}\mathrm{T}$ as a function of the inter-particle center-to-center distance $r_{1,2}$ in terms of the total particle diameter d_{tot} for dispersion A (----), B (– · –), C (——), D (– · ·) and E (——) particles (eq B-7.2).

Appendix C: London-van der Waals Interactions

For two identical magnetite spheres, having an iron oxide core diameter $d_{\mathrm{core}} = 2\ a_{\mathrm{core}}$ as in Figure 7.1, at an inter-particle distance $r_{1,2} \geqslant d_{\mathrm{tot}}$ the London-van der Waals interaction is [146, 148, 149]:

$$U_{\mathrm{LvdW}}\left(r_{1,2}\right) = -\frac{A}{12}\Gamma \tag{C-7.1}$$

with:

$$\Gamma = \frac{1}{\Omega^2 - 1} + \frac{1}{\Omega^2} + 2\ln\left(\frac{\Omega^2 - 1}{\Omega^2}\right) \tag{C-7.2}$$

In eqs C-7.1 and C-7.2, A is the Hamaker constant and the parameter $\Omega = r_{1,2}/d_{\mathrm{core}}$. The non-retarded Hamaker constant for two macroscopic equal phases across a medium can be approximated by [148]:

$$A = \frac{3}{4}k_{\mathrm{B}}\mathrm{T}\left(\frac{\epsilon_1 - \epsilon_3}{\epsilon_1 + \epsilon_3}\right)^2 + \frac{3h\nu_e}{16\sqrt{2}} \frac{\left(n_1^2 - n_3^2\right)^2}{\left(n_1^2 + n_3^2\right)^{3/2}} \tag{C-7.3}$$

The largest contribution to the Hamaker constant in eq C-7.3 comes from the refractive index difference. Since the refractive index of oleic acid adsorbed onto the surface of magnetite particles is approximately equal to the refractive index of decalin, we discard the oleic acid and replace it with solvent. This assumption allows a simple calculation of the Hamaker constant. Substituting in eq C-7.3 the Planck constant $h = 6.62607 \cdot 10^{-34}\,\mathrm{J\,s}$, an absorption frequency $\nu_e = 3 \cdot 10^{15}\,\mathrm{s}^{-1}$ [148], dielectric constants $\epsilon_1 = 20$ and $\epsilon_3 = 2.2$, and refractive indices $n_1 = 2.42$ and $n_3 = 1.474$ [74,140] for magnetite and *cis-trans*-decahydronaphtalene respectively, yields $A = 15.92 \cdot 10^{-20}\,\mathrm{J}$. Note that the London-van der Waals interaction energy at close contact for dispersions A-E particles (Figure C-7.1) does not diverge because the iron oxide cores are prevented from touching each other by the adsorbed oleic acid layer. The London-van der Waals interaction energy is much shorter ranged compared to the magnetic dipole-dipole interaction (Figure B-7.1).

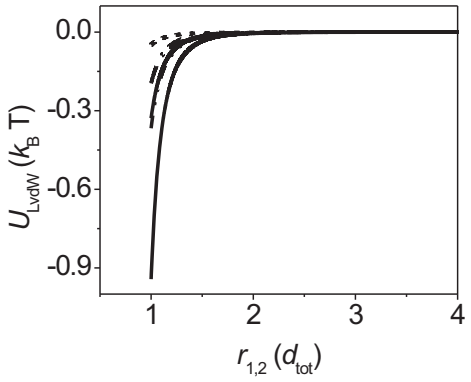

Figure C-7.1: The London-van der Waals interaction U_{LvdW} in $k_{\mathrm{B}}\mathrm{T}$ as a function of the inter-particle center-to-center distance d_{p} in terms of the total particle diameter d_{tot} for dispersion A (----), B (– – –), C (——), D (– · ·) and E (——) particles (eq C-7.1).

Appendix D: Depletion Induced Interactions

The dispersions studied here are at least three component systems containing colloids dispersed in a mixture of solvent and oleic acid. This composition may result in depletion induced attraction. We estimate the depletion attraction via:

$$\frac{U_{\mathrm{di}}}{\Pi} = -\frac{4}{3}\pi\sigma_{\mathrm{di}}^3\left[1 - \frac{3}{4}\frac{r_{1,2}}{\sigma_{\mathrm{di}}} + \frac{1}{16}\left(\frac{r_{1,2}}{\sigma_{\mathrm{di}}}\right)^3\right] \tag{D-7.1}$$

where $\Pi = c_{\mathrm{oa}}\,R\,\mathrm{T}$ is the osmotic pressure with c_{oa} the free oleic acid concentration in mM and R the gas constant (8.3145 J K^{-1} mol^{-1}) [74], $r_{1,2}$ is the center-to-center distance and σ_{di} is the radius of the coated magnetite particle including the shell from which the free oleic acid is excluded. Computing Π from the average free oleic acid

concentration (52 mM), $r_{1,2} = a_{\mathrm{tot}}$ from the TEM radius (Table 7.1) and the 2 nm oleic acid layer and assuming that $\sigma_{\mathrm{di}} = a_{\mathrm{tot}} + 1.0\,\mathrm{nm}$, the maximum depletion induced attraction for dispersion B to E particles varies from -1.27 to -1.92 $k_{\mathrm{B}}\,\mathrm{T}$. However, the free oleic acid may lower the osmotic pressure significantly by associating into dimers [153, 154] or even micelles, since the critical micelle concentration in hexane is approximately 12 mM [155]. Dimer or micelle formation decreases the depletion attraction drastically to values way above -1.0 $k_{\mathrm{B}}\,\mathrm{T}$. The strength of the depletion induced attraction is negligible and is therefore not taken into account in the overall pair-interaction potential.

Appendix E: Steric and Solvation Interactions

The steric repulsion arising from the entanglement of oleic acid molecules when two magnetite particles are separated by a distance $d_{\mathrm{core}} < r_{1,2} < d_{\mathrm{tot}}$ results in a significant decrease in entropy that is not balanced by an enthalpy contribution since decahydronaphtalene is a good solvent for oleic acid. Therefore, the sum of interaction potentials should contain a hard-sphere pair-interaction potential with at close contact $U_{\mathrm{tot}} = \infty$ at $r_{1,2} = d_{\mathrm{tot}}$. Moreover, from sedimentation velocity experiments, we have evidence for the presence of an additional repulsive interaction. Dispersion A particles settle at a slower rate than expected for hard-spheres; i.e. $K_s = 12$ instead of $K_s = 6.55$ in eq 7.8. Using the slope K_s obtained from experiment and assuming that the dispersion A particles are monodisperse and perfect spheres, an effective volume fraction can be introduced to force the concentration dependent sedimentation of dispersion A to follow that of hard-spheres. From the effective volume fraction, the accompanied increase in particle radius Δa can be calculated via:

$$\Delta a = a_{\mathrm{h}} \left(\sqrt[3]{\frac{K_s}{6.55}} - 1 \right) \tag{E-7.1}$$

a_{h} is the hydrodynamic radius obtained from the sedimentation coefficient at infinite dilution, s°. Substitution of $K_s \approx 12$ in eq E-7.1 yields $\Delta a \approx 1\,\mathrm{nm}$.

Rather than introducing a hard-sphere pair-interaction potential for which $U_{\mathrm{rep}} = \infty$ for $r_{1,2} \leqslant d_{\mathrm{tot}} + 2\Delta a$ and $U_{\mathrm{rep}} = 0$ for $r_{1,2} > d_{\mathrm{tot}} + 2\Delta a$, a more elegant and physically more relevant interaction can be used. The repulsive interaction term U_{si} in eq 7.12 must be very short ranged and therefore possibly results from forces between the adsorbing particle surfaces; i.e. a solvation force arising from the disjoining pressure when two surfactant-covered surfaces approach each other with in between liquid layers of solvent in which the particles are dispersed [150]. Liquid layers of solvent molecules are likely to be present since decahydronaphtalene is a good solvent for oleic acid.

Generally, the repulsive solvation interaction, U_{si}, has the form [148, 151]:

$$U_{\mathrm{si}} = u_{\circ}\, e^{-\frac{r_{1,2}-d_{\mathrm{tot}}}{\lambda_{\circ}}} \tag{E-7.2}$$

$\lambda_{\circ}$ is the decay length and $u_{\circ}$ a constant that depends on the solvation of the surfaces. Small decay lengths are usually associated with large values for $u_{\circ}$ [148]. Here, we expect a very small decay length because decalin is a highly non-polar solvent and consequently there is almost no ordering or structure formation of solvent molecules, except in and in the vicinity of the oleic acid layer in which solvent molecules penetrate. Substituting the width that happens to be approximately half the length of a decahydronaphtalene molecule of 308 pm for $\lambda_{\circ}$ and 50 k_{B} T for $u_{\circ}$, generates a short-ranged repulsion, needed to accomplish total or overall pair-interaction potentials for dispersions A-E particles with minima that are close to the interaction energies $U_{\mathrm{att}} = U_{\mathrm{mag}} + U_{\mathrm{LvdW}}$ evaluated at $r_{1,2} = d_{\mathrm{tot}} + 2\Delta a$, as it should be.

Part 4

Repulsive Colloids

8

Salt- and Concentration Dependent Sedimentation Velocity of Rigid Colloidal Rods

Abstract

A study of the effect of ionic strength on the concentration dependent sedimentation velocity (SV) for a dispersion of rigid boehmite-silica rods is presented. Experimental results are compared to predictions from theory for hard rods using input parameters obtained from transmission electron microscopy and static light scattering. Addition of salt lowers the sedimentation velocity concentration dependence, which is eventually similar to the prediction from theory for uncharged rigid rods. Above 50 mM NaCl the rods gel into a fine network that tends to settle in the earth's gravitational field. Furthermore, we compare SV absorbance and interference optical data and discuss which optics is the most suitable for boehmite-silica dispersions. We also report a convenient method to determine the specific particle volume of core-shell colloids from SV interference optical data.

8.1. Introduction

The sedimentation behavior of colloidal spheres as a function of particle weight concentration has been widely studied and there is extensive literature concerning this topic (for example refs. [106–108, 156–158]). In contrast, information on the concentration dependent sedimentation of rigid rods is very limited to date [106]. The majority of studies on the sedimentation velocity (SV) of elongated or rod-like particles is restricted to bio-organic macromolecules [3,4,17,18,159,160] that are usually (semi)-flexible, i.e. a contour length that exceeds the persistence length. This finite flexibility of bio-organic rods complicates the modeling compared to rigid rods.

Generally, colloidal rods dispersed in an aqueous medium are charged. Since a theory [161] is available that predicts the concentration dependence for hard rigid rods, it is interesting to investigate the effect of ionic strength on the concentration dependent sedimentation velocity for charged rods. Our aim here is to, firstly, thoroughly characterize a boehmite-silica rod dispersion using a combination of techniques and, secondly, to study the concentration dependent sedimentation rate of these rigid, charged rods as a function of added salt. Experimental results are compared to theory [161] that predicts the concentration dependent sedimentation velocity of hard rigid rods.

In contrast to monitoring the sedimentation velocity in the earth's gravitational field with a cathetometer [107], analytical ultracentrifugation offers a higher precision and accuracy [162] and provides more information that is, among others, contained in the shape of the sedimentation velocity boundaries [1]. The sedimentation velocity can be monitored with the commercially available interference and absorbance optical systems. We compare SV data from these two complementary optical systems to highlight their capabilities, advantages, how they can serve as a useful tool for the study of colloidal dispersions in general and, in particular, for the dispersion employed here. We address what sort of information can be obtained from these SV optical data.

8.2. Theory

For dilute dispersion, the average sedimentation coefficient $\left\langle s_{20,\mathrm{w}} \right\rangle$ for monodisperse particles in water at 20 °C, which have only hydrodynamic interactions and excluded volume effects, i.e. hard particles that are e.g. uncharged, as a function of the particle volume fraction ϕ_{tot} can be approximated by:

$$\frac{\left\langle s_{20,\mathrm{w}} \right\rangle}{s^{\circ}_{20,\mathrm{w}}} = 1 - K_s \phi_{\mathrm{tot}} + O\left(\phi^2_{\mathrm{tot}}\right) \tag{8.1}$$

with $s^{\circ}_{20,\mathrm{w}}$ the sedimentation coefficient at infinite dilution. $s^{\circ}_{20,\mathrm{w}}$ and $s_{20,\mathrm{w}}$ are hereafter denoted as s° and s respectively. The concentration dependence coefficient K_s can be

determined from experiments via:

$$K_s = \frac{k_c}{s^\circ \overline{\nu}_\mathrm{p}} \tag{8.2}$$

substituting k_c and s° that are obtained from an unconstrained fit, i.e. k_c and s° are fitted, of $\langle s \rangle$ versus the total particle weight concentration, c_tot, with:

$$\langle s \rangle = s^\circ - k_c c_\mathrm{tot} + O\left(c_\mathrm{tot}^2\right) \tag{8.3}$$

The sedimentation coefficient for infinitely diluted rigid cylinders with a molecular weight m_p, aspect ratio $p = L_\mathrm{tot}/D_\mathrm{tot}$ (L_tot and D_tot are, respectively, the total cylinder length and diameter) and a partial specific volume $\overline{\nu}_\mathrm{p}$, dispersed in a medium with viscosity η_s and density ρ_s, is:

$$s^\circ = \frac{m_\mathrm{p}\left(1 - \overline{\nu}_\mathrm{p}\rho_\mathrm{s}\right)}{f^\circ} \tag{8.4}$$

Here, f° is the friction coefficient [163]:

$$f^\circ = 3\pi\eta_\mathrm{s} L_\mathrm{tot}\left(\ln p + \gamma\right)^{-1} \tag{8.5}$$

So for a cylinder with mass-density ρ_tot and mass:

$$m_\mathrm{p} = \frac{\pi D_\mathrm{tot}^2 L_\mathrm{tot}}{4\,\overline{\nu}_\mathrm{p}} \tag{8.6}$$

we find:

$$s^\circ = \frac{D_\mathrm{tot}^2\left(\rho_\mathrm{p} - \rho_\mathrm{s}\right)}{12\,\eta_\mathrm{s}}\left(\ln p + \gamma\right) \tag{8.7}$$

Clearly, the sedimentation coefficient of rigid cylinders at infinite dilution depends only weakly on the aspect ratio and, therefore, on the rod length. The function γ in eqs 8.5 and 8.7, accounts for the so-called end-effect correction and depends on the aspect ratio. For aspect ratios within $2 < p < 30$, the numerical form of γ reads [163]:

$$\gamma = 0.312 + 0.565\,p^{-1} - 0.100\,p^{-2} \tag{8.8}$$

In general, the sedimentation coefficient for pure non-associating solutes decreases with increasing concentration, i.e. $K_s > 0$. The magnitude of K_s strongly depends on the particle geometry and increases from its minimum for spheres to a maximum for highly expanded particle shapes e.g. rigid rods that are long and thin.

Dogic *et al.* [161] reported a calculation of the leading-order concentration dependence. Employing hydrodynamic interaction tensors for rigid rods, treated as strings of spherical beads within a mean-field approximation, valid for dilute dispersions of hard

rigid rods, the result of Dogic *et al.* [161] for K_s as a function of the aspect ratio p reads:

$$K_s = \frac{6.4 + \frac{2}{9}p}{2\ln(p) - \left(\nu_\perp + \nu_\parallel\right)} p, \text{ for } p >> 1 \tag{8.9}$$

with the numerical corrections $\nu_\perp$ and $\nu_\parallel$. For cylindrical rods with $p > 20$, $\nu_\perp$ and $\nu_\parallel$ are -0.84 and 0.21, respectively [164]. Eq 8.9 was found to be in fair agreement with experimental values for filamentous bacteriophage *fd* virus [161] with $p = 130$ and rigid silica rods [14] with p equal to 13 and 24. It is to be expected that the electrical double layer surrounding charged rods enhances K_s since the electric double layer repulsion increases the effective particle volume and consequently the settling particles are fully exposed to the retarding solvent backflow associated with the sedimentation. If this is indeed the case, addition of salt should decrease K_s towards the prediction by eq 8.9. To study the effect of ionic strength on K_s for charged rigid rods, a careful analysis employing a well-characterized rod dispersion is required. In the following section 8.3, the methods and instrumentation employed for the characterization of the boehmite-silica colloidal rod dispersion and the sedimentation velocity experiments are described.

8.3. Materials and Methods

8.3.1. Sample Preparation

The boehmite-silica core-shell rods studied here were prepared by van Bruggen (1995), following the method reported in ref. [165]. We fractionated the product from synthesis by repeated preparative centrifugation (Beckman Coulter^{TM} Avanti^{TM} J-20 XP, J.S.-25 rotor) to purify and isolate the boehmite-silica rods. Sedimented particles were re-dispersed in Milli-Q demiwater pH 5.5. After several preparative centrifugation steps the super-stock dispersion was obtained from which three dilution series, each comprising samples of equidistant particle weight concentrations, with respectively 0, 10 and 50 mM added NaCl, were prepared. The weight concentration of the super-stock solution was determined by evaporating the solvent of 3 x 1 mL super-stock dispersion and weighing the residue using a precision balance (Mettler Toledo AX205 Delta Range).

8.3.2. Particle Characterization

The average total length L_{tot} and total diameter D_{tot} (including the silica layer) of the rods were determined from TEM-images (Philips Tecnai 12 TEM at 120 kV, EMU), Table 8.1 and Figure 8.2. The rod length was also determined from a static light scattering (SLS) experiment using a wavelength at which the sample does not absorb. The natural logarithm of the scattered light intensity (corrected for the filter, sensitivity and gain) versus the squared magnitude of the scattering vector, q^2, was

fitted with [88, 166]:

$$\ln I(q) = \ln I(0) - \frac{R_g^2}{3} q^2, \text{ for } qR_g < 2.5 \tag{8.10}$$

to obtain an average rod length from the radius of gyration, R_g, via [88, 166]:

$$L_{\text{tot}} = \sqrt{12\, R_g^2} \tag{8.11}$$

For a comparison of experimental results to predictions from theory for K_s for hard rigid rods, particle volume fractions were computed from particle weight concentrations using a specific particle volume of 0.41 mL g^{-1}. The specific particle volume was determined from the number average particle dimensions (TEM, 500 particles) and bulk densities [74] for boehmite (3.44 g mL^{-1}) and silica (1.70 g mL^{-1}).

In addition, the specific particle volume was determined independently from bulk densities using the differential (or specific) index of refraction $\partial n/\partial c$. The specific index of refraction was obtained from the total fringe displacement, Y_{tot}, via [25]:

$$Y_{\text{tot}} = \sum \left(c_i \frac{\partial n}{\partial c_i} \right) \frac{l}{\lambda} \tag{8.12}$$

Here, c_i is the concentration of component i, l is the cell path length (12 mm) and λ is the optical wavelength (675 nm). Y_{tot} for the total initial loading concentration, was determined for each sedimentation velocity run by extrapolating the fitted plateau concentrations (fringe displacement) of each sedimentation velocity scan included in the analysis with a polynomial to the time at which the rotor started to accelerate $t = 0$. If the dispersion contains one species only, $\partial n/\partial c$ in eq 8.12 can be taken out of the summation and the specific refractive index can be calculated by substitution of Y_{tot}, $\sum c_i = c_{\text{tot}}$, l and λ into eq 8.12.

Subsequently, the specific particle volume can be computed from $\partial n/\partial c$ by substitution of the particle (n_{p}) and solvent (n_{s}, increases with the added salt concentration) refractive indices in:

$$\frac{\partial n}{\partial c} = \frac{n_{\text{p}} - n_{\text{s}}}{\rho_{\text{p}}} \tag{8.13}$$

For core-shell particles, the refractive index, required to determine the specific particle volume via eq 8.13, can be calculated from a volume weighted particle refractive index:

$$n_{\text{p}} = n_{\text{boehmite}} \phi_{\text{core}} + n_{\text{silica}} \phi_{\text{shell}} \tag{8.14}$$

where $n_{\text{boehmite}} = 1.65$ and $n_{\text{silica}} = 1.45$ are the refractive indices [74] of boehmite and silica, ϕ_{core} and ϕ_{shell} are the average volume fractions of, respectively, the boehmite-core and silica-shell.

The results obtained from the two methods to determine the specific particle volume are discussed in section 8.4.1.

8.3.3. Sedimentation Velocity

Sedimentation velocity experiments were performed using an analytical ultracentrifuge (Beckman Coulter™ Optima™ XL-I AUC, standard 12 mm epon-charcoal filled double sector centerpieces with sapphire or quartz windows in an An-60 Ti rotor) equipped with an interference and absorbance optical system. For comparison, radial scans were acquired with both optical systems. The analysis of the effect of the ionic strength on the concentration dependent sedimentation velocity was done using the sedimentation velocity interference optical data.

Sedimentation velocity scans were recorded at 6,500 rpm and 20.0 ± 0.1 °C during approximately 2.5 h, to obtain for each sample at least 120 scans suited for analysis. Sedimentation coefficients, corrected for solvent density and viscosity variations due to the added salt and temperature variation, were determined from the differential sedimentation coefficient distributions maxima, obtained from the enhanced van Holde-Weischet (vHW) analysis [43, 44] implemented in *UltraScan* [23].

Furthermore we assume the uncertainty of sedimentation coefficients to be ± 1.47% [162], accounting for the error introduced by (1) algorithms used for deriving s values from data (± 0.30%), (2) temperature of the rotor (± 0.80%) and (3) precision of cell alignment in the rotor and of the radial values used (± 0.37%). The uncertainty in concentration was calculated from the errors as reported in the product specifications for the Gilson Pipetman® P pipettes and the Mettler Toledo AX205 Delta Range precision balance and using standard error propagation relations.

8.4. Results and Discussion

8.4.1. Dispersion Characterization

It is evident from SV interference optical data (Figure 8.1) that the dispersion as obtained from the synthesis [165] contains 'low molecular weight' species that are not detected by the absorbance optics. A careful study of the concentration dependent sedimentation velocity of the boehmite-silica rods requires removal of this debris that may increase the effective solvent viscosity. The isolation of boehmite-silica rods by repeated preparative centrifugation, is confirmed by interference sedimentation velocity scans (Figure 8.1). Using absorbance optics only, these contaminants would not have been detected. Consequently, the increased viscosity and density that decrease the sedimentation rate species due to the presence of small species, result in the determination of an apparent stronger concentration dependency for the rods [1]. The advantage of the absorbance optics, namely being selective and sensitive, is also its drawback. Therefore, it is recommended to use both optical systems when possible. However, the system must satisfy certain conditions, discussed in section 8.4.2, for both the absorbance and interference optical systems to work properly.

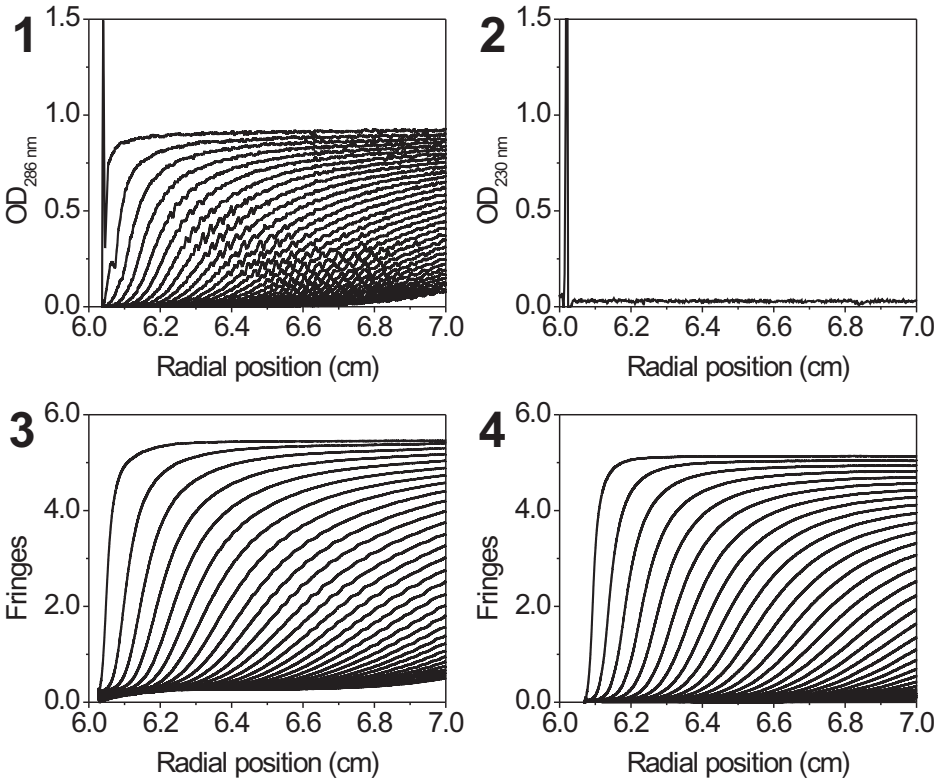

Figure 8.1: Selection of sedimentation velocity scans, see section 8.3.3 for experimental details. Graph 1 (absorbance optics) and 3 (interference optics) show the rod dispersion as-synthesized. The initial loading concentrations c_{tot} of the samples shown in graph 1, 2 and 3 are approximately 3.74 mg mL^{-1} and in graph 4 $c_{\mathrm{tot}} \approx 3.50\,\mathrm{mg\ mL}^{-1}$. Note that the attenuance peak in graph 1 is not the sample meniscus but is part of the sedimentation boundary, in contrast to the peak in graph 2 that represents the air-sample interface. The scans in graphs 1 and 2, the latter was recorded after the SV experiment (all boehmite-silica rods have accumulated at the sector bottom), do not show a significant baseline. The absence of a baseline may lead to an erroneous interpretation, resulting in drawing the (wrong) conclusion that the rod dispersion is pure. 'Low molecular weight' species are clearly detected by the interference optics (see graph 3). The latter 'contaminants' were removed by preparative centrifugation as confirmed by the 'zero-baseline' in graph 4.

Another advantage of using the interference optics when measuring a dilution series is that the (partial) specific particle volume can be obtained from the total fringe displacements with initial loading concentration combined with the refractive indices of particle and solvent. To validate the specific particle volume of 0.40 mL g^{-1} obtained from sedimentation velocity interference optical data ($\partial n/\partial c$ method), we compare it to the specific particle volume of $0.41\,\mathrm{mL\,g}^{-1}$ calculated from TEM particle dimensions combined with bulk densities. The results of these two methods agree very well, ensuring a reliable conversion of particle weight concentration into volume fraction via $\phi_{\mathrm{tot}} = \overline{\nu}_{\mathrm{p}} c_{\mathrm{tot}}$ required for eq 8.1. The small difference between the two experimentally

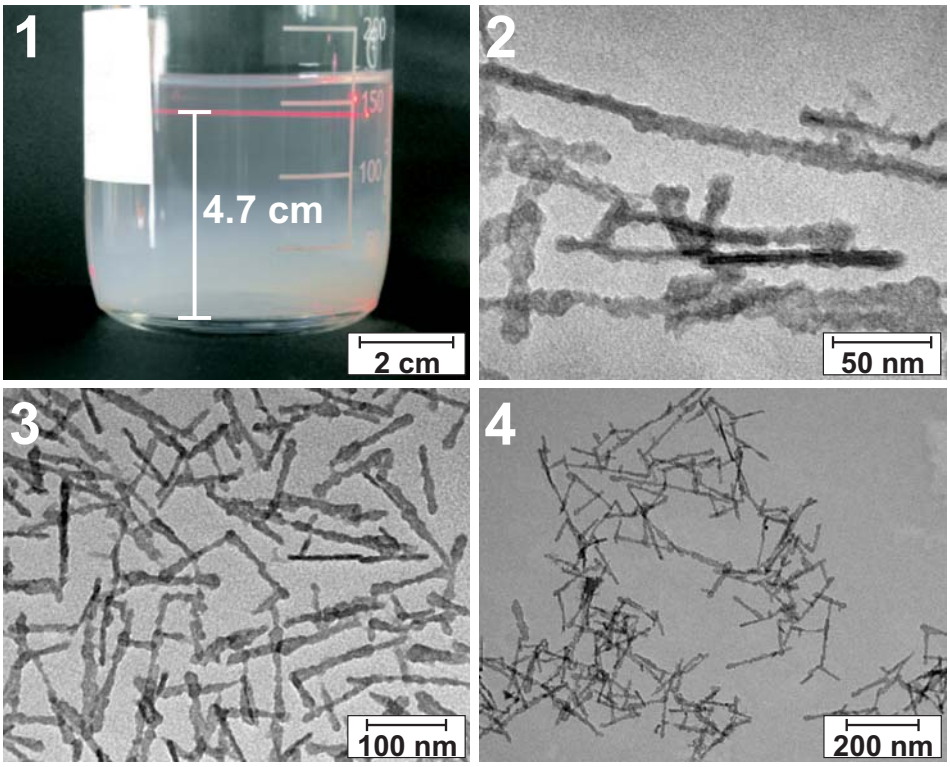

Figure 8.2: Image 1 is a photograph of the sedimentation-diffusion equilibrium distribution of the boehmite-silica stock dispersion as-synthesized. This distribution has been developed over a few years. Presence of boehmite rods in the upper region of the dispersion, i.e. at a height of 4.7 cm, is evident from the scattered laser beam. TEM-images 2, 3 and 4 show that the boehmite-silica core-shell particles, with a silica layer of approximately 2 nm, exhibit size and shape polydispersity.

obtained specific particle volumes may be explained on account of the limited accury and precision of the calculated refractive index of the core-shell rods and the shape and size polydispersity of the rods.

It is evident from TEM micrographs (Figure 8.2 and Table 8.1) that the boehmite-silica core-shell rods employed here exhibit size and shape polydispersity. These TEM-images do not show individual rods (Figure 8.2), which suggests, upon careful visual inspection, that the rods have associated into doublets and triplets. The rods, however, are negatively charged since the pH of the dispersions is approximately 5.5. At this pH the silica shell has negative charges in the form of OH^- groups. Charge-charge interaction has a significant effect on the physical properties of rods dispersed in a medium with a low ionic strength.

The sedimentation-diffusion equilibrium profile developed during long time storage (Figure 8.2) confirms the expectation that the rods are charged. Presence of rods in the upper region of the dispersion column is evident from the scattered light intensity of a laser beam directed through this region. The scattered light is most intens at small

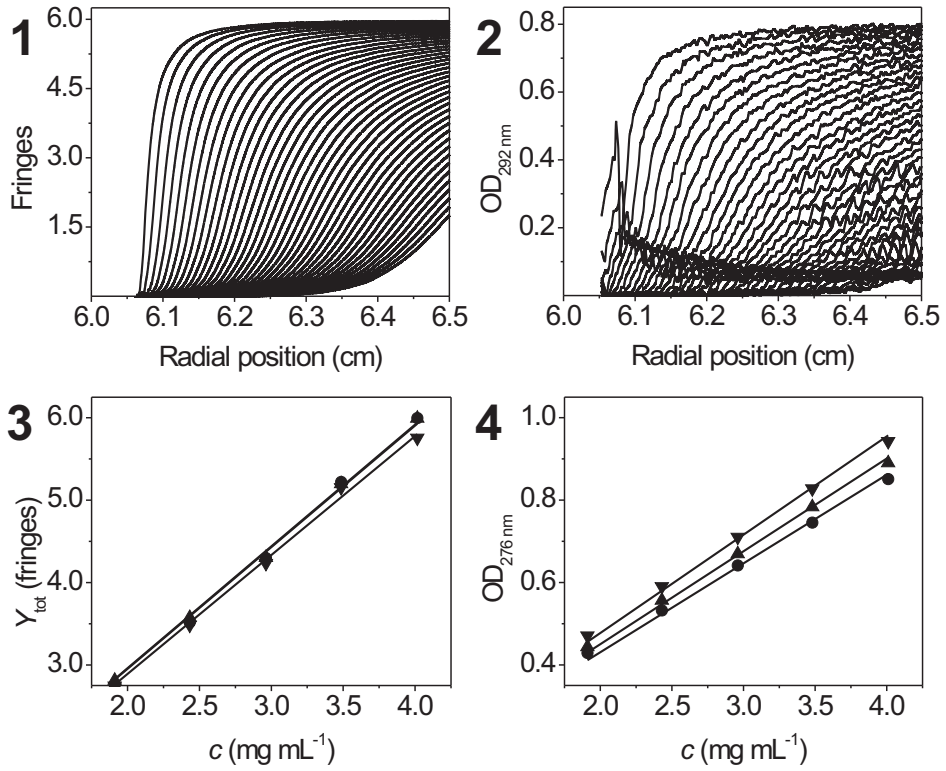

Figure 8.3: Selected sedimentation velocity profiles (40 scans recorded during the early and mid sedimentation velocity run) for a 4.02 mg mL^{-1} sample to which no salt was added, recorded with the interference (graph 1) and the absorbance (graph 2) optical systems, see section 8.3.3 for experimental details. The time between scans in graph 1 is $\approx$ 1 min. and in graph 2 $\approx$ 1 min. and 12 s. A steep concentration gradient, and consequently a steep gradient in refractive index, results in reflection of light as seen in the attenuance scans (graph 2). The peaks due to these steep gradients are equivalent to the well-known meniscus phenomenon. This effect decreases during the time course of the sedimentation velocity run because of diffusion and radial dilution. Graph 3 shows the total fringe displacements at 675 nm, obtained from a polynomial fitting routine implemented in the enhanced vHW analysis [43, 44] (*UltraScan* [23]) for interference sedimentation velocity data (Beckman Coulter™ Optima™ XL-I AUC), as a function of initial loading concentration. The attenuance (OD at 272 nm) vs. weight concentration, recorded with a Varian Cary 1E UV-Visible spectrophotometer (path lenght is 10 mm), is plotted in graph 4. All correlation coefficients of linear constrained fits, shown in graphs 3 and 4 (—, y-intercept $\equiv 0$ at $c = 0$, slope is floated) for 0 (•), 10 (▲) and 50 (▼) mM added NaCl, exceed 0.9998 within the particle and salt concentrations of the boehmite-silica rod dispersions employed here.

angles, indicating that the particles causing this scattering are fairly large. It seems plausible that the intensity of the scattered laser light manifests an inflated [54–56] sedimentation-diffusion (SD) equilibrium distribution. The gravitational length:

$$L_{\mathrm{G}} = \frac{k_{\mathrm{B}}\mathrm{T}}{m_{\mathrm{p}}\left(1 - \overline{\nu}_{\mathrm{p}}\rho_{\mathrm{s}}\right)g} \tag{8.15}$$

Table 8.1: Particle Dimensions [a]

	N_a [b] nm	σ_a [c] nm	σ_r [d] %	p_{TEM} [e]	p_{SLS} [f]
L_{tot} [g]	112.8	26.3	23	9.6	47.4
D_{tot} [g]	11.7	3.0	26		

[a] All quantities were determined including 500 particles.

[b] N_a, number average total length L_{tot} and total width D_{tot} determined from TEM-images.

[c] Absolute standard deviation (TEM).

[d] Relative standard deviation (TEM).

[e] Average aspect ratio from TEM dimensions.

[f] Aspect ratio from the SLS rod length and TEM rod width.

[e,f] The uncertainty in p is approximately 34%.

[g] Total rod length, L_{tot}, and diameter, D_{tot}, including a silica layer of 2 nm.

with g the gravitational acceleration, for rods with a buoyant mass of $4.16 \cdot 10^{-20}$ kg, calculated by substituting a sedimentation coefficient of 1029 S (Table 8.2) and a length and width of, respectively, 112.8 nm and 11.7 nm, Table 8.1, in eq 8.4 combined with 8.5, is 0.99 cm. With this gravitational length and assuming a concentration of 10 mg mL^{-1} at the bottom, the concentration at a height of 4.7 cm would be approximately 0.09 mg mL^{-1}. Additionally, modeling the rods using TEM particle dimensions (Table 8.1) and bulk mass densities, results in a gravitational length of 2.35 cm and a rod concentration of 1.36 mg mL^{-1} at 4.7 cm, using the same boundary condition for the particle weight concentration at the bottom of 10 mg mL^{-1}. For a weight concentration of 0.09 to 1.36 mg mL^{-1}, the scattered light intensity would be much lower than observed. This confirms that particle charge indeed inflates the SD-equilibrium distribution.

Increasing the ionic strength results in screening of particle charges that may result in gel-formation due to decreased inter-particle repulsions. Spontaneous gel formation was observed for dispersions with a 1:1 electrolyte concentration larger than 50 mM. This observation confirms the findings by van Bruggen [167]. The time required for gelation of the boehmite-silica rods is approximately a few days up to a week. Complete settling of the rods in the earth's gravitational field, typically within two days, was not observed. Instead, a sharp solvent-dispersion interface halfway the sample vial remained unchanged over weeks, indicating that a steady state was reached.

8.4.2. Sedimentation Boundaries

Sharp solvent-dispersion interfaces were also observed during the early stage of a sedimentation velocity run in the analytical ultracentrifuge. Sedimentation velocity scans of such interfaces show a steep concentration- and refractive index gradient. Attenuance sedimentation velocity profiles show sharp meniscus like peaks, caused by the

Table 8.2: Sedimentation Velocity [a]

[NaCl] [b] mM	s° [c] S	s° [d] S	k_c [e] S mL mg^{-1}	K_s [e]	K_s [f]	p [g]
0	894 ± 18	433 ± 13	73 ± 6	199 ± 16	16 (11; 21)	78 (74; 82)
10	908 ± 21		32 ± 7	86 ± 18		43 (37; 50)
50	1029 ± 24		28 ± 8	66 ± 19		36 (27; 43)

[a] All sedimentation coefficients were obtained from the enhanced van Holde-Weischet analysis implemented in *UltraScan*.

[b] Added sodium chloride concentration for which the electric double layer thickness $\kappa^{-1} \approx 9.64\,\text{nm}\ (\text{mM}/c)^{-0.5}$ (with c the salt concentration of a 1:1 electrolyte in mM) is, respectively, –, 3.0 and 1.4 nm.

[c] Sedimentation coefficients at infinite dilution obtained from experiments, eq 8.3. Slope and y-intercept are fitted. The uncertainty of s° is $> \pm 1.47\%$ [162].

[d] Theoretical sedimentation coefficient at infinite dilution, calculated with eqs 8.4 and 8.5 and particle dimensions from TEM.

[e] Concentration dependence coefficients, k_s, obtained from a linear unconstrained fit, eq 8.3. K_s was obtained from a linear constrained fit, eq 8.1, i.e. y-intercept = 1 and slope is floated.

[f] Predicted concentration dependence coefficient from eq 8.9. Approximate uncertainty limits of the aspect ratio (Table 8.1) are shown between parentheses.

[g] Effective aspect ratio obtained from experimental K_s values and eq 8.9. Approximate uncertainty limits (Table 8.1) are shown between parentheses.

reflection of light, i.e. bending of the light beam, due to a steep (refractive index) gradient formed by particles that do not absorb at that wavelength, graph 2 in Figure 8.3. In other words, the refractive index gradient bends the light beam that, consequently, misses the opening in the slit assembly. In contrast, recording sedimentation velocity boundaries using the interference optics, which requires a refractive index gradient, yields in this case high quality data as can be seen by comparing graph 1 with graph 2 in Figure 8.3. The attenuance, however, between 229 and 433 nm and the fringe displacements at 675 nm are highly linear, graph 3 and 4 in Figure 8.3.

Extinction coefficients at wavelengths in between 229 nm and 433 nm range from 0.04 to 0.40 OD mL cm^{-1} mg^{-1}. At 675 nm the extinction coefficients of the three dispersions with, respectively, 0, 10 and 50 mM NaCl are very small, i.e. below 0.01 OD mL cm^{-1} mg^{-1}, indicating that the dispersions do not absorb significantly at 675 nm, something which is required for AUC sedimentation interference experiments. The differential fringe displacements for the three dilution series are in between 1.2986 to 1.2104 fringes mL cm^{-1} mg^{-1}. Therefore, recording sedimentation boundaries with the interference optics yield more reliable data due to a much higher signal-to-noise ratio compared to the absorbance optics, which is, in addition, strongly affected by the steep refractive index gradients that result in attenuance peaks that hamper the sedimentation velocity data analysis.

Steep concentration gradients due to boundary self-sharpening are indicative for a

negative concentration dependency of the sedimentation velocity, which is discussed in the next section 8.4.3, because of hydrodynamic interactions and excluded volume effects that are enhanced by repulsive charge interactions.

8.4.3. Sedimentation Velocity

The negative concentration dependency of s for boehmite-silica core-shell rods is evident from the shift of the integral sedimentation coefficient distributions towards larger s values with decreasing concentration, Figure 8.4. In addition, the self-sharpening of sedimentation boundaries for concentrated dispersions is clearly confirmed by the increased width of the (differential) sedimentation coefficient distributions upon dilution. The effect of decreasing concentration on the differential sedimentation coefficient distribution width of the dispersion with 50 mM NaCl is significantly larger in comparison to the dispersions with 0 and 10 mM NaCl, Figure 8.5. For the latter two dispersions, repulsions resulting from charge interactions between particles dominates.

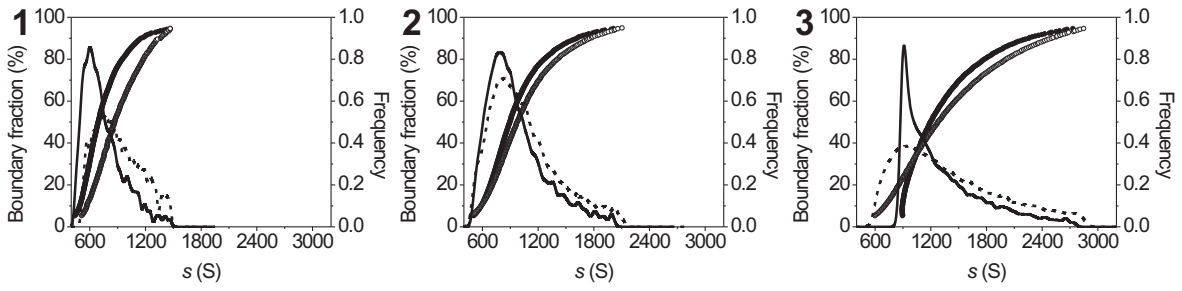

Figure 8.4: Integral G(s), left y-axis (• and ○), and differential, right y-axis (—— and ----), sedimentation coefficient distributions, obtained from an enhanced vHW analysis [43, 44] (*UltraScan* [23]), for the most concentrated (4.02 mg mL^{-1}, • and ——) and diluted (1.91 mg mL^{-1}, ○ and ----) samples of the dispersions with 0 (graph 1), 10 (graph 2) and 50 (graph 3) mM added NaCl.

Addition of 50 mM salt, while keeping the particle concentration at a constant value of 4.02 mg mL^{-1}, results in an a shift of the sedimentation coefficient distribution towards larger s. Whereas addition of 50 mM NaCl and maintaining the particle concentration of 1.91 mg mL^{-1} constant, increases the width of the sedimentation coefficient distribution, Figure 8.5. Adding 50 mM salt and lowering the particle concentration from 4.02 to 1.91 mg mL^{-1} results in an increase of the differential sedimentation coefficient distribution width and a shift of the integral sedimentation coefficient distribution towards larger s.

For all three dispersions, the concentration dependent sedimentation coefficients, corresponding to frequency maxima of the differential sedimentation coefficient distributions, are linear in weight concentration and volume fraction, Figure 8.6.

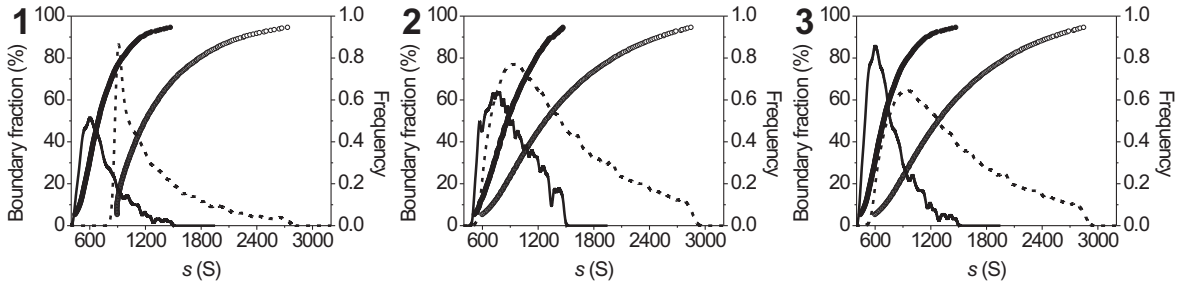

Figure 8.5: Integral G(s), left y-axis (• and ○), and differential, right y-axis (—— and ----), sedimentation coefficient distributions, obtained from an enhanced vHW analysis [43, 44] (*UltraScan* [23]), for the most concentrated (4.02 mg mL^{-1}) and diluted (1.91 mg mL^{-1}) samples of the dispersions with 0 (• and ——) and 50 mM (○ and ----) added NaCl. Graph 1: most concentrated 0 mM and 50 mM NaCl samples, graph 2: most diluted 0 mM and 50 mM NaCl samples and graph 3: most concentrated 0 mM NaCl sample and most diluted 50 mM NaCl sample.

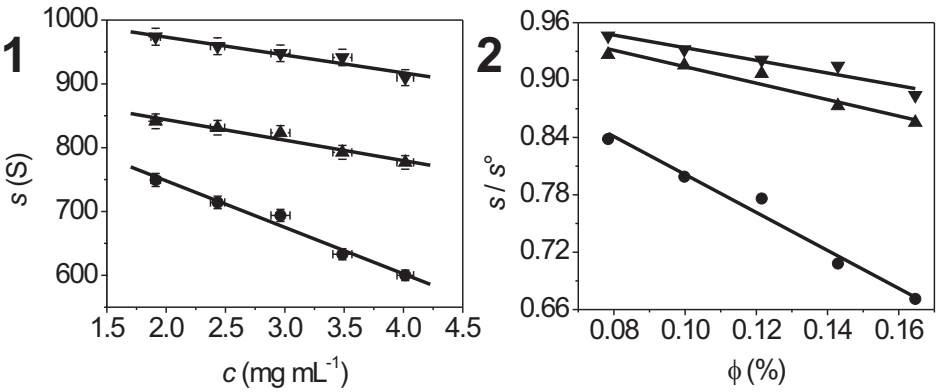

Figure 8.6: Sedimentation coefficients as a function of the total weight concentration c_{tot}, graph 1, and reduced sedimentation coefficients (eq 8.1) vs. volume fraction ϕ_{tot}, graph 2, for the dispersions with 0 (•), 10 (▲) and 50 (▼) mM added NaCl. Volume fractions were calculated from the total weight concentration using a specific particle volume of 0.41 mL g^{-1}.

Table 8.2 shows that the extrapolated experimental value for the sedimentation coefficient at infinite dilution, s°, is larger than the value calculated from eq 8.4 (combined with eq 8.5) or eq 8.7, substituting the average TEM particle dimensions (Table 8.1). The discrepancy is very likely due to the significant polydispersity in rod diameter D_{tot} (note that s° scales with D_{tot} squared). Furthermore, eqs 8.5 and 8.7 have been derived for smooth cylinders, whereas our rods have a more irregular shape and resemble sphero-cylindres (Figure 8.2); the effect of shape details on s° is difficult to assess.

The measured sedimentation velocity of the rods (Figure 8.6) decreases linearly with concentration, as expected from Dhont's calculation for rigid rods [161]. Added salt clearly weakens this concentration dependence (see Figure 8.7). This must be due to

the compression of electrical double-layers surrounding the charged rods, which lowers the excluded volume per rod. In other words, salt diminishes the exposure of rods to the solvent backflow that is the main cause of hindered settling [108]. For the highest salt concentration in this study one would expect the coefficient K_s to approach the prediction from eq 8.9 for uncharged rods. However, the calculated K_s is considerably larger than the experimental value for the highest ionic strength (see Figure 8.7). We used here as input for eq 8.9 the number-averaged dimensions for single rods (see Table 8.1) as obtained from TEM-pictures. It is, however, highly questionable whether the rods in dispersion are really sedimenting and diffusing as single entities. Van Bruggen [168] argued that 'cross-like' doublets of rods are present in dispersions of silica-coated boehmite rods because the increased excluded volume is opposed by the so-called twist effect. The rods tend to decrease their interaction free energy by adopting cross-like structures, a phenomenon quantified by the twist parameter [169] $h = \kappa^{-1}/D_{\text{eff}}$. Indeed, TEM images (Figure 8.2) suggest the presence of rod doublets and possibly triplets, although TEM images should always be interpretated with caution due to the sample treatment (drying, exposure to the electron beam). It is in any case clear that the rod-dispersions do not contain large aggregates because they would have been detected during the ultracentrifugation experiments. However, static light scattering (SLS) results (Figure 8.8) show that the dispersions indeed contain small associates of rods. Figure 8.8 shows SLS data collected at sufficiently small scattering angles such that the Guinier approximation [88] is valid ($q\,R_g < 2.5$, here $0.85 < q\,R_g < 1.17$ for $L_{\text{tot}} = 554\,\text{nm}$). The Guinier plot logarithm of the scattering intensity versus wave vector squared is linear (Figure 8.8), which points to the presence of fairly uniform scatterers. Fitting eq 8.10 to these data, we find via eq 8.11 that a corresponding effective cylinder length of $L = 554\,\text{nm}$. This finding is consistent with the large majority of rods being irreversibly associated into units with an effective length of about twice the value of a single rod. This association has little effect on s°, because s° is mainly determined by the rod thickness (see eq 8.7). However, according to eq 8.9, K_s must be very sensitive to a change in aspect ratio of sedimenting objects. If we substitute in eq 8.9 an effective aspect ratio $p = 554/11.7 \approx 47$, the calculated value for K_s agrees fairly well with the experimental observations (see Figure 8.7).

Thus the results found here, namely a decrease in the concentration dependence coefficient K_s with increasing salt concentration, confirm the expectation that adding sufficient salt, to compress the electric double-layer and to screen the inter-particle repulsions, weakens the concentration dependence of s, Figure 8.7. For the rods employed here, an ionic strength exceeding 50 mM NaCl results in gelation, which then, obviously, makes the system unsuitable for the determination of the concentration dependent sedimentation velocity of colloidal rods. However, sedimentation velocity [51] and sedimentation equilibrium experiments (analytical ultracentrifugation) on gels are

possible [8]. The latter experiment may yield the concentration dependent swelling pressure [49, 50].

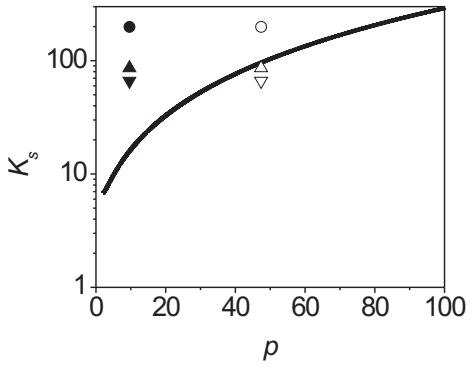

Figure 8.7: Concentration dependence coefficients K_s computed from sedimentation velocity experiments (Table 8.2) on the dispersions with 0 (• and ○), 10 (▲ and △) and 50 (▼ and ▽) mM added NaCl for the aspect ratio for single rods from TEM (solid symbols), and the effective aspect ratio determined with light scattering (open symbols). Increasing the ionic strength decreases the concentration dependence of the sedimentation velocity.

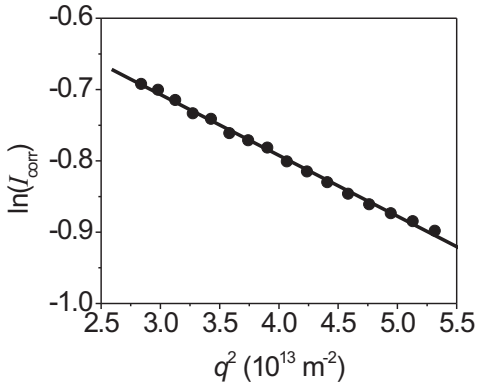

Figure 8.8: Guinier plot of SLS data (•), i.e. log of scattered intensities corrected for the filter, sensitivity and gain, $\ln(I_{\text{corr}})$, versus the squared magnitude of the scattering vector, q^2 (20 to 27.5° using a wavelength of 546.1 nm, where the absorbance of the sample is negligible), for an aqueous dispersion containing 0.045 mg mL^{-1} silica-boehmite rods ($\phi_{\text{tot}} = 1.8 \cdot 10^{-5}$ using $\overline{\nu}_{\text{p}} = 0.41$ mL g^{-1}) without added salt. The rod-length obtained from a linear unconstrained fit (——) is approximately 554 nm.

8.5. Conclusions

The charge-stabilized boehmite-silica dispersions employed here are suited to study the concentration dependent sedimentation velocity of inorganic rods for a comparison

to predictions from theory. However, the rods seem to have associated into structures for which the effective length is twice as large as the individual rod length. Presumably, reversible association of boehmite rods led to the formation of irreversible aggregates due to the deposition of a silica shell onto the boehmite needles that "glued" the rods together. However, the settling behavior as a function of particle weight concentration is still linear in the colloid volume fraction- and added salt concentration range studied here. Charge effects, increasing the effective excluded volume of particles, contribute significantly to the pronounced concentration dependent sedimentation rate. Addition of salt decreases this concentration dependence due to the compression of electric double layers. For an aspect ratio in between the aspect ratios determined from TEM and SLS, the experimental results agree fairly well with the prediction from theory for hard rigid rods.

As we showed here by comparing the interference and absorbance optical data, AUC can be used to assess the purity of colloidal dispersions and to verify the efficiency of fractionation via preparative centrifugation. Furthermore, the interference optics used to monitor the sedimentation rate offers an elegant way to determine the specific particle volume, a quantity required for the comparison of experiments with theory.

8.6. Acknowledgement

We thank Emile Bakelaar for helping with the SLS measurements, Bonny W.M. Kuipers for helpful discussions, and Stefano Saccana for his assistance with the glow-discharge TEM-grid preparation.

Addendum

Bibliography

[1] H. K. Schachman. *Ultracentrifugation in Biochemistry*. Academic Press, New York and London, 1959.

[2] J. Liu and S. J. Shire. Analytical Ultracentrifugation in the Pharmaceutical Industry. *J. Pharm. Sci.*, 88(12):1237–1241, 1999.

[3] S. E. Harding, A. J. Rowe, and J. C. Horton (editors). *Analytical Ultracentrifugation in Biochemistry and Polymer Science*. Royal Society of Chemistry, Cambridge, 1992.

[4] D. J. Scott, S. E. Harding, and A. J. Rowe (editors). *Analytical Ultracentrifugation: Techniques and Methods*. Royal Society of Chemistry, Cambridge, 2005.

[5] T. Svedberg and J. B. Nichols. Determination of Size and Distribution of Size of Particle by Centrifugal Methods. *J. Am. Chem. Soc.*, 45(12):2910–2917, 1923.

[6] T. Svedberg and H. Rinde. The Ultra-Centrifuge, a New Instrument for the Determination of Size and Distribution of Size of Particle in Amicroscopic Colloids. *J. Am. Chem. Soc.*, 46(12):2677–2693, 1924.

[7] T. Svedberg and K. O. Pedersen. *The Ultracentrifuge*. Clarendon Press, Oxford, 1940.

[8] H. Cölfen. Analytical Ultracentrifugation of Colloids. In D. J. Scott, S. E. Harding, and A. J. Rowe (editors), *Analytical Ultracentrifugation: Techniques and Methods*, pages 501–583. Royal Society of Chemistry, Cambridge, 2005.

[9] L. W. Janssen, F. Zernike, and R. Brinkman. De Ultracentrifuge, Methode en Resultaten. *Ned. T. Natuurkunde*, 8:209–248, 1941.

[10] P. F. Mijnlieff. *Sedimentation and Diffusion of Colloidal Electrolytes, with Applications to Proteins and Sodiumlaurylsulfate*. PhD thesis, Utrecht University, 1958.

[11] R. C. Groot. *The Ultracentrifugation of Oil in Water Emulsions*. PhD thesis, Utrecht University, 1965.

[12] M. M. Kops-Werkhoven. *Dynamic Interactions of Silica Particles in Nonpolar Solvents*. PhD thesis, Utrecht University, 1982.

[13] J. W. Jansen. *Attractive Interactions in Sterically Stabilized Silica Dispersions*. PhD thesis, Utrecht University, 1986.

[14] D. M. E. Thies-Weesie. *Sedimentation and Liquid Permeation of Inorganic Colloids*. PhD thesis, Utrecht University, 1995.

[15] L. N. Donselaar. *Silica-Magnetite Colloids and Magnetic Fluids*. PhD thesis, Utrecht University, 1998.

[16] G. H. Koenderink. *Rotational and Translational Diffusion in Colloidal Mixtures*. PhD thesis, Utrecht University, 2003.

[17] K. L. Planken, G. H. Koenderink, R. Roozendaal, and A. P. Philipse. Monodisperse DNA Restriction Fragments: I. Synthesis and Characterization. *J. Colloid Interface Sci.*, 291(1):120–125, 2005.

[18] G. H. Koenderink, K. L. Planken, R. Roozendaal, and A. P. Philipse. Monodisperse DNA Restriction Fragments: II. Sedimentation Velocity and Equilibrium Experiments. *J. Colloid Interface Sci.*, 291(1):126–134, 2005.

[19] I. L. Validzic. *Reversible Aggregation on Nanometer Length Scales (from Simple Salts to Viruses).* PhD thesis, Utrecht University, 2004.

[20] J. Lebowitz, M. S. Lewis, and P. Schuck. Modern Analytical Ultracentrifugation in Protein Science: A Tutorial Review. *Protein Sci.*, 11(9):2067–2079, 2002.

[21] H. Fujita. *Mathematical Theory of Sedimentation Analysis*, volume 11 of *Physical Chemistry; A Series of Monographs*. Academic Press, New York and London, 1962.

[22] H. Fujita. *Foundations of Ultracentrifugal Analysis*, volume 42 of *Chemical Analysis; A Series of Monographs on Analytical Chemistry and Its Applications*. Wiley-Interscience, New York, London, Sydney and Toronto, 1975.

[23] B. Demeler. UltraScan 9.5 - A Comprehensive Data Analysis Software Package for Analytical Ultracentrifugation Experiments. In D. J. Scott, S. E. Harding, and A. J. Rowe (editors), *Analytical Ultracentrifugation: Techniques and Methods*, pages 210–230. Royal Society of Chemistry, Cambridge, 2005.

[24] S. K. Bhattacharyya, P. Maciejewska, L. Börger, M. Stadler, A. M. Gülsün, H. B. Cicek, and H. Cölfen. Development of a Fast Fiber Based UV-Vis Multiwavelength Detector for an Ultracentrifuge. In C. Wandrey and H. Cölfen (editors), *Analytical Ultracentrifugation VIII*, volume 131 of *Progress in Colloid and Polymer Science*, pages 9–22. Springer, Berlin, Heidelberg, New York, 2006.

[25] M. T. Laue. Choosing Which Optical System of the Optima^{TM} XL-I Analytical Ultracentrifuge to Use, A-1821A. Application Information, sIA-Solution Interaction Analysis, Beckman Instruments, Inc., Fullerton, California, 1996.

[26] T. M. Laue, A. L. Anderson, and B. J. Weber. Prototype Fluorimeter for the XLA/XLI Analytical Ultracentrifuge. In *Proc. SPIE-Int. Soc. Opt. Eng.*, volume 2985, pages 196–204, 1997.

[27] I. K. MacGregor, A. L. Anderson, and T. M. Laue. Fluorescence Detection for the XLI Analytical Ultracentrifuge. *Biophys. Chem.*, 108(1-3):165–185, 2004.

[28] T. Laue. Analytical Ultracentrifugation: A Powerful 'New' Technology in Drug Discovery. *Drug Discovery Today: Technologies*, 1(3):309–315, 2004.

[29] T. M. Laue, J. B. Austin, and D. A. Rau. A Light Intensity Measurement System for the Analytical Ultracentrifuge. In C. Wandrey and H. Cölfen (editors), *Analytical Ultracentrifugation VIII*, volume 131 of *Progress in Colloid and Polymer Science*, pages 1–8. Springer, Berlin, Heidelberg, New York, 2006.

[30] P. Deo, N. Deo, and P. Somasundaran. Complexation of Hydrophobically Modified Polyelectrolytes with Surfactants: Anionic Poly(Maleic Acid/Octyl Vinyl Ether)/Anionic Sodium Dodecyl Sulfate. *Langmuir*, 21(22):9998–10003, 2005.

[31] Beckman Coulter^{TM} ProteomeLab^{TM} XL-A/XL-I, Protein Characterization System. Instruction Manual, Centrifuge Instrument Systems Development Center of Beckman Coulter Inc., Palo Alto, California, 2003.

[32] I. L. Validzic, G. van Hooijdonk, S. Oosterhout, and W. K. Kegel. Thermodynamic Stability of Clusters of Molybdenum Oxide. *Langmuir*, 20(8):3435–3440, 2004.

[33] N. Deo and P. Somasundaran. Disintegration of Liposomes by Surfactants: Mechanism of Protein and Cholesterol Effects. *Langmuir*, 19(6):2007–2012, 2003.

[34] S. Kubowicz, A. F. Thünemann, R. Weberskirch, and H. Möhwald. Cylindrical Micelles of α-Fluorocarbon-ω-Hydrocarbon End-Capped Poly(N-Acylethylene Imine)s. *Langmuir*, 21(16):7214–7219, 2005.

[35] P. Schuck and B. Demeler. Direct Sedimentation Analysis of Interference Optical Data in Analytical Ultracentrifugation. *Biophys. J.*, 76(4):2288–2296, 1999.

[36] K. E. van Holde. *Physical Biochemistry*. Foundations of Modern Biochemistry Series. Prentice-Hall, Englewood Cliffs, New Jersey, 1971.

[37] A. P. Philipse. Particulate Colloids: Aspects of Preparation and Characterization. In J. Lyklema (editor), *Fundamentals of Interface and Colloid Science*, volume IV, pages 2.1–2.71. Elsevier Academic Press, Amsterdam, 2005.

[38] G. G. Stokes. On the Effect of the Internal Friction of Fluids on the Motion of Pendulums. *Trans. Cambridge Phil. Soc.*, 9:8–106, 1850.

[39] A. Fick. Über Diffusion. *Ann. Physik u. Chem.*, 94:59–86, 1855.

[40] A. Einstein. Über die von der Molekularkinetischen Theorie der Wärme Geforderte Bewegung von in Ruhenden Flüssigkeiten Suspendierten Teilchen [AdP 17, 549 (1905)]. *Ann. Phys.*, 14(S1):182–193, 2005.

[41] O. Lamm. Die Differentialgleichung der Ultrazentrifugierung. *Ark. Mat. Astron. Fysik.*, 21B(2):1–4, 1929.

[42] H. Faxén. Über eine Differentialgleichung aus der Physikalischen Chemie. *Arkiv Mat. Astron. Fysik*, 21, B(3):1–6, 1929.

[43] K. E. van Holde and W. O. Weischet. Boundary Analysis of Sedimentation-Velocity Experiments with Monodisperse and Paucidisperse Solutes. *Biopolymers*, 17(6):1387–1403, 1978.

[44] B. Demeler and K. E. van Holde. Sedimentation Velocity Analysis of Highly Heterogeneous Systems. *Anal. Biochem.*, 335(2):279–288, 2004.

[45] E. Brookes and B. Demeler. Genetic Algorithm Optimization for Obtaining Accurate Molecular Weight Distributions from Sedimentation Velocity Experiments. In C. Wandrey and H. Cölfen (editors), *Analytical Ultracentrifugation VIII*, volume 131 of *Progress in Colloid and Polymer Science*, pages 33–40. Springer, Berlin, Heidelberg, New York, 2006.

[46] B. Demeler and E. Brookes. Monte Carlo Analysis of Sedimentation Experiments. *Colloid Polym. Sci.*, 286(2):129–137, 2008.

[47] E. Brookes and B. Demeler. Parallel Computational Techniques for the Analysis of Sedimentation Velocity Experiments in UltraScan. *Colloid Polym. Sci.*, 286(2):139–148, 2008.

[48] R. Zhang and P. Somasundaran. Abnormal Micellar Growth in Sugar-Based and Ethoxylated Nonionic Surfactants and Their Mixtures in Dilute Regimes Using Analytical Ultracentrifugation. *Langmuir*, 20(20):8552–8558, 2004.

[49] W. Borchard. Swelling Pressure Equilibrium of Swollen Crosslinked Systems in an External Field. I: Theory. In W. Borchard (editor), *Progress in Analytical Ultracentrifugation*, volume 86 of *Progress in Colloid and Polymer Science*, pages 84–91. Springer, Berlin and Heidelberg, 1991.

[50] G. Holtus, H. Cölfen, and W. Borchard. Swelling Pressure Equilibrium of Swollen Crosslinked Systems in an External Field. II: The Determination of Molecular Parameters of Gelatin/Water Gels from the Swelling Pressure-Concentration Curves. In W. Borchard (editor), *Progress in Analytical Ultracentrifugation*, volume 84 of *Progress in Colloid and Polymer Science*, pages 92–101. Springer, Berlin and Heidelberg, 1991.

[51] W. Borchard and A. Straatmann. Sedimentation and Diffusion Coefficients in Polymer Solutions and Gels. In M. D. Lechner and L. Börger (editors), *Analytical Ultracentrifugation VII*, Progress in Colloid and Polymer Science, pages 14–18. Springer, Berlin and Heidelberg, 2004.

[52] A. Torres, A. Cuetos, M. Dijkstra, and R. van Roij. Sedimentation of Charged Colloids: The Primitive Model and the Effective One-Component Approach. *Phys. Rev. E*, 75(4):041405–1–8, 2007.

[53] J. Zwanikken and R. van Roij. The Sediment of Mixtures of Charged Colloids: Segregation and Inhomogeneous Electric Fields. *Europhys. Lett.*, 71(3):480–486, 2005.

[54] A. P. Philipse and G. H. Koenderink. Sedimentation-Diffusion Profiles and Layered Sedimentation of Charged Colloids at Low Ionic Strength. *Adv. Colloid Interface Sci.*, 100-102:613–639, 2003.

[55] M. Raşa, B. H. Erné, B. Zoetekouw, R. van Roij, and A. P. Philipse. Macroscopic Electric Field and Osmotic Pressure in Ultracentrifugal Sedimentation-Diffusion Equilibria of Charged Colloids. *J. Phys.: Condens. Matter*, 17(15):2293–2314, 2005.

[56] M. Raşa and A. P. Philipse. Evidence for a Macroscopic Electric Field in the Sedimentation Profiles of Charged Colloids. *Nature*, 429(6994):857–860, 2004.

[57] S. Ye, J. W. Strzalka, B. M. Discher, D. Noy, S. Zheng, P. L. Dutton, and J. K. Blasie. Amphiphilic 4-Helix Bundles Designed for Biomolecular Materials Applications. *Langmuir*, 20(14):5897–5904, 2004.

[58] J. Tarus, R. A. Agbaria, K. Morris, S. Mwongela, A. Numan, L. Simuli, K. A. Fletcher, and I. M. Warner. Influence of the Polydispersity of Polymeric Surfactants on the Enantioselectivity of Chiral Compounds in Micellar Electrokinetic Chromatography. *Langmuir*, 20(16):6887–6895, 2004.

[59] A. Müller and S. Roy. En Route from the Mystery of Molybdenum Blue via Related Manipulatable Building Blocks to Aspects of Materials Science. *Coord. Chem. Rev.*, 245(1-2):153–166, 2003.

[60] A. Müller, Y. Zhou, H. Bögge, M. Schmidtmann, T. Mitra, E. T. K. Haupt, and A. Berkle. "Gating" the Pores of a Metal Oxide Based Capsule: After Initial Cation Uptake Subsequent Cations are Found Hydrated and Supramolecularly Fixed Above the Pores. *Angew. Chem. Int. Edit.*, 45(3):460–465, 2006.

[61] A. Müller, L. Toma, H. Bögge, M. Henry, E. T. K. Haupt, A. Mix, and F. L. Sousa. Reactions Inside a Porous Nanocapsule/Artificial Cell: Encapsulates' Structuring Directed by Internal Surface Deprotonations. *Chem. Commun.*, (32):3396–3398, 2006.

[62] A. Müller, S. K. Das, S. Talismanov, S. Roy, E. Beckmann, H. Bögge, M. Schmidtmann, A. Merca, A. Berkle, L. Allouche, Y. Zhou, and L. Zhang. Trapping Cations in Specific Positions in Tuneable "Artificial Cell" Channels: New Nanochemistry Perspectives. *Angew. Chem. Int. Edit.*, 42(41):5039–5044, 2003.

[63] A. Müller, E. Krickemeyer, H. Bögge, M. Schmidtmann, S. Roy, and A. Berkle. Cover Picture: Angew. Chem. Int. Ed. 19/2002. *Angew. Chem. Int. Edit.*, 41(19):3509, 2002.

[64] A. Müller, B. Botar, H. Bögge, P. Kögerler, and A. Berkle. A Potassium Selective 'Nanosponge' with Well Defined Pores. *Chem. Commun.*, 8(24):2944–2945, 2002.

[65] D. G. Kurth, P. Lehmann, D. Volkmer, A. Müller, and D. Schwahn. Biologically Inspired Polyoxometalate-Surfactant Composite Materials. Investigations on the Structures of Discrete, Surfactant-Encapsulated Clusters, Monolayers, and Langmuir-Blodgett Films of

$(DODA)_{40}(NH_4)_2[(H_2O)_n$ subset of $Mo_{132}O_{372}(CH_3CO_2)_{30}(H_2O)_{72}]$. *J. Chem. Soc. Dalton*, (21):3989–3998, 2000.

[66] A. Müller, S. Polarz, S. K. Das, E. Krickemeyer, H. Bögge, M. Schmidtmann, and B. Hauptfleisch. 'Open and Shut' for Guests in Molybdenum - Oxide-Based Giant Spheres, Baskets, and Rings Containing the Pentagon as a Common Structural Element. *Angew. Chem. Int. Edit.*, 38(21):3241–3245, 1999.

[67] S. Roy. *Giant Polyoxomolybdates: Syntheses, Structure and Stability Studies; from Syntheses of Extended Structures to Novel Host Design, Stability Investigations in Solution and Perspectives for a Future Mechanistic Study*. PhD thesis, Universität Bielefeld, 2005.

[68] A. Müller, E. Krickemeyer, H. Bögge, M. Schmidtmann, B. Botar, and M. O. Talismanova. Drawing Small Cations Into Highly Charged Porous Nanocontainers Reveals "Water" Assembly and Related Interaction Problems. *Angew. Chem. Int. Edit.*, 42(18):2085–2090, 2003.

[69] A. Müller, E. Krickemeyer, H. Bögge, M. Schmidtmann, and F. Peters. Organizational Forms of Matter: An Inorganic Super Fullerene and Keplerate Based on Molybdenum Oxide. *Angew. Chem. Int. Edit.*, 37(24):3360–3363, 1998.

[70] T. M. Schuster and T. M. Laue. *Modern Analytical Ultracentrifugation: Acquisition and Interpretation of Data for Biological and Synthetic Polymer Systems*. Birkhäuser, Boston, Mass., 1994.

[71] D. Volkmer, B. Bredenkötter, J. Tellenbröker, P. Kögerler, D. G. Kurth, P. Lehmann, H. Schnablegger, D. Schwahn, M. Piepenbrink, and B. Krebs. Structure and Properties of the Dendron-Encapsulated Polyoxometalate $(C_{52}H_{60}NO_{12})_{12}\{[Mn(H_2O)]_3(SbW_9O_{33})_2\}$, a First Generation Dendrizyme. *J. Am. Chem. Soc.*, 124(35):10489–10496, 2002.

[72] M. C. Baker, P. A. Lyons, and S. J. Singer. Velocity Ultracentrifugation and Diffusion of Silicotungstic Acid. *J. Am. Chem. Soc.*, 77(7):2011–2012, 1955.

[73] B. Demeler. Hydrodynamic Methods. In L. K. Buehler and H. H. Rashidi (editors), *Bioinformatics Basics: Applications in Biological Science and Medicine*, pages 226–255. CRC, Boca Raton, Fla.; London, 2nd edition, 2005.

[74] D. R. Lide. *CRC Handbook of Chemistry and Physics: A Ready-Reference Book of Chemical and Physical Data*. CRC, Boca Raton, Fla.; London, 81st edition, 2000.

[75] B. Demeler and H. Saber. Determination of Molecular Parameters by Fitting Sedimentation Data to Finite-Element Solutions of the Lamm Equation. *Biophys. J.*, 74(1):444–454, 1998.

[76] W. Cao and B. Demeler. Modeling Analytical Ultracentrifugation Experiments with an Adaptive Space-Time Finite Element Solution of the Lamm Equation. *Biophys. J.*, 89(3):1589–1602, 2005.

[77] Y. Zhu, A. Cammers-Goodwin, B. Zhao, A. Dozier, and E. C. Dickey. Kinetic Precipitation of Solution-Phase Polyoxomolybdate Followed by Transmission Electron Microscopy: A Window to Solution-Phase Nanostructure. *Chem. Eur. J.*, 10(10):2421–2427, 2004.

[78] T. Liu, B. Imber, E. Diemann, G. Liu, K. Cokleski, H. Li, Z. Chen, and A. Müller. Deprotonations and Charges of Well-Defined $\{Mo_{72}Fe_{30}\}$ Nanoacids Simply Stepwise Tuned by pH Allow Control/Variation of Related Self-Assembly Processes. *J. Am. Chem. Soc.*, 128(49):15914–15920, 2006.

[79] M. L. Kistler, A. Bhatt, G. Liu, D. Casa, and T. Liu. A Complete Macroion-"Blackberry" Assembly-Macroion Transition with Continuously Adjustable Assembly Sizes in $\{Mo_{132}\}$ Water/Acetone Systems. *J. Am. Chem. Soc.*, 129(20):6453–6460, 2007.

[80] W. Brown. *Dynamic Light Scattering: The Method and Some Applications*. Clarendon Press, Oxford, 1993.

[81] S. Roy, K. L. Planken, R. Kim, D. v. d. Mandele, and W. K. Kegel. Direct Evidence on the Existence of $\{Mo_{132}\}$ Keplerate-Type Species in Aqueous Solution. *Inorg. Chem.*, 46(21):8469–8471, 2007.

[82] H. Cölfen. Analytical Ultracentrifugation of Nanoparticles. *Polymer News*, 29(4):101–116, 2004.

[83] H. G. Müller. Determination of Very Broad Particle Size Distributions Via Interference Optics in the Analytical Ultracentrifuge. In M. D. Lechner and L. Börger (editors), *Analytical Ultracentrifugation VII*, volume 127 of *Progress in Colloid and Polymer Science*, pages 9–13. Springer, Berlin, Heidelberg, New York, 2004.

[84] P. Schuck. Size-Distribution Analysis of Macromolecules by Sedimentation Velocity Ultracentrifugation and Lamm Equation Modeling. *Biophys. J.*, 78(3):1606–1619, 2000.

[85] P. Schuck. Diffusion-Deconvoluted Sedimentation Coefficient Distribution for the Analysis of Interacting and Non-Interacting Protein Mixtures. In D. J. Scott, S. E. Harding, and A. J. Rowe (editors), *Analytical Ultracentrifugation: Techniques and Methods*, pages 26–49. Royal Society of Chemistry, Cambridge, 2005.

[86] E. M. Claesson and A. P. Philipse. Thiol-Functionalized Silica Colloids, Grains, and Membranes for Irreversible Adsorption of Metal(oxide) Nanoparticles. *Colloids Surf. A*, 297(1-3):46–54, 2007.

[87] B. J. Berne and R. Pecora. *Dynamic Light Scattering: With Applications to Chemistry, Biology, and Physics*. Dover Publications, Mineola, N.Y., 2000.

[88] J. K. G. Dhont. *An Introduction to Dynamics of Colloids*, volume 2 of *Studies in Interface Science*. Elsevier, Amsterdam and Oxford, 1996.

[89] M. V. Petoukhov, P. V. Konarev, A. G. Kikhney, and D. I. Svergun. ATSAS 2.1 - Towards Automated and Web-Supported Small-Angle Scattering Data Analysis. *J. Appl. Crystallogr.*, 40(s1):s223–s228, 2007.

[90] M. A. Pfeifer, G. J. Williams, I. A. Vartanyants, R. Harder, and I. K. Robinson. Three-Dimensional Mapping of a Deformation Field Inside a Nanocrystal. *Nature*, 442(7098):63–66, 2006.

[91] R. Pecora (editor). *Dynamic Light Scattering: Applications of Photon Correlation Spectroscopy*. Plenum, New York, 1985.

[92] R. Finsy, P. de Groen, L. Deriemaeker, and M. van Laethem. Singular Value Analysis and Reconstruction of Photon Correlation Data Equidistant in Time. *J. Chem. Phys.*, 91(12):7374–7383, 1989.

[93] D. H. Everett. *Basic Principles of Colloid Science*. Royal Society of Chemistry, Cambridge, 1988.

[94] P. Schuck, M. A. Perugini, N. R. Gonzales, G. J. Hewlett, and D. Schubert. Size-Distribution Analysis of Proteins by Analytical Ultracentrifugation: Strategies and Application to Model Systems. *Biophys. J.*, 82(2):1096–1111, 2002.

[95] A. Müller and C. Serain. Soluble Molybdenum Blues - 'Des Pudels Kern'. *Acc. Chem. Res.*, 33(1):2–10, 2000.

[96] T. Liu. Supramolecular Structures of Polyoxomolybdate-Based Giant Molecules in Aqueous Solution. *J. Am. Chem. Soc.*, 124(37):10942–10943, 2002.

[97] T. Liu. Erratum: Supramolecular Structures of Polyoxomolybdate-Based Giant Molecules in Aqueous Solution (Journal of the American Chemical Society (2002) 124 (10942-10943)). *J. Am. Chem. Soc.*, 126(1):406, 2004.

[98] G. Liu and T. Liu. Strong Attraction Among, the Fully Hydrophilic $\{Mo_{72}Fe_{30}\}$ Macroanions. *J. Am. Chem. Soc.*, 127(19):6942–6943, 2005.

[99] T. Liu. An Unusually Slow Self-Assembly of Inorganic Ions in Dilute Aqueous Solution. *J. Am. Chem. Soc.*, 125(2):312–313, 2003.

[100] G. Liu and T. Liu. Thermodynamic Properties of the Unique Self-Assembly of $\{Mo_{72}Fe_{30}\}$ Inorganic Macro-Ions in Salt-Free and Salt-Containing Aqueous Solutions. *Langmuir*, 21(7):2713–2720, 2005.

[101] A. A. Verhoeff, M. L. Kistler, A. Bhatt, J. Pigga, J. Groenewold, M. Klokkenburg, S. Veen, S. Roy, T. Liu, and W. K. Kegel. Charge Regulation as a Stabilization Mechanism for Shell-Like Assemblies of Polyoxometalates. *Phys. Rev. Lett.*, 99(6):066104, 1–4, 2007.

[102] B. Chen, H. Jiang, V. Zhu, A. Cammers, and J. P. Selegue. Monitoring the Growth of Polyoxomolybdate Nanoparticles in Suspension by Flow Field-Flow Fractionation. *J. Am. Chem. Soc.*, 127(12):4166–4167, 2005.

[103] E. Balogh, A. M. Todea, A. Müller, and W. H. Casey. Rates of Ligand Exchange Between Fe^{III}-OH_2 Functional Groups on a Nanometer-Sized Aqueous Cluster and Bulk Solution. *Inorg. Chem.*, 46(17):7087–7092, 2007.

[104] A. Müller, S. Sarkar, S. Q. N. Shah, H. Bögge, M. Schmidtmann, S. Sarkar, P. Kögerler, B. Hauptfleisch, A. X. Trautwein, and V. Schünemann. Archimedean Synthesis and Magic Numbers: 'Sizing' Giant Molybdenum-Oxide-Based Molecular Spheres of the Keplerate Type. *Angew. Chem. Int. Edit.*, 38(21):3238–3241, 1999.

[105] I. Tinoco, K. Sauer, and J. C. Wang. *Physical Chemistry: Principles and Applications in Biological Sciences*. Prentice-Hall, Englewood Cliffs, N.J.; London, 3rd edition, 1995.

[106] A. P. Philipse. Colloidal Sedimentation (and Filtration). *Curr. Opin. Colloid Interface Sci.*, 2(2):200–206, 1997.

[107] D. M. E. Thies-Weesie, A. P. Philipse, G. Nägele, B. Mandl, and R. Klein. Nonanalytical Concentration Dependence of Sedimentation of Charged Silica Spheres in an Organic Solvent: Experiments and Calculations. *J. Colloid Interface Sci.*, 176(1):43–54, 1995.

[108] G. K. Batchelor. Sedimentation in a Dilute Dispersion of Spheres. *J. Fluid Mech.*, 52(2):245–268, 1972.

[109] J. W. Jansen, C. G. de Kruif, and A. Vrij. Attractions in Sterically Stabilized Silica Dispersions: IV. Sedimentation. *J. Colloid Interface Sci.*, 114(2):501–504, 1986.

[110] M. Klokkenburg, C. Vonk, E. M. Claesson, J. D. Meeldijk, B. H. Erné, and A. P. Philipse. Direct Imaging of Zero-Field Dipolar Structures in Colloidal Dispersions of Synthetic Magnetite. *J. Am. Chem. Soc.*, 126(51):16706–16707, 2004.

[111] M. Klokkenburg, R. P. A. Dullens, W. K. Kegel, B. H. Erné, and A. P. Philipse. Quantitative Real-Space Analysis of Self-Assembled Structures of Magnetic Dipolar Colloids. *Phys. Rev. Lett.*, 96(037203):0372031–0372034, 2006.

[112] H. A. Kramers. Brownian Motion in a Field of Force and the Diffusion Model of Chemical Reactions. *Physica*, 7(4):284–304, 1940.

[113] D. L. Weaver. Effective Diffusion Coefficient of a Brownian Particle in a Periodic Potential. *Physica A*, 98(1-2):359–362, 1979.

[114] M. Smoluchowski. Versuch Einer Mathematischen Theorie der Koagulationskinetik Kolloider Lösungen. *Z. Phys. Chem.*, 92:129, 1917.

[115] D. C. Harris. *Quantitative Chemical Analysis*. W.H. Freeman, New York, 4th edition, 1995.

[116] J. Behlke and O. Ristau. Lammnum: A Program to Study Self-Associating Macromolecules in Sedimentation Velocity Experiments. In D. J. Scott, S. E. Harding, and A. J. Rowe (editors),

Analytical Ultracentrifugation: Techniques and Methods, pages 122–132. Royal Society of Chemistry, Cambridge, 2005.

[117] D. A. Yphantis. Equilibrium Ultracentrifugation of Dilute Solutions. *Biochemistry*, 3(3):297–317, 1964.

[118] R. Piazza, T. Bellini, and V. Degiorgio. Equilibrium Sedimentation Profiles of Screened Charged Colloids - a Test of the Hard-Sphere Equation of State. *Phys. Rev. Lett.*, 71(25):4267–4270, 1993.

[119] W. B. Russel, D. A. Saville, and W. R. Schowalter. *Colloidal Dispersions*. Cambridge University Press, Cambridge, 1989.

[120] D. Y. C. Chan, D. Henderson, J. Barojas, and A. M. Homola. The Stability of a Colloidal Suspension of Coated Magnetic Particles in an Aqueous Solution. *IBM Journal of Research and Development*, 29(1):11–17, 1985.

[121] S. Charles and R. Massart. Physico-Chemistry of Magnetic Fluids: Preparation and Properties. In B. M. Berkovski and V. G. Bashtovoi (editors), *Magnetic Fluids and Applications Handbook*, pages 3–235. Begell House, New York; Wallingford, 1996.

[122] P. W. Rouw and C. G. de Kruif. Adhesive Hard Sphere Colloidal Dispersions. I. Diffusion Coefficient as a Function of Well Depth. *J. Chem. Phys.*, 88(12):7799, 1988.

[123] J. Garcia de la Torre. Sedimentation Coefficients of Complex Biological Particles. In S. E. Harding, A. J. Rowe, and J. C. Horton (editors), *Analytical Ultracentrifugation in Biochemistry and Polymer Science*, pages 333–345. Royal Society of Chemistry, Cambridge, 1992.

[124] G. W. Schwert. The Molecular Size and Shape of the Pancreatic Proteases. I. Sedimentation Studies on Chymotrypsinogen and on α- and γ-Chymotrypsin. *J. Biol. Chem.*, 179(2):655–664, 1949.

[125] P. I. C. Teixeira, J. M. Tavares, and M. M. T. da Gama. The Effect of Dipolar Forces on the Structure and Thermodynamics of Classical Fluids. *J. Phys.: Condens. Matter*, 12(33):R411–R434, 2000.

[126] C. Holm and J. J. Weis. The Structure of Ferrofluids: A Status Report. *Curr. Opin. Colloid Interface Sci.*, 10(3-4):133–140, 2005.

[127] A. P. Philipse and D. Maas. Magnetic Colloids from Magnetotactic Bacteria: Chain Formation and Colloidal Stability. *Langmuir*, 18(25):9977–9984, 2002.

[128] L. N. Donselaar, P. M. Frederik, P. Bomans, P. A. Buining, B. M. Humbel, and A. P. Philipse. Visualisation of Particle Association in Magnetic Fluids in Zero-Field. *J. Magn. Magn. Mater.*, 201:58–61, 1999.

[129] B. H. Erné, K. Butter, B. W. M. Kuipers, and G. J. Vroege. Rotational Diffusion in Iron Ferrofluids. *Langmuir*, 19(20):8218–8225, 2003.

[130] M. Klokkenburg, B. H. Erné, and A. P. Philipse. Thermal Motion of Magnetic Iron Nanoparticles in a Frozen Solvent. *Langmuir*, 21(4):1187–1191, 2005.

[131] L. N. Donselaar and A. P. Philipse. Interactions Between Silica Colloids with Magnetite Cores: Diffusion, Sedimentation and Light Scattering. *J. Colloid Interface Sci.*, 212(1):14–23, 1999.

[132] L. N. Donselaar, A. P. Philipse, and J. Suurmond. Concentration-Dependent Sedimentation of Dilute Magnetic Fluids and Magnetic Silica Dispersions. *Langmuir*, 13(23):6018–6025, 1997.

[133] A. Seifert and N. Buske. Analytical Ultracentrifugation of Magnetic Fluids. *J. Magn. Magn. Mater.*, 122(1-3):115–118, 1993.

[134] H. Wang and C. S. Wen. Concentration-Dependent Sedimentation of Stable Magnetic Dispersions. *J. Colloid Interface Sci.*, 213(2):606–608, 1999.

[135] A. Bee, R. Massart, and S. Neveu. Synthesis of Very Fine Maghemite Particles. *J. Magn. Magn. Mater.*, 149(1-2):6–9, 1995.

[136] S. Sun and H. Zeng. Size-Controlled Synthesis of Magnetite Nanoparticles. *J. Am. Chem. Soc.*, 124(28):8204–8205, 2002.

[137] M. Klokkenburg, J. Hilhorst, and B. H. Erné. Surface Analysis of Magnetite Nanoparticles in Cyclohexane Solutions of Oleic Acid and Oleylamine. *Vib. Spectrosc.*, 43(1):243–248, 2007.

[138] R. H. Kodama. Magnetic Nanoparticles. *J. Magn. Magn. Mater.*, 200(1-3):359–372, 1999.

[139] R. E. Rosensweig. *Ferrohydrodynamics*. Cambridge University Press, Cambridge, 1985.

[140] D. R. Lide. *Handbook of Organic Solvents*. CRC, Boca Raton, Fla.; London, 1995.

[141] R. J. Goldberg. Sedimentation in the Ultracentrifuge. *J. Phys. Chem.*, 57(2):194–202, 1953.

[142] J. J. Correia, M. L. Johnson, T. Laue, W. E. Stafford, and R. C. Williams. Spinning with Dave: David Yphantis Contributions to Ultracentrifugation. *Biophys. Chem.*, 108(1-3):23–42, 2004.

[143] J. P. Johnston and A. G. Ogston. A Boundary Anomaly Found in the Ultracentrifugal Sedimentation of Mixtures. *Trans. Faraday Soc.*, 42:789–799, 1946.

[144] K. Butter, P. H. H. Bomans, P. M. Frederik, G. J. Vroege, and A. P. Philipse. Direct Observation of Dipolar Chains in Iron Ferrofluids by Cryogenic Electron Microscopy. *Nat. Mater.*, 2(2):88–91, 2003.

[145] K. Butter, P. H. Bomans, P. M. Frederik, G. J. Vroege, and A. P. Philipse. Direct Observation of Dipolar Chains in Ferrofluids in Zero Field Using Cryogenic Electron Microscopy. *J. Phys.: Condens. Matter*, 15(15), 2003.

[146] P. C. Scholten. How Magnetic can a Magnetic Fluid be? *J. Magn. Magn. Mater.*, 39(1-2):99–106, 1983.

[147] G. A. van Ewijk. *Phase Behavior of Mixtures of Magnetic Colloids and Non-Adsorbing Polymer*. PhD thesis, Utrecht University, 2001.

[148] J. N. Israelachvili. *Intermolecular and Surface Forces*. Academic Press, London, 2nd edition, 1991.

[149] H. C. Hamaker. The London-van der Waals Attraction Between Spherical Particles. *Physica*, 4(10):1058–1072, 1937.

[150] Y. L. Chen, Z. H. Xu, and J. Israelachvili. Structure and Interactions of Surfactant-Covered Surfaces in Nonaqueous (Oil Surfactant Water) Media. *Langmuir*, 8(12):2966–2975, 1992.

[151] N. V. Churaev and B. V. Derjaguin. Inclusion of Structural Forces in the Theory of Stability of Colloids and Films. *J. Colloid Interface Sci.*, 103(2):542–553, 1985.

[152] R. E. Rosensweig. Heating Magnetic Fluid with Alternating Magnetic Field. *J. Magn. Magn. Mater.*, 252(1-3 Spec. Iss.):370–374, 2002.

[153] D. H. Lee and R. A. Condrate Sr. FTIR Spectral Characterization of Thin Film Coatings of Oleic Acid on Glasses: I. Coatings on Glasses from Ethyl Alcohol. *J. Mater. Sci.*, 34(1):139–146, 1999.

[154] D. H. Lee, R. A. Condrate Sr, and W. C. Lacourse. FTIR Spectral Characterization of Thin Film Coatings of Oleic Acid on Glasses: Part II. Coatings on Glass from Different Media such as Water, Alcohol, Benzene and Air. *J. Mater. Sci.*, 35(19):4961–4970, 2000.

[155] V. V. Korolev, A. G. Ramazanova, and A. V. Blinov. Adsorption of Surfactants on Superfine Magnetite. *Russ. Chem. Bull.*, 51(11):2044–2049, 2002.

[156] G. K. Batchelor. Sedimentation in a Dilute Polydisperse System of Interacting Spheres - 1. General Theory. *J. Fluid Mech.*, 119:379–408, 1982.

[157] G. K. Batchelor and C. S. Wen. Sedimentation in a Dilute Polydisperse System of Interacting Spheres - 2. Numerical Results. *J. Fluid Mech.*, 124:495–528, 1982.

[158] D. M. E. Thies-Weesie, A. P. Philipse, and H. N. W. Lekkerkerker. Sedimentation of Bidisperse, Uncharged Colloidal Sphere Suspensions: Influence of Viscosity and Irregular Surfaces. *J. Colloid Interface Sci.*, 177(2):427–438, 1996.

[159] R. T. Kovacic and K. E. van Holde. Sedimentation of Homogeneous Double-Strand DNA Molecules. *Biochemistry*, 16(7):1490–1498, 1977.

[160] T. Nicolai and M. Mandel. Dynamic Light Scattering by Aqueous Solutions of Low Molar Mass DNA Fragments in the Presence of NaCl. *Macromolecules*, 22(5):2348–2356, 1989.

[161] Z. Dogic, A. P. Philipse, S. Fraden, and J. K. G. Dhont. Concentration-Dependent Sedimentation of Colloidal Rods. *J. Chem. Phys.*, 113(18):8368–8380, 2000.

[162] N. Errington and A. J. Rowe. Probing Conformation and Conformational Change in Proteins is Optimally Undertaken in Relative Mode. *Eur. Biophys. J.*, 32(5):511–517, 2003.

[163] M. M. Tirado, C. L. Martinez, and J. G. de la Torre. Comparison of Theories for the Translational and Rotational Diffusion Coefficients of Rod-Like Macromolecules. Application to Short DNA Fragments. *J. Chem. Phys.*, 81(4):2047–2052, 1984.

[164] J. G. Garcia de la Torre and V. A. Bloomfield. Hydrodynamic Properties of Complex, Rigid, Biological Macromolecules: Theory and Applications. *Q. Rev. Biophys.*, 14(1):81–139, 1981.

[165] M. P. B. van Bruggen. Preparation and Properties of Colloidal Core-Shell Rods with Adjustable Aspect Ratios. *Langmuir*, 14(9):2245–2255, 1998.

[166] B. Chu and P. J. W. Debye. *Molecular Forces: Based on the Baker Lectures of P. J. W. Debye.* Wiley-Interscience, New York; London, 1967.

[167] M. P. B. van Bruggen, M. Donker, H. N. W. Lekkerkerker, and T. L. Hughes. Anomalous Stability of Aqueous Boehmite Dispersions Induced by Hydrolyzed Aluminium Poly-Cations. *Colloids Surf. A*, 150(1-3):115–128, 1999.

[168] M. P. B. van Bruggen, H. N. W. Lekkerkerker, and J. K. G. Dhont. Long-Time Translational Self-Diffusion in Isotropic Dispersions of Colloidal Rods. *Phys. Rev. E*, 56(4):4394–4403, 1997.

[169] A. Stroobants, H. N. W. Lekkerkerker, and T. Odijk. Effect of Electrostatic Interaction on the Liquid Crystal Phase Transition in Solutions of Rodlike Polyelectrolytes. *Macromolecules*, 19(8):2232–2238, 1986.

Summary

In this thesis several case studies of the sedimentation velocity employing fundamentally different colloidal dispersions are presented. The common feature of these colloids is that they are all inorganic. Since the various colloids studied here have essentially two distinct dominant interactions, i.e. attractive and repulsive interactions, this thesis is, apart from the first two chapters, divided in three parts accordingly. Sedimentation velocity experiments on non-interacting, attractive and repulsive colloids are discussed in, respectively, part two, part three and part four.

After a brief introduction to this thesis in chapter 1, in which also some historical facts are addressed, basic analytical ultracentrifugation theory and experiments are discussed in chapter 2. Along with this discussion some instrument issues are highlighted. The optical systems of the Beckman Coulter^{TM} Optima^{TM} XL-A and XL-I analytical ultracentrifuges that were employed, are reviewed in more detail, with special emphasis on some common pitfalls encountered in analytical ultracentrifugation sedimentation experiments.

In chapter 3, which together with chapter 4 makes up the second part addressing the sedimentation velocity of non-interacting colloids, the existence of discrete single molecular $\{Mo_{132}\}$ Keplerate-type clusters in aqueous solution is demonstrated. Starting from a discrete spherical $\{Mo_{132}\}$ cluster the formation of an 'open' basket type $\{Mo_{116}\}$ defect structure is shown for the first time in solution using analytical ultracentrifugation sedimentation velocity experiments.

The second case study of non-interacting colloids, presented in chapter 4, reveals a method to determine the particle size distribution of, in this case, small colloidal silica spheres via analytical ultracentrifugation. Using this method, the average particle size, variance, standard deviation and relative polydispersity can be obtained from a single sedimentation velocity (SV) analytical ultracentrifugation (AUC) run. The particle size distribution (*psd*) from the enhanced van Holde-Weischet analysis, which also accounts for the dynamic light scattering results quite well, equals the *psd* from a continuous distribution of sedimentation coefficients analysis. The SV AUC interference optical data also yield the specific particle volume, such that distributions of sedimentation coefficients for colloidal spheres can be converted directly to particle size distributions. Our results show that SV AUC experiments may yield a quantitative particle size distribution without a priori knowledge of the particle size and the shape

of the size distribution.

The third part of this thesis, chapters 5–7, illustrates possible effects if the net-interaction results in colloid-colloid attraction. In chapter 5, a sedimentation velocity analytical ultracentrifugation study on spherical polyoxometalates that exhibit supramolecular structure formation is reported. Here, we show that the self-assembly can be monitored by UV-Vis spectrophotometry. The particle shape and absolute molar weight of the $\{Mo_{72}Fe_{30}\}$ monomers and trends in the sedimentation coefficient distributions for 'giant' vesicles are determined from sedimentation velocity experiments. For the monomers, the procedure of the sedimentation velocity data analysis comprises a sequence of analyses involving the van Holde-Weischet analysis, 2-dimensional spectrum analysis and Genetic Algorithm optimization to obtain sedimentation coefficients, diffusion coefficients and molecular weights from globally fitted multi-speed sedimentation velocity experimental data using supercomputers. The analysis of experimental data via this method is, to our knowledge, reported for the first time. Combined with dynamic light scattering data, the sedimentation velocity experiments reveal that after 3 years at room temperature, the vesicles are constituted of two $\{Mo_{72}Fe_{30}\}$ layers. This suggests that the single-layer vesicles are thermodynamically meta-stable. Furthermore, we found proof that in aqueous solution the $\{Mo_{72}Fe_{30}\}$ monomers release small solutes that are possibly ligands. The critical aggregation concentration for $\{Mo_{72}Fe_{30}\}$ is at least 2 to 4 times smaller than reported elsewhere.

The self-association of $\{Mo_{72}Fe_{30}\}$ monomers to form large superstructures studied via SV AUC, is followed by a theoretical treatment of a monomer-dimer self-association in chapter 6. In this chapter, an equation is derived for the linear concentration dependent sedimentation velocity of attractive colloids that reversibly associate into dimers. Within our approach that is based on an anisotropic interaction potential, the magnitude of this concentration dependence is primarily determined by the dimerization equilibrium constant. We also show how this dimerization affects the osmotic equation of state and conclude that, in principal, both the sedimentation velocity and the sedimentation-diffusion equilibrium may be employed to determine the binding energy from the equilibrium constant for associating colloids or macromolecules, at concentrations low enough for only dimerization to occur.

The model for the concentration dependent sedimentation velocity of attractive colloids, discussed in chapter 6, is used in chapter 7 to interpret experimental results from SV AUC measurements on magnetic colloids. In the latter chapter a systematic analytical ultracentrifugation study on the concentration dependent sedimentation velocity of magnetic iron oxide (Fe_3O_4) colloids as a function of magnetic dipole moment, tuned by adjusting the particle volume is presented. The sedimentation velocity behavior of the smallest particles, core diameter $\approx 4.8\,\mathrm{nm}$, resembles that of isotropic repulsive spheres. On increase of the dipole moment, however, a sharp transition occurs to

a large, still linear positive concentration dependence, manifesting a strong effect of dipolar attractions. We compare our observations with calculations based on a pair-distribution function, as well as a phenomenological model (chapter 6) that quantifies the concentration dependent sedimentation rate via the mass action law for reversible colloid-colloid association. Furthermore, we show that colloids with sufficiently large magnetic dipoles exhibit sedimentation velocity boundary broadening. Increasing the concentration of such colloids, shifts the sedimentation coefficient distribution towards larger sedimentation coefficients in contrast to repulsive colloids.

Finally, in the fourth part of this thesis a system of colloidal repulsive rods is investigated that is in many aspects very different from the systems employed in the previous case studies. SV AUC experiments were conducted to study the effect of ionic strength on the concentration dependent sedimentation velocity for a dispersion of rigid boehmite-silica rods. Experimental results are compared to predictions from theory for hard rods using input parameters obtained from transmission electron microscopy and static light scattering. Addition of salt lowers the sedimentation velocity concentration dependence, which is eventually similar to the prediction from theory for uncharged rigid rods. Above 50 mM NaCl the rods gel into a fine network that tends to settle in the earth's gravitational field. Furthermore, we compare SV absorbance and interference optical data and discuss which optics is the most suitable for boehmite-silica dispersions. We also report a convenient method to determine the specific particle volume of core-shell colloids from interference optical data.

Samenvatting in het Nederlands voor een Breder Publiek

Vrijwel iedereen is bekend met centrifugatie, zeker wanneer men beschikt over een wasmachine of een sla-centrifuge. Elk wasprogramma bevat een stap waarin de trommel met natte was snel wordt rondgedraaid waarbij het wasgoed door de trommel wordt tegengehouden en het water door de gaatjes naar buiten wordt geslingerd. Het water dat in de rondte draait, vlucht weg uit het midden door de centrifugale of middelpuntvliedende kracht. Vandaar de termen middelpuntvliedend (vlieden = vluchten) en centrifugaal (centrum = midden en fugere = vluchten). Het transport van water tijdens centrifugatie in een wasmachine is analoog aan het transport van materiaal bestaande uit kleine deeltjes in een analytische ultracentrifuge. Het aardse zwaartekrachtveld, waarin krachten naar de aarde toe zijn gericht, is goed te vergelijken met een centrifugaal veld waarbij de krachten vanuit het middelpunt (radiaal) naar buiten gericht zijn.

Naast de centrifugatie van was in een wasmachine is er nog een voorbeeld van sedimentatie waarmee de meeste mensen bekend zullen zijn: wanneer men een glazen knikker aan een lucht-water oppervlak plaatst en vervolgens loslaat, dan zinkt de knikker naar de bodem van het vat waarin zich het water bevindt. In eerste instantie zal de knikker steeds sneller zinken totdat de wrijvingskracht (weerstand) even groot is als de zwaartekracht die de knikker ondervindt. De knikker zal vanaf dat moment zinken met een constante snelheid. Dit wordt de sedimentatiesnelheid wordt genoemd. De snelheid hangt af van de grootte van de knikker, een bonk (grote knikker) zinkt immers sneller dan een pinkie (hele kleine knikker), maar ook van de vorm. Een bolvormig object zinkt sneller dan wanneer het object een andere vorm zou hebben (vierkant- of staafvormig).

Met een analytische ultracentrifuge kan men de sedimentatiesnelheid meten van deeltjes die aanvankelijk gelijkmatig verdeeld zijn over een vloeistof die zich in een afgesloten cel in de rotor (lees: wastrommel) bevindt. Het uitzakken van de deeltjes wordt waargenomen door het bepalen van de doorlaatbaarheid van licht of door de breking van het licht te meten aan de hand van interferentie patronen (zie omslag van dit proefschrift). In principe kan men met een analytische ultracentrifuge twee soorten metingen verrichten. De eerste is de reeds genoemde sedimentatiesnelheid, de tweede is

een sedimentatie-diffusie evenwichtsmeting. Bij deze tweede soort meting wordt er net zo lang gedraaid totdat een evenwichtsconcentratie verdeling van deeltjes is ontstaan die niet meer verandert in de tijd. Een sedimentatie-diffusie evenwichtsverdeling is analoog aan de barometrische hoogte verdeling. Mensen die wel eens de bergen in gaan, zijn hiermee bekend. Naarmate men steeds verder klimt, wordt de lucht ijler. De concentratie van luchtmoleculen wordt steeds lager met toenemende hoogte, gemeten vanaf het aardoppervlak. Wanneer men het verloop van deze concentratie met toenemende hoogte kent, kan men het gewicht van de desbetreffende moleculen of deeltjes bepalen.

In dit proefschrift staan enkele studies van de sedimentatiesnelheid van hele kleine deeltjes beschreven. Deze kleine deeltjes, ook wel colloïden genoemd (van het Griekse woord $\kappa o \lambda \lambda \alpha$, wat 'lijm' betekend), hebben een afmeting van een miljoenste tot een duizendste van een millimeter (nanometer-micrometer). Colloïden zijn dus groter dan atomen, maar veel kleiner dan de dikte van ons hoofdhaar. Door hun afmeting kunnen deze deeltjes met moderne technieken als elektronenmicroscopie over het algemeen goed worden waargenomen. Het gedrag van deeltjes waarvan de afmeting tussen een nanometer en een micrometer ligt wordt in grote mate beïnvloed door warmte beweging die ook Brownse beweging wordt genoemd. Deze warmte beweging, die analoog is aan diffusie, maakt onder andere dat de natuurkundige eigenschappen van deze deeltjes vertaald kunnen worden naar het gedrag dat atomen en moleculen vertonen. Dit laatste is tevens de verklaring dat er veel fundamenteel (basaal) onderzoek wordt gedaan naar colloïden. Dit proefschrift is daar een voorbeeld van.

De hier onderzochte colloïden zijn onder te verdelen in drie categorieën, die elk in een apart deel van dit proefschrift aan de orde komen. Het eerste deel is bedoeld als achtergrond informatie voor analytische ultracentrifugatie. In de drie delen die hierop volgen, worden achter een volgens onderzoeken naar de sedimentatiesnelheid van niet-wisselwerkende deeltjes, van deeltjes die elkaar aantrekken en van deeltjes die elkaar afstoten beschreven. In de laatste twee gevallen, elkaar aantrekkende en afstotende deeltjes, staat, naast de sterkte van deze wisselwerking, de verandering centraal van de sedimentatiesnelheid als functie van de deeltjes concentratie.

Na een korte inleiding, waarin enkele historische feiten worden aangehaald, volgt in hoofdstuk 2 een beschouwing van de basale theorie die ten grondslag ligt aan analytische ultracentrifugatie. Tevens worden in deze beschouwing de twee typen metingen beschreven (sedimentatiesnelheids- en sedimentatie-diffusie evenwichtsmetingen), evenals de belangrijkste technische aspecten van de gangbare analytische ultracentrifuge.

In hoofdstuk 3, dat samen met hoofdstuk 4 het tweede deel van dit proefschrift vormt, wordt verslag gedaan van de karakterisering met behulp van sedimentatiesnelheidsmetingen van twee soorten kleine bolvormige moleculen bestaande uit onder meer 132 molybdeen atomen (een metaal) en 30 liganden (eenheden die een complex vormen

met in dit geval molybdeen). Deze liganden zijn voor de twee soorten moleculen respectievelijk acetaat (acetaat is de geconjugeerde base van azijnzuur) en sulfaat. De in hoofdstuk 3 bestudeerde bolvormige moleculen zijn allemaal precies even groot. De gelijkvormigheid en de uniforme afmetingen, worden in de colloïdchemie aangeduid met *monodispers* (mono = hetzelfde, dispers = verdeling). Met dit onderzoek werd er voor het eerst vastgesteld dat de betreffende deeltjes ook in een waterige oplossing bestaan. Bovendien bleek uit dit onderzoek dat een bolvormig deeltje van molybdeen en acetaat een bolkapje kan afsplitsen, iets wat tot nu toe alleen was aangetoond voor gekristalliseerde bolletjes.

Wanneer kleine deeltjes in het laboratorium gemaakt worden, zijn deze meestal niet gelijkvormig en hebben ze geen uniforme afmetingen. Met andere woorden, de synthetische deeltjes zijn *polydispers* (poly = veel, dispers = verdeling). In de fysische en colloïdchemie worden vaak deeltjes in een vloeistof bestudeerd om fysische eigenschappen, waaronder fasescheiding, vast te stellen en beter te kunnen begrijpen. De grootte van de te bestuderen deeltjes, evenals de deeltjes vorm- en grootte verdeling (variëteit in vorm en grootte) bepalen in zekere mate het fysisch-chemisch gedrag. Het is dus belangrijk om te weten wat de karakteristieken van deze deeltjes zijn voordat men het gedrag als bijvoorbeeld fasescheiding gaat bestuderen. In hoofdstuk 4 staat beschreven hoe men op een model onafhankelijke manier de vorm- en grootte verdeling van in dit geval kleine deeltjes van glas met behulp van sedimentatiesnelheidsmetingen kan bepalen. Het blijkt dat men met de analytische ultracentrifuge verkregen resultaten redelijk goed de experimentele data van dynamische lichtverstrooïngsexperimenten kan beschrijven.

In hoofdstuk 5 wordt er teruggegrepen op gelijksoortige deeltjes als beschreven in hoofdstuk 3, bolvormige deeltjes die monodispers zijn voor wat betreft vorm en grootte. Deze deeltjes zijn onder andere opgebouwd uit molybdeen en ijzer. Het fundamentele verschil met de deeltjes in hoofdstuk 3 is dat deze deeltjes elkaar relatief sterk aantrekken en zich aan elkaar binden. Het gevolg is het ontstaan van wederom bolvormige grote structuren bestaande uit kleine molybdeen-ijzer bollen. Opmerkelijk is dat deze grote structuren hol zijn (bolschil), net als een voetbal. Dus zowel de bouwstenen als de grotere structuren zijn beide bolvormig. Hiernaast moet nog worden opgemerkt dat de kleine molybdeen-ijzer bouwstenen monodispers zijn, daarentegen zijn de grotere structuren behoorlijk polydisperse. Zowel de bouwstenen als de grote structuren zijn uitvoerig gekarakteriseerd via sedimentatiesnelheidsmetingen. Omdat de grote structuren pas na lange tijd gevormd zijn, is de bewaartijd, evenals de temperatuur gevarieerd. Zo is in dit onderzoek de vorm en de massa van de ijzer-molybdeen bouwstenen bepaald. Voor deze bepaling is gebruik gemaakt van geavanceerde computer technieken zoals relationele data-bases, supercomputer netwerken in Texas die in dit geval vanuit Utrecht

werden aangestuurd en high-tech analyse software met onder andere een Genetic Algortihm opmization die voor het eerst is toegepast op experimentele sedimentatiesnelheid analytische ultracentrifugatie data. Verder is er voor het eerst vastgesteld dat de grote bolschil structuren niet uit een enkele laag van molybdeen-ijzer bollen zijn opgebouwd, maar dat deze ook voorkomen als een dubbele bolschil structuur. Tot op de dag van vandaag veronderstelde men dat de grote structuren zijn opgebouwd uit een enkele laag molybdeen-ijzer bollen. Voordat er vorming van grote structuren optreedt, moet de concentratie van de bouwstenen een bepaalde waarde hebben. Onder deze zogenoemde kritische aggregatie concentratie worden er geen grotere structuren gevormd. Met behulp van analytische ultracentrifugatie is er hier vastgesteld dat de kritische aggregatie concentratie veel lager ligt dan tot nu toe werd gerapporteerd. De twee hierop volgende hoofdstukken gaan ook over deeltjes die elkaar aantrekken, toch is het associatiegedrag (het samen plakken van deeltjes) volledig anders.

Hoofdstuk 6 en 7, die onderdeel zijn van het derde deel (aantrekkende deeltjes) van dit proefschrift, zijn een verhandeling over in dit geval magnetische deeltjes die, wanneer zij zich in een kop-staart configuratie bevinden (de Noordpool van het ene magnetische deeltje nadert de Zuidpool van het andere magneetje), elkaar aantrekken en tijdelijk aan elkaar blijven plakken. Naar aanleiding van het sedimentatiesnelheidsgedrag dat is vastgesteld aan de hand van observaties en resultaten afkomstig van analytische ultracentrifugatie experimenten aan magnetische bolvormige deeltjes, die relatief polydispers zijn, is hier een fenomenologische theorie opgesteld om de sedimentatiesnelheid voor deeltjes die elkaar aantrekken te kunnen voorspellen en te kunnen interpreteren. Deze theorie met de bijbehorende wiskundige afleiding, die wordt vergeleken met twee al bestaande theoretische modellen, staat beschreven in hoofdstuk 6. De magnetische deeltjes, bestaande uit ijzeroxide (roest), kunnen in principe ketens vormen wanneer de concentratie en/of het magnetisch dipool moment (sterkte van de magneet) voldoende groot is. Door middel van de reeds eerder genoemde Brownse beweging (diffusie), waardoor de deeltjes voortdurend in willekeurige richtingen door de colloïdale dispersie verplaatst worden, kunnen de deeltjes elkaar naderen en botsen. Een botsing kan resulteren in de vorming van een complex of associaat (meerdere deeltjes die aan elkaar vast zitten en één groter object vormen). Voor de experimenten die hier beschreven zijn, is de concentratie van magnetische deeltjes dusdanig dat de vorming en de aanwezigheid van doubletten aangetoond kunnen worden met behulp van analytische ultracentrifugatie. Doubletten zijn twee enkele deeltjes die aan elkaar plakken en daarmee in feite een enkel groter deeltje vormen (dumb-bell of ook wel halter genoemd). De levensduur van een dergelijk doublet, in combinatie met de relatief lage concentratie van magnetische deeltjes, is niet lang genoeg om nog een derde deeltje tegen te komen dat dan op zijn beurt weer vast zou kunnen plakken aan de reeds twee geassocieerde deeltjes. Sedimentatiesnelheid analytische ultracentrifugatie experimenten, experimentele resultaten en

vergelijkingen met de eerder genoemde theoretische modellen staan beschreven in hoofdstuk 7. In vergelijking met de monodisperse molybdeen-ijzer bollen die grote bolschil structuren vormen bestaande uit vele molybdeen-ijzer bollen (grootte orde 1000), is het lineaire associatiegedrag van de relatief polydisperse magnetische ijzeroxide deeltjes die ketens vormen, in vele opzichten anders.

Het vierde en laatste inhoudelijke deel van dit proefschrift is een uiteenzetting van experimenten met een colloïdale dispersie bestaande uit kleine starre boehmiet staven die zijn voorzien van een dun laagje glas (silica). Deze deeltjes verschillen in vele opzichten van de deeltjes waarvan het sedimentatiegedrag is onderzocht zoals beschreven in voorafgaande hoofdstukken (hoofdstuk 3 tot en met 7). Deze verschillen zijn: ten eerste de vorm (staafvormig in plaats van bolvormig), ten tweede de afmeting (de staven zijn groter dan alle andere deeltjes beschreven in dit proefschrift) en ten derde als gevolg van elektrische lading stoten de boehmiet-silica elkaar af. Deze verschillen resulteren in een niet vergelijkbare concentratie afhankelijke sedimentatiesnelheid. Met andere woorden, de sedimentatiesnelheid neemt af met toenemende deeltjes concentratie, dit in tegenstelling tot deeltjes die elkaar aantrekken waardoor de sedimentatiesnelheid toeneemt met de deeltjes concentratie. Door de deeltjes concentratie en de hoeveelheid toegevoegd (keuken) zout te variëren, is het sedimentatiegedrag van de desbetreffende boehmiet-silica staven bestudeerd. Ionen, geladen atomen of moleculen die in dit geval afkomstig zijn van het toegevoegde zout, schermen de lading af van de staven waardoor deze elkaar minder sterk afstoten. Experimentele resultaten worden in hoofdstuk 8 vergeleken met een theorie die de concentratie afhankelijke sedimentatie van ongeladen staafvormige deeltjes voorspelt. De resultaten bevestigen de veronderstelling dat afstoting door elektrische lading de concentratie afhankelijkheid van de sedimentatiesnelheid vergroot. Door toevoeging van zout reduceert deze afhankelijkheid uiteindelijk tot een waarde die redelijk te vergelijken is met de theorie.

List of Publications

This thesis is partly based on the following articles:

Published Articles

- K. L. Planken, G. H. Koenderink, R. Roozendaal, and A. P. Philipse. Monodisperse DNA Restriction Fragments: I. Synthesis and Characterization. *J. Colloid Interface Sci.*, 291(1):120–125, 2005.
- G. H. Koenderink, K. L. Planken, R. Roozendaal, and A. P. Philipse. Monodisperse DNA Restriction Fragments: II. Sedimentation Velocity and Equilibrium Experiments. *J. Colloid Interface Sci.*, 291(1):126–134, 2005.
- K. L. Planken, S. Roy, R. Kim, D. v. d. Mandele, and W. K. Kegel. Direct Evidence on the Existence of $\{Mo_{132}\}$ Keplerate-Type Species in Aqueous Solution. *Inorg. Chem.*, 46(21):8469–8471, 2007 (chapter 3).

Articles to be Submitted

- K. L. Planken, B. W. M. Kuipers, and A. P. Philipse. Model Independent Determination of Colloidal Silica Size Distributions via Analytical Ultracentrifugation (chapter 4).
- K. L. Planken, W. K. Kegel, M. Bode, S. J. Veen, A. A. Verhoeff, B. M. W. Kuipers, and A. P. Philipse. Sedimentation Velocity of Self-Associating $\{Mo_{72}Fe_{30}\}$ Monomers (chapter 5).
- K. L. Planken, M. Klokkenburg, J. Groenewold, and A. P. Philipse. Concentration Dependent Sedimentation of Attractive Magnetite Colloids with Tunable Dipolar Attractions and Thermodynamics of Dimerization (chapters 6 and 7).
- K. L. Planken and A. P. Philipse. Salt- and Concentration Dependent Sedimentation Velocity of Rigid Colloidal Rods (chapter 8).

Curriculum Vitae

Karel Lodewijk Planken, the author of this thesis, was born on the 1st of November 1975 in s'-Gravenhage (The Hague, The Netherlands), the residence of the Dutch government. From 1985 till 1989 he lived in Germany, where he attended a German elementary school. After finishing the *Vrije School* (Waldorf or Rudolf Steiner school), he obtained his *VWO diploma* in 1995 at the Teisterband College Culemborg in Zeist (The Netherlands). From 1995 till 1997 he fulfilled his military service at the Land Forces of the Royal Dutch Army, Communication and Control Squad (1 year) after which he was employed as a taxi driver, garbage collector and as a fellow worker at a rubber factory. Karel Planken was also part-time employed as a personal fitness trainer from 2001-2004.

In 1997 he decided to study tropical agriculture at the *Internationale Agrarische Hogeschool Larenstein* in Deventer (The Netherlands). Here, he rediscovered how inspiring chemistry can be. In order to be admitted to the Utrecht University to study chemistry, he obtained the required *VWO* physics certificate (cum laude) at the James Boswell Institute in Utrecht. In 1998 Karel Planken started studying chemistry. He passed al physical chemistry and biochemistry exams that were offered. In 2003 he finished his chemistry study and obtained his Master of Science degree with distinction (cum laude), with a minor in biochemistry (in a physico-biochemistry setting) and a major in physical and colloid chemistry. His minor and major both concerned the same research project at the Van 't Hoff Laboratory for Physical and Colloid Chemistry on monodisperse DNA restriction fragments. This project involved the synthesis of a model system, specifically designed to investigate the effects of limited flexibility on the transport properties of elongated macromolecules.

After graduating chemistry he joined the Van 't Hoff Laboratory for Physical and Colloid Chemistry as a PhD student under the supervision of Prof. Dr. Albert P. Philipse. During his PhD study Karel Planken actively helped to design the Master class Colloid Chemistry program for Highschool students. He designed and compiled the Master class Colloid Chemistry Reader and also designed the experiments.

In 2006 and 2007 he was a co-instructor at the *UltraScan* workshops in San Antonio Texas (USA). Plus in 2006 in London (UK) and in 2007 Hannover (Germany) at, respectively, the 15^{th} and 16^{th} International Symposium on Analytical Ultracentrifugation. *UltraScan* is a comprehensive data analysis software package for analytical

ultracentrifugation experiments. Karel Planken also worked on the *UltraScan* documentation and software improvements (detecting bugs, try outs and suggestions for improvements).

The research results he obtained during his PhD study are reported in this thesis and were presented at international conferences as the 18^{th} Conference of the European Colloid and Interface Society (ECIS) in Almeria (Spain), *UltraScan* workshop in San Antonio Texas (USA), 15^{th} AUC-symposium in London (UK), 16^{th} AUC-symposium in Hannover (Germany) and at the fair *Het Instrument* in the Jaarbeurs in Utrecht (requested by Beckman Coulter Netherlands B.V.), but also at Dutch conferences as the *Vloeistoffen en Grensvlakken* (NWO/CW) meeting in Lunteren (The Netherlands).

After his PhD study that ended in November 2007, he worked three months as a teacher in physical pharmacy at the Biopharmacy and Pharmaceutical Technology section of the Pharmaceutical Sciences department Utrecht University. Currently he is a researcher at the Van 't Hoff Laboratory for Physical and Colloid Chemistry.

Word of Gratitude

I thank the Van 't Hoff Laboratory for the opportunity of conducting my PhD study and making available a spectrum of equipment and great instruments, especially the beautiful analytical ultracentrifuge(s). I have to admit that our lab houses many friendly and certainly clever people.

Dear Prof. Dr. A.P. Philipse, a.k.a. Albert, I thank you for your support. I especially appreciated your help with scientific writing. Also I enjoyed our collaboration when we were working together on teaching. Although we have had some hard times when I postponed the physical interpretation of my research results – because my attention was drawn to technical aspects of the experiments and the analytical ultracentrifuge – once some potential explanations popped up you were unstoppable. Thanks for that, I hope you enjoyed it as much as I did. In the end, I think that when we are conducting physical-chemistry research we complement each other quite well.

Here I express my gratitude to all my present and former group-members who were responsible for the nice atmosphere and who were almost always available for questions (answered or not) I had regarding my work at the lab. Henk Lekkerkerker, Willem Kegel, Jan Groenewold, Gert Jan Vroege, Andrei Petukhov, Ben Erné, Martijn Oversteegen, Roel Dullens, Dirk Aarts, Rik Wensink, Maria Claesson, Gijsje Koenderink, Stefano Saccana, Alan Wouterse, Mark Klokkenburg, Bonny Kuipers, Maurice Mourad, Emile Bakelaar, Sandra Veen, Lia Verhoeff, Volkert de Villeneuve, Daniela Kraft, Dima Byelov, Marieke Bode, and Dominique Thies-Weesie, you were all in one way or another indispensable for the success of my stay at the lab. Marina Uit de Bulten-Weerensteyn and Mieke Lanen, I enjoyed working with you and thank you for all your (mental) support. Jan Groenewold, our useful discussions were always a pleasure for me, thank you. Kees de Kruif I thank you for carefully proofreading this thesis and I very much enjoyed our discussions.

Dear Mark, at last I can thank you for the great time we had. I will always remember you and our tight, strong and very successful collaboration that started in 1998. Who could have ever thought when we started our chemistry studies that we would end up working together as PhD students on the same project at the same lab? In the end I sediment your beautiful magnetite colloids.

Andrei Petukhov, thank you for all your help and kindness. I cherish the few Russian words you learned me. Dima Byelov, the new post-doc you employed, became my room

mate who freshened up the vibes in our room. Sandra and Dima thanks for being nice room mates and giving me the necessary criticism. Volkert de Villeneuve, I enjoyed sharing our LaTeX troubles and I thank you for all your help, including the corrections and suggestions concerning these acknowledgements.

Dear Borries Demeler, I still remember our first contact (May 12, 2004) as if it was yesterday. At that time I discovered the existence of *UltraScan* (version 6.0) and I questioned you about the speed prediction and the value σ (reduced effective molecular weight). I made the classical error regarding the unit of the gas constant, which is expressed in erg K^{-1} mol^{-1} in the USA, whereas we express it in S.I.-units in Europe (J K^{-1} mol^{-1}). What I found very surprising when I attended the *UltraScan* workshop in the summer of 2004, is that you, Helmut Cölfen and I lived in the same region of Germany (Ruhrpott), that we are all three involved in AUC and that we met in Texas. What are the odds of that? Admittedly, I would not have come this far without you and your wonderful software package. Your dedication and devotion to AUC and biophysical science are admirable. Being a co-instructor at the *UltraScan* workshop in Texas and at the AUC symposia (Hannover, London) was really a great pleasure for me. The monthly *UltraScan* Access Grid seminars via the internet were/are really a success. I have learned many things from those seminars and I strongly recommend everybody who is working with AUC, especially beginners, to attend them. I should mention here the very special and kind people you have gathered around you as well. Emre Brookes, the implementation of the GA optimization is really a step forward in the AUC data analysis, something which also contributed to this thesis. Jeremy Mann and Virgil Shirf, I thank you for your kindness, patience and contributions to the great atmosphere at the workshops that I assisted in San Antonio.

Helmut Cölfen I thank you for the nice contact we had and especially for taking part in the thesis defense committee. Antje Völkel, I cherish and will remember times spent together at conferences, it was really nice.

I thank Beckman Coulter Nederland B.V. for the financial contributions that enabled me to serve as a co-instructor at the *UltraScan* workshops held in February 2006 and June 2007 in San Antonio (Texas, USA). Gerrit Portiér and Melle de Jong are thanked for their helpfulness whenever that was needed. I appreciated your almost regular visits. Ronald de Vries I especially thank you for sharing many technical insights regarding the AUC instrument. It was a great pleasure to tinker together with the AUC's to eventually assess what should be repaired or replaced. At last the XL-A at the Van 't Hoff Laboratory is functioning very well with a huge lamp intensity that is even not comparable to when the machine was delivered.

Dear Aad and Joke Planken-Korving my beloved parents, at last I formally thank you with this thesis for all your mental and financial support. Your faith in me, but also your trust and confidence in my work were and certainly still are vital for my success.

Without you I would never have accomplished my chemistry studies, set aside finishing a PhD study in physical-chemistry. In fact there are no words to express my gratitude to you. I deeply respect your way of thinking and attitude to life. Please remember that I cherish and love you, Karel. Nils Planken, my one and only big brother, I respect your achievements in life and especially in science. I am aware that it was not easy at all for you, but let me thank you for the things we share. I am really proud of you and Beatrijs Hauer. Here I also thank all the members of the families Planken and Korving who always showed interest in what I was doing.

Francien Jonge Poerink, how can I thank you for your support? I still wonder how you could bear living with me and my PhD study (or is it the other way around?). What can I say? I am out of words... love Karel.

Christie and Leo van Witsen-Jonge Poerink I thank you for the nice and sometimes highly necessary distraction. You are both very special and hearty people. Cas Bool, I really felt the need to express here that I value our friendship, which already lasts for more than thirty years. Thanks for being there for me.

Joeri Saal, I now take this opportunity to thank you for your help and support during the start of my chemistry studies. In my opinion, your help also contributed to the success of this thesis, many thanks. Kees van Veen I thank you for connecting me to the internet that I used a lot for the AUC data analysis and other PhD work. I think what the Dutch say is true: *beter een goede buur dan een verre vriend*. Finally I thank Maria Pollman for carefully proofreading the summary in Dutch, it has really improved.